UNIVERSITY OF HELSINKI REPORT SERIES IN PHYSICS

HU-P-D211

SEARCH FOR THE HIGGS BOSON IN THE ALL-HADRONIC FINAL STATE USING THE CDF II DETECTOR

Francesco Devoto

Division of Elementary Particle Physics
Department of Physics
Faculty of Science
University of Helsinki
and
Helsinki Institute of Physics
Helsinki, Finland

ACADEMIC DISSERTATION

To be presented for public criticism, with the permission of the Faculty of Science of the University of Helsinki, in the auditorium E204 of the Physicum building, Gustaf Hällströmin katu 2, on November 13^{th}, 2013, at 14 o'clock.

Helsinki 2013

Supervisor:

Prof. Risto Orava
Department of Physics
University of Helsinki
Finland

Reviewers:

Prof. Richard Brenner
Department of Physics & Astronomy
Uppsala Universitet
Sweden

Dr. Marek Tasevsky
Institute of Physics of Prague
Academy of Sciences of the Czech Republic
Czech Republic

Opponent:

Dr. Christophe Royon
CEA Saclay
France

Report Series in Physics HU-P-D211
ISSN 0356-0961
ISBN 978-952-10-8942-8 (printed version)
ISBN 978-952-10-8943-5 (electronic version)
http://ethesis.helsinki.fi
Unigrafia

Helsinki 2013

To Alice, Dulcinea, Esmeralda . . .

Abstract

This thesis reports the result of a search for the Standard Model Higgs boson in events containing four reconstructed jets associated with quarks. For masses below 135 GeV/c^2, the Higgs boson decays to bottom-antibottom quark pairs are dominant and result primarily in two hadronic jets. An additional two jets can be produced in the hadronic decay of a W or Z boson produced in association with the Higgs boson, or from the incoming quarks that produced the Higgs boson through the vector boson fusion process. The search is performed using a sample of $\sqrt{s} = 1.96$ TeV proton-antiproton collisions corresponding to an integrated luminosity of 9.45 fb^{-1} recorded by the CDF II detector. The data are in agreement with the background model and 95% credibility level upper limits on Higgs boson production are set as a function of the Higgs boson mass. The median expected (observed) limit for a 125 GeV/c^2 Higgs boson is 11.0 (9.0) times the predicted standard model rate.

Author's Contribution

This dissertation presents the work the author carried out in the field of experimental particle physics during the years 2010 till 2012. This monograph describes in all details the search for the Standard Model Higgs boson in the all-hadronic final state at the Tevatron proton-antiproton collider. The results were published in February 2013:

- T. Aaltonen *et al.* (CDF Collaboration), *Search for the Higgs boson in the all-hadronic final state using the full CDF data set*, **JHEP02(2013)004**.

The analysis described in this dissertation had been carried out in collaboration with other three researchers of the Accademia Sinica of Taiwan. The author's main contribution to the analysis was in developing the *b*-jet energy correction, the classification of Higgs bosons events, and the VBF-NN correction. He also helped in the testing of the Tag Rate Function and in the final limit calculation.

Acknowledgements

First of all I would like to express my gratitude to my supervisor Prof. Risto Orava, who gave me the opportunity to work and increase my knowledge in particle physics. Thanks to him I had the opportunity to follow my dreams and for this I will be eternally grateful!

I would like to thank Dr. Christophe Royon for being the opponent for my thesis defence and Prof. Richard Brenner and Dr. Marek Taševský by reviewing this thesis and for the precious advices given.

I am very grateful to Dr. Yen-Chu Chen, Dr. Ankush Mitra, and Dr. Song-Ming Wang for the opportunity to collaborate with them in this research and for their endless patience. They were an essential guide for my professional growth and there are not words which can describe my grateful. Thank you very much!

My deep gratitude goes to Prof. Paul Hoyer, Prof. Katri Huitu, Dr. Tuula Mäki, and Dr. Kenneth Österberg for reading parts of this thesis and giving helpful comments.

A very special thanks goes out to Prof. Masud Chaichan, Prof. Paul Hoyer, and Prof. Katri Huitu for having incite my love for theoretical physics, their lectures were source of charm and inspiration.

I am thankful to Dr. Mikko Sainio for having answered all my bureaucratic questions during these years, his door was always open, and to Prof. Julin Rauno for the financial support, indispensable for the travels to Fermilab.

A particular grateful goes to Timo Aaltonen and Erik Brücken for their friendship and for the endless support given to me by answering all my questions.

I can not forget all the friends that I met during these years here in Helsinki Andrea, Christian, Giacomo, Michela, Stefano, Viola, and, in particular, Sam for often helping me in language matters.

I am extremely grateful to my parents for their support and for letting me fulfill my dreams in complete freedom.

Last but not least I would like to thank the Little Red Fox for being always in my mind and heart, for Her support and Her wonderful smile, because there is always a Her, sometimes real, sometimes not and other times is just a memory...

Contents

Introduction

The Higgs boson is the physical manifestation of the hypothesized mechanism that provides mass to fundamental particles in the Standard Model theory.
Direct searches at the Large Electron-Positron (LEP) collider, the Tevatron and the Large Hadron Collider (LHC) have excluded the Standard Model Higgs boson masses, except within the range $122-128$ GeV/c^2. In July 2012, the ATLAS and CMS collaborations reported the observation of a Higgs-like particle at a mass of ~ 125 GeV/c^2, and the Tevatron reported evidence for a particle decaying into a bottom-antibottom quark pair produced in association with a W/Z boson for masses within the range $120-135$ GeV/c^2.

The Tevatron accelerator collided proton and antiproton with a central of mass energy equal to 1.96 TeV and a final luminosity up to $10^{32}\,\mathrm{cm}^{-2}\mathrm{s}^{-1}$.
The Collider Detector at Fermilab (CDF) was one of the two experimental apparatuses located along its ring, together with the DØ experiment. Until the Tevatron shut-down on 30 September 2011, CDF collected data corresponding to ~ 12 fb^{-1} of integrated luminosity, which allows the research of the fundamental interactions. One of its most important observations was the discovery of the top-quark in 1995. The CDF collaboration is still focusing on the research of possible new physical phenomena, such as supersymmetric and exotic models, the research of the Higgs boson and precision measurements of the physics parameters of the top-quark.

This thesis reports the results for a search of the Standard Model Higgs boson in events containing four reconstructed jets associated with quarks (all-hadronic final state). The search is performed using a sample of proton-antiproton collisions corresponding to an integrated luminosity of 9.45 fb^{-1} recorded by the CDF detector.

The dominant Standard Model Higgs boson production modes are direct production with gluons ($gg \to H$) and quarks ($q\bar{q} \to H$). The most sensitive searches at the Tevatron are based on Standard Model Higgs boson decays to bottom-antibottom quark pairs ($b\bar{b}$) in the hypothesis of low mass Higgs ($m_H < 135\,\mathrm{GeV}/c^2$).

Two production mechanisms are investigated in this thesis: vector boson fusion (VBF) and associated vector boson production (VH). The VBF channel identifies the process $p\bar{p} \to q\bar{q}'H \to q\bar{q}'b\bar{b}$, where two incoming quarks each radiate a weak boson, which subsequently fuses into a Higgs boson. The VH channel denotes the process $p\bar{p} \to W/Z + H \to q\bar{q}' + b\bar{b}$. In both channels, the Higgs boson decays to $b\bar{b}$, and is produced in association with two other quarks ($q\bar{q}'$). Data is tested against the hypothesis of the presence of Higgs boson with mass in the range $100 \leq m_H \leq 150\,\mathrm{GeV}/c^2$.

Searches for a Higgs boson performed in other final states, e.g. leptons, jets, and missing energy have the advantage of a smaller background, but the Higgs boson signal yield is also very small. The all-hadronic search channel has larger potential signal contributions but suffers from substantial QCD multi-jet background contributions, the $b\bar{b}$ signature is overwhelmed by the QCD $b\bar{b}$ production.

Searches for events where the Higgs boson is produced in association with a vector boson ($V = W$ or Z) are more promising. The VH associated production cross section is smaller by an order of magnitude compared to the direct production, but the identification of the accompanying vector boson reduces the QCD background, making searches for VH the most sensitive one at low Higgs-boson mass.

The hadronic modes investigated in this search exploit the larger branching fraction and thus have the largest signal yields among all the search channels at CDF. The major challenge is the modeling and suppression of the large background from QCD multi-jets.

The experimental resolution of the invariant mass of the two b-jets, m_{bb}, has a significant effect on the sensitivity of this search. To improve the m_{bb} resolution, a neural network is trained to estimate the correction factor required to obtain the best possible estimate of the parent b-parton energy from the measured jet energy.

The critical component to this analysis is an accurate prediction of the QCD background. A data driven model is devised to predict the two-tagged background from the background-rich single-tagged data. The assumption is that the two-tagged background distribution has the same shape as the single-tagged distribution, but that they diverge by a scale factor. The scale factor is called the Tag Rate Function (TRF). The TRF is the probability of a jet being b-tagged in the event where another jet is tagged as a b-jet. The probability is measured in a kinematic region that has very little contribution from the Higgs signal. This measured probability is applied onto the single-tagged events in the signal region to predict the double b-tagged QCD background. The key issue of this method is to make sure that the technique can correctly predict the shapes of the kinematic distributions of the double b-tagged QCD multi-jet events which will be used later in the signal-background discrimination training. The development and testing of the TRF was one of the most important parts of this analysis.

A multivariate discriminant has the ability to combine the information from several variables. This improves the ability to separate a Higgs signal from background events far greater than a standard cut-based analysis. For this reason, an artificial neural network was developed to combine all this information. The two processes investigated in this analysis, VBF and VH, have different kinematics. The two channels were trained separately and the outputs were combined as inputs to a final neural network. The output of the final training is used to calculate the final results of the analysis.

Chapter 1

Theoretical Overview

The Standard Model is a consistent, completed and computable theory of the fundamental interactions between elementary particles, it explains with success most of the measured processes of elementary particle physics, governed by the weak, electromagnetic and strong interactions.

1.1 Introduction

Everything around us is composed of atoms. The name atom comes from the ancient Greek ἄτομος, from ἀ *not* and τέμνω *I cut*, which means uncuttable or indivisible, something that cannot be divided further. The concept of an atom as an indivisible component of matter was first proposed by early Indian and Greek philosophers.

In the 18^{th} and 19^{th} centuries, chemists provided the physical basis for this idea by showing that certain substances could not be further broken down by chemical methods, and they applied the ancient philosophical name of atom to this chemical entity.

During the late 19^{th} and early 20^{th} centuries, physicists discovered subatomic components and structure inside the atom, thereby demonstrating that the chemical atom was divisible. The new constituents of atom were called: protons, neutrons and electrons. Later it was discovered that the protons and neutrons are composed of other smaller particles: quarks and gluons. Until now there is no experimental evidence that electrons, quarks and gluons are composed of other elements.

The particles made of quarks and gluons are called *hadrons*. A hadron can be classified by the number of quarks of which it is made. If it is composed of three quarks it is called a baryon, and if it is composed of a quark-antiquark pair, it is a meson. Due to a phenomenon known as color confinement, quarks are never directly observed or found in isolation; they can be found only within hadrons. Quarks, gluons and electrons are the most common constituents of the ordinary matter, but they are not the only ones. In addiction to the electron there are two other particles with similar characteristics: the muon (μ) and the tau lepton (τ). Each one of these particles is accompanied by a corresponding neutral particle, the neutrino: the electron (ν_e), the muon (ν_μ) and the tau neutrino (ν_τ). All these particles are called leptons.

There are six types of quarks, distinguished by their flavor: up (u), down (d), strange (s), charm (c), bottom (b), and top (t).

Up and down quarks have the lowest masses of all quarks and they are the constituents of protons and neutrons, the other quarks are created in high energy physical processes. The heaviest quark, the top quark, of which the mass is $173.93 \pm 1.64(\text{stat}) \pm 0.87(\text{syst})$ GeV/c^2 [1], was discovered only in 1995 [2], since its discovery required particle accelerators of high energy, but its existence was predicted by theory years before [3].

Fermions	Family			Charge	Spin
Leptons	e	μ	τ	-1	1/2
	ν_e	ν_μ	ν_τ	0	1/2
Quarks	u	c	t	+2/3	1/2
	d	s	b	-1/3	1/2

Table 1.1: Quarks and leptons in the Standard Model theory. The charge is in electric charge unity.

The quarks and the leptons are classified into three families (table 1.1) and for each particle exists a corresponding anti-particle with opposite charge. All members of the three families are, directly or indirectly, observed and, for now, there is no experimental evidence for the existence of a fourth family.

The number of light neutrino types is strictly connected to the number of fermion generations. The most precise measurements of the number of light neutrinos, N_ν, come from studies of Z production in e^+e^- collisions. The invisible partial width, Γ_{inv}, is obtained by subtracting the measured visible partial widths, corresponding to Z decays into quarks (Γ_{had}) and charged leptons (Γ_l), from the total Z width (Γ_Z):

$$\Gamma_{inv} = \Gamma_Z - \Gamma_{had} - 3\Gamma_l. \tag{1.1}$$

The invisible width is assumed to be due to the N_ν light neutrinos species each contributing the neutrino partial width Γ_ν as given by the Standard Model theory: $\Gamma_{inv} = N_\nu \Gamma_\nu$. In order to reduce the model dependence, the Standard Model value for the ratio of the neutrino to charged leptonic partial widths, $(\Gamma_\nu/\Gamma_l)_{SM} = 1.991 \pm 0.001$ [4], is used instead of $(\Gamma_\nu)_{SM}$ to determine the number of light neutrino types:

$$N_\nu = \frac{\Gamma_{inv}}{\Gamma_l}\left(\frac{\Gamma_l}{\Gamma_\nu}\right)_{SM}. \tag{1.2}$$

The combined result from the four LEP experiments is $N_\nu = 2.984 \pm 0.008$ [4] (figure 1.1).

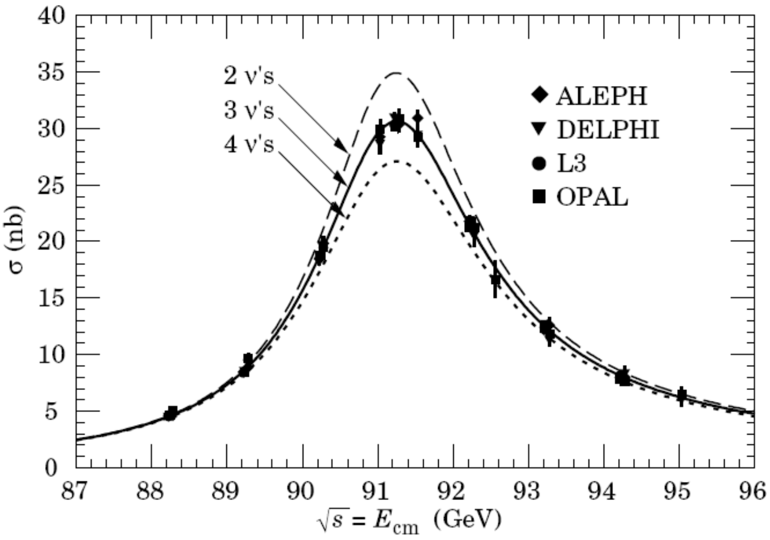

Figure 1.1: Cross section of the process $e^+e^- \rightarrow hadrons$ in function of the center of mass energy. The different curves show the prediction for a number of light neutrino families equal to two, three and four, respectively [4].

Quarks and leptons have an intrinsic spin equal to 1/2. The particles with half-integer spin and that obey Fermi-Dirac statistic are called fermions. The elementary particles that mediate the fondamental forces are characterized by spin equal to 1. These particles obey Bose-Einstein statistic and are called bosons.

According to the present understanding, there are four fundamental interactions or forces:

- **Electromagnetic**. This interaction is experienced by particles with electric charge. The particle mediating for this interaction is the photon (γ). Because the photon is massless, the interaction has infinite range.
- **Weak**. This interaction causes the radioactive decay of subatomic particles and initiates the process known as hydrogen fusion in stars. It is mediated by W and Z bosons, they are much heavier than protons or neutrons and it is the high mass that accounts for the very short range of the weak interaction.
- **Strong**. This is the interaction that holds quarks together to form protons, neutrons and other hadrons and, also, it binds protons and neutrons (nucleons) together to form the nucleus of an atom. The strong interaction is thought to be mediated by gluons, acting upon quarks, antiquarks, and other gluons. Gluons, in turn, are thought to interact with quarks and gluons because they carry a type of charge called *color charge*.
- **Gravitation**. It is mediated, presumably, by the graviton. The long range of gravitation makes it responsible for such large-scale phenomena as the structure of galaxies, black holes, and the expansion of the universe. Gravitation also explains astronomical phenomena on more modest scales, such as planetary orbits, as well as everyday experience.

Interaction	Gauge Boson	Massa(GeV/c^2)	Charge	Spin
Electromagnetic	γ	0	0	1
Weak	Z	91.187 ± 0.007	0	1
	$W^{\pm}$	80.417 ± 0.10	± 1	1
Strong	g	0	0	1

Table 1.2: The Standard Model gauge bosons [4].

The electromagnetic, weak and strong interactions are described by the Standard Model theory. It has three parts that describe those interactions: quantum electrodynamics (QED), weak theory and quantum chromodynamics (QCD). QED is the oldest and it was established by the quantization of the classic electrodynamic field. The weak theory was developed during the 1950s and 1960s.

It introduced the idea that the weak interactions are mediated by massive intermediate vector bosons.

During the sixties, the weak and electromagnetic interactions were unified into a single theory, the electro-weak theory, by Glashow [5], Salam [6] and Weinberg [7], using the Higgs mechanism of the spontaneous symmetry breaking. Veltman and t'Hooft [8] verified, during the seventies, that the electro-weak theory is renormalizable. The theory predicted the existence of neutral current interactions, observed by the Gargamelle experiment [9] at CERN in 1973. It also predicted the existence of the massive gauge bosons observed in 1983 by UA1 [10, 11] and UA2 [12] experiments, both located at CERN.

QCD describes the interactions between quarks and gluons. It has two peculiar properties: confinement and asymptotic freedom. The first property means that the force between quarks does not diminish as they are separated. Because of this, it would take an *infinite* amount of energy to separate two quarks; they are forever bound into hadrons such as the proton and the neutron. The second property means that in very high-energy reactions, quarks and gluons interact very weakly. This prediction of QCD was first published in the early 1970s by Politzer [13] and by Wilczek and Gross [14].

The interactions of the Standard Model theory are determined by symmetries, the gauge symmetries. The theory is described by a Lagrangian density which is invariant under transformations connected to these symmetries. The Lagrangian density describes the kinematics and the interactions of the various particles. The Higgs mechanism is used to explain in what way the particles acquire mass and it will be described in section 1.3, after the description of the Standard Model Lagrangian density and the symmetries in section 1.2.

1.2 The Lagrangian Density of the Electro-Weak Theory

The QED, the weak and, consequently, the electro-weak theories are gauge theories, i.e. theories invariant under gauge transformations. The invariance of the electro-weak Lagrangian density under local gauge transformations specifies the form of the interaction between fields. These interactions are mediated by the gauge bosons γ, $W^{\pm}$ and Z^0 and their form is obtained considering the local transformations belonging to the unitary product group $SU(2) \times U(1)$ where $SU(2)$ is the group of 2×2 unitary matrices with determinant equal to 1 and $U(1)$ is the group of one-dimensional unitary matrices, i.e. phases [15].

The Lagrangian density of leptons in the electro-weak theory can be ob-

tained starting from the assertions that all leptons are massless and the spinor wave-functions which describe the leptonic fields are written in terms of left and right-handed fields, this because the $SU(2)$ currents involve only the left-handed leptons.
With these assumptions the free Lagrangian density can be written as:

$$\mathcal{L}_0(x) = \sum_{l=e,\mu,\tau} \bar{\Psi}_l^L(x) i\gamma_\mu \partial^\mu \Psi_l^L(x) + \bar{\psi}_l^R(x) i\gamma_\mu \partial^\mu \psi_l^R(x) + \bar{\psi}_{\nu_l}^R(x) i\gamma_\mu \partial^\mu \psi_{\nu_l}^R(x). \quad (1.3)$$

Here $\Psi_l^L(x)$ and, its adjoint, $\bar{\Psi}_l^L(x)$ are the *weak isospinors* defined as:

$$\begin{cases} \Psi_l^L(x) = \begin{pmatrix} \psi_{\nu_l}^L(x) \\ \psi_l^L(x) \end{pmatrix} \\ \bar{\Psi}_l^L(x) = \left(\bar{\psi}_{\nu_l}^L(x),\, \bar{\psi}_l^L(x) \right), \end{cases} \quad (1.4)$$

and $\psi_{l,\nu_l}^L(x)$ and $\psi_{l,\nu_l}^R(x)$ describe the leptonic left and right-handed fields, respectively, the quantity $\partial_\mu = \partial/\partial x^\mu$ is the partial derivative respect to the component of the space-time four-vector x^μ and γ^μ are 4×4 Dirac matrices which satisfy the anti-commutation relations:

$$\{\gamma_\mu, \gamma_\nu\} = 2g_{\mu\nu}, \quad \text{with} \quad \begin{cases} g_{00} = -g_{11} = -g_{22} = -g_{33} = +1 \\ g_{\mu\nu} = 0 \quad \text{if} \quad \mu \neq \nu. \end{cases} \quad (1.5)$$

As mentioned before, the form of the electro-weak interactions can be deduced from the invariance of the Lagrangian density under local phase transformations. The transformation laws for the $SU(2) \times U(1)$ group can be written as:

$$SU(2): \begin{cases} \Psi_l^L(x) \to \Psi_l^{L\prime}(x) = e^{ig\tau_j\omega_j(x)/2} \Psi_l^L(x) \\ \bar{\Psi}_l^L(x) \to \bar{\Psi}_l^{L\prime}(x) = \bar{\Psi}_l^L(x) e^{-ig\tau_j\omega_j(x)/2} & (1.6a) \\ \psi_{l,\nu_l}^R(x) \to \psi_{l,\nu_l}^{R\prime}(x) = \psi_{l,\nu_l}^R \quad \text{(invariant)} \\ \bar{\psi}_{l,\nu_l}^R(x) \to \bar{\psi}_{l,\nu_l}^{R\prime}(x) = \bar{\psi}_{l,\nu_l}^R(x) \quad \text{(invariant)} & (1.6b) \end{cases}$$

$$U(1): \begin{cases} \psi(x) \to \psi'(x) = e^{ig'Yf(x)} \psi(x) \\ \bar{\psi}(x) \to \bar{\psi}'(x) = \bar{\psi}(x) e^{-ig'Yf(x)}, \end{cases} \quad (1.7)$$

where $\omega_j(x), j = 1,2,3$, and $f(x)$ are arbitrary real differentiable functions of x, g and g' are the coupling constants, τ_j are the 2×2 Pauli matrices and Y is the hypercharge. The *right handed* fields in the equations (1.6) are *weak isoscalars*, they are considered invariant under $SU(2)$ transformations.

The invariance of the Lagrangian density (1.3) is obtained by introducing the gauge fields $W_j^\mu(x)$ and $B^\mu(x)$ and by substituting the derivative ∂^μ with the covariant derivative D^μ defined as:

$$\partial^\mu \rightarrow D^\mu = \partial^\mu + ig\tau_j W_j^\mu(x)/2 + ig' Y B^\mu(x). \tag{1.8}$$

The gauge fields $W_j^\mu(x)$ and $B^\mu(x)$ follow the infinitesimal transformation laws:

$$\begin{cases} W_i^\mu(x) \rightarrow W_i^{\mu\prime}(x) = W_i^\mu(x) - \partial^\mu \omega_i(x) - g\varepsilon_{ijk}\omega_j(x) W_k^\mu(x) \\ B^\mu(x) \rightarrow B^{\mu\prime}(x) = B^\mu(x) + \partial^\mu f(x). \end{cases} \tag{1.9}$$

With these substitutions the Lagrangian density can be written as:

$$\begin{aligned} \mathcal{L}^L(x) &= \bar{\Psi}_l^L(x) i\gamma_\mu D^\mu \Psi_l^L(x) + \bar{\psi}_l^R(x) i\gamma_\mu D^\mu \psi_l^R(x) + \bar{\psi}_{\nu_l}^R(x) i\gamma_\mu D^\mu \psi_{\nu_l}^R(x) \\ &= \mathcal{L}_0(x) + \mathcal{L}_I(x), \end{aligned} \tag{1.10}$$

the term $\mathcal{L}_0(x)$ is the density for the free leptons (1.3) and $\mathcal{L}_I(x)$ describes the electro-weak interaction of leptons.

The form $\mathcal{L}_I(x)$ can be modified rewriting the fields W_j^μ and B^μ in terms of two non-Hermitian gauge fileds W^μ and $W^{\mu\dagger}$:

$$\begin{cases} W^\mu(x) = \dfrac{1}{\sqrt{2}}\left[W_1^\mu(x) - iW_2^\mu(x)\right] \\ W^{\mu\dagger(x)} = \dfrac{1}{\sqrt{2}}\left[W_1^\mu(x) + iW_2^\mu(x)\right], \end{cases} \tag{1.11}$$

and two Hermitian fields Z^μ and A^μ:

$$\begin{cases} W_3^\mu(x) = \cos\vartheta_W Z^\mu(x) + \sin\vartheta_W A^\mu(x) \\ B^\mu(x) = -\sin\vartheta_W Z^\mu(x) + \cos\vartheta_W A^\mu(x), \end{cases} \tag{1.12}$$

where ϑ_W is the Weinberg angle. The coupling constants g and g' are related to the electric charge, e, and ϑ_W through the relation:

$$g\sin\vartheta_W = g'\cos\vartheta_W = e. \tag{1.13}$$

Introducing the charged leptonic currents $J_\mu(x)$ and $J^\dagger_\mu(x)$, defined as:

$$\begin{cases} J_\mu(x) = \sum\limits_l \bar{\psi}_l(x)\gamma_\mu(1-\gamma_5)\psi_{\nu_l}(x) \\ J^\dagger_\mu(x) = \sum\limits_l \bar{\psi}_{\nu_l}(x)\gamma_\mu(1-\gamma_5)\psi_l(x), \end{cases} \tag{1.14}$$

where γ_5 is the fifth anti-commuting γ-matrix defined by:

$$\gamma_5 = i\gamma_0\gamma_1\gamma_2\gamma_3, \quad \text{with} \quad \{\gamma_\mu, \gamma_5\} = 0, \quad (\gamma_5)^2 = 1, \quad \gamma_5^\dagger = \gamma_5, \tag{1.15}$$

the final form of $\mathcal{L}_I(x)$ can be written as:

$$\begin{aligned} \mathcal{L}_I(x) = &- s_\mu(x)A^\mu(x) \\ &- \frac{g}{2\sqrt{2}}\left[J^\dagger_\mu(x)W^\mu(x) + J_\mu(x)W^{\mu\dagger(x)}\right] \\ &- \frac{g}{\cos\vartheta_W}\left[J_{3\mu}(x) - \sin^2\vartheta_W s_\mu(x)/e\right] Z^\mu(x), \end{aligned} \tag{1.16}$$

where $s_\mu(x)$ is the electromagnetic current and

$$J_{3\mu}(x) = \frac{1}{2}\left[\bar{\psi}^L_{\nu_l}(x)\gamma_\mu\psi^L_{\nu_l}(x) - \bar{\psi}^L_l(x)\gamma_\mu\psi^L_l(x)\right]. \tag{1.17}$$

The Lagrangian density (1.10) describes the free leptons and their interaction with the gauge fields. The complete Lagrangian density must also contain terms which describe these gauge bosons when no leptons are present. These new terms must be $SU(2) \times U(1)$ gauge invariant.
The Lagrangian density for the gauge bosons can be written as:

$$\begin{aligned} \mathcal{L}^B(x) = &- \frac{1}{4}B_{\mu\nu}(x)B^{\mu\nu}(x) - \frac{1}{4}G_{i\mu\nu}(x)G_i^{\mu\nu}(x) = \\ &- \frac{1}{4}B_{\mu\nu}(x)B^{\mu\nu}(x) - \frac{1}{4}F_{i\mu\nu}(x)F_i^{\mu\nu}(x) \\ &+ \text{interaction terms}, \end{aligned} \tag{1.18}$$

where:

$$\begin{cases} B^{\mu\nu}(x) = \partial^\mu B^\nu(x) - \partial^\nu B^\mu(x) \\ F_i^{\mu\nu}(x) = \partial^\mu W_i^\nu(x) - \partial^\nu W_i^\mu(x) \\ G_i^{\mu\nu}(x) = \partial^\mu W_i^\nu(x) - \partial^\nu W_i^\mu(x) - g\varepsilon_{ijk} W_j^\mu(x) W_k^\nu(x). \end{cases} \tag{1.19}$$

The first two terms represent the Lagrangian density of the free gauge fields that, by the terms of $A^\mu(x)$, $Z^\mu(x)$ and $W^\mu(x)$, become:

$$\mathcal{L}_0^B(x) = -\frac{1}{4}F_{\mu\nu}(x)F^{\mu\nu}(x) - \frac{1}{2}F^\dagger_{W\mu\nu}(x)F_W^{\mu\nu}(x) - \frac{1}{4}Z_{\mu\nu}(x)Z^{\mu\nu}(x), \tag{1.20}$$

where $F^{\mu\nu}(x) = \partial^\mu A^\nu(x) - \partial^\nu A^\mu(x)$ is the electromagnetic field tensor, $F_W^{\mu\nu}(x)$ is the same tensor for the W boson, and $Z^{\mu\nu}(x)$ is the one for the Z boson. The interaction terms of the equation (1.18) represent the self-interactions of the gauge bosons, which are one of the most remarkable characteristic of the theory. They are present because the $W_i^\mu(x)$ fields, which interact through the isospin weak current, themselves are weak isospin vectors, carrying a weak charge isospin. This is in contrast with the QED, where the electromagnetic interactions are transmitted by photons and they are charge-less, consequently there are no photon self-interaction terms in QED.

1.3 Spontaneous Symmetry Breaking

Until now the leptons and gauge bosons are considered massless, but the experimental evidence contradicts this assumption, except for the photon.
For example to describe the massive bosons, $W^\pm$ and Z^0, a mass term can be added to the Lagrangian density (1.20) [15]:

$$m_W^2 W_\mu^\dagger(x) W^\mu(x) + \frac{1}{2}m_Z^2 Z_\mu(x) Z^\mu(x). \tag{1.21}$$

The addition of these mass terms makes the theory non-invariant under the $SU(2) \times U(1)$ gauge transformations. Adding a mass term for the leptons to the Lagrangian density (1.3) has the same consequence.
A solution to this problem is supplied by the Higgs mechanism, based on the idea that the gauge symmetry breaks spontaneously. The spontaneous symmetry breaking means that the theory is gauge invariant, but the ground state does not show that symmetry.

The energy levels of the system can be either non-degenerate or degenerate. The interesting case is the second one, where the energy eigenstate is not invariant but transforms under the gauge transformations. In this case there is no unique eigenstate which represents the ground state, but if, *arbitrarily*, one of the degenerate states is chosen as ground state, it does not show the symmetry. The mechanism to obtain an asymmetric ground state is known as *spontaneous symmetry breaking*.

1.3.1 The Higgs Mechanism

The simplest example of the field theory in which it is possible to see the spontaneous symmetry breaking is the Goldstone model. In this model, it asserts that the Lagrangian density [15]:

$$\begin{aligned}\mathcal{L}_G(x) &= (\partial_\mu \varphi^*(x))(\partial^\mu \varphi(x)) - \mu^2|\varphi(x)|^2 - \lambda|\varphi(x)|^4 \\ &= (\partial_\mu \varphi^*(x))(\partial^\mu \varphi(x)) - V(\varphi),\end{aligned} \tag{1.22}$$

is invariant under global phase transformations. To generalize it, passing to local phase transformations, it is necessary to introduce a gauge field, $A_\mu(x)$, the covariant derivative:

$$\partial_\mu \to D_\mu = \partial_\mu + iqA_\mu(x), \tag{1.23}$$

and adding to the Lagrangian density, a term for the free gauge field:

$$-\frac{1}{4}F_{\mu\nu}(x)F^{\mu\nu}(x), \quad \text{where} \quad F_{\mu\nu} = \partial_\mu A_\nu(x) - \partial_\nu A_\mu(x). \tag{1.24}$$

In this way, the Higgs Lagrangian density is:

$$\mathcal{L}_H(x) = [D_\mu \varphi(x)]^*[D^\mu \varphi(x)] - V(\varphi(x)) - \frac{1}{4}F_{\mu\nu}(x)F^{\mu\nu}(x), \tag{1.25}$$

where:

$$\varphi(x) = \frac{1}{\sqrt{2}}\left[\varphi_1(x) + i\varphi_2(x)\right] \tag{1.26}$$

is a complex scalar field, μ^2 and λ are arbitrary parameters, and the potential $V(\varphi)$ is:

$$V(\varphi(x)) = \mu^2|\varphi(x)|^2 + \lambda|\varphi(x)|^4. \tag{1.27}$$

This Lagrangian density is invariant under the local gauge transformations $U(1)$:

$$\begin{cases} \varphi(x) \to \varphi'(x) = \varphi(x)\, e^{-iqf(x)} \\ \varphi^*(x) \to \varphi^{*\prime}(x) = \varphi^*(x)\, e^{iqf(x)} \\ A_\mu(x) \to A'_\mu(x) = A_\mu(x) + \partial_\mu f(x), \end{cases} \tag{1.28}$$

where $f(x)$ is an arbitrary differentiable real function.

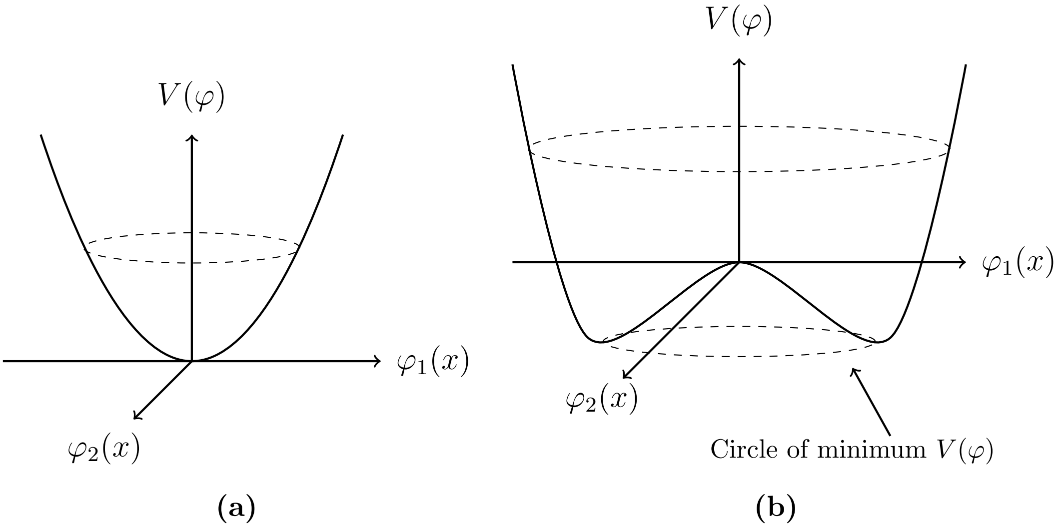

(a) **(b)**

Figure 1.2: The potential energy density $V(\varphi) = \mu^2|\varphi(x)|^2 + \lambda|\varphi(x)|^4$ with $\lambda > 0$, (a) $\mu^2 > 0$ and (b) $\mu^2 < 0$.

To study the energy level of the system, it is necessary to study the form of the complex scalar field potential $V(\varphi)$ (figure 1.2) defined in the equation (1.27). For the energy of the field bounded from below, the parameter λ is required to be positive ($\lambda > 0$). For the sign of the other parameter, μ^2, two cases are possible: $\mu^2 > 0$ and $\mu^2 < 0$. In the first case ($\mu^2 > 0$) the minimum value of the energy coincides with both $\varphi(x)$ and $A_\mu(x)$ vanishing, therefore the spontaneous symmetry breaking cannot occur (figure 1.2a). In the second case ($\mu^2 < 0$) the vacuum state is not unique and there is symmetry breaking (figure 1.2b). The Lorentz invariance is obtained when the gauge field, $A_\mu(x)$, vanishes in correspondence with the vacuum state. The potential $V(\varphi)$ presents a circle of minima corresponding to the $\varphi(x)$ field equal to φ_0:

$$\varphi_0 = \left(\frac{-\mu^2}{2\lambda}\right)^{\frac{1}{2}} e^{i\vartheta}, \qquad 0 \leq \vartheta < 2\pi. \tag{1.29}$$

The value of the angle ϑ is not significant and it can be chosen to be equal to zero ($\vartheta = 0$):

$$\varphi_0 = \left(\frac{-\mu^2}{2\lambda}\right)^{\frac{1}{2}} = \frac{v}{\sqrt{2}}, \qquad v = \left(\frac{-\mu^2}{\lambda}\right)^{\frac{1}{2}}. \tag{1.30}$$

Introducing the $\sigma(x)$ and $\eta(x)$ fields such that:

$$\varphi(x) = \frac{1}{\sqrt{2}}\left[v + \sigma(x) + i\eta(x)\right], \tag{1.31}$$

the Higgs Lagrangian density (1.25) becomes:

$$\begin{aligned}\mathcal{L}_H(x) = & \frac{1}{2}\partial_\mu\sigma(x)\partial^\mu\sigma(x) - \frac{1}{2}\left(2\lambda v^2\right)\sigma^2(x)\\ & + \frac{1}{2}\partial_\mu\eta(x)\partial^\mu\eta(x)\\ & - \frac{1}{4}F_{\mu\nu}(x)F^{\mu\nu}(x) + \frac{1}{2}\left(qv\right)^2 A_\mu(x)A^\mu(x)\\ & + qvA_\mu(x)\partial^\mu\eta(x)\\ & + \alpha + \beta,\end{aligned} \tag{1.32}$$

where the α and β terms include the interaction terms among the fields and the constant terms.

The first line of the equation (1.32) describes a real Klein-Gordon field with a charge-less boson, spin equal to 0 and mass $\sqrt{2\lambda v^2}$. The term, $A_\mu(x)\partial^\mu\eta(x)$, shows that $A_\mu(x)$ and $\eta(x)$ are not independent, therefore the second and third lines of the equation (1.32) do not describe a massless scalar boson and massive vector boson, respectively. This complexity is also manifested by the number of degrees of freedom for the two Lagrangian density (1.25) and (1.32). In the equation (1.25) four degrees of freedom appear: two for the complex scalar field $\varphi(x)$ and two for the massless real vector field $A_\mu(x)$. In equation (1.32), the real scalar fields $\sigma(x)$ and $\eta(x)$ present one degree of freedom each and the massive real vector field $A_\mu(x)$ contributes with three degrees of freedom, i.e. the transformed Lagrangian density would appear to have five degrees of freedom.

Obviously, a change of variables cannot modify the number of degrees of freedom of a system. The conclusion is that the Lagrangian density (1.32) presents an unphysical field which does not represent a real particle and can be eliminated.

For each complex field $\varphi(x)$ it is possible to find a gauge transformation like (1.28) that transforms the $\varphi(x)$ field into a real field:

$$\varphi(x) = \frac{1}{\sqrt{2}}\left[v + \sigma(x)\right], \tag{1.33}$$

which removes the scalar field $\eta(x)$ from the equation (1.32). This type of gauge is called *unitary gauge*. Substituting the new form of the $\varphi(x)$ field (1.33) into equation (1.25) gives:

$$\mathcal{L}(x) = \mathcal{L}_0(x) + \mathcal{L}_I(x), \tag{1.34a}$$

with:

$$\begin{aligned}
\mathcal{L}_0(x) =& \frac{1}{2}\left[\partial^\mu \sigma(x)\right]\left[\partial_\mu \sigma(x)\right] - \frac{1}{2}\left(2\lambda v^2\right)\sigma^2(x) \\
& - \frac{1}{4}F_{\mu\nu}(x)F^{\mu\nu}(x) + \frac{1}{2}\left(qv\right)^2 A_\mu(x)A^\mu(x) \qquad (1.34\text{b}) \\
\mathcal{L}_I(x) =& -\lambda v \sigma^3(x) - \frac{1}{4}\lambda\sigma^4(x) \\
& + \frac{1}{2}q^2 A_\mu(x)A^\mu(x)\left[2v\sigma(x) + \sigma^2(x)\right] \\
& + \frac{1}{4}v^2\lambda. \qquad (1.34\text{c})
\end{aligned}$$

Here, $\mathcal{L}_0(x)$ contains the quadratic terms without coupling terms between $\sigma(x)$ and $A_\mu(x)$ and $\mathcal{L}_I(x)$ contains the high-order interaction and the constant term. Treating $\mathcal{L}_I(x)$ with the perturbation theory, $\mathcal{L}_0(x)$ can be interpreted as the free Lagrangian density of a real Klein-Gordon field $\sigma(x)$ and a massive real vector field $A_\mu(x)$. In this way, $\sigma(x)$ leads to neutral scalar bosons with masses equal to $\sqrt{2\lambda v^2}$ and $A_\mu(x)$ leads to neutral vector bosons with mass $|qv|$.

The starting point was the Lagrangian density (1.25) for a complex scalar field and a massless real vector field and the conclusion is the Lagrangian density (1.34) for a real scalar field and a massive real vector field. The number of degrees of freedom is four in both cases. Of the two degrees of freedom of the initial complex field $\varphi(x)$, one is absorbed by the vector field $A_\mu(x)$ which, in the process, becomes massive and the other one appears as a real field $\sigma(x)$. This procedure, that introduces a massive vector boson without destroying the gauge invariance of the Lagrangian density, is called the *Higgs mechanism* and the massive boson with spin-0 associated to the $\sigma(x)$ field is called the *Higgs boson*.

1.3.2 The Lagrangian Density in the Unitary Gauge

The Lagrangian density, obtained in section 1.2 can be summarized as [15]:

$$\mathcal{L}(x) = \mathcal{L}^L(x) + \mathcal{L}^B(x), \tag{1.35}$$

where $\mathcal{L}^L(x)$ is the leptonic Lagrangian density (1.10) and $\mathcal{L}^B(x)$ is the Lagrangian density for the gauge bosons (1.18). The masses of the leptons and bosons are obtained by applying the Higgs mechanism to this model adding the Higgs Lagrangian density $\mathcal{L}^H(x)$:

$$\mathcal{L}^H(x) = \left[D^\mu \Phi(x)\right]^\dagger \left[D_\mu \Phi(x)\right] - \mu^2 \Phi^\dagger(x)\Phi(x) - \lambda \left[\Phi^\dagger(x)\Phi(x)\right]^2, \tag{1.36}$$

to the Lagrangian density (1.35), where:

$$D^\mu = \partial^\mu + ig\tau_j W_j^\mu(x)/2 + ig'YB^\mu(x), \tag{1.37}$$

and:

$$\Phi(x) = \begin{pmatrix} \varphi_a(x) \\ \varphi_b(x) \end{pmatrix} \tag{1.38}$$

is the Higgs field.
The transformation laws of $\Phi(x)$ under $SU(2) \times U(1)$ gauge transformations are for the $SU(2)$ group:

$$\begin{cases} \Phi(x) \rightarrow \Phi'(x) = e^{ig\tau_j\omega_j(x)/2}\Phi(x) \\ \Phi^\dagger(x) \rightarrow \Phi^{\dagger\prime}(x) = \Phi^\dagger(x)e^{-ig\tau_j\omega_j(x)/2}, \end{cases} \tag{1.39}$$

and for the $U(1)$ group:

$$\begin{cases} \Phi(x) \rightarrow \Phi'(x) = e^{ig'Yf(x)}\Phi(x) \\ \Phi^\dagger(x) \rightarrow \Phi^{\dagger\prime}(x) = \Phi^\dagger(x)e^{-ig'Yf(x)}. \end{cases} \tag{1.40}$$

As described in section 1.3.1, the energy density, with the values of $\mu^2 < 0$ and $\lambda > 0$, has a minimum for:

$$\Phi(x) = \Phi_0 = \begin{pmatrix} \varphi_a^0 \\ \varphi_b^0 \end{pmatrix}, \tag{1.41}$$

with:

$$\Phi_0^\dagger \Phi_0 = |\varphi_a^0|^2 + |\varphi_b^0|^2 = \frac{-\mu^2}{2\lambda}. \tag{1.42}$$

To obtain spontaneous symmetry breaking, a particular value Φ_0, compatible with equation (1.42), can be chosen as the ground state, this value can be:

$$\Phi_0 = \begin{pmatrix} \varphi_a^0 \\ \varphi_b^0 \end{pmatrix} = \begin{pmatrix} 0 \\ v/\sqrt{2} \end{pmatrix}, \qquad v = \sqrt{-\mu^2/\lambda} \quad (> 0), \tag{1.43}$$

and the Higgs field can be parameterized in terms of its deviation from the constant field Φ_0:

$$\Phi(x) = \frac{1}{\sqrt{2}} \begin{pmatrix} \eta_1(x) + i\eta_2(x) \\ v + \sigma(x) + i\eta_3(x) \end{pmatrix}. \tag{1.44}$$

The terms of lepton masses are obtained by introducing an interaction term between the leptonic and the Higgs field; the Lagrangian density becomes:

$$\mathcal{L}(x) = \mathcal{L}^L(x) + \mathcal{L}^B(x) + \mathcal{L}^H(x) + \mathcal{L}^{LH}(x), \tag{1.45}$$

and the term $\mathcal{L}^{LH}(x)$ is the Yukawa term:

$$\begin{aligned} \mathcal{L}^{LH}(x) = &- \sum_l g_l \left[\bar{\Psi}_l^L(x) \psi_l^R(x) \Phi(x) + \Phi^\dagger(x) \bar{\psi}_l^R(x) \Psi_l^L(x) \right] \\ &- \sum_l g_{\nu_l} \left[\bar{\Psi}_l^L(x) \psi_{\nu_l}^R(x) \tilde{\Phi}(x) + \tilde{\Phi}^\dagger(x) \bar{\psi}_{\nu_l}^R(x) \Psi_l^L(x) \right], \end{aligned} \tag{1.46}$$

with:

$$\tilde{\Phi}(x) = -i\left[\Phi^\dagger(x)\tau_2\right]^T = \begin{pmatrix} \phi_b^*(x) \\ -\phi_a^*(x) \end{pmatrix}, \tag{1.47}$$

which does not present mixing terms among the leptons.
As seen in section 1.3.1, it is possible to find a gauge transformation, the unitary gauge, such that the $\eta_i(x)$ vanishes:

$$\Phi(x) = \frac{1}{\sqrt{2}}\begin{pmatrix} 0 \\ v+\sigma(x) \end{pmatrix}. \tag{1.48}$$

Substituting this into equation (1.45), the complete electro-weak Lagrangian density is obtained:

$$\mathcal{L}(x) = \mathcal{L}_0(x) + \mathcal{L}_I(x), \tag{1.49a}$$

where $\mathcal{L}_0(x)$ describes the free particles:

$$\begin{aligned}\mathcal{L}_0(x) = {} & \bar{\psi}_l(i\partial\!\!\!/ - m_l)\psi_l + \bar{\psi}_{\nu_l}(i\partial\!\!\!/ - m_{\nu_l})\psi_{\nu_l} \\ & -\frac{1}{4}F_{\mu\nu}F^{\mu\nu} \\ & -\frac{1}{2}F^\dagger_{W\mu\nu}F^{\mu\nu}_W + m_W^2 W^\dagger_\mu W^\mu \\ & -\frac{1}{4}Z_{\mu\nu}Z^{\mu\nu} + \frac{1}{2}m_Z^2 Z_\mu Z^\mu \\ & +\frac{1}{2}(\partial^\mu\sigma)(\partial_\mu\sigma) - \frac{1}{2}m_H^2\sigma^2,\end{aligned} \tag{1.49b}$$

and $\mathcal{L}_I(x)$ describes the various interactions among leptons, weak and Higgs bosons:

$$\mathcal{L}_I(x) = \mathcal{L}_I^{LB}(x) + \mathcal{L}_I^{BB}(x) + \mathcal{L}_I^{HH}(x) + \mathcal{L}_I^{HB}(x) + \mathcal{L}_I^{HL}(x), \tag{1.49c}$$

with:

$$\begin{aligned}\mathcal{L}_I^{LB}(x) = {} & e\bar{\psi}_l\gamma_\mu\psi_l A^\mu \\ & - \frac{g}{2\sqrt{2}}\left[\bar{\psi}_{\nu_l}\gamma_\mu\left(1-\gamma_5\right)\psi_l W^\mu + \bar{\psi}_l\gamma_\mu\left(1-\gamma_5\right)\psi_{\nu_l}W^{\dagger\mu}\right] \\ & - \frac{g}{4\cos\vartheta_W}\bar{\psi}_{\nu_l}\gamma_\mu\left(1-\gamma_5\right)\psi_{\nu_l}Z^\mu \\ & - \frac{g}{4\cos\vartheta_W}\bar{\psi}_l\gamma_\mu\left(1-4\sin^2\vartheta_W-\gamma_5\right)\psi_l Z^\mu, \qquad (1.49\mathrm{d})\end{aligned}$$

$$\begin{aligned}\mathcal{L}_I^{BB}(x) = {} & ig\cos\vartheta_W\left[\ \left(W_\mu^\dagger W_\nu - W_\nu^\dagger W_\mu\right)\partial^\mu Z^\nu \right. \\ & \qquad \left. + \left(\partial_\mu W_\nu - \partial_\nu W_\mu\right)W^{\nu\dagger}Z^\mu - \left(\partial_\mu W_\nu^\dagger - \partial_\nu W_\mu^\dagger\right)W^\nu Z^\mu\ \right] \\ & + ie\left[\ \left(W_\mu^\dagger W_\nu - W_\nu^\dagger W_\mu\right)\partial^\mu A^\nu \right. \\ & \qquad \left. + \left(\partial_\mu W_\nu - \partial_\nu W_\mu\right)W^{\nu\dagger}A^\mu - \left(\partial_\mu W_\nu^\dagger - \partial_\nu W_\mu^\dagger\right)W^\nu A^\mu\ \right] \\ & + g^2\cos^2\vartheta_W\left[W_\mu W_\nu^\dagger Z^\mu Z^\nu - W_\nu W^{\nu\dagger}Z_\mu Z^\mu\right] \\ & + e^2\left[W_\mu W_\nu^\dagger A^\mu A^\nu - W_\nu W^{\nu\dagger}A_\mu A^\mu\right] \\ & + eg\cos\vartheta_W\left[W_\mu W_\nu^\dagger\left(Z^\mu A^\nu + A^\mu Z^\nu\right) - 2W_\nu W^{\nu\dagger}A_\mu Z^\mu\right] \\ & + \frac{1}{2}g^2 W_\mu^\dagger W_\nu\left[W^{\mu\dagger}W^\nu - W^\mu W^{\nu\dagger}\right], \qquad (1.49\mathrm{e})\end{aligned}$$

$$\mathcal{L}_I^{HH}(x) = \frac{1}{4}\lambda\sigma^4 - \lambda v\sigma^3, \qquad (1.49\mathrm{f})$$

$$\begin{aligned}\mathcal{L}_I^{HB}(x) = {} & \frac{1}{2}vg^2W_\mu^\dagger W^\mu\sigma + \frac{1}{4}g^2W_\mu^\dagger W^\mu\sigma^2 \\ & + \frac{vg^2}{4\cos^2\vartheta_w}Z_\mu Z^\mu\sigma + \frac{g^2}{8\cos^2\vartheta_W}Z_\mu Z^\mu\sigma^2, \qquad (1.49\mathrm{g})\end{aligned}$$

$$\mathcal{L}_I^{HL}(x) = -\frac{1}{v}m_l\bar{\psi}_l\psi_l\sigma - \frac{1}{v}m_{\nu_l}\bar{\psi}_{\nu_l}\psi_{\nu_l}\sigma. \qquad (1.49\mathrm{h})$$

In this way the lepton and the gauge boson masses are:

$$m_l = vg_l/\sqrt{2}, \qquad m_{\nu_l} = vg_{\nu_l}/\sqrt{2}, \qquad (1.50)$$

$$m_W = \sqrt{\left(\frac{\alpha\pi}{G_F\sqrt{2}}\right)}\frac{1}{\sin\vartheta_W}, \qquad m_Z = \sqrt{\left(\frac{\alpha\pi}{G_F\sqrt{2}}\right)}\frac{2}{\sin 2\vartheta_W}, \qquad (1.51)$$

where G_F is the Fermi coupling constant and α is the fine structure constant; and finally the Higgs boson mass:

$$m_H = \sqrt{-2\mu^2} = \sqrt{2\lambda v^2}. \tag{1.52}$$

The only massless boson remains the photon, for which the theory predicts its null mass.

1.4 Quantum Chromodynamics

Nucleons, pions and other hadrons are bound states of more fundamental fermions called quarks. In the simple quark model, the observed baryons are assumed to be bound states of three quarks, while the mesons are assumed to be bound states of a quark and an antiquark. The quark model gives a successful description of the observed hadron spectrum, but it presents two particular characteristics [15]: there is no experimental evidence of free quarks or other fractionally charged states (like two quark bound states) and the space-spin wave-function of the baryons are symmetric under interchange of quarks of the same flavor.

These phenomena are both explained by the theory of color, developed by Han, Nambu and Greenberg in the sixties. The main point of the theory is that in addition to the space and spin degree of freedom, the quarks have another degree of freedom, the color, from which the name quantum chromodynamics follows.

The quarks exist in three different states of colors (r, g, b) represented by the color spinors:

$$r = \begin{pmatrix} 1 \\ 0 \\ 0 \end{pmatrix}, \quad g = \begin{pmatrix} 0 \\ 1 \\ 0 \end{pmatrix}, \quad b = \begin{pmatrix} 0 \\ 0 \\ 1 \end{pmatrix}. \tag{1.53}$$

The quark wave-function can be written as the product of a space-spin part (ψ) and a color part (χ^c): $\Psi = \psi\chi^c$. In the same way as the spin wave-functions are acted on by spin operators, the color wave-functions are acted on by color operators which can be represented by eight linearly independent, apart from the unit matrix, three-dimensional Hermitian matrices:

$$\hat{F}_i = \frac{1}{2}\lambda_i \quad (i = 1, \ldots, 8), \tag{1.54a}$$

where λ_i are:

$$\lambda_1 = \begin{pmatrix} 0 & 1 & 0 \\ 1 & 0 & 0 \\ 0 & 0 & 0 \end{pmatrix}, \quad \lambda_2 = \begin{pmatrix} 0 & -i & 0 \\ i & 0 & 0 \\ 0 & 0 & 0 \end{pmatrix}, \quad \lambda_3 = \begin{pmatrix} 1 & 0 & 0 \\ 1 & -1 & 0 \\ 0 & 0 & 0 \end{pmatrix},$$

$$\lambda_4 = \begin{pmatrix} 0 & 0 & 1 \\ 0 & 0 & 0 \\ 1 & 0 & 0 \end{pmatrix}, \quad \lambda_5 = \begin{pmatrix} 0 & 0 & -i \\ 0 & 0 & 0 \\ i & 0 & 0 \end{pmatrix}, \quad \lambda_6 = \begin{pmatrix} 0 & 0 & 0 \\ 0 & 0 & 1 \\ 0 & 1 & 0 \end{pmatrix},$$

$$\lambda_7 = \begin{pmatrix} 0 & 0 & 0 \\ 0 & 0 & -i \\ 0 & i & 0 \end{pmatrix}, \quad \lambda_8 = \frac{1}{\sqrt{3}} \begin{pmatrix} 1 & 0 & 0 \\ 0 & 1 & 0 \\ 0 & 0 & -2 \end{pmatrix}. \tag{1.54b}$$

The $\hat{F}_i$ are the color generators, they correspond to the τ-matrices of isospin and satisfy the commutation relations:

$$\left[\hat{F}_i, \hat{F}_j\right] = i f_{ijk} \hat{F}_k, \tag{1.55}$$

where f_{ijk} are completely antisymmetric structure constants that vanish if there are two identical indices.

The color charges are conserved, but because they do not commute with each other, they cannot have simultaneous eigenvalues. The only color charges that commute are $\hat{F}_3$ and $\hat{F}_8$ and the color states, χ^c, are eigenstates of both. These eigenvalues are listed in table 1.3.

State	$\hat{F}_3$	$\hat{F}_8$
r	$\frac{1}{2}$	$\frac{1}{2}\sqrt{3}$
g	$-\frac{1}{2}$	$\frac{1}{2}\sqrt{3}$
b	0	$-\frac{1}{\sqrt{3}}$

Table 1.3: Values of color charges for the color states of quarks. For antiquarks the values are reversed.

The characteristics of the absence of free quarks and the symmetry of the space-spin wave-function of the baryons are easily explained with the hypothesis of color confinement. Under this hypothesis, free hadrons exist only in color singlet states, χ_h^c, satisfying:

$$\hat{F}_i \chi_h^c = 0 \quad (i = 1, \ldots, 8) \tag{1.56}$$

and in particular:

$$\hat{F}_3 = \hat{F}_8 = 0 \tag{1.57}$$

for any hadron. The values in table 1.3 show that states with just one quark or with two quarks are forbidden, but the combinations of quark-antiquark or of three quarks are allowed. From table 1.3 and equation (1.57), the wave-function of a baryon, composed of three quarks, can be written as a combination of quarks in the three different state of colors:

$$\begin{aligned} \chi_B^c &= r_1 g_2 b_3 - g_1 r_2 b_3 + b_1 r_2 g_3 - b_1 g_2 r_3 + g_1 b_2 r_3 - r_1 b_2 g_3 \\ &= \sum_{ijk} \varepsilon_{ijk} r_i g_j b_k, \end{aligned} \tag{1.58}$$

where, for example, r_3 means that the third quark is in an r state.
Because the Levi-Civita symbol, ε_{ijk}, is totally antisymmetric, the space-spin wave-function, ψ, of the total wave-function, $\Psi = \psi\chi_B^c$, due to the Pauli principle, must be symmetric under the interchange of identical quarks.
The Lagrangian density for free quarks can be written as:

$$\mathcal{L}(x) = \bar{\Psi}^f(x)\left(i\partial\!\!\!/ - m_f\right)\Psi^f(x), \tag{1.59}$$

where $\Psi^f(x)$ and $\bar{\Psi}^f(x)$ are the combination of three Dirac fields $\psi^f_{r,g,b}(x)$:

$$\begin{cases} \Psi^f(x) = \begin{pmatrix} \psi^f_r(x) \\ \psi^f_g(x) \\ \psi^f_b(x) \end{pmatrix} \\ \bar{\Psi}^f(x) = \left(\bar{\psi}^f_r(x),\, \bar{\psi}^f_g(x)\, \bar{\psi}^f_b(x)\right). \end{cases} \tag{1.60}$$

To have the Lagrangian density (1.59) invariant under the local phase transformations:

$$\begin{cases} \Psi^f(x) \to \Psi^{f\prime}(x) = e^{ig_s\lambda_j\omega_j(x)/2}\Psi^f(x) \\ \bar{\Psi}^f(x) \to \bar{\Psi}^{f\prime}(x) = \bar{\Psi}^f(x)e^{-ig_s\lambda_j\omega_j(x)/2}, \end{cases} \tag{1.61}$$

where $\omega_j(x)(j = 1, \ldots, 8)$ are arbitrary real differentiable functions, and g_s is the coupling constant, it is necessary to introduce a gauge field, $A^\mu_j(x)$, that transforms as:

$$A_i^\mu(x) \to A_i^{\mu\prime}(x) = A_i^\mu(x) - \partial^\mu \omega_i(x) - g_s f_{ijk} \omega_j(x) A_k^\mu(x), \tag{1.62}$$

and the covariant derivative, D^μ, defined as:

$$D^\mu = \partial^\mu + i g_s \lambda_j A_j^\mu(x)/2. \tag{1.63}$$

The Lagrangian density for the quarks can be written as:

$$\mathcal{L}_q(x) = \bar{\Psi}^f(x) \left(i \not{D} - m_f \right) \Psi^f(x) = \mathcal{L}_0(x) + \mathcal{L}_I(x), \tag{1.64}$$

where:

$$\mathcal{L}_I(x) = -\frac{1}{2} g_s \bar{\Psi}^f(x) \gamma_\mu \lambda_j \Psi^f(x) A_j^\mu(x). \tag{1.65}$$

This Lagrangian density describes the quarks fields and their interactions with gluon fields, but there must be a term that describes the gluons when no quarks are present, and this term must be $SU(3)$ gauge invariant.
The term to add to the Lagrangian density (1.64) is:

$$\mathcal{L}_G = -\frac{1}{4} G_{i\mu\nu}(x) G_i^{\mu\nu}(x), \tag{1.66}$$

where:

$$\begin{aligned} G_i^{\mu\nu}(x) &= F_i^{\mu\nu}(x) + g_s f_{ijk} A_j^\mu(x) A_k^\nu(x) \\ &= \partial^\nu A_i^\mu - \partial^\mu A_i^\nu + g_s f_{ijk} A_j^\mu(x) A_k^\nu(x). \end{aligned} \tag{1.67}$$

Chapter 2

Phenomenology Overview

As described in chapter 1, the Higgs boson is the physical manifestation of the mechanism that provides mass to fundamental particles in the Standard Model theory [16–18].

In this search, two production mechanisms are investigated: associated vector boson production (VH) and vector boson fusion (VBF). The VH channel denotes the process $p\bar{p} \to W/Z + H \to q\bar{q}' + b\bar{b}$. The VBF channel identifies the process $p\bar{p} \to q\bar{q}'H \to q\bar{q}'b\bar{b}$, where the two incoming quarks each radiate a W or Z boson, which subsequently fuse into a Higgs boson. In both channels, the Higgs boson decays into a bottom-antibottom quark pair, $b\bar{b}$. This decay mode is the dominant one for Higgs boson masses (m_H) less than 135 GeV/c^2 [19].

2.1 Higgs Boson Phenomenology

The Higgs boson mass, m_H, is not predicted by the Standard Model theory, but it is possible to estimate a range of validity through theoretical calculation and results from accelerator experiments.

The situation described here is that existed in the year 2010, the time this search started.

2.1.1 Theoretical Constraints on the Higgs Boson Mass

The theoretical constraints can be derived from the assumptions on the energy range in which the Standard Model theory is valid before perturbation theory breaks down and new phenomena should emerge. These constraints are obtained by including the unitarity constraints required in scattering amplitudes, the perturbativity of the Higgs self-coupling and the stability of the vacuum in the electro-weak theory.

Unitarity Constraint

The Standard Model theory is a quantum field theory. In this context, the total probability that any physical observable can be measured by an observer is conserved and equal to unity. This is translated in terms of the scattering amplitude, that the S matrix, which contains all information of the initial and final states of a process, is unitary. This condition produces an upper bound for the Standard Model Higgs boson mass.
One of the reason to abandon the old Fermi theory for the weak interaction was that it violates unitarity at energies close to the Fermi scale, $\Lambda \sim 300$ GeV. This particular problem is solved with the introduction of the intermediate massive vector boson theory [15].

However there is a potential problem in the Standard Model theory for energies higher than the Fermi scale. The interactions of the longitudinal components of the massive gauge bosons, W_L and Z_L, grow with their momenta. This would eventually lead to cross sections which increase with energy which would then violate unitarity at some stage, for example in the WW scattering process $W_L^+W_L^- \to W_L^+W_L^-$, at high energies. The unitarity of the scattering amplitude for this process can be studied writing it in terms of the Legendre polynomials:

$$A = 16\pi \sum_{l=0}^{\infty}(2l+1)P_l(\cos\vartheta)a_l, \tag{2.1}$$

where P_l are the Legendre polynomials, ϑ is the scattering angle and a_l are the partial waves of orbital angular momentum l. For a $2 \to 2$ process the cross section is given by $d\sigma/d\Omega = |A|^2/(64\pi^2 s)$ with $d\Omega = 2\pi d\cos\vartheta$ and the total cross section can be written as:

$$\begin{aligned}\sigma &= \frac{8\pi}{s}\sum_{l,l'=0}^{\infty}(2l+1)(2l'+1)a_l a_{l'}\int_{-1}^{1} d\cos\vartheta P_l(\cos\vartheta)P_{l'}(\cos\vartheta) \\ &= \frac{16\pi}{s}\sum_{l=0}^{\infty}(2l+1)|a_l|^2.\end{aligned} \tag{2.2}$$

The optical theorem puts in relation the cross section with the imaginary part of the amplitude in the forward direction through the relation:

$$\sigma = \frac{1}{s}Im[A(\vartheta=0] = \frac{16\pi}{s}\sum_{l=0}^{\infty}(2l+1)|a_l|^2, \tag{2.3}$$

obtaining in this way the unitary conditions:

$$\begin{aligned} |a_l|^2 = Im(a_l) &\Rightarrow [Re(a_l)]^2 + [Im(a_l)]^2 = Im(a_l) \\ &\Rightarrow [Re(a_l)]^2 + [Im(a_l) - \frac{1}{2}]^2 = \frac{1}{4}, \end{aligned} \tag{2.4}$$

this can be interpreted as the equation of a circle of radius $1/2$ and center $(0, 1/2)$ in the plane $[Re(a_l), Im(a_l)]$ and the real part of the unitary condition is:

$$|Re(a_l)|^2 < \frac{1}{2}. \tag{2.5}$$

Considering the amplitude for $J = 0$ partial wave [20] and a Higgs boson mass smaller than $\sqrt{s}$:

$$\begin{aligned} a_0 &= \frac{1}{16\pi s}\int_{-s}^{0} dt A(t) \\ &= -\frac{m_H^2}{16\pi v^2}\left[2 + \frac{m_H^2}{s - m_H^2} - \frac{m_H^2}{s}\log\left(1 + \frac{s}{m_H^2}\right)\right] \overset{s \gg m_H^2}{\rightarrow} -\frac{m_H^2}{8\pi v^2}, \end{aligned} \tag{2.6}$$

where s is the center of mass energy and v is connected to the Higgs boson mass and to the self coupling, λ, through the relation $v^2 = m_H^2/2\lambda$, the upper limit is obtained:

$$m_H < 870 \text{ GeV}/c^2. \tag{2.7}$$

Same analysis can be done for any channel of the theory: $Z_L Z_L$, HH, $Z_L H$, $W_L^+ H$, $W_L^+ Z_L$, etc. With these other contributions the limit becomes:

$$m_H < 710 \text{ GeV}/c^2. \tag{2.8}$$

Thus, in the Standard Model theory, if the Higgs boson mass exceeds values of $\mathcal{O}(700)\text{GeV}/c^2$, unitarity will be violated unless new phenomena appear and restore it.

Constraint from the Perturbativity of the Higgs Self-Coupling

The Standard Model theory remains a perturbation theory in particular with processes involving the Higgs self-coupling, that introduce another upper bound on the Higgs boson mass. The fact that for large values of Higgs boson masses the perturbation theory is put at risk, is well known. It can be shown considering the decay of the Higgs boson into massive gauge bosons ($H \to VV$). For example, the decay width of the Higgs boson into two Z bosons, including the one and two-loop radiative corrections is [20]:

$$\begin{aligned} \Gamma(H \to ZZ) &\sim \frac{m_H^3}{32\pi v^2}\left[1 + 3\hat{\lambda} + 62\hat{\lambda}^2 + \mathcal{O}(\hat{\lambda}^3)\right] \\ &= \Gamma_{Born}\left[1 + 3\hat{\lambda} + 62\hat{\lambda}^2 + \mathcal{O}(\hat{\lambda}^3)\right], \end{aligned} \tag{2.9}$$

where $\hat{\lambda} = \lambda/(16\pi^2)$. If the perturbativity of the calculation remains, i.e. each term in the expansion is smaller than its predecessor, it is possible to derive an upper limit for the Higgs boson mass. For a very large Higgs boson mass, $\mathcal{O}(10\ \mathrm{TeV}/c^2)$, the one-loop term can be approximated by the Born term, $3\hat{\lambda} \sim 1$, in consequence the perturbative series is not convergent. With a value of m_H of an order of magnitude smaller, $\mathcal{O}(1\ \mathrm{TeV}/c^2)$, the two-loop contribution becomes comparable with the one-loop term, $3\hat{\lambda} \sim 62\hat{\lambda}^2$. To preserve the perturbativity in the expansion, the Higgs boson mass must have a value smaller than 1 TeV/c^2.

The risk to have a perturbative series that does not converge can also be seen in the scattering of longitudinal gauge bosons.
In the case of the $W_L^+W_L^- \to W_L^+W_L^-$ scattering [21–24] the perturbation theory is not applicable for Higgs boson masses above $m_H \sim 700\ \mathrm{GeV}/c^2$.

Triviality Constraint

A consequence of the quantum corrections is that the couplings and the masses, which appear in the Standard Model Lagrangian, depend on the considered energy. This effect is seen also in the quartic Higgs coupling which will be monotonically increasing with the energy scale $|Q|$.

The Renormalization Group Equation (RGE) for the quartic Higgs coupling λ can be used to define a range of the energy scale where the Standard Model theory is valid, obtaining, in this way, an upper limit for the Higgs boson mass.

The variation of the quartic Higgs coupling, λ, with the energy scale Q in terms of the RGE can be written as [25–30]:

$$\frac{d}{d\log Q^2}\lambda(Q^2) = \frac{3}{4\pi^2}\lambda^2(Q^2). \tag{2.10}$$

Its solution, in terms of the electro-weak symmetry breaking scale, $Q_0 = v$, can be written as:

$$\lambda(Q^2) = \frac{\lambda(v^2)}{1 - \frac{3}{4\pi^2}\lambda^2(v^2)\log\frac{Q^2}{v^2}}. \tag{2.11}$$

In the case of $Q^2 \ll v^2$ the quartic coupling goes to zero, $\lambda \to 0$, and the theory is said to be trivial, i.e. non interacting since the coupling is zero [31].
The other limit gives the bound sought. Indeed at a certain point the quartic coupling becomes infinite if the energy scale Q increases. The point where this happens is called Landau pole which corresponds to the energy:

$$\Lambda_C = v \exp\left(\frac{4\pi^2}{3\lambda}\right) = v \exp\left(\frac{4\pi^2 v^2}{3m_H^2}\right). \tag{2.12}$$

The Standard Model theory is a φ^4 theory and for these theories to remain perturbative at all scales it is necessary to have a coupling $\lambda = 0$, thus rendering the theory trivial. Through the RGE for the quartic Higgs self-coupling, it is possible to establish the energy domain in which the Standard Model theory is valid, i.e. the energy cut-off Λ_C below which the self-coupling λ remains finite.
If the cut-off is large, for instance $\Lambda_C \sim 10^{16}$ GeV, the Higgs mass should be small to avoid the Landau pole, $m_H < 200$ GeV/c^2.
If the cut-off is small, $\Lambda_C \sim 10^3$ GeV, the Higgs boson mass can be rather large, around the order of 1 TeV.
If the cut-off is chosen at the Higgs boson mass, $\Lambda_C = m_H$, the Higgs boson mass should be $m_H < 700$ GeV/c^2 to have the value of the quartic coupling finite. However according to simulations of gauge theories on the lattice, a rigorous bound is found at $m_H < 640$ GeV/c^2 [32, 33], which is in agreement with the bound obtained by the perturbation theory.

Stability Requirement and Lower Bound

Fermions and gauge bosons also have a contribution to the running of the quartic coupling, λ, and it is necessary include them into the calculation.

The Higgs boson couplings are proportional to the particle masses, then the main contribution comes from the top quarks and the massive gauge boson.

The one-loop RGE for the quartic coupling, including the fermion and the gauge boson contributions, becomes [25–30]:

$$\begin{aligned}\frac{d\lambda}{d\log Q^2} \simeq \frac{1}{16\pi^2}\,[\,&12\lambda^2 + 16\lambda\lambda_t^2 - 3\lambda_t^4 \\ &- \frac{3}{2}\lambda(3g_2^2 + g_1^2) + \frac{3}{16}(2g_2^4 + (g_2^2 + g_1^2)^2)\,]\,,\end{aligned} \tag{2.13}$$

where the top quark Yukawa coupling is given by $\lambda_t = \sqrt{2}m_t/v$ and g_1, g_2 are the hypercharge and weak coupling constants, respectively.

When the value of λ is not too large, the additional contributions produce a change in the triviality bounds. In particular the scale at which the new physics should appear depends on the value of the top quark mass.

For $\lambda \ll \lambda_t$, the solution of equation (2.13), considering the weak scale as the reference point, is:

$$\lambda(Q^2) = \lambda(v^2) + \frac{1}{16\pi^2}\left[-12\frac{m_t^4}{v^4} + \frac{3}{16}(2g_2^4 + (g_2^2 + g_1^2)^2)\right]\log\frac{Q^2}{v^2}. \tag{2.14}$$

If the coupling λ is too small, the top quark contribution is dominant and it could reach negative values, $\lambda(Q^2) < 0$. In this case the vacuum is not stable anymore. However, in the case of $\lambda(Q^2) > 0$ [34–38], the Higgs boson mass presents a lower limit:

$$m_H^2 > \frac{v^2}{8\pi^2}\left[-12\frac{m_t^4}{v^4} + \frac{3}{16}(2g_2^4 + (g_2^2 + g_1^2)^2)\right]\log\frac{Q^2}{v^2}, \tag{2.15}$$

connected to the cut-off energy Λ_C:

$$\begin{cases} \Lambda_C \sim 10^3 \text{ GeV} \Rightarrow m_H > 70 \text{ GeV}/c^2 \\ \Lambda_C \sim 10^{16} \text{ GeV} \Rightarrow m_H > 130 \text{ GeV}/c^2. \end{cases} \tag{2.16}$$

Combined Triviality and Stability Bounds

With a value of the cut-off energy of ~ 1 TeV, the positivity and the finiteness of the self-coupling λ sets a lower bound at 70 GeV/c^2 and an upper bound at 1 TeV for the Higgs boson mass [38–41].

The stability (lower band) and the triviality (upper band) constraints [41] are shown in figure 2.1, where the allowed region for the Higgs boson mass is shown as function of the scale of new physics Λ_C. The various experimental and theoretical uncertainties are taken into account with the width of the bands.

In conclusion, if the scale of new physics Λ_C is of the order of TeV, the Higgs boson mass is allowed to be in the range:

$$50 < m_H < 800 \text{ GeV}/c^2. \tag{2.17}$$

Otherwise, if it is required that the Standard Model is valid up to the Grand Unification scale, $\Lambda_{GUT} \sim 10^{16}$ GeV, the Higgs boson mass range is:

$$130 < m_H < 180 \text{ GeV}/c^2. \tag{2.18}$$

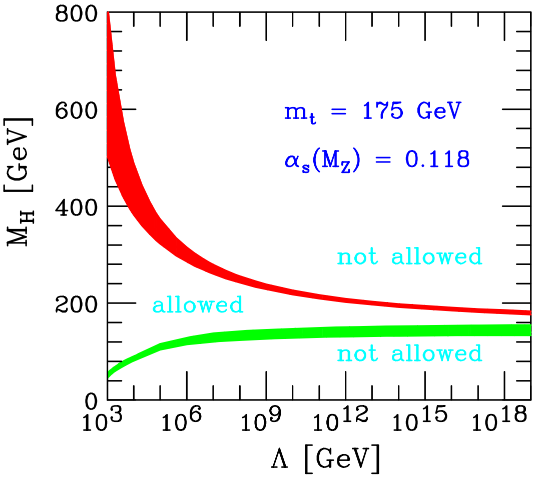

Figure 2.1: The triviality (upper) bound and the vacuum stability (lower) bound on the Higgs boson mass as a function of the new physics or cut–off scale Λ_C for a top quark mass $m_t = 175 \pm 6$ GeV/c^2 and $\alpha_s(m_Z) = 0.118 \pm 0.002$; the allowed region lies between the bands and the colored/shaded bands illustrate the impact of various uncertainties [41].

2.1.2 Experimental Constraints on the Higgs Boson Mass

The experimental constraints on the Higgs boson mass can be find from the direct searches at LEP, Tevatron and LHC collider.

The direct searches of the Standard Model Higgs boson started at the LEP collider. The interesting results have been obtained when the center of mass energy reached the value of $\sqrt{s} = 209$ GeV. The dominant production channel was the associated vector boson process $e^+e^- \to ZH$ [42, 43]. The search has been conducted in several final states topologies with an hadronic Higgs decay $(b\bar{b})$ associated to a leptonic Z decay $(\nu\bar{\nu}, l^+l^-, \tau^+\tau^-)$, or conversely $(H \to \tau^+\tau^-$,

$Z \to b\bar{b}$). In the end of year 2000 the LEP collaboration presented a result of the presumed observation of a Standard Model Higgs boson around 115 GeV/c^2, but the excess of 1.7σ was not significant enough to claim a discovery [44]. The combination of the results from the OPAL, L3, DELPHI and ALEPH experiments at LEP excluded the presence of the Higgs boson for mass values less than 114.4 GeV/c^2 at 95% confidence level. This direct search limit is rather robust as it has been obtained in pure electro-weak processes at lowest order.

The direct search for the Standard Model Higgs boson was one of the main goals of Tevatron collider and started more than a decade ago.
For searches for low mass Higgses, $m_H < 135$ GeV/c^2, the main production channels are the Higgs-strahlung processes $p\bar{p} \to HV$ with $V = W, Z$, which decay leptonically via $W \to l\nu$[1], $Z \to l^+l^-$ or $Z \to \nu\bar{\nu}$ and its most sensitive decay channels is the hadronic $H \to b\bar{b}$ decay.
For searches for high mass Higgses, $m_H > 135$ GeV/c^2, the sensitivity is dominated by the search for $H \to W^+W^- \to l^+\nu l^-\bar{\nu}$ produced in gluon fusion channel $gg \to H$.
In addition to those high-sensitivity channels also other production and decay channels are analyzed, as $H \to \gamma\gamma$, $H \to ZZ \to l^+l^-l'^+l'^-$, $q\bar{q}b\bar{b}$ from $WH(ZH)$ and in VBF with the decay $H \to b\bar{b}$, $t\bar{t}H$ with $H \to b\bar{b}$, $H \to \tau^+\tau^-$, $H \to W^+W^- \to l\nu q\bar{q}$ and $W(Z)H \to W(Z)WW \to l^\pm l^\pm + X$.
The combination of the results from CDF and DØ experiments excluded the presence of the Higgs boson for mass values in the range $147 \leq m_H \leq 180$ GeV/c^2 at 95% confidence level. This is displayed in figure 2.2 where the ratio between the 95% confidence level exclusion cross section and the predicted Standard Model cross section are shown as a function of the Higgs boson mass with the regions excluded by the LEP and LHC results. When the ratio falls below the unity, the Standard Model Higgs boson mass is excluded.

In the beginning of 2010 [45], the LHC took first proton-proton collision data at the center of mass energy of 7 TeV. Because of the overwhelming background and the limited trigger capabilities, searches with fully hadronic final states, coming from gluon or vector boson fusion with Higgs boson decay via $H \to b\bar{b}$ or $H \to WW(ZZ) \to 4$ quarks, are not considered sensitive searches. On the other hand, final states containing at least one photon, electron, muon, or a hadronic tau lepton decay in association with large missing transverse momentum contain valuable information. In contrast to the searches at Tevatron channels with low branching ratios, such as $H \to \gamma\gamma$ and $H \to ZZ \to l^+l^-l'^+l'^-$ are also accessible due to the larger production cross section at the LHC. These two channels are

---

[1] l denotes an electron or muon.

considered the *golden channels* at LHC, they provide the highest sensitivity over a large mass range.

In 2012 ATLAS and CMS experiments [46, 47] have reported the observation of a Higgs-like particle. With this results the range of validity of m_H was definitively reduced into a small area around the value of 125 GeV/c^2. In the same period, the Tevatron collaborations have reported evidence for a particle decaying to $b\bar{b}$ produced in association with a W/Z boson for masses within the range 120-135 GeV/c^2 [48].

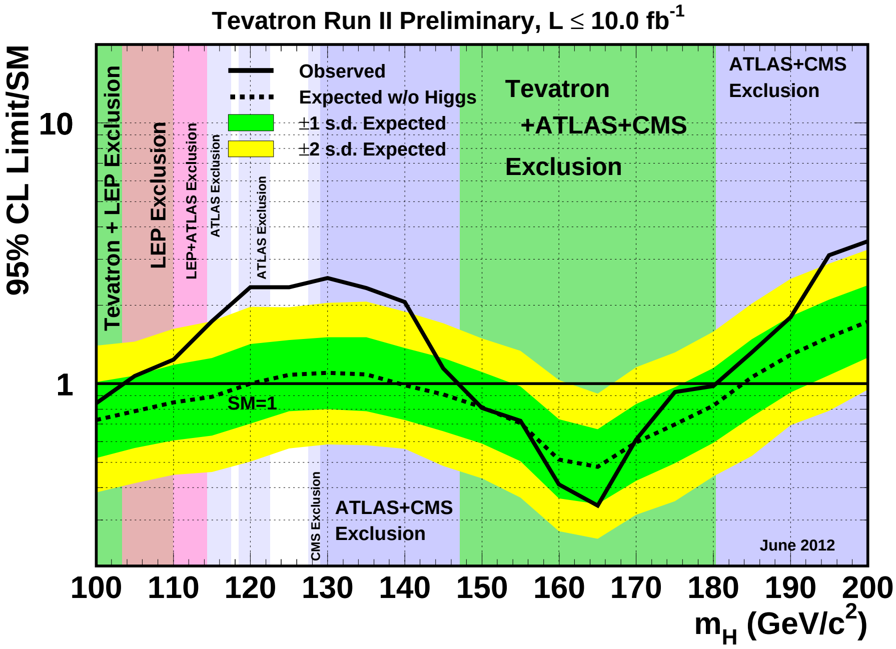

Figure 2.2: Observed and expected 95% confidence level upper limits on the ratios to the Standard Model cross section at Tevatron [49].

2.2 Higgs Boson Production at Hadron Collider

In the Standard Model, the Higgs boson couples preferentially to heavy particles, like the gauge bosons W and Z, the top and bottom quark. This is the basic principle on which the production mechanisms for the Higgs particle at hadron colliders is based. The four main production processes at hadron collider are: the gluon-gluon fusion mechanism ($gg \to H$) [50], the vector boson fusion processes ($qq \to qq + V^*V^* \to qq + H$) [51–54], the associated production with

W/Z bosons ($q\bar{q} \to V^* \to V + H$) [55–57] and the associated Higgs production with heavy top [58–61] or bottom quarks ($gg, q\bar{q} \to q\bar{q} + H$) [62–64], the corresponding Feynman diagrams are shown in figure 2.3 and their total cross sections at Tevatron are shown in figure 2.4.

The pair production of the Higgs boson via the gluon fusion mechanism $gg \to HH$, which proceeds through top and bottom quark loops [65–68], the associated double production with massive gauge boson $q\bar{q} \to HHV$ [69, 70] and the vector boson fusion mechanisms $qq \to V^*V^* \to HHqq$ [71–76] have smaller production cross sections (order of few femto barns) than the single Higgs production mechanism, because of the suppression by the additional electro-weak couplings.

The processes where the Higgs is produced in association with one [77–79], two [80–82] or three [83] hard jets in gluon-gluon fusion, the associated Higgs production with gauge boson pairs [84] and the production with a vector boson and two jets [85, 86] are also suppressed.

Also other production processes exist but they present a significantly smaller production cross section of the order of $0.1 - 1.0$ fb [87–90].

Interesting production channels are the diffractive processes [91–93], in particular the exclusive central diffractive processes [94–96] where the mechanism is mediated by color singlet exchanges leading to the diffraction of the incoming hadrons and a centrally produced Higgs boson. These processes present a cross section of the order of $0.9 - 5.5$ fb.

For processes involving strongly interacting particles the lowest order cross sections are affected by large uncertainties arising from higher order corrections. The associated vector boson production and the vector boson fusion will be described in detail in the next sections (sections 2.2.1-2.2.2), they are the main objects of this research.

The cross section for a generic process $p\bar{p} \to AB$ can be calculated considering the incoming parton as massless[2] with the center of mass energy s and the parton center of mass energy equal to $\hat{s} = x_1 x_2 s$, where x_1 (x_2) is the momentum fraction of the first (second) parton. The result is [97]:

$$\begin{gathered}\sigma(p\bar{p} \to AB) = \sum_{i,j} \int_0^1 f_i(x_1) dx_1 \int_0^1 f_j(x_2) dx_2 \hat{\sigma}_{ij}(\hat{s} = x_1 x_2 s) \\ \Theta\left(\hat{s} \geq (m_A + m_B)^2\right),\end{gathered} \tag{2.19}$$

---

[2] The mass of the proton (antiproton) can be neglected with respect to the center of mass energy of the collider. In the Tevatron case the center of mass energy is 1.96 TeV and the mass of proton (antiproton) is $\sim 1\mathrm{GeV}/c^2$.

where $\hat{\sigma}_{ij}$ is the partonic cross section $ij \to AB$, Θ is the step function, m_A and m_B are the masses of the two final particles and the sum is over all possible initial partonic states. With the replacement $x_2 = \hat{s}/(x_1 s)$ and reordering the interval of variation of $\hat{s}$ and x_1, the equation (2.19) becomes:

$$\begin{aligned} \sigma(p\bar{p} \to AB) &= \sum_{i,j} \int_0^1 f_i(x_1) dx_1 \int_{(m_A+m_B)^2}^{x_1 s} \frac{d\hat{s}}{s} f_j\left(\frac{\hat{s}}{x_1 s}\right) \hat{\sigma}_{ij}(\hat{s}) \\ &= \sum_{i,j} \int_{(m_A+m_B)^2}^{s} d\hat{s} \frac{\hat{\sigma}_{ij}}{s} \int_{\hat{s}/s}^{1} f_i(x_1) f_j\left(\frac{\hat{s}}{x_1 s}\right) \frac{dx_1}{x_1}. \end{aligned} \tag{2.20}$$

Using the variables $\tau_{AB} = (m_A + m_B)^2/s$ and $\tau = \hat{s}/s$, the final result is:

$$\begin{aligned} \sigma(p\bar{p} \to AB) &= \sum_{i,j} \int_{\tau_{AB}}^1 d\tau \hat{\sigma}_{ij}(\hat{s} = \tau s) \int_\tau^1 f_i(x) f_j\left(\frac{\tau}{x}\right) \frac{dx}{x} \\ &= \sum_{i,j} \int_{\tau_{AB}}^1 d\tau \hat{\sigma}_{ij}(\hat{s} = \tau s) \frac{d\mathcal{L}^{ij}}{d\tau}(\tau), \end{aligned} \tag{2.21}$$

where the quantity $d\mathcal{L}^{ij}/d\tau(\tau)$ is called ij-luminosity.

2.2.1 Associated Vector Boson Production

The cross section for the associated vector boson process (figure 2.5):

$$\begin{aligned} q_1(p_1)\bar{q}_2(p_2) &\to V^*(k_1 = p_1 + p_2) \\ &\to V(k_2 = p_3 + p_4) H(k) \to q_3(p_3)\bar{q}_4(p_4) H(k), \end{aligned} \tag{2.22}$$

where p_i the quark momenta, k_i the vector boson momenta, k the Higgs boson momentum and $V = W, Z$, with $\hat{s} = k_1^2 = (p_1 + p_2)^2$ being the center of mass energy of the partonic subprocess, can be obtained considering the equation (2.21).

The total cross section is obtained averaging over the quark spins and colors, dividing by the flux factor, and integrating over the three–particle phase–space. Ignoring the decay products of the final vector boson and the Higgs particle, the integrated cross section at leading order (LO) is [20]:

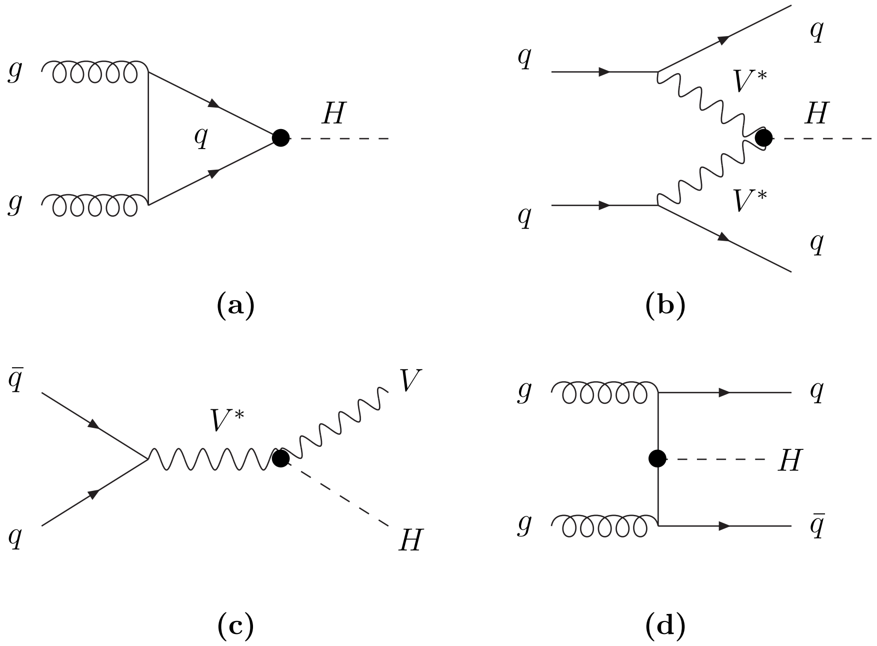

(a) **(b)**

(c) **(d)**

Figure 2.3: The dominant Standard Model Higgs boson production mechanisms in hadronic collisions: (a) the gluon-gluon mechanism, (b) the vector boson fusion process, (c) the associated production with W/Z bosons and (d) the associated Higgs production with heavy quarks.

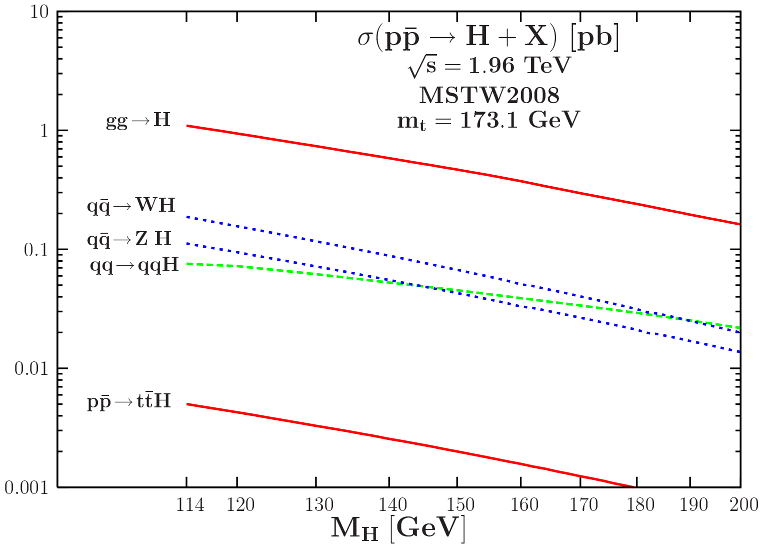

Figure 2.4: The total cross sections for Higgs production at the Tevatron as function of the Higgs boson mass [20].

$$
\begin{aligned}
\hat{\sigma}_{LO}(q\bar{q} \to VH) = & \frac{G_F^2 m_V^4}{288\pi\hat{s}}(\hat{v}_q^2 + \hat{a}_q^2)\lambda^{1/2}(m_V^2, m_H^2; \hat{s}) \\
& \frac{\lambda(m_V^2, m_H^2; \hat{s}) + 12m_V^2/\hat{s}}{(1 - m_V^2/\hat{s})^2},
\end{aligned}
\tag{2.23}
$$

where $\lambda(m_V^2, m_H^2; \hat{s})$ is the two-body phase space function $\lambda(x, y; z) = (1 - x/z - y/z)^2 - 4xy/z^2$ and the reduced fermion couplings to the gauge bosons are: $\hat{a}_f = 2I_f^3, \hat{v}_f = 2I_f^3 - 4Q_f s_W^2$ for $V = Z$ and $\hat{v}_f = \hat{a}_f = \sqrt{2}$ for $V = W$.

This process can be viewed as the Drell-Yan production of a virtual vector boson with $k_1^2 \neq m_V^2$, which then splits into a real vector boson and a Higgs particle.

The total production cross section is then obtained by convolving the equation (2.23) with the parton densities and summing over the contributing partons:

$$
\sigma_{LO}(pp \to VH) = \int_{\tau_0}^{1} d\tau \sum_{q,\bar{q}} \frac{d\mathcal{L}^{q\bar{q}}}{d\tau} \hat{\sigma}_{LO}(\hat{s} = \tau s), \tag{2.24}
$$

where $\tau_0 = (m_V + m_H)^2/s$, s is the total hadronic center of mass energy and the parton luminosity is defined at a factorization scale μ_F in terms of the parton densities $q_i(x_i, \mu_F^2)$ by:

$$
\sum_{q,\bar{q}} \frac{d\mathcal{L}^{q\bar{q}}}{d\tau} = \sum_{q_1,\bar{q}_2} \int_{\tau}^{1} \frac{dx}{x} \left[q_1(x, \mu_F^2)\, \bar{q}_2(\tau/x, \mu_F^2) \right]. \tag{2.25}
$$

Figure 2.6 shows the total production cross sections as a function of the Higgs boson mass for the Tevatron and the LHC in both the $W^{\pm}H$ and ZH channels [20]. The cross sections for $W^{\pm}$ final states are approximately two times larger than the ones for the ZH final state at both colliders.

2.2.2 Vector Boson Fusion Production

The matrix element squared [20] for the massive vector boson fusion process (figure 2.7)

$$
\begin{aligned}
q_1(p_1)q_2(p_2) & \to V^*(k_1 = p_3 - p_1)V^*(k_2 = p_4 - p_2)q_3(p_3)q_4(p_4) \\
& \to q_3(p_3)q_4(p_4)H(k),
\end{aligned}
\tag{2.26}
$$

with p_i are the quark momenta, k_i are the vector boson momenta, k is the Higgs

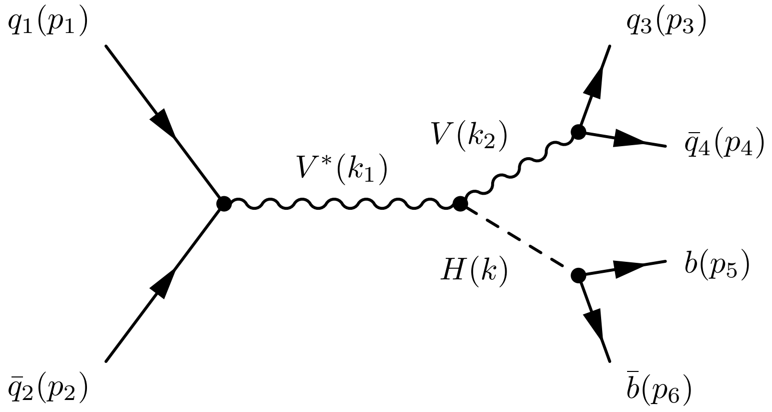

Figure 2.5: Feynman diagram for the associated vector boson process (VH).

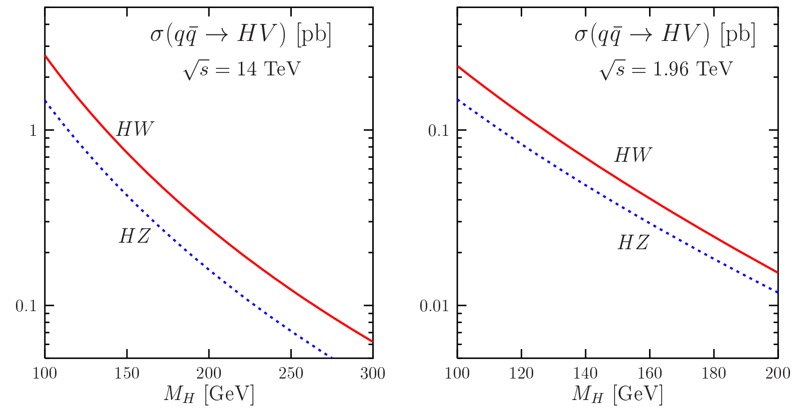

Figure 2.6: Total production cross sections of Higgs bosons in the associated vector boson processes at leading order at the (left) LHC and at the (right) Tevatron [20].

boson momentum and $V = W, Z$, is given by:

$$|\mathcal{M}|^2 = 4\sqrt{2} N_c^f G_F^3 m_V^8 \frac{C_+(p_1 \cdot p_2)(p_3 \cdot p_4) + C_-(p_1 \cdot p_4)(p_2 \cdot p_3)}{(k_1^2 - m_V^2)^2 (k_2^2 - m_V^2)^2} \tag{2.27}$$

where, in terms of the vector and axial-vector couplings of the gauge bosons to fermions $\hat{a}_f = 2I_f^3$, $\hat{v}_f = 2I_f^3 - 4Q_f s_W^2$ for $V = Z$ and $\hat{v}_f = \hat{a}_f = \sqrt{2}$ for $V = W$, $C_\pm$ read

$$C_\pm = (\hat{v}_{q_1}^2 + \hat{a}_{q_1}^2)(\hat{v}_{q_3}^2 + \hat{a}_{q_3}^2) \pm 4\hat{v}_{q_1}\hat{a}_{q_1}\hat{v}_{q_3}\hat{a}_{q_3}. \tag{2.28}$$

The differential distribution at LO is:

$$d\hat{\sigma}_{LO} = \frac{1}{4}\frac{1}{9}\frac{1}{2\hat{s}} \times |\mathcal{M}|^2 \times \frac{1}{(2\pi)^5} \frac{d^3k}{2dE_H} \frac{d^3p_3}{2dE_3} \frac{d^3p_4}{2dE_4} \delta^4(p_1 + p_2 - p_3 - p_4 - k). \tag{2.29}$$

Integrating over the variables p_3 and p_4 in the rest frame of the two quarks $\vec{p}_3 + \vec{p}_4 = 0$ [20]:

$$\frac{d\hat{\sigma}_{LO}}{dE_H d\cos\vartheta} = \frac{G_F^3 m_V^8}{9\sqrt{2}\pi^3 \hat{s}} \frac{p_H}{32 s_1 s_2 r} \Big[C_+ \mathcal{H}_+ + C_- \mathcal{H}_- \Big] \tag{2.30}$$

with

$$\begin{cases} \mathcal{H}_+ = (h_1+1)(h_2+1)\left[\dfrac{2}{h_1^2-1} + \dfrac{2}{h_2^2-1} - \dfrac{6s_\chi^2}{r} + \left(\dfrac{3t_1t_2}{r} - c_\chi \right) \dfrac{\ell}{\sqrt{r}} \right] \\ \qquad - \left[\dfrac{2t_1}{h_2-1} + \dfrac{2t_2}{h_1-1} + \left(t_1 + t_2 + s_\chi^2\right) \dfrac{\ell}{\sqrt{r}} \right] \\ \mathcal{H}_- = 2(1-c_\chi)\left[\dfrac{2}{h_1^2-1} + \dfrac{2}{h_2^2-1} - \dfrac{6s_\chi^2}{r} + \left(\dfrac{3t_1t_2}{r} - c_\chi \right) \dfrac{\ell}{\sqrt{r}} \right], \end{cases} \tag{2.31}$$

and

$$\begin{aligned} s_{1,2} &= \sqrt{\hat{s}}(\varepsilon_\nu \pm p_H \cos\vartheta), \quad h_{1,2} = 1 + 2m_V^2/s_{1,2}, \quad t_{1,2} = h_{1,2} + c_\chi h_{2,1} \\ c_\chi &= 1 - \frac{2\hat{s}s_\nu}{s_1 s_2} = 1 - s_\chi^2, \quad r = h_1^2 + h_2^2 + 2c_\chi h_1 h_2 - s_\chi^2, \\ \ell &= \log \frac{h_1 h_2 + c_\chi + \sqrt{r}}{h_1 h_2 + c_\chi - \sqrt{r}}, \end{aligned} \tag{2.32}$$

where $p_H = \sqrt{E_H^2 - m_H^2}$ is the Higgs boson momentum, $\varepsilon_\nu = \sqrt{\hat{s}} - E_H$ and $s_\nu = \varepsilon_\nu^2 - p_H^2$ are the energy and the invariant mass of the final state quark pair. The partonic total cross section, $\hat{\sigma}_{LO}(qq \to qqH)$, is obtained integrating the differential cross section over the region:

$$-1 < \cos\vartheta < 1 \quad \text{and} \quad m_H < E_H < \frac{\sqrt{\hat{s}}}{2}\left(1 + \frac{m_H^2}{\hat{s}}\right). \tag{2.33}$$

The total cross section at LO is obtained summing over the contributing partons, considering the two subprocesses WW and ZZ fusion channels and folding it with the parton luminosities. The figure 2.8 shows the total cross sections as a function of the Higgs boson mass for Tevatron and LHC.

The values of the cross section are rather large at LHC, in particular in the mass range $100 < m_H < 200$ GeV/c^2, but they are smaller at Tevatron, around one order of magnitude of difference. The reason of this discrepancy is due to the fact that the main contribution originates from longitudinal gauge bosons, which have cross sections that grow with energy, and the partonic cross sections rise logarithmically with the center of mass energy of the subprocess, $\hat{\sigma} \propto \log \hat{s}/m_V^2$, giving much larger rates at high energies.

It is also interesting to notice that at LHC the main contribution to the cross section comes from the WW fusion channel, $\sigma(WW \to H) \sim 3\sigma(ZZ \to H)$. This is due to the fact that the W boson couplings to fermions are larger than those of the Z boson.

2.3 Higgs Boson Decay

In the Standard Model, once the Higgs mass is fixed, the profile of the Higgs particle is uniquely determined. The Higgs couplings to gauge bosons and fermions are directly proportional to the masses of the particles and the Higgs boson will have the tendency to decay into the heaviest ones allowed by phase space. Since the pole masses of the gauge bosons and fermions are known all the partial

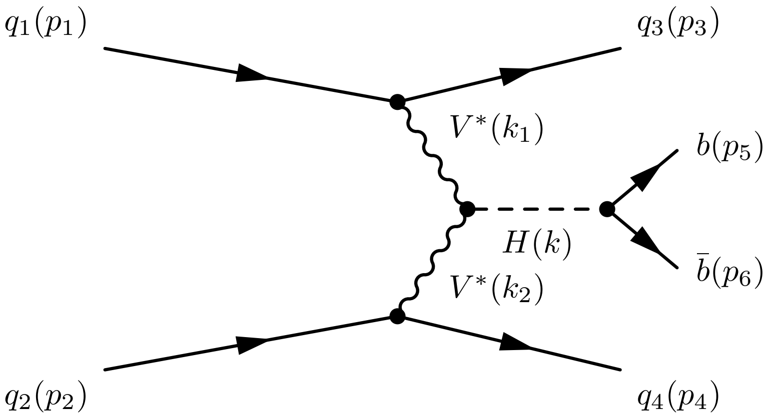

Figure 2.7: Feynman diagram for the vector boson fusion process (VBF).

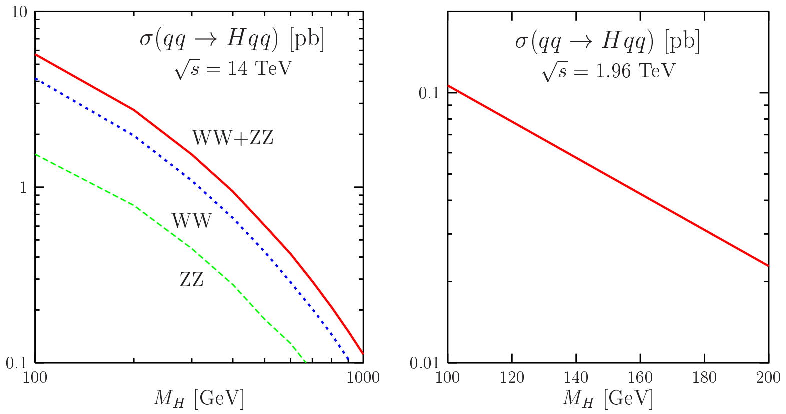

Figure 2.8: Individual and total production cross sections in the vector fusion $qq \to V^*V^* \to Hqq$ processes at leading order at the (left) LHC and total production cross section at the (right) Tevatron [20].

widths for the Higgs decays into these particles can be predicted. The Higgs boson branching ratios are shown in figure 2.9.

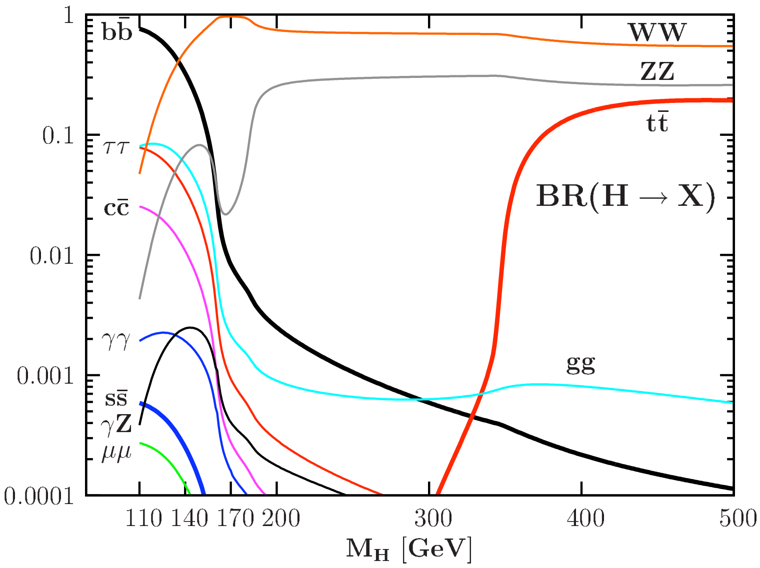

Figure 2.9: The Standard Model Higgs boson decay branching ratios over the Higgs boson mass range relevant at the Tevatron and the LHC [20].

The partial width of the Higgs boson decay into fermion pairs is given by [20]:

$$\Gamma(H \to f\bar{f}) = \frac{G_F N_c}{4\sqrt{2}\pi} m_H \, m_f^2 \, \beta_f^3, \tag{2.34}$$

with $\beta_f = (1 - 4m_f^2/m_H^2)^{1/2}$ being the velocity of the fermions in the final state and $N_c = 3\,(1)$ the color factor for quarks (leptons).
In case of Higgs boson decay into quark pairs, the equation (2.34) becomes [20]:

$$\Gamma(H \to q\bar{q}) = \frac{3G_F}{4\pi\sqrt{2}} m_H m_q^2 \left(1 - 4\frac{m_q^2}{m_H^2}\right)^{\frac{3}{2}}. \tag{2.35}$$

Equation (2.35) shows that the partial width is proportional to the square of the quark mass and the dominant decay channel is obtained with the bottom quark. As mentioned before, the Higgs boson decay into bottom quark pairs is the most important decay mode for light Higgs masses at Tevatron where the presence of leptons and missing energy (ll, $l\nu$, $\nu\bar{\nu}$) in the final states helps to reduce the background.

2.4 All-Hadronic Higgs Cross Section Values

The production cross sections of the processes investigated in this analysis are modeled by using PYTHIA [98] Monte Carlo program with the CTEQ5L [99] parton distribution function (PDF) at LO. The Monte Carlo predictions are scaled to the higher-order calculations of inclusive cross sections, and differential cross sections [49].

The cross section values in the associated vector boson process are obtained multiplying the production cross sections with the branching ratios for the vector boson to jets (for the W boson is 67.60% [49] and for the Z boson is 69.91% [49]) and the branching ratio for the Higgs boson which decays into a pair of bottom-antibottom quarks. The uncertainties applied on the VH cross section values are calculated following the procedure described in [49, 100] and their values are $\pm 5\%$. The equivalent results for the vector boson fusion process are obtained multiplying the production cross sections with the branching ratio of the same Higgs boson decay process. For the VBF process, the procedure to calculate the cross section uncertainties is described in [49, 101] and their values are $\pm 10\%$. The values of the cross sections are listed in table 2.1a [49] and plotted in figure 2.10a for the different Higgs boson mass hypotheses considered in this analysis.

The values of the branching ratios for the process $H \rightarrow b\bar{b}$ are listed in table 2.1b and plotted in figure 2.10b for the same mass points and their uncertainties are estimated to be $\sim 2\%$ [102].

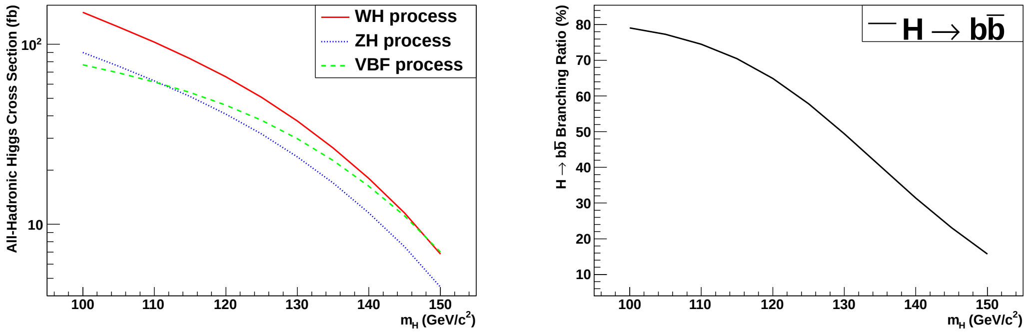

(a) (b)

Figure 2.10: The all-hadronic Higgs (a) cross section in the associated vector boson and vector boson fusion process and (b) the values of the branching ratio for the process $H \rightarrow b\bar{b}$ used in this analysis [49].

Higgs Mass (GeV/c^2)	WH (fb)	ZH (fb)	VBF (fb)
100	150.31	89.97	76.96
105	124.73	75.39	69.39
110	102.59	62.60	61.70
115	83.16	51.21	53.90
120	65.85	40.93	45.90
125	50.60	31.72	37.76
130	37.40	23.66	29.87
135	26.55	16.95	22.62
140	17.96	11.57	16.28
145	11.51	7.48	11.10
150	6.83	4.48	6.99

(a)

Branching Ration (%)
79.10
77.30
74.50
70.50
64.90
57.80
49.40
40.40
31.40
23.10
15.70

(b)

Table 2.1: The values of the all-hadronic Higgs (a) cross sections in the associated vector boson and vector boson fusion channel and (b) the values of the branching ratio for the process $H \to b\bar{b}$ for various Higgs boson mass hypotheses considered in this analysis [49].

Chapter 3

Tevatron Collider and CDF Experiment

The Tevatron collider and the CDF experiment were built at the Fermi National Accelerator Laboratory (Fermilab), near Chicago in the United States.
Fermilab's accelerator complex comprises ten particle accelerators and storage rings, among which the Tevatron was the largest. After the Tevatron shutdown, Fermilab's research activity is not over, different experiments are still in running and others are scheduled. At Fermilab the world's most powerful high-energy neutrino beam is produced and proton and neutron beams for various experiments are provided, such as the Mini Booster Neutrino Experiment (MiniBooNE), the SciBar Booster Neutrino Experiment (SciBooNE) and the Main Injector Neutrino Oscillation Search (MINOS).

3.1 Accelerator Chain

Before being injected into the Tevatron, the protons and antiprotons were produced and accelerated to an energy of 150 GeV by a series of accelerators, the accelerator chain (figure 3.1). The initial proton for the proton beams were produced from hydrogen gas. A portion of those protons were used to create antiprotons. Once enough antiprotons were accumulated, they were loaded into the Tevatron with protons traveling in the opposite direction. A summary of the accelerator chain with their initial and final kinematic energies is shown in the table 3.1.

The first part of the accelerator chain is the Pre-accelerator [104, 105], or Preacc. It consists of the source housed in an electrically charged dome. The source converts hydrogen gas to ionized hydrogen gas (H^-). The ionized gas is

Accelerator	Initial kinematic energy	Final kinematic energy	Destination of beam
Pre-accelerator	~ 0 keV	750 keV	Linac
Linac	750 keV	400 MeV	Booster
Booster	400 MeV	8 GeV	Main Injector
Main Injector	8 GeV	8 GeV	Recycler
		120 GeV	Antiproton source
		150 GeV	Tevatron
Recycler	8 GeV	8 GeV	Main Injector
Antiproton source	8 GeV	8 GeV	Main Injector
Tevatron	150 GeV	980 GeV	Tevatron

Table 3.1: The initial and final kinematic energies of the various accelerators which compose the accelerator chain [103].

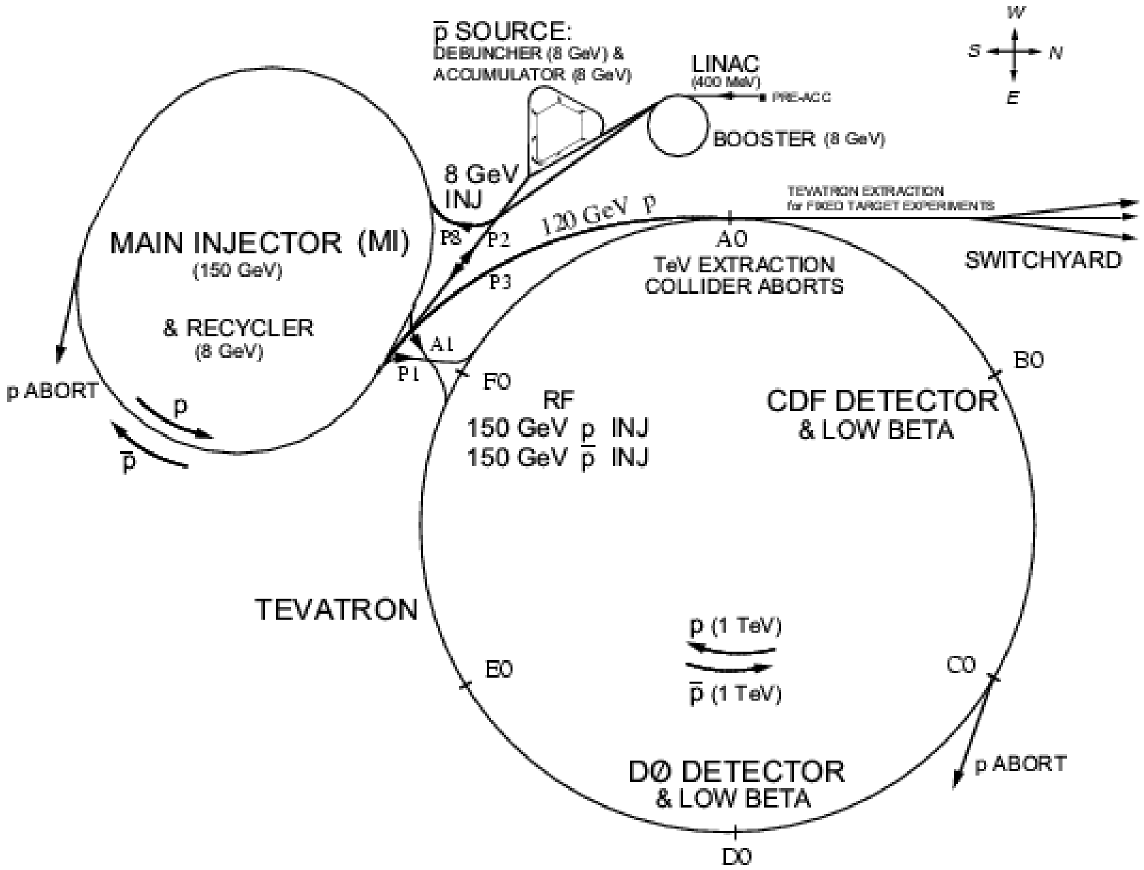

Figure 3.1: Fermilab accelerator complex [103].

allowed to accelerate through a column from the charged dome to the grounded wall to an energy of 750 keV.
After beam exits the accelerating column, it travels through a transfer line and enters into the Linear Accelerator [105], or Linac, the next level in the accelerator chain. It accelerates the H^- ions up to an energy of 400 MeV through two sets of radio frequency (RF) stations. The first set operates at a frequency of 201 MHz and accelerate the beam from 750 keV to 116 MeV. The last set of RF stations operates at 805 MHz and accelerate the beam to 400 MeV.
After the beam is accelerated by the Linac, the 400 MeV H^- ions are send via a transfer line to the Booster [106], the first circular accelerator. It consists of a series of magnets arranged around a 75 m radius circle, with 19 RF cavities with a frequency of 37.86 MHz, when the ions are injected, and which increases to 52.81 MHz at extraction time.
The 400 MeV H^- ions beam passes through a carbon stripping foil, which removes the electrons and leaves only the protons. The protons beam is accelerated to the energy of 8 GeV and directed to the Main Injector via a transfer line.

The Main Injector (MI) [107] is a roughly elliptical synchrotron, seven times the circumference of the Booster and slightly more than half the circumference of the Tevatron. In the Main Injector ring both protons and antiprotons are accelerated from 8 up to 150 GeV before being injected into the Tevatron. The Main Injector also accelerates the protons used for the production of the antiprotons. In that case the protons are accelerated up to 120 GeV and sent to the Antiproton Source. In the same tunnel at about 1.20 m above the Main Injector, it is located an antiproton storage ring, the Recycler Ring [107]. Its name derives from the characteristic to recover the scarse antiprotons after the Tevatron data taking was complete.

Even though large improvements have been made over the years, the time required to accumulate an adequate number of antiprotons still is the largest bottleneck in reaching high luminosities in the proton-antiproton collider. Typically for every 10^5 protons striking an antiproton production target, only about 2 antiprotons are captured and stored.
The Fermilab Antiproton Source [108] is made of a target station, two rings called Debuncher and Accumulator and the connections with the Main Injector. The antiprotons are produced bombarding a production target with a 120 GeV proton beam extracted from the Main Injector. The target is made up of Inconel, a nickel-iron alloy, it can tollerate higher stresses caused by the rapid beam heating. Beyond the target the Lithium Lens module focuses a portion of the 8 GeV antiprotons coming off of the target reducing their angular component (figure 3.2).

The negative charged particles with an energy around 8 GeV are bent by a pulsed dipole magnet and injected into the Debuncher. The other particles are absorbed with a beam dump.
In the Debuncher, the antiproton beam size is reduced by the horizontal and vertical betatron stochastic cooling. Also its momentum spread is reduced by RF bunch rotation and adiabatic debunching. Then they are injected and stored into the Accumulator. The Debuncher and the Accumulator reside in the same triangular storage ring.

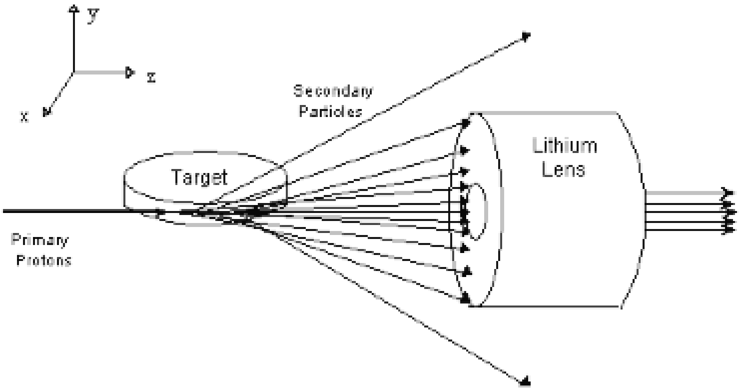

Figure 3.2: Antiproton lithium lens [108].

The antiprotons, from the Antiproton Source, are sent to the Main Injector where they circulate for a few seconds but are not accelerated, before being transferred into the Recycler. The Recycler then stores this beam for many hours. During this storage, the antiproton beam is cooled, so to reduce the longitudinal and transverse spread of the beam. After this operation other antiprotons can be injected and stored. In this way, the Recycler is able to provide higher intensity and lower emittance antiprotons bunches for the collider physics program.

3.2 Tevatron Collider

The Tevatron [103] (figure 3.1) was the highest energy proton-antiproton circular synchrotron with eight accelerating cavities, 6.86 km of circumference and 980 GeV of energy by beam. It ceased operations on September 30th 2011, due to completion and activation of the Large Hadron Collider (LHC) at CERN in Geneva; its name is connected to the energy it could reach, which was of the order of *tera electron volt* or TeV.
During its about 30 years activity, started in 1983 accelerating protons to 512 GeV,

the Tevatron research program was divided in two significant periods. The period from the 1992 until the 1996 is called Run I and during this period the top quark was discovered. The Run I is divided in two phases, Run Ia which ended in May 1993 and Run Ib which was initiated in December of 1993. After many upgrades in November 2001 the second research program, Run II, started which was protracted until 2011. Also the Run II is divided in two phases, Run IIa ended in the end of 2004 and Run IIb started in 2005 and ended in 2011.

The primary purpose of the Tevatron was to act as a storage ring where protons and antiprotons could collide with each other and producing secondary particles. The protons and antiprotons were injected at 150 GeV and then accelerated up to 980 GeV. After the final energy was reached, the two particle beams passed through each other for several hours, unless the beam was lost because some components failed. In case the number of collisions per second was too low to be useful for the experiments, the store[1] was ended and the Tevatron was prepared for a new store.

The Tevatron was not a perfect circle, it was divided into six symmetric sectors labeled A through F. Each sector started with a section called *zero* location and then the rest of the sector was composed of four areas called *houses*, labeled 1 through 4. The houses consisted of a number of repeating series of magnets called cells. Each cell had ten magnets, two quadrupoles and eight dipoles. A cell started with a quadrupole followed by four dipoles that were followed themselves by another quadrupole and four more dipoles. The magnets used in the Tevatron were made up of a superconducting niobium/titanium alloy that needed to be kept extremely cold (∼4 K) to remain being a superconductor. The benefit of having superconducting magnets was the increased magnetic fields possible when high currents can be run through thin wires without the fear of damage related to excessive resistive heating. This low operating temperature was responsible for the Tevatron's extensive cryogenic plumbing and magnet protection systems.

The proton and the antiproton beam, injected into the Tevatron, was composed by tree trains of twelve bunches for a total of thirty-six proton bunches (figure 3.3). Each train was separated by 2.617 ms and each bunch was injected one at time separated by 396 ns, which gave a bunch crossing rate of 2.5 MHz. The number of protons and antiprotons per bunch was $\sim 2.70 \cdot 10^{11}$ and $\sim 7.00 \cdot 10^{10}$, respectively. The beams were monitored to check their quality. If any portion of the bunch had undesired intensity, emittance, etc then they could be aborted and the operation restarted.

The colliding beam accelerators are designed such that its constituent beams

---

[1] The term *store* means the stable situation of 980 GeV proton and antiproton collisions.

will only collide in regions monitored by detectors. In the case of the Tevatron, there were two interaction points: the B0 section, where the CDF experiment was located and the D0 section, where was the DØ experiment.
The Tevatron presented just one beam pipe where the proton and antiproton beams circulated. The beam passed each other everywhere in the machine without colliding. This was possible because horizontally and vertically oriented separators were arranged around the ring. The purpose of those separators was to allow the formation of helical beam orbits. The effect of the separators was undone just before the particles entered into one of the two collision halls allowing the beams to collide. Upon exiting the collision hall both beams returned to the helical orbit.

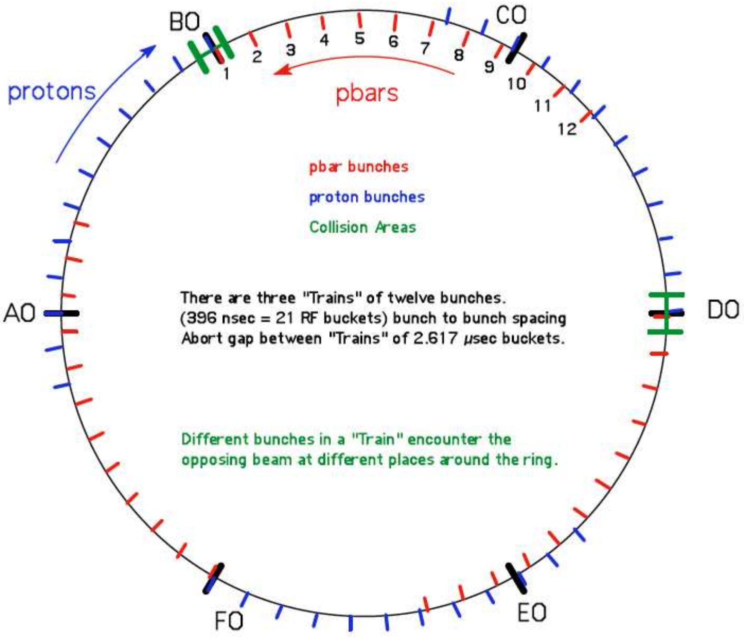

There are three "Trains" of twelve bunches.
(396 nsec = 21 RF buckets) bunch to bunch spacing
Abort gap between "Trains" of 2.617 μsec buckets.

Different bunches in a "Train" encounter the
opposing beam at different places around the ring.

Figure 3.3: Bunch and train spacing of the protons and antiprotons around the Tevatron [103].

The collider beam experiments have an advantage over the fixed-target experiments due to the center-of-mass energy attainable for the creation of new particles. In the fixed-target this energy goes as the square root of the initial beam energy, $\sqrt{E}$, in the colliding ones the center-of-mass energy is given by the sum of the energy of the two beams. In the Tevatron case, because the energy of the single beam was 980 GeV, the total available energy for the secondary particles was 1.96 TeV. However the collider beam experiments present a disadvantage connected to the fact that the collision rate is low.

The two beams rotating in the accelerator ring have, approximately, a Gaussian shape. Each particle has a probability of interacting with another particle traveling in the opposite direction. This probability is the interaction cross section, σ_{int}. The rate of interaction is given by:

$$R = \sigma_{int} L \tag{3.1}$$

where L is the luminosity. The luminosity is a measure of how the particles in both bunches are interacting with each other. It is a function of the revolution frequency, f, and of the area that the beam occupies. The proton and antiproton bunches can have different cross sectional areas, which can be defined in terms of the width of the Gaussian shape.
The luminosity at Tevatron can be written as:

$$L = \frac{f n N_p N_{\bar{p}}}{2\pi(\sigma_p^2 + \sigma_{\bar{p}}^2)} F\left(\frac{\sigma_l}{\beta^*}\right) \tag{3.2}$$

where N_p and $N_{\bar{p}}$ are the number of particles in each bunch, n is the number of bunches in either, σ_p and $\sigma_{\bar{p}}$ are the standard deviations of the beam spatially at the interaction point in the detector and they measure the width of the bunches. $F(\sigma_l/\beta^*)$ is a form factor that depends on the bunch length, σ_l, and the beta function at the interaction point, β^*. The average luminosity in Run Ib was $1.6 \cdot 10^{31} cm^{-2} s^{-1}$. During the Run II the Tevatron archived a peak of luminosity of $4 \cdot 10^{32}\ cm^{-2} s^{-1}$ in April 2010 (figure 3.4).

Starting from equation (3.1), the total number of interaction for a physics process is obtained by integrating over time:

$$N = \sigma_{int} \int L\, dt = \sigma_{int} \mathcal{L}. \tag{3.3}$$

The integrated luminosity $\mathcal{L}$ describes the quantity of data archived. During the Run II Tevatron archived an integrated luminosity of about 12 fb^{-1}.

3.3 CDF Experiment

The CDF Run II [110] was a solenoidal detector developed to measure the properties of final-state particles produced in proton-antiproton collisions at Tevatron accelerator. Its purpose was to answer the open questions of high energy physics like the characterization of the properties of the top quark, improve the precision

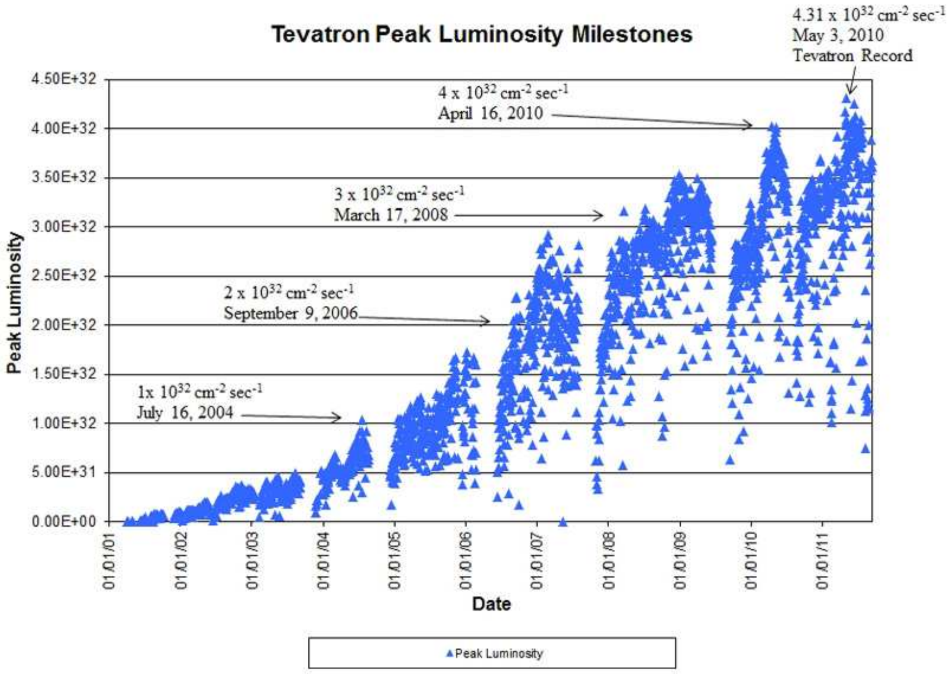

Figure 3.4: Tevatron peak luminosity [109].

of the electro-weak measurements, as the mass of the W and Z boson, search of new physics, as Higgs boson, etc.

The CDF detector (figure 3.5) weighed about $5 \cdot 10^6$ kg and it was about 12 m long in all three dimensions. The detector was divided in different sub-detectors. The informations from each of these sub-detectors are combined to reconstruct the interaction between the particles. From the interaction point outwards there are located: the beam pipe, the silicon detector, the central outer tracker, the solenoid magnet, the electromagnetic and hadronic calorimeters and the muon detectors.

3.3.1 Coordinate System

CDF used a right-handed coordinate system. The positive x-axis is pointed outwards from the center of Tevatron, the positive y-axis is pointed vertically direction upwards and the positive z-axis is pointed into the direction of the proton beam (figure 3.6a). Because of the cylindrical symmetry a polar coordinate system is more useful.

The polar coordinate system is defined from the center of the beam line with the radius r defined from the center of the detector outwards, the polar angle ϑ

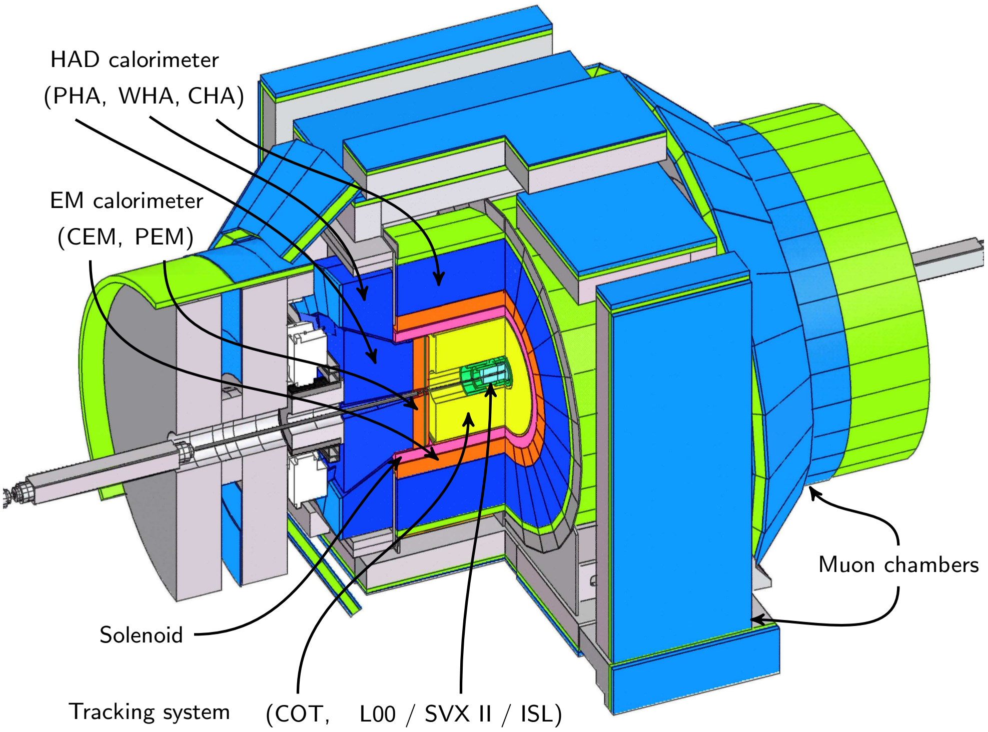

Figure 3.5: CDF II apparatus [111].

measured from the proton direction and the azimuthal angle φ measured from the Tevatron plane.

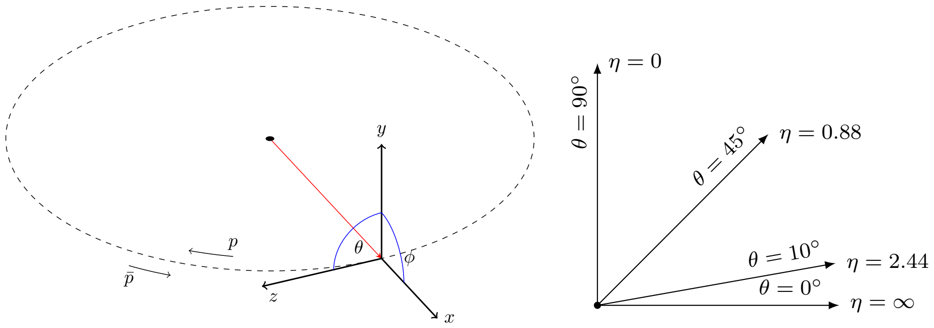

(a) **(b)**

Figure 3.6: (a) The CDF coordinate system [111] and (b) the pseudo-rapidity.

In a collider the particles collide head-on with no significant momentum in the plane perpendicular to the z-axis, the transverse plane. Due to momentum conservation, the final state particles must have zero *total* transverse energy and momentum. For this reason the transverse plane represents an important source of information for the collision. The transverse energy E_T and the transverse momentum p_T are defined by:

$$\begin{cases} E_T = E \sin\vartheta \\ p_T = p \sin\vartheta . \end{cases} \tag{3.4}$$

These quantities are invariant under longitudinal relativistic transformations. Another quantity invariant under longitudinal boosts is the difference between the rapidities of two particles. The rapidity is defined as:

$$y = \frac{1}{2} \log\left(\frac{E + p_z}{E - p_z}\right) = \tanh^{-1}\left(\frac{p_z}{E}\right) . \tag{3.5}$$

Under a boost with velocity β, the rapidity becomes: $y \to y - \tanh^{-1}\beta$. The shape of the rapidity distribution, dN/dy, is invariant i.e. the particle production is constant as a function of rapidity. In case the momentum of the particles is much greater than their own mass, $p \gg m$, the rapidity can be approximated by the pseudo-rapidity (figure 3.6b), defined as:

$$\eta = -\log\left[\tan\left(\frac{\vartheta}{2}\right)\right] . \tag{3.6}$$

The pseudo-rapidity is used to measure the longitudinal angle of the emerging particles instead of the polar angle ϑ. Because it is an approximation of the rapidity, the particle production is also constant as a function of the pseudo-rapidity.

3.3.2 Tracking Systems

The tracking system (figure 3.7) was the heart of the CDF apparatus. It was divided into two parts, the silicon vertex detector and the Central Outer Tracker (COT). The silicon vertex detector was the innermost tracking system and it consisted of three sub-detectors: the Layer 00 (L00), the Silicon Vertex Detector (SVX II) and the Intermediate Silicon Layers (ISL).

The tracking systems were contained in a superconducting solenoid, 1.5 m in radius and 4.8 m in length, which generated a 1.4 T magnetic field parallel to the beam axis.

The L00 [112] (figure 3.8a) was a silicon detector placed directly on the beam pipe (r=1.25 cm). Due to the position, very close to the interaction point, the radiation was very high requiring a detector with a high radiation tolerance. The detector had six narrow (128 channels) and six wide (256 channels) silicon modules in φ at r=1.35 cm and r=1.62 cm respectively, and six readout modules in z direction, with two sensors bonded together in each module for a total length of 96 cm. The sensors were mounted on a carbon-fiber support structure with integrated cooling. To save space, eliminate material and protect the readout chips from radiation, the hybrid circuit boards containing the front-end electronics (13824 channels) were mounted on separate cooling structure beyond the end off the silicon sensors. The sensors were connected to the readout chips via long fine-pitch signal cables. The sensors were single-side p-in-n silicon with 25 (50) μm implant (readout) pitch. The addiction of intermediate strips that were not read out improved the spatial resolution down to the signal-noise ratio without significant degradation in efficiency or two-hit separation. The L00 covered the pseudo-rapidity region $|\eta| \leq 4.0$.

The SVX II [110] (figure 3.8a) was built in three cylindrical barrels with a total length of 96 cm, covering the pseudo-rapidity region $|\eta| \leq 2.0$. Each barrel support had layers of double sided silicon microstrip detectors between radii of 2.4 and 10.7 cm. Three of the layers combined an $r - \varphi$ measurement on one side with 90° stereo measurement on the other, and the remaining two layers combined $r - \varphi$ with small angle stereo at 1.2°. The silicon crystals were supported by low mass substrates in assemblies called ladders. Twelve ladders of the appropriate width made a layer, and the 60 ladders in each barrel were mounted between two precision-machined beryllium bulkheads which carried the water cooling channels for the readout electronics. The total of 405504 channels in the system were connected to radiation-hardened readout chips mounted on electrical hybrids on the surface of the silicon detectors. The high speed and dual porting of the readout allowed the SVX II information to be used for impact parameter discrimination in the Silicon Vertex Trigger (SVT) processor of the Level-2 trigger.

The ISL [110] (figure 3.8a) consists of a single layer placed at a radius of 22 cm and two layers placed at radii of 20 cm in the central region and 28 cm in the plug region, $1.0 \leq |\eta| \leq 2.0$. The SVX II and ISL together could be considered a single silicon tracking and b-tagging system which covered the region $|\eta| \leq 2.0$. The ISL was made by double sided silicon with 55 μm strip pitch on the axial side and 73 μm pitch on the stereo side with a 1.2° stereo angle. The silicon crystals were mounted in assembled ladder similar to SVX II. Because the radiation level was low at large radii, it was possible to use longer strips to reduce the channel count. The ISL readout electronics were identical to the SVX II.

Tracking in the pseudo-rapidity region $|\eta| \leq 1.0$ was done with a large open cell drift chamber. The goal of the COT [110] (figure 3.8b) was to reproduce in the high luminosity Run II environment the positive characteristics of the Run I Central Tracking Chamber (CTC). The simplest strategy for operating a wire chamber in Run II was to ensure that the maximum drift time is less than the 132 ns bunch spacing. The COT was designed to operate with a maximum drift of 100 ns by reducing the maximum drift distance and by using a gas mixture with a faster drift velocity. The gas was a mixture of argon (Ar), ethane (Et) and tetrafluoromethane (CF_4) in the ratio Ar:Et:CF_4=50:35:15.
The basic drift cell had a line of 12 sense wires alternating with shaper wires every 3.8 mm, running down the middle of two gold-on-mylar cathode planes which were separated by $\sim$2 cm. With a total of 2520 drift cells and 30240 readout channels, the COT provided 96 measurements in the area between the radii of 44 and 132 cm. The COT was read out using a pipelined time-to-digital converter (TDC) which was standard for CDF II wire chamber systems. The tracking information was available for the Level-1 trigger.

3.3.3 Calorimeter System

Outside the solenoid, the calorimetry system [113] covered the pseudo-rapidity region $|\eta| \leq 3.0$. The calorimeters had an important role in the physics program, they measured the energy of both neutral and charged particles.

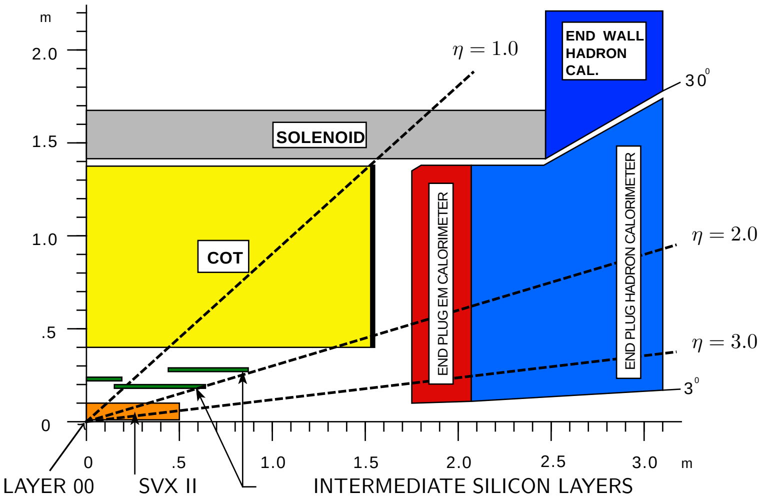

Figure 3.7: The CDF tracking system [110].

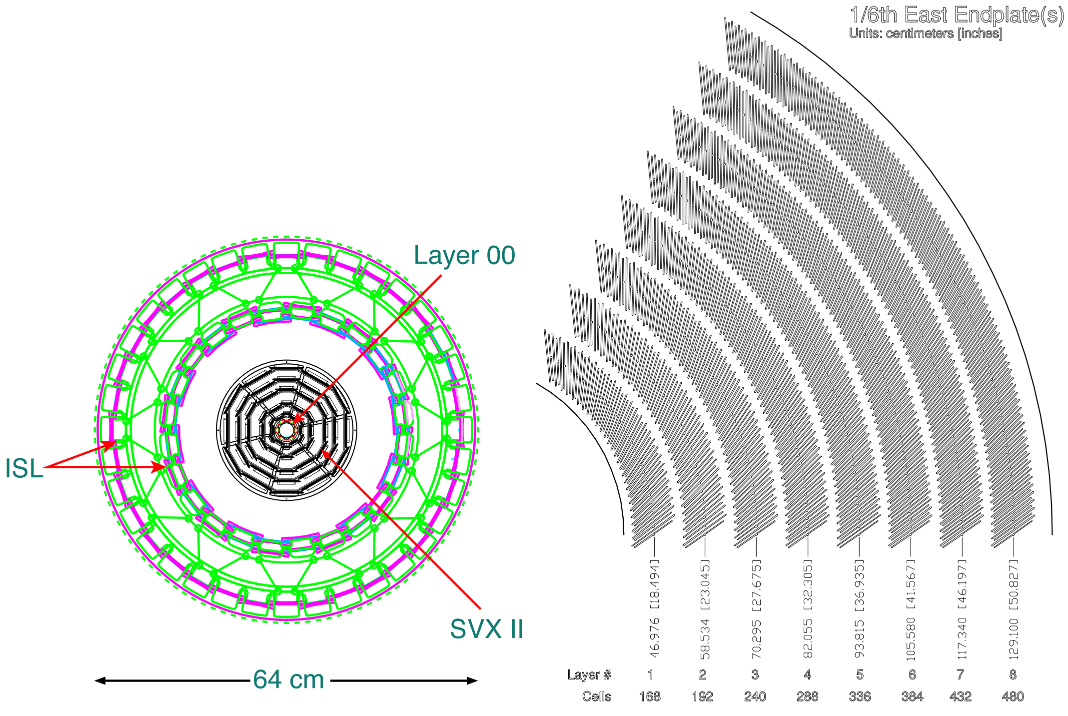

(a) **(b)**

Figure 3.8: (a) The CDF silicon vertex detector and (b) the COT system [110].

The calorimeter system was composed by alternating layers of the absorber and a scintillating material. A particle which passed through the calorimeter interacted with it producing a shower of other particles with lower energy. This process continued until the energy of the particle did not reach a given value depending on the material passed through.
A portion of the energy of the particle from the shower was absorbed by the scintillating material. This energy was emitted in form of light which was collected by photomultiplier tubes (PMTs) and converted to an electric analog signal and amplified for electronic readouts. These readout allow to determinate the energy of the incident particle. Figure 3.9 shows one quadrant of the CDF calorimeter system, divided into five parts. The CEM and PEM were the central and (end)plug electromagnetic calorimeters, respectively, and the CHA, WHA, and PHA are the central, endwall, and (end)plug hadron calorimeters, respectively.

The calorimeter was composed by blocks called wedges. Each wedge was composed by a portion of the CHA in the upper region and by a CEM covering an azimuthal angle φ of 15° in the lower region. The full transverse plane was covered with 24 wedges with the presence of minus small cracks between them. In η direction, the calorimeter was divided in 22 sections. The $\eta - \phi$ regions were called towers and represented the segmentation of the calorimeter detectors. To have a finer segmentation some portions of plug wedges were divided into two subregions.

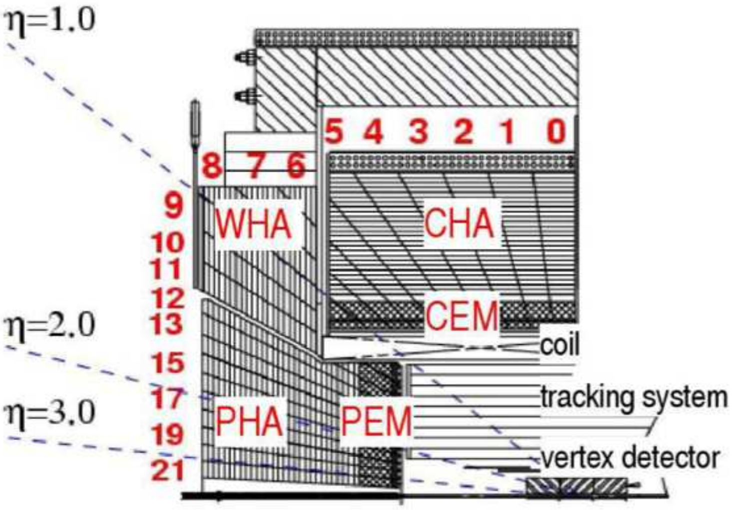

Figure 3.9: The CDF calorimeter system [110].

Electromagnetic Calorimeter

The electromagnetic (EM) calorimeter was a lead/scintillator sampling device with a unit layer composed of 4.5 mm of lead and 4 mm of scintillator. The photons and electrons produced cascade of lower-energy particles. The electrons interacted with the calorimeter material via bremsstrahlung process. The photons interacted electromagnetically via the photoelectric effect, Compton scattering, and pair production. The CEM was segmented with 24 φ towers and 10 η towers with a size of $\Delta\eta \times \Delta\varphi = 0.11 \times 15^\circ$. In the plug region the size of the η towers varied connected to the geometry of the detectors and the φ towers had a dimension of $\Delta\varphi = 7.5^\circ$. The resolution of the energy measurement of the electromagnetic calorimeters was proportional to the number of particles produced by the shower. The CEM and PEM σ_E/E resolution was $13.5\%/\sqrt{E} \oplus 2\%$ and $16.0\%/\sqrt{E} \oplus 1\%$, respectively.

Hadronic Calorimeter

The hadronic (HAD) calorimeter was a 23 layer iron and scintillator sampling device with a unit layer composed of 5 cm iron and 6 mm scintillator. The neutral and charged hadrons interacted with the iron in the hadron calorimeters via inelastic nuclear processes. The hadrons fragmentation can produce neutral and charged pions, protons, neutrons, and kaons, this produced a reduction of the energy of the incident particles. The neutral pions and eta mesons can decay to a pair of collinear photons, which, interacting electromagnetically, produced an electromagnetic cascade (some of which was produced and measured in the EM calorimeter). The charged secondaries, interacting hadronically with the iron, transfered energy through ionization and excitation of iron nuclei; they may also produce more protons or neutrons through interactions with nuclei. The CHA, WHA, and PHA energy resolutions, compared to electromagnetic cascades, were much poorer, because limited by sampling and intrinsic fluctuations of the detector and readout material. The CHA, WHA, and PHA σ_E/E resolution were $\sim 50\%/\sqrt{E} \oplus 3\%$, $\sim 75\%/\sqrt{E} \oplus 4\%$ and $\sim 80\%/\sqrt{E} \oplus 5\%$, respectively.

Shower Maximum Detector

The hadronic showers contained an electromagnetic component from the decay of the neutral pions and eta mesons. The electromagnetic calorimeter was designed to capture these showers but they cannot recognize perfectly between the photons from the event vertex and photons from neutral meson decays. For this purpose a shower maximum detector (SMX) was designed.

The central shower maximum detector (CES) was a gas chamber composed of orthogonal anode strips and cathode wires with 64 wires and 128 strips per wedge.

The anode wires, positioned long the z axis direction, permitted the measurement of the local CES x position, and the cathode strips, positioned long the x axis direction, measured the local CES z position. The position resolution was about ± 1 mm for 50 GeV electromagnetic showers.

The plug shower maximum detector (PES) was a chamber composed of two layers of scintillating strips divided into 8 sectors, each covering an azimuthal angle of 45°, providing a position resolution for high momentum EM showers of about ± 1 mm.

3.3.4 Muon Detection System

The CDF muon system was composed by four different sub-detectors: the Central Muon Detector (CMU), the Central Muon Upgrade (CMP), the Central Muon Extension and the Intermediate Muon Detection (IMU). This system of scintilletors and proportional chambers covered the pseudo-rapidity region $|\eta| \leq 2.0$. The absorbers for these systems were the calorimeter steel, the magnet return yoke, additional steel walls and the steel from the Run I forward muon toroids. The reason to have four system was connected to geometrical and engineering problems of covering the full η region.

The CMU consisted of 144 modules with 16 rectangular cells per module, located behind the CHA, covering the range $|\eta| \leq\sim 0.6$.

Each cell was 6.35 cm × 2.68 cm × 226 cm in size and had a 50 μm stainless steel wire in the center. The 16 cells in a module were stacked long the radial direction, with a small φ offset between the first and third and the second and fourth layers. The first and third (and second and fourth) φ cells had their wires connected together in the read-out, and each wire pair was instrumented with a time-to-digital converter (TDC) to measure the muon's location in φ, and an analog-to-digital converter (ADC) on each end to measure the muon's location in z via charge division.

The CMP consisted of a second set of muon chambers behind an additional 60 cm of steel in the region $|\eta| \leq\sim 0.6$. The chambers were rectangular, single-wire drift tubes configured in four layers with alternate half-cell staggering, with dimension 2.5 cm × 15 cm. The chambers were run in proportional mode with a maximum drift time of approximately 1.4 μs. The tubes were made of aluminum extrusions with 0.26 cm walls, having a single wire in the center and field shaping cathode strips on the top and bottom. They were typically 640 cm long,

with some shorter sections on the bottom of the detector to avoid obstructions. The extrusions were glued into four-tube stacks with a half-cell staggering of the second and fourth layers relative to the first and third. Preamplifiers were mounted on one end of the stacks. Signals were read out by a single TDC per wire, and trigger hits were formed from coincidences of nearby wires that were used in association with trigger information from the CMU chambers.
A layer of scintillation counters (CSP) was installed on the outside surface of the wall drift chambers, with respect to the interaction point. The counters were rectangular in shape: 2.5 cm × 15 cm × 320 cm. Each counter covers two upgrade chambers in width and half the chamber in length. The total number of scintillation counters was 216. The counters were read out by single phototubes which were located at the center of the array. The east and west counters were offset in x to allow the inter-leaving of phototubes at the middle, minimizing the space occupied by the photomultiplier tubes assembly.

The central extension consisted of conical sections of drift tubes (CMX) and scintillation counters (CSX) located at each end of the central detector and covering the pseudo-rapidity region $\sim 0.6 \leq |\eta| \leq \sim 1.0$.
The CMX drift tubes were arrayed as a logical extension of the central system. They differed from those of the CMP only in length, 180 cm long, with a total of 1536 of installed tubes. A layer of four CSX scintillation counters was installed on both the inside and the outside surfaces of each 15° CMX sector. The counters were trapezoidal in shape with the same length (180 cm) as the drift tubes and with a width of 30 cm at the smaller end and 40 cm at the larger end. The counters on the inside and outside layers were half-cell staggered with respect to each other thereby doubling the effective granularity of the system. The total number of scintillation counters in the conical sections was 256.

The IMU was designed to trigger on muons with $|\eta| \leq 1.5$ and to identify offline muons with $|\eta| \leq 2.0$. The heart of the detector was a barrel of CMP-like chambers and CSP-like scintillation counters mounted on the outer radius of the Forward Muon System (FMU) toroids. Additionally, there were pinwheels of counters on the end-wall and between the toroids for triggering. A muon was identified by a stub in the chambers, with a time-stamp provided by the barrel counters in coincidence with the pinwheel counter projective with the vertex. There was a substantial volume of steel between the barrel and pinwheel counters. The IMU was behind 6.2-20 interaction lengths of steel, on average more shielding than the CMP.

The FMU was built around two pairs of toroids, one pair at positive rapidity, the other at negative. There were electrode-less drift chambers installed between the toroids and on the outer and inner faces of the toroids. Two additional planes of scintillation counters was installed. The FMU had fewer channels per unit rapidity, and therefore higher occupancy, than the central detectors.

3.3.5 Trigger and Data Acquisition System

Because the rate at which the data can be stored on tape was much lower than the collision rate, it was necessary to find a way to reduce it. This role was played by the trigger, an event selection system, which is of great importance in a hadron collider experiment. For the Tevatron Run II the collision rate was effective equal to the crossing rate of 7.6 MHz while the tape writing speed was less than 50 Hz, that because from the Run Ib to the Run II the luminosity increased by an order of magnitude but the rate of data written to tape increased only by a factor of 3 to 5. The role of the trigger was to highlight the events with potential interesting physics from the large number of minimum bias events combining the informations from the various sub-detectors (figure 3.10).

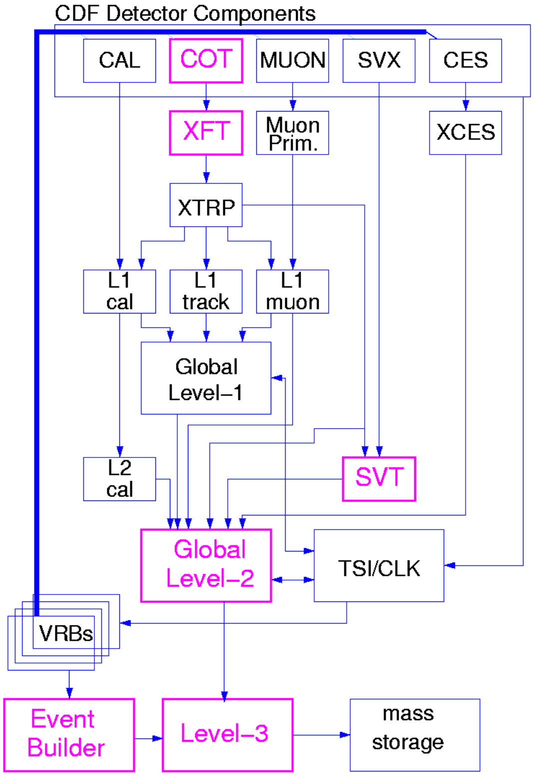

Figure 3.10: The CDF trigger system and data flow [110].

The CDF trigger system was divided into a three level architecture where each level reduces sufficiently the rate to allow the processing in the next level with minimal dead-time. The Level-1 system used custom designed hardware to find physics objects based on a subset of the detector information and made a decision based on simple counting of these objects. The Level-2 trigger used custom hardware to allow limited event reconstruction which can be processed in programmable processors. The Level-3 trigger used the full detector resolutions to fully reconstruct events in processor farms.

The Level-1 trigger had a 5.5 μs latency, this allowed the transmission and processing of the trigger signals to make the trigger decision. This implied that each detector element had a local data buffering for the 42 beam crossings that occurred during the latency period.

If an event was accepted by the Level-1 trigger, the front-end electronics sent the data to one of four on-board Level-2 buffers. With a 40 kHz accept rate at Level-1 this system was sufficient to have a limit dead-time $\leq$10% at full luminosity for the anticipated 20 μs Level-2 processing time. The system allowed to have a 300 Hz rate out of the Level-2 trigger. The events selected by Level-2 were transferred to the Level-3 trigger processor farms where the events were reconstructed and filtered using the complete event data with 30-50 Hz rate written to the permanent storage.

The Data Acquisition System was responsible for collecting data fragments from front-end electronics systems for events satisfying the Level-2 trigger and sending them to the Level-3 trigger subsystem. There, complete events were built and more sophisticated algorithms were used to classify events and determine whether they should be saved. Events passing the Level-3 trigger criteria were sent to the mass storage.

3.3.6 Good Run List

The period of time during which the detector collects data was called *run*. Each run could contain the information from few to million collision events, this was connected to the duration of the store period and how long the detector components worked properly during it. The runs were labeled with a number, the *run number*. At the end of each run, each detector components were evaluated if they were functioning properly with a set of bits, the *good run bits*, marked true [114]. The runs, or part of them, resulted usable for the analysis if the necessary detector components worked well and the corresponding run numbers were listed in a text file, the *Good Run List*.

The list used in this analysis is `goodrun_qcd_si_v45.list` [115], which contains all of the runs with a functional silicon tracker for the QCD analysis, corresponding to an integrated luminosity of 9.45 fb^{-1}.

Chapter 4

Jet Identification Tools

4.1 Multi-Jet Triggers

A jet is a narrow cone of hadrons and other particles produced in the hadronization of quarks or gluons. For analyses at CDF which present in their final state more than one jet, *multi-jets*, different trigger algorithm were designed to select events with these signatures. The two algorithms used in this analysis are the TOP_MULTIJET [116] and VH_MULTIJET [117] calorimeter trigger.

The TOP_MULTIJET calorimeter trigger was designed for the Run I period to select all-hadronic events in top-antitop processes at low luminosity.
The definition of TOP_MULTIJET trigger, used in this analysis, is:

- Level-1: at least one calorimeter tower with $E_T \geq 20$ GeV (L1_JET20),
- Level-2: at least four calorimeter clusters with $E_T \geq 15$ GeV, and $\sum E_T \geq 175$ GeV (L2_FOUR_JET15_SUMET175),
- Level-3: at least four jets with $E_T \geq 15$ GeV (L3_FOUR_JET15).

As can be seen from the trigger structure, the TOP_MULTIJET is driven by the Level-2 trigger which is the tightest selection criteria.
The proposal of the Level-1 (L1CAL) and Level-2 (L2CAL) calorimeter trigger (figure 3.10) is to trigger on electrons, photons, jets, total event transverse energy (SumEt), and missing transverse energy (MET).
For CDF Run II, all calorimeter tower energy information was digitized every 132 ns and the physical towers were summed into trigger towers, weighted to yield transverse energy. The trigger tower energy data was then sent to both the L1CAL and L2CAL systems.
Electrons and photons were triggered considering the electromagnetic energy

deposited into a trigger tower. Otherwise, the jets were triggered considering both the electromagnetic and hadronic energy deposited into a trigger tower.
L1CAL also calculated the event SumEt and MET using the electromagnetic and hadronic energy information.
The main task of the L2CAL was to find clusters using the E_T of the trigger towers. The clustering algorithm was based on a simple algorithm implemented in hardware, *PacMan* (section 4.2.1).
The L2CAL system does not re-calculate the event SumEt and MET; rather, it still uses the values evaluated from L1CAL. This design feature limits its trigger selection capability for triggers with global transverse energy requirements. The Level-3 trigger used another jet clustering algorithm described in section 4.2.1, *JetClu*.
The PacMan algorithm had good performance at lower luminosities for Run II. However, as the occupancy in the calorimeter increases with luminosity, the simple hardware-based L2CAL system loses its rejection power. The higher occupancy produces large fake clusters with high (fake) E_T in the L2CAL system, resulting in a high Level-2 accept once rate saturating the bandwidth downstream of Level-2 at high luminosity.

During the 2007 shutdown, the hardware and software parts of the L2CAL system were updated introducing the Pulsar boards and changing the clustering algorithm from PacMan to *L2Cone* (section 4.2.1).
The new board allowed to re-calculate the event SumEt and MET using the full resolution trigger tower energy information available at Level-2. Also the jet reconstruction using a cone algorithm, done at Level-3, was moved to Level-2.
The resolution of MET at Level-2 is close to that at Level-3, in this way the Level-2 rate for Higgs and SUSY triggers that require E_T is reduced. This is the key point for preserving these triggers at high instantaneous luminosity.

One of the two channels investigated in this analysis is the *VH* process (section 2.2.1). Because the TOP_MULTIJET trigger was designed to select all-hadronic events in top-antitop processes, it is not optimal for the signal of the *VH* channel for two reasons: first of all, both the low mass Higgs and the vector bosons are lighter than the top quark, so the jets produced from the Higgs and the vector boson decays will be softer than that of the top quarks'. Therefore, the SumEt threshold of 175 GeV is too tight for this signal.
Secondly, since the signature of the *VH* process is already four jets, a looser cut such as requiring three jets will be more efficient for collecting signals than using TOP_MULTIJET which requires four or more jets.
For these reason another multi-jet trigger was introduced, the VH_MULTIJET, defined as:

- Level-1: at least one calorimeter tower with $E_T \geq 20$ GeV (L1_JET20),
- Level-2: at least three calorimeter clusters with $E_T \geq 20$ GeV, and $\sum E_T \geq 130$ GeV (L2_THREE_JET20_SUMET130),
- Level-3: absent.

VH_MULTIJET and TOP_MULTIJET triggers use the same cluster algorithm, L2Cone.

The Monte Carlo samples can present differences with the recorded data due to the correct simulation of the multi-jet trigger. To correct these differences a scale factor, calculated for each multi-jet trigger, is applied. The scale factor values used in this analysis are summarized in table 4.1 [118].

Trigger	Integrated Luminosity (fb^{-1})	Monte Carlo Scale Factor
TOP_MULTIJET (PacMan)	2.364	0.959 ± 0.034
TOP_MULTIJET (L2Cone)	0.643	1.024 ± 0.036
VH_MULTIJET (L2Cone)	6.439	1.014 ± 0.036

Table 4.1: The recorded integrated luminosity for the different trigger versions and the corresponding Monte Carlo scale factor.

4.2 Jet Clustering Algorithms and Jet Energy Scale

The study of scattering processes in hadron collisions often depends on the determination of the four-momenta of quarks and gluons produced in these collisions. The measurement of these four-momenta is made through the reconstruction of hadronic jets, resulting from quark or gluon fragmentation.

At CDF the jets are observed as clustered energy depositions in the calorimeters. The value of the jets energy is corrected to correspond to the energy of the parent parton. The precision of the correction can determine the precision of many measurements.

The original parton transverse energy can be estimated by correcting the jet for instrumental effects and for radiation and fragmentation effects:

$$\begin{aligned} p_T^{parton} &= \left(p_T^{jet} \times C_\eta - C_{MI}\right) \times C_{Abs} - C_{UE} + C_{OOC} \\ &= p_T^{particle} - C_{UE} + C_{OOC}, \end{aligned} \tag{4.1}$$

where p_T^{parton} is the transverse momentum of the parent parton, p_T^{jet} is the transverse momentum measured in the calorimeter jet, $p_T^{particle}$ is the transverse momentum of the particle jet and the Cs are the correction factors. The $p_T^{particle}$ is the result of application of all instrumental effects which corresponds to the sum of the momenta of the hadrons, leptons and photons within the jet cone. The correction factor C_η, or $\eta-$dependent correction, is applied to make jet energy uniform along the pseudo-rapidity η. The C_{MI} factor, or Multiple Interaction correction, is the energy to subtract from the jet due to pile-up of multiple interactions in the same bunch crossing. The C_{Abs} factor, or Absolute correction, is the correction of the calorimeter response to the momentum of the particle jet. The C_{UE} and C_{OOC} factors, or Underlying Event and Out-Of-Cone corrections, correct for parton radiation and hadronization effects due to the finite size of the jet cone algorithm that is used.

In this analysis the four-momentum of the jets are corrected using the Out-Of-Cone correction factor.

4.2.1 Jet Clustering Algorithms

The energy of a jet is calculated from the energy deposited in the calorimeter towers using different types of clustering algorithms [119].

As mentioned before, the L2CAL system used two different jet clustering algorithms: PacMan and L2Cone. At Level-3 trigger and offline, the jets are clustered by another algorithm the JetClu algorithm. Both L2Cone and JetClu are cone algorithms and for these algorithms the jets are clustered with a fixed cone size in which the center of the jet is defined as $(\eta_{jet},\ \varphi_{jet})$ and the size of the jet cone as $\Delta R = \sqrt{(\eta_{tower} - \eta_{jet})^2 + (\varphi_{tower} - \varphi_{jet})^2}$. The possible value of ΔR are 0.4, 0.7, or 1.0.

The PacMan algorithm selects and combines contiguous regions of trigger towers creating clusters. The clustering begins by searching for a tower with energy above a *seed* threshold ($E_T \geq 3$ GeV) and adding all the adjacent towers above a second lower *shoulder* threshold ($E_T \geq 1$ GeV). The operation finishes when no more shoulder towers adjacent to the cluster are found. The cluster location correspond to the location of the seed tower. Because the seed tower is the first tower found above the seed threshold, its location could not coincide with the true jet centroid, especially at high luminosity when the calorimeter occupancy is high.

The L2Cone algorithm is similar to JetClu algorithm, but in order to save processing time the clustering is done in a single iteration. The trigger towers are ordered above seed threshold in E_T. Beginning with the highest E_T seed, the E_T of all towers that satisfy a shoulder threshold in a cone of $\Delta R = 0.4$ around the seed, are summed and not included in another cluster, they are flagged as *used*. These operations are repeated using the next unused seed tower until all seeds are used. In this way the Level-2 jets found using this algorithm are nearly equivalent to offline jets in terms of E_T, centroid, and efficiency.

The JetClu algorithm groups calorimeter towers with $E_{Ti} > 1$ GeV into jets. $E_{Ti} = E_i \sin\vartheta_i$ is the transverse energy of a tower with respect to the z-position of the proton-antiproton interaction, and the energy E_i is the sum of the energies measured in the electromagnetic and hadronic compartments of that tower. Firstly *seed* towers are defined in order of decreasing E_{Ti}. For each seed tower the towers within a radius of size ΔR with respect to its position are used to build *clusters*. When an initial list of clusters is done, the cluster transverse energy and the location of the cluster is calculated. This procedure is repeated iteratively, a new list of towers around the new center is determined. The jet E_T and direction are recalculated until the list of towers assigned to the clusters are stable. This is the case when the geometrical center of the tower correspond to the cluster centroid. Overlapping jets are merged if they overlap by more than 50%. If the overlap is smaller than 50%, each tower in the overlap region is assigned to the nearest jet.

In Monte Carlo simulation, the particle jets are obtained using the same jet clustering algorithm on stable final state particles, i.e. the stable particles are used instead of the towers.

4.2.2 Jet Energy Scale

It is often desirable to reconstruct the energy of the original parton rather than the energy of the jet, e.g. for the measurement of the top quark mass or the search for the Higgs boson, where parton energies are used to compute the invariant mass of the decaying products. The reconstruction of the parton energy from the particle jet energy is subject to several difficulties. A fraction of the parton energy can be lost from the jet cone due to final state gluon radiation (FSR) at large angles with respect to the parent parton or due to particles exiting the cone either in the fragmentation process or due to low p_T particles bending in the magnetic field. This energy is called Out-Of-Cone (OOC) energy. On the other hand the particle jet can also have contributions not related to the actual mother parton of the hard interaction of interest defining the jet, such as particles from the initial state gluon radiation (ISR), or particles from spectator partons with color connection to the other partons of the proton (Beam-Beam-Remnant, BBR). These two contributions are called Underlying Event (UE).

Final state radiation and hadronization effects are correlated with the primary jet direction and the jet energy and are expected to decrease with increasing distance from the jet core.

The OOC and UE corrections are obtained from PYTHIA [98] dijet samples using particle jets which match a primary parton within $\Delta R < 0.4$.

The jets are reconstructed at the calorimeter and particle level using the standard CDF jet clustering algorithm with cone radii of 0.4, 0.7 and 1.0. Jets are required to be in the central region ($0.2 < |\eta| < 0.6$).

The energy outside the jet cone depends strongly on the cone size. For the smallest cone size, $\Delta R_{jet} = 0.4$, the OOC corrections is about +18% at $p_T^{particle} = 20$ GeV/c.

4.3 Bottom Quark Jet Identification Algorithms

The identification of jets resulting from heavy quark fragmentation is an essential tool both for the measurement of Standard Model processes and in the search for physics beyond this model.
CDF presents several algorithms for the identification, or tagging, of the bottom-quark jets (b-jets), the two used in this analysis are the SecVtx and the JetProb algorithm.

4.3.1 SecVtx Algorithm

The SecVtx algorithm [120] is based on the identification of the secondary vertices to identify the bottom quark (b quark) decays.

The secondary vertex is shifted with respect to the primary one. To select the tracks which are coming from the secondary vertex, it is necessary to identify the position of the interaction point with good precision. To achieve this, the vertex with the high total scalar sum of transverse momentum of associated tracks is identified. The position of the primary vertex is determined by fitting the tracks within a ±1 cm window in z direction around this vertex. In the fit are considered the tracks with impact parameter significance relative to the beam-line, defined as the ratio of the impact parameter, d_0, to its uncertainties, $|S_{d_0}| = |d_0/\sigma_{d_0}| < 3$, where σ_{d_0} includes the uncertainty on both the track and the beam-line positions. The tracks which contribute with a $\chi^2 > 10$ to the fit are removed and the fit is repeated. This procedure is repeated until a vertex with no tracks over the χ^2 cut is found. If no tracks survive to this selection the beam-line profile is used for the primary vertex position estimate.

To identify the secondary vertex, only the tracks inside the jet cone are considered. On these tracks a set of cuts involving the transverse momentum, the number of silicon hits attached to the tracks, the quality of those hits, and the χ^2/d.o.f. of the final track fit are applied to reject the unsuitable tracks. A jet is defined *taggable* if it has two tracks which pass these selection cuts. Shifted tracks in the jet are selected based on the significance of their impact parameter with respect to the primary vertex and are used as input to the SecVtx algorithm. The algorithm uses a two step approach to find the secondary vertices. In the first step, using tracks with $p_T > 0.5$ GeV/c and a impact parameter significance $|S_{d_0}| > 2.5$, the algorithm tries to reconstruct a secondary vertex which includes at least three tracks with at least one of them with $p_T > 1$ GeV/c. If this step is unsuccessful, the algorithm, in the second step, modifies the requirements making them more strict. It attempts to reconstruct a vertex with two tracks with $p_T > 1$ GeV/c and $|S_{d_0}| > 3$ and one track must have $p_T > 1.5$ GeV/c. Once a secondary vertex is found in a jet, the two dimensional decay length of the secondary vertex L_{xy} (figure 4.1) is calculated as the projection onto the jet axis, in the $r - \varphi$ view only, of the vector pointing from the primary vertex to the secondary vertex. The sign of L_{xy} is defined relative to the jet direction, specifically by the absolute difference $|\varphi|$ between the jet axis and the secondary vertex vector (positive for $< 90°$, negative for $> 90°$). Secondary vertices corresponding to the decay of bottom and charm quarks are expected to have large positive L_{xy} while the secondary vertices from random mis-measured tracks are expected to be less shifted from the primary vertex. To reduce the background from the false secondary vertices (mistags), a good secondary vertex is required to have $L_{xy}/\sigma_{L_{xy}} > 3$ (positive tag) or $L_{xy}/\sigma_{L_{xy}} < -3$ (negative tag), where $\sigma_{L_{xy}}$, the total estimated uncertainty on L_{xy} including the error on the primary vertex, is estimated vertex-by-vertex but is typically 190 μm. The negative tags are useful for calculating the false positive tag rate. A tagged jet is defined to be a jet containing a good secondary vertex. The SecVtx algorithm will find at most one good vertex per jet.

4.3.2 JetProb Algorithm

The jet probability algorithm [121] is the other algorithm used to identify the jets produced from the hadronization process of a light or a heavy parton. The hadrons with long lifetime decay giving rise to tracks shifted from the primary

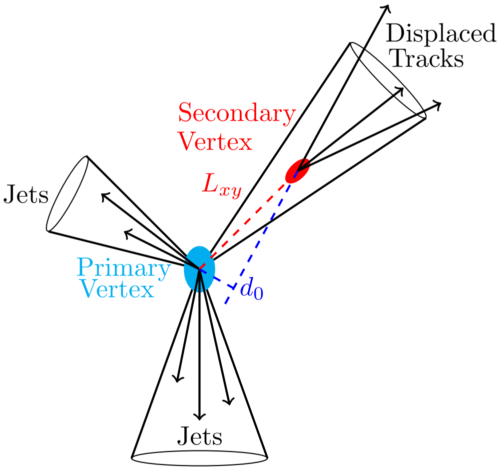

Figure 4.1: A secondary vertex reconstruction. L_{xy} is the distance of the secondary vertex from the primary vertex in the plane orthogonal to the proton beam direction. The impact parameter of a track is marked as d_0 [120].

interaction vertex. This algorithm uses tracks associated with a jet to determine the probability for these to come from the primary vertex of the interaction. The calculation of the probability is based on the impact parameters, d_0 of the tracks in the jet and their uncertainties. The sign of the impact parameter is defined positive (negative) if the angle φ between the jet axis and the perpendicular to the track from the primary vertex is smaller (bigger) than $\pi/2$ (figure 4.2a).

The jets originate from a light parton should come from the primary vertex. Due to the finite tracking resolution, these tracks are reconstructed with a non-zero impact parameter and have equal probability of being positively or negatively signed (figure 4.3a). The width of the impact parameter distribution from these tracks is due to the tracking detector resolution and multiple scatterings.

The jets originate from a heavy parton generate long-lived hadrons. Before to decaying, they travel some distance along the jet direction, and they decay preferentially with a positive signed impact parameter (figure 4.2b) as it can be seen in figure 4.3b.

The tracking resolution can be extracted from the data by fitting the negative side of the signed impact parameter distribution of primary jets. The signed impact parameter significance, defined as the ratio of the impact parameter to its uncertainty, is parameterized to minimize the contribution of a related quantity. With these parameterizations, the probability (the track probability) that a track from a jet, with a certain impact parameter significance, can be computed to be consistent with originating from the primary vertex.

By construction, the probability for tracks originating from the primary vertex is uniformly distributed from 0 to 1. The tracks from long-lived parton have a large impact parameter respect to the primary vertex, this produces a peak at 0 into the probability distribution. The jet probability value of a jet is based on the track probability value that are associated to the jet. In this analysis a jet is identified as a *b*-jet if the jet probability value is ≤ 0.01.

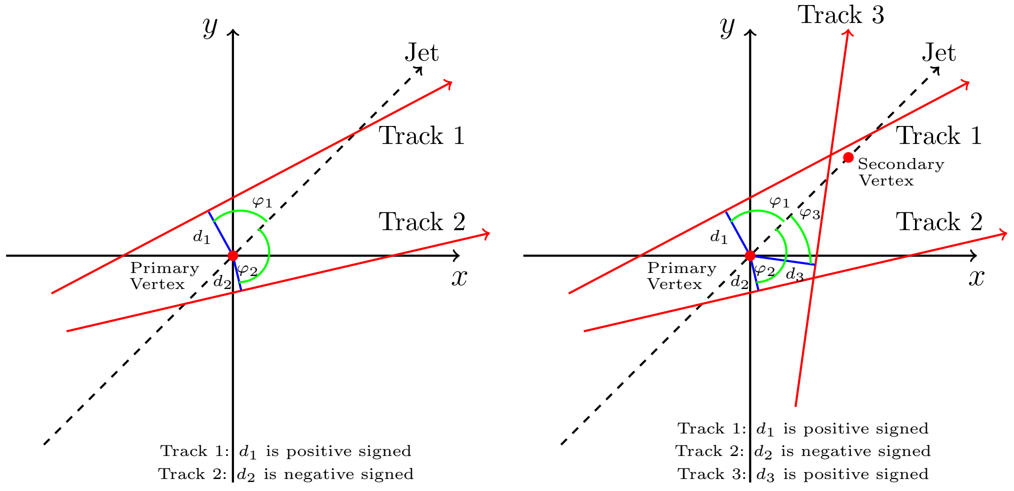

(a) **(b)**

Figure 4.2: Tracks from the (a) primary and (b) secondary vertex [122].

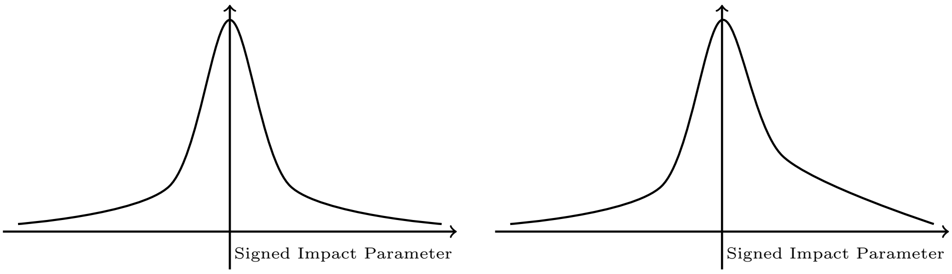

(a) **(b)**

Figure 4.3: Signed impact parameter distribution for the tracks from the (a) primary and (b) secondary vertex [122].

4.4 Neural Network Overview

Inspired by biological neural networks, the Artificial Neural Networks (NNs) [123] are massively parallel computing systems consisting of an extremely large number of simple processors (neurones) with many interconnections, which use some *organizational* principles believed to be used in the human brain.

A simple computational model for an artificial neuron is a binary threshold unit. This mathematical model computes a weighted sum of its n input signals, $x_j = 1, 2, \ldots, n$, and returns 1 if this sum is above a certain threshold u and 0 if below. Mathematically it can be represented as:

$$y = \vartheta \left(\sum_{j=1}^{n} w_j x_j - u \right), \tag{4.2}$$

where ϑ is a unit step function at 0, and w_j is the synapse weight associated with the j-th input.

This neuron model has been generalized in many ways. An obvious one is to use an activation function other than the threshold function, such as a piecewise linear, sigmoid, or Gaussian. The most frequently function used in NNs is the sigmoid function. This is the function used in this analysis.

NNs can be viewed as weighted directed graphs in which artificial neurons are nodes and directed edges (with weights) are connections between neuron outputs and neuron inputs. Based on the architecture, NNs can be classified into two categories:

- feed-forward networks, in which graphs have no loops
- recurrent (or feedback) networks, in which loops occur because of feedback connections.

The most common family of feed-forward networks is the multilayer perceptron, here the neurons are organized into layers that have unidirectional connections between them. Feed-forward networks are memory-less in the sense that their response to an input is independent of the previous network state. Recurrent, or feedback, networks, on the other hand, are dynamic systems. When a new input pattern is presented, the neuron outputs are computed. Because of the feedback paths, the inputs to each neuron are then modified, which leads the network to enter a new state.

The learning algorithms are connected to the network architecture. A learning process in the NN context can be viewed as the problem of updating network architecture and connection weights such that a network can efficiently perform a specific task. The network usually must learn the connection weights from available training patterns. Performance is improved over time by iteratively updating the weights in the network. NNs' ability to automatically learn from examples makes them attractive and exciting. Instead of following a set of rules specified by human experts, NNs appear to learn underlying rules (like input-output relationships) from the given collection of representative examples. This is one of the major advantages of neural networks over traditional expert systems.

In the supervised learning paradigm, the network is given a desired output for each input pattern. During the learning process, the actual output y generated by the network may not equal the desired output d. The basic principle of error-correction learning rules is to use the error signal $(d-y)$ to modify the connection weights to gradually reduce this error. The perceptron learning rule is based on this error-correction principle. A perceptron consists of a single neuron with adjustable weights, w_j, $j = 1, 2, \ldots, n$, and threshold u. Given an input vector $\mathbf{x} = (x_1, \ldots, x_n)$, the net input to the neuron is:

$$v = \sum_{j=1}^{n} w_j x_j - u. \tag{4.3}$$

The output of the perceptron is +1 if $v > 0$, and 0 otherwise. In a two-class classification problem, the perceptron assigns an input pattern to one class if $y = 1$, and to the other class if $y = 0$. The linear equation

$$\sum_{j=1}^{n} w_j x_j - u = 0, \tag{4.4}$$

defines the decision boundary (a hyperplane in the n-dimensional input space) that halves the space.

In general, a standard L-layer feed-forward network consists of an input stage, (L-1) hidden layers, and an output layer of units successively connected (fully or locally) in a feed-forward fashion with no connections between units in the same layer and no feedback connections between layers.

The most popular class of multilayer feed-forward networks is the *multilayer perceptrons* in which each computational unit employs either the thresholding function or the sigmoid function. Multilayer perceptrons can form arbitrarily complex decision boundaries and represent any boolean function. The development of the *back-propagation* learning algorithm for determining weights in a multilayer perceptron has made these networks the most popular among researchers and users of neural networks. All NNs in this analysis are multilayer perceptrons.

Chapter 5

All-Hadronic Higgs Search

The analysis described in this thesis refers to a search for the Standard Model Higgs boson using a data sample corresponding to an integrated luminosity of 9.45 fb^{-1} of $p\bar{p}$ collisions at $\sqrt{s} = 1.96$ TeV recorded by the CDF II experiment [124].

As described in chapter 2, the two production mechanisms investigated are the associated vector boson production (VH) and the vector boson fusion (VBF), where the Higgs boson decays into a pair of bottom-antibottom quarks ($b\bar{b}$), in association with two other quarks ($q\bar{q}'$) in both processes. The Higgs boson mass range considered is $100 \leq m_H \leq 150$ GeV$/c^2$.

Searches for a Higgs boson in final states containing leptons, jets, and missing energy have the advantage of a smaller background; the Higgs boson signal yields are, however, very small. The all-hadronic search channel, described here, has larger potential signal contributions but suffers from substantial QCD multi-jet background, and the main challenge is to construct a model that reduces the latter.

5.1 Search Strategy

In this research, the dominant background consists of the QCD multi-jet events. Simulation of this events is computationally intensive and an accurate reproduction of the multi-jet spectrum is difficult. To model this background, a data-driven technique (section 5.4), is used to avoid the need of generating large volumes of QCD multi-jet simulation samples.

The overwhelming QCD multi-jet background is suppressed by relying on multivariate techniques, that combine information from multiple variables to identify potential Higgs boson events. A total of eleven artificial neural networks

(NN) [125, 126] are used to improve the resolutions of the variables sensitive to Higgs production and to separate signal and background contributions.

Since this analysis is focused on Higgs boson decays to $b\bar{b}$, it is important to have the best possible resolution for m_{bb}. In section 5.5, the neural network used to correct the energies of b-jets is described.

The jets not identified as b-jets (q-jets) associated with each Higgs production process have unique angular and kinematic distributions. These variables are used in three neural networks to identify the q-jets of the Higgs boson events; the process is described in section 5.6.

The QCD multi-jet events are a mixture of quark and gluon jets, whereas the jets in the Higgs signal are emitted by quark jets. Typically the gluon jets appear somewhat wider than quark jets, thus the jet width can be used to discriminate quarks from gluons and improve the discrimination of the QCD multi-jet background from Higgs signal. In section 5.7, the technique for measuring the jet width and the neural network used to remove detector and kinematic dependences is described.

Section 5.8 describes the final two-stage neural network used to extract a potential signal contribution from the background. The two-stage neural network can identify Higgs bosons produced by three different processes simultaneously. The first stage is based on three separate neural networks trained specifically to separate backgrounds from either WH, ZH, or VBF Higgs production, respectively, to exploit the unique characteristics of each signal process. The outputs of the three process-specific neural networks are used as inputs to a second neural network and, subsequently, its output is used for the calculation of the statistical limit.

All neural networks in this analysis are trained using statistically independent samples after passing the selection criteria described in section 5.2.

5.2 Event Selection

The selection criteria allow to remove events unnecessary for this analysis. The selected event must be in the Good Run List (section 3.3.6) and they pass the multi-jet trigger (section 5.3). The position of the reconstructed primary vertex along the beam axis (V_z) must be less than 60 cm, in this way about 97% of all events are retained ensuring that the tracks coming from the vertex are in a well-instrumented region of the detector.

Because this is an all-hadronic analysis, the events with isolated leptons or missing transverse energy significance[1] greater than 6.0 (indicative of the presence of neutrinos) are removed to ensure an event sample independent from other Higgs boson searches at CDF.

The events should have four or five jets with $E_T > 15$ GeV and fall in the pseudo-rapidity region of $|\eta| < 2.4$. The jets are reconstructed from the calorimeter towers using a cone algorithm with fixed radius, $\Delta R = 0.4$, in the $\eta - \varphi$ space [127]. The jet E_T measurements are corrected for detector effects (section 4.2.2). Also the events with six jets are considered, but only for the calculation of the systematic uncertainties (chapter 6).

To reduce the QCD multi-jet background, exactly two bottom-quark jets (b-jets) are required. The algorithms used to identify the b-jets are the SecVtx (section 4.3.1) and the JetProb algorithms (section 4.3.2). An additional energy correction is applied to jets identified as b-jets (section 5.5).

After the selection, jets are ordered by descending E_T and the ones with the four highest E_T are considered. The scalar sum of the selected jet E_Ts (SumEt) is required to exceed 220 GeV, and two of the four must be identified as b-jets.

To increase the signal-to-background ratio, two independent b-tagging categories are considered: SS in which both jets are tagged by SecVtx algorithm, and SJ in which one jet is tagged by SecVtx and the other by JetProb algorithm. If a jet is tagged by both algorithms, it is classified as tagged by SecVtx, because this algorithm has a lower rate of misidentifying a light jet as a b-jet. For a jet with an E_T of 50 GeV, the SecVtx algorithm presents a misidentifying rate of $\sim 0.6\%$ [120] and the JetProb algorithm one of $\sim 1.4\%$ [121]. Other b-tagging combinations, such as events in which both jets are tagged only by JetProb algorithm, are not considered in this analysis because the relative increase in background contributions is substantially larger than that for the signal.

The signal region is defined by requirements on the invariant mass of the two b-tagged jets (m_{bb}) and the two untagged jets (m_{qq}). The range for m_{bb} is defined by the mass of the Higgs boson searched for. The VH process features two intermediate resonances, one from the potential Higgs boson decay, in m_{bb} (figure 5.1a), and another from the W/Z decay, in m_{qq} (figure 5.1b). The VBF process shares the same m_{bb} resonance but the two q-jets are not produced from the decay of a particle. However, these two q-jets tend to be produced with of large η separation which gives a large effective m_{qq} mass.

---

[1] The missing transverse energy significance is defined as the ratio of the missing transverse energy to the square root of the total transverse energy. The missing transverse energy, $\not{E}_T = |\vec{\not{E}}_T|$, where $\vec{\not{E}}_T$ is defined by, $\vec{\not{E}}_T = -\sum_i E_T^i \hat{n}_i$, where i is calorimeter tower number with $|\eta| < 3.6$, $\hat{n}_i$ is a unit vector perpendicular to the beam axis and pointing at the ith calorimeter tower.

The Higgs boson search region is defined as $75 < m_{bb} < 175$ GeV/c^2 .and. $m_{qq} > 50$ GeV/c^2 (figure 5.1c).
The other regions in the m_{bb}-m_{qq} plane used in this analysis are the TAG region (figure 5.1c), defined as [$40 < m_{qq} < 45$ GeV/c^2 .and. $65 < m_{bb} < 250$ GeV/c^2] .or. [$m_{qq} > 45$ GeV/c^2 .and. ($65 < m_{bb} < 70$ GeV/c^2 .or. $200 < m_{bb} < 250$ GeV/c^2)], the CONTROL region (figure 5.1c), defined as [$45 < m_{qq} < 50$ GeV/c^2 .and. $70 < m_{bb} < 200$ GeV/c^2] .or. [$m_{qq} > 50$ GeV/c^2 .and. ($70 < m_{bb} < 75$ GeV/c^2 .or. $175 < m_{bb} < 200$ GeV/c^2)]; and the NJET6 control region, defined as sharing the same m_{bb} and m_{qq} criteria as the signal region, but contains events with six reconstructed jets. These control regions present a very little or absent contribution from the Higgs signal.

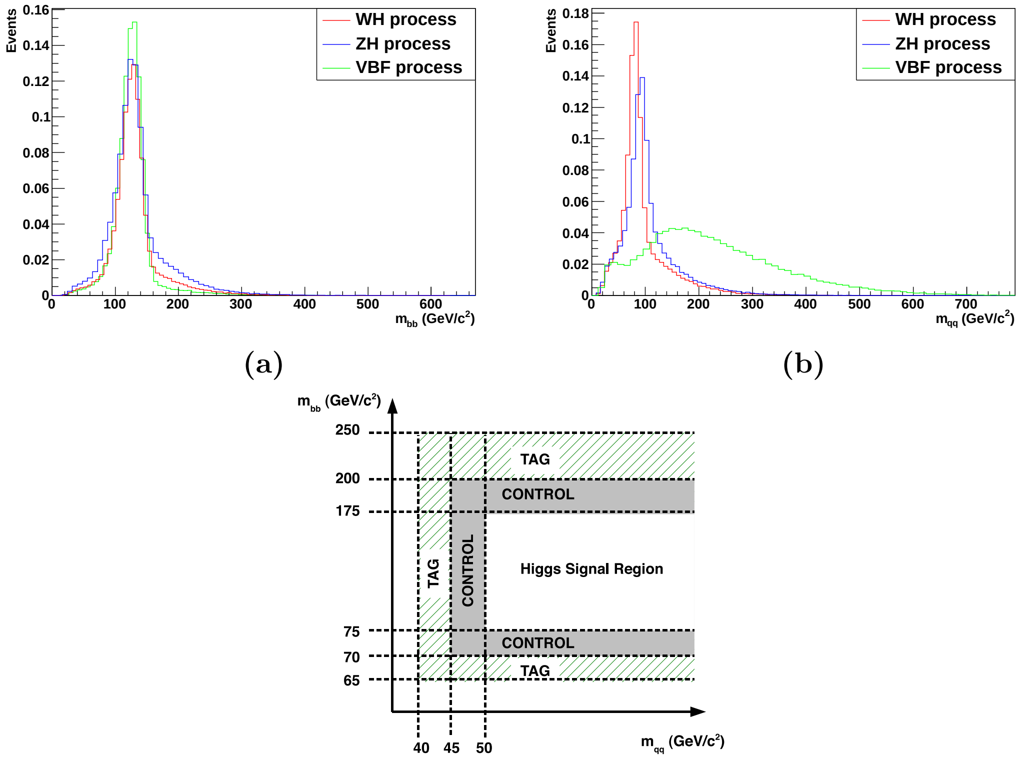

(a)

(b)

(c)

Figure 5.1: The (a) m_{bb} and (b) m_{qq} distributions for 125 GeV/c^2 Higgs boson mass hypothesis. These distributions are used to define the (c) Higgs signal region and control regions in the m_{bb}-m_{qq} plane. The TAG region is used to derive the Tag Rate Function for modeling the QCD multi-jet background. The CONTROL region is used to test and derive systematic uncertainties of this background model.

5.3 Data and Monte Carlo Samples for Signal and Background

The data for this analysis were collected by two triggers: TOP_MULTIJET and VH_MULTIJET (section 4.1). They are designed to select events with 4 high p_T jets with large SumEt which are characteristic of an all-hadronic Higgs event. The first 3.0 fb^{-1} of the CDF data was collected by using the TOP_MULTIJET trigger and the remaining 6.4 fb^{-1} by VH_MULTIJET.

The backgrounds having a similar final state signature as the all-hadronic Higgs signal originate from the QCD multi-jet production, top-quark pair production, single-top-quark production, $W \to q'\bar{q}$ plus $b\bar{b}$ or charm-quark pair ($c\bar{c}$) production ($W + HF$), $Z \to b\bar{b}, c\bar{c}$ plus jets production (Z+jets), and diboson production (WW, WZ, ZZ). The background sources, except the QCD multi-jet production, are referred to as non-QCD backgrounds. About 98% of the total background comes from the QCD multi-jet production, which is estimated from a data-driven technique described in section 5.4. Signal and non-QCD backgrounds yields are estimated from a Monte Carlo (MC) simulation. The $W + HF$ and Z+jets contributions are modeled by the ALPGEN [128] generator that simulates the bosons plus parton production, and PYTHIA [98] for modeling parton showers. The other non-QCD backgrounds and the signal are modeled by using PYTHIA [98]. All MC-simulated samples use the CTEQ5L [99] parton distribution function (PDF) at leading order (LO), scaled to the higher-order calculations of cross section, and are processed through the full CDF detector simulation [129], based on GEANT [130], that includes the trigger simulation. Events which pass the trigger simulation are scaled by the trigger dependent scale factors given in table 4.1.

A scale factor is applied to account for the difference in b-tagging efficiency measured in data and with Monte Carlo. The scale factor for the SecVtx tag is 0.950 ± 0.050, and the one for the JetProb tag is 0.690 ± 0.040 [131]. Therefore, the effective scale factor for SS category is 0.902 ± 0.067, and for SJ category 0.655 ± 0.051.

In tables 5.1 and 5.2, the number of signal and background events expected and observed in this analysis after passing the event selection are summarized [124]. The non-QCD backgrounds are estimated by Monte Carlo, assuming the cross sections given in table 5.3 [132].

The expected signal yield in the SS (SJ) channel is 27.1 ± 4.1 (9.1 ± 1.4) for $m_H = 125$ GeV/c^2 [124]. The selected number of data events for SS (SJ) are 87272 (46818) [124]. The number of QCD multi-jet events in each channel is estimated as the difference between the number of data events and the predicted number of non-QCD events estimated with Monte Carlo (neglecting the potential Higgs boson contribution). In the final fit used to extract a potential Higgs boson signal, the overall normalization of the QCD multi-jet background is treated as an unconstrained parameter.

Signal Region	WH		ZH		VBF		Total	
Higgs Mass (GeV/c^2)	SS	SJ	SS	SJ	SS	SJ	SS	SJ
100	17.8	6.4	13.8	4.4	10.2	3.4	41.8	14.2
105	16.7	6.1	12.9	4.1	9.9	3.5	39.5	13.7
110	15.5	5.6	12.5	4.1	10.0	3.4	38.0	13.1
115	14.3	5.2	11.1	3.6	9.3	3.3	34.7	12.1
120	13.0	4.6	9.9	3.2	8.8	3.0	31.7	10.8
125	10.9	3.8	8.3	2.7	7.8	2.6	27.0	9.1
130	9.0	3.1	6.8	2.2	6.6	2.3	22.4	7.6
135	7.0	2.5	5.3	1.7	5.5	1.8	17.8	6.0
140	5.1	1.8	3.9	1.3	4.2	1.5	13.2	4.6
145	3.5	1.2	2.6	0.9	3.0	1.0	9.1	3.1
150	2.2	0.8	1.7	0.6	2.0	0.7	5.9	2.1

Table 5.1: Expected number of signal events passing the event selection for the SS and SJ b-tagging categories.

5.4 QCD Multi-Jet Background Prediction

The critical component of this analysis is an accurate prediction of the QCD background, as it is the dominant background.

Kinematic features of the QCD multi-jet background are predicted using a data-driven method. The two-tagged background distribution is scaled function of the single-tagged distribution (figure 5.2). The scale factor which was deduced from the single-tagged data is a multi-dimensional function, called Tag Rate Function (TRF) [124]. The TRF is the probability of a jet being b-tagged (probe jet) in an event that already has one other jet tagged as a b-jet. The probability is measured in a kinematic region that has very little contribution from the Higgs signal, the TAG region (figure 5.1c). This is applied to the single-tagged events in the signal region to predict the double b-tagged QCD background.

The key issue of this method is to make sure that the technique can correctly predict the shapes of the kinematic distributions of the two-tagged QCD multi-

Backgrounds	SS Category	SJ Category
$t\bar{t}$	1032 ± 156	384 ± 57
Single top s channel	111 ± 19	38 ± 6
Single top t channel	44 ± 7	26 ± 4
$W + b\bar{b}$	77 ± 40	29 ± 15
$W + c\bar{c}$	8 ± 4	7 ± 4
$Z(\rightarrow b\bar{b}/c\bar{c})$+jets	873 ± 452	338 ± 175
WW	6 ± 1	6 ± 1
WZ	20 ± 3	8 ± 1
ZZ	21 ± 3	8 ± 1
Total non-QCD	2192 ± 480	844 ± 185
Data	87272	46818
QCD multi-jet	85080	45974
Higgs signal (125 GeV/c^2)	27 ± 4	9 ± 1

Table 5.2: Expected number of the background and signal ($m_H = 125$ GeV/c^2) events that pass the event selection for the SS and SJ b-tagging categories. The number of QCD multi-jet events is estimated as the difference between data and predicted non-QCD backgrounds (neglecting the potential Higgs contribution). The uncertainties of the signal and non-QCD background rate predictions include statistical and systematic rate uncertainties, such as cross section and integrated luminosity, as described in section 6.

Process	Cross Section	Source
$t\bar{t}$	7.04 pb	CDF Note 10606 [132]
Single Top S channel	1.05 pb	CDF Note 10606 [132]
Single Top T channel	2.10 pb	CDF Note 10606 [132]
WW	11.34 pb	CDF Note 10606 [132]
WZ	3.47 pb	CDF Note 10606 [132]
ZZ	3.62 pb	CDF Note 10606 [132]
$W + b\bar{b}$	24.70 pb	(Alpgen+Pyhtia LO x 1.4 K_NLO)
$W + c\bar{c}$	40.64 pb	(Alpgen+Pythia LO x 1.4 K_NLO)
$Z \rightarrow b\bar{b}/c\bar{c} + jj$	700.26 pb	(Pythia LO x 1.4 K_NLO)

Table 5.3: The cross sections for the non-QCD backgrounds and the sources used.

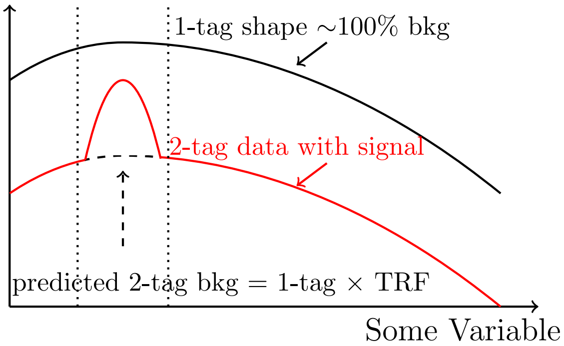

Figure 5.2: TRF principle. The black line corresponds to the single-tagged distribution (background). The two-tagged background is assumed to be a scaled version of the single-tagged distribution (red line). The TRF is derived from the regions outside the signal peak.

jet events. This TRF method does not necessarily predict the right normalization of the two-tagged QCD background.

The TRF is applied to data samples with exactly one jet b-tagged by SecVtx to predict the distribution of events with two b-tagged jets. The TRF is parameterised as a function of three variables: E_T of the probe jet, η of the probe jet, and ΔR between the tagged b-jet and the probe jet, and implemented as a three-dimensional histogram:

$$TRF(E_T, |\eta|, \Delta R) = \frac{\text{Number of events with 2 tagged jets}(E_T, |\eta|, \Delta R)}{\text{Number of events with 1 or 2 tagged jet}(E_T, |\eta|, \Delta R)} \tag{5.1}$$

The choice of variables used to parameterise the TRF is motivated by the kinematics of the QCD multi-jet background and the characteristics of the b-tagging algorithms. For example, the production of b-jets from gluon splitting has a different ΔR distribution compared to direct production, and the probe jet E_T and η express aspects of the b-tagging algorithms and QCD multi-jet production. The TRFs are measured separately for SS and SJ events, which are obtained from events in the TAG region (figure 5.1c). To validate the background model, the TRF is tested in the TAG (for self-consistency), CONTROL and the NJET6 control region comparing the TRF predicted distribution of variables used in this analysis with the two-tagged data and any shape difference is propagated as an uncertainty of the QCD multi-jet model.

5.4.1 Tuning the Modeling of m_{qq}

The TRF generated via this method does predict well the shapes of more kinematic variables. The most important variables in this analysis are m_{bb} and m_{qq}, but the m_{qq} variable is not perfectly modelled. Possible reasons for the mismatching are that the ratio of two b-tagged over one b-tagged events is assumed to be flat; this assumption holds, in general, but could fail locally in the m_{bb}-m_{qq} phase space. Another reason is that, while developing the TRF, both one b-tagged and two b-tagged events contribute to the denominator. When predicting two b events in the signal region only one b-tagged events are used. This creates slight inconsistency in the composition of the denominator. These are limitations of this method.

The residual mis-modeling is corrected reweighting events as a function of the observed m_{qq}. The correction function is derived from a fit to the ratio of the observed m_{qq} over the same quantity predicted by TRF in events from the TAG region [124].

Figures 5.3-5.8 show a comparison of the observed data and background predictions in the signal region for the variables used in the final signal discrimination neural network (section 5.8) after application of the m_{qq} correction function. The modeling of some variables is not perfect, but the differences are still within the shape uncertainties of the QCD multi-jet prediction.

5.5 b-jets Energy Correction

The experimental resolution of the invariant mass of the two b-jets, m_{bb}, has a significant effect on the sensitivity of the search. To improve the m_{bb} resolution, a neural network, for each b-tagging algorithm and production process, is trained to estimate the correction factor required to obtain the best possible estimate of the parent b parton energy from the measured jet energy [135].

Nine variables, describing a given jet, are used to train the neural network for SecVtx tagged jets. These are the jet E_T (section 4.2.2), the jet transverse momentum (section 3.3.1), the E_T before the application of jet energy correction (uncorrected jet E_T), the transverse mass[2], the decay length (L_{xy}) of the jet in the transverse plane[3] and its uncertainty (σ_L), the p_T of the secondary vertex, the maximum p_T of the tracks inside the jet cone, and the p_T sum of all tracks within the jet cone.

---

[2] The transverse mass is defined as $(p_T/p)m$, where m is the invariant mass of the jet.

[3] The decay length is defined as the transverse distance between the primary vertex and the reconstructed secondary vertex in the SecVtx b-tagged jet.

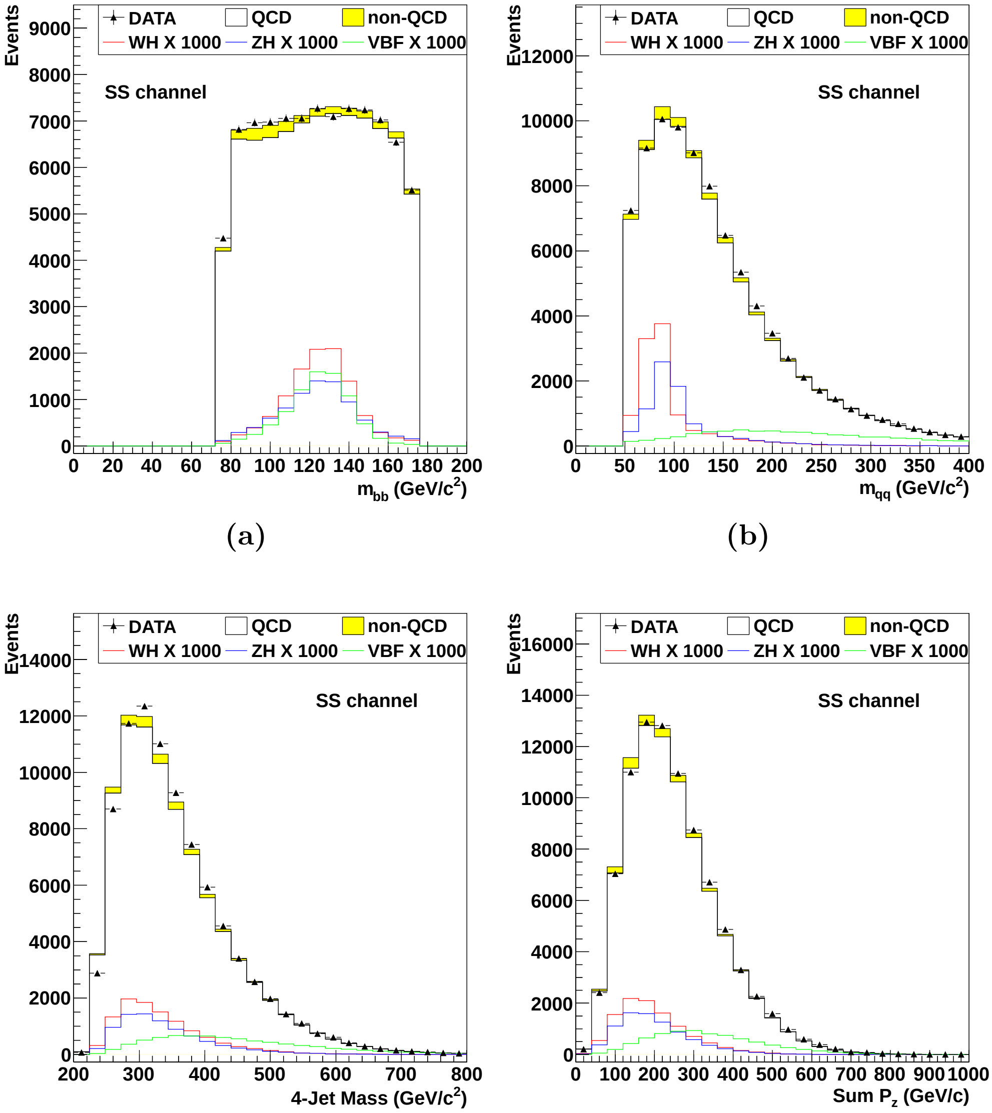

(a) **(b)**

(c) **(d)**

Figure 5.3: Data (double b-tagged) are compared with QCD multi-jet background prediction derived from the single b-tagged data multiplied by the TRF in distributions of (a) m_{bb}, (b) m_{qq}, (c) the invariant mass of four-jets system, and (d) the sum of the momenta along z direction for each of the four jets in the search signal region. The m_{qq} variable distribution is obtained after the application of the m_{qq} correction described in section 5.4.1.

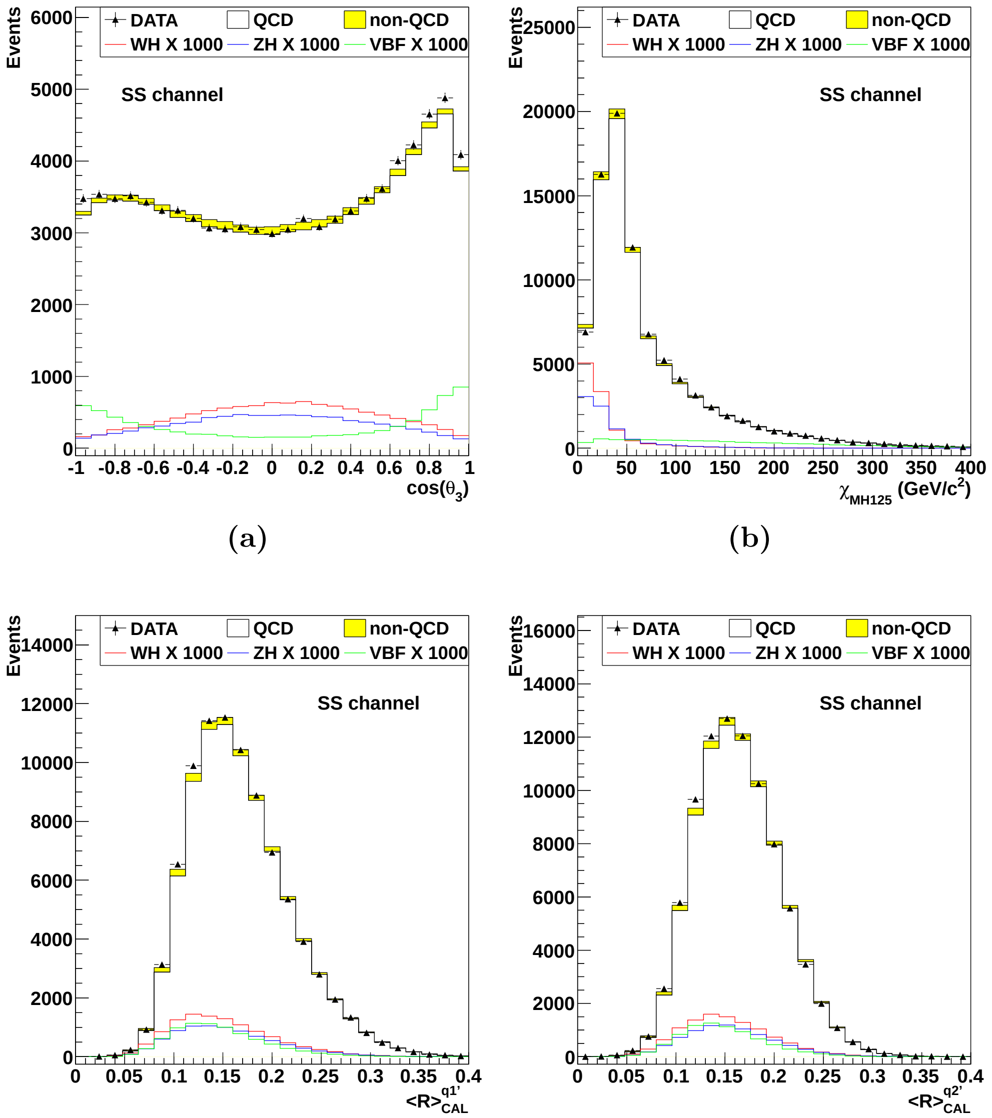

(a) (b)

(c) (d)

Figure 5.4: Data (double b-tagged) are compared with QCD multi-jet background prediction derived from the single b-tagged data multiplied by the TRF in distributions of (a) the cosine of the leading-jet scattering angle in the four-jet rest-frame [133], (b) the χ variable [134], and (c) the calorimeter jet width of the first and (d) second leading untagged jet.

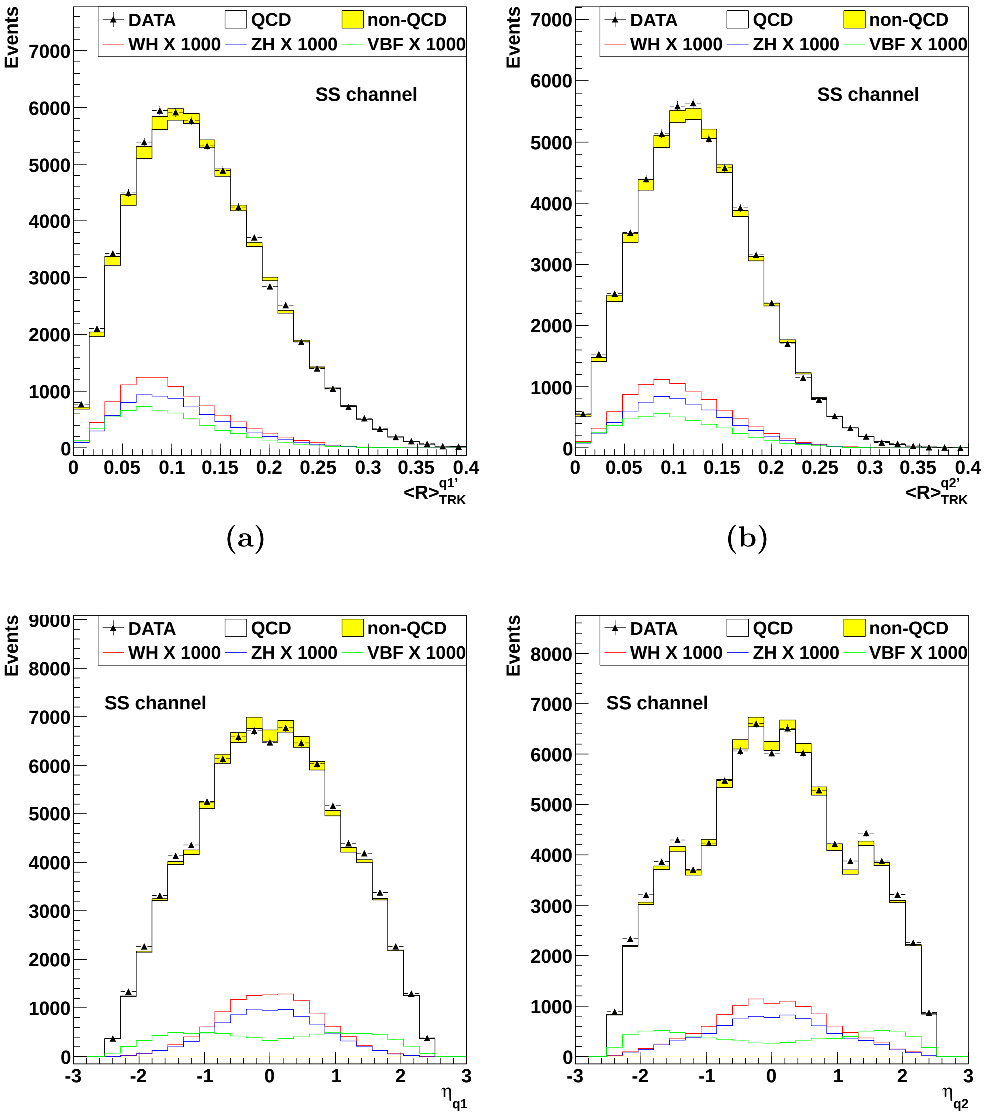

(a) (b)

(c) (d)

Figure 5.5: Data (double b-tagged) are compared with QCD multi-jet background prediction derived from the single b-tagged data multiplied by the TRF in distributions of (a) the tracker jet width of the first and (b) second leading untagged jet, (c) the η angle of the first leading untagged jet and (d) second leading untagged jet.

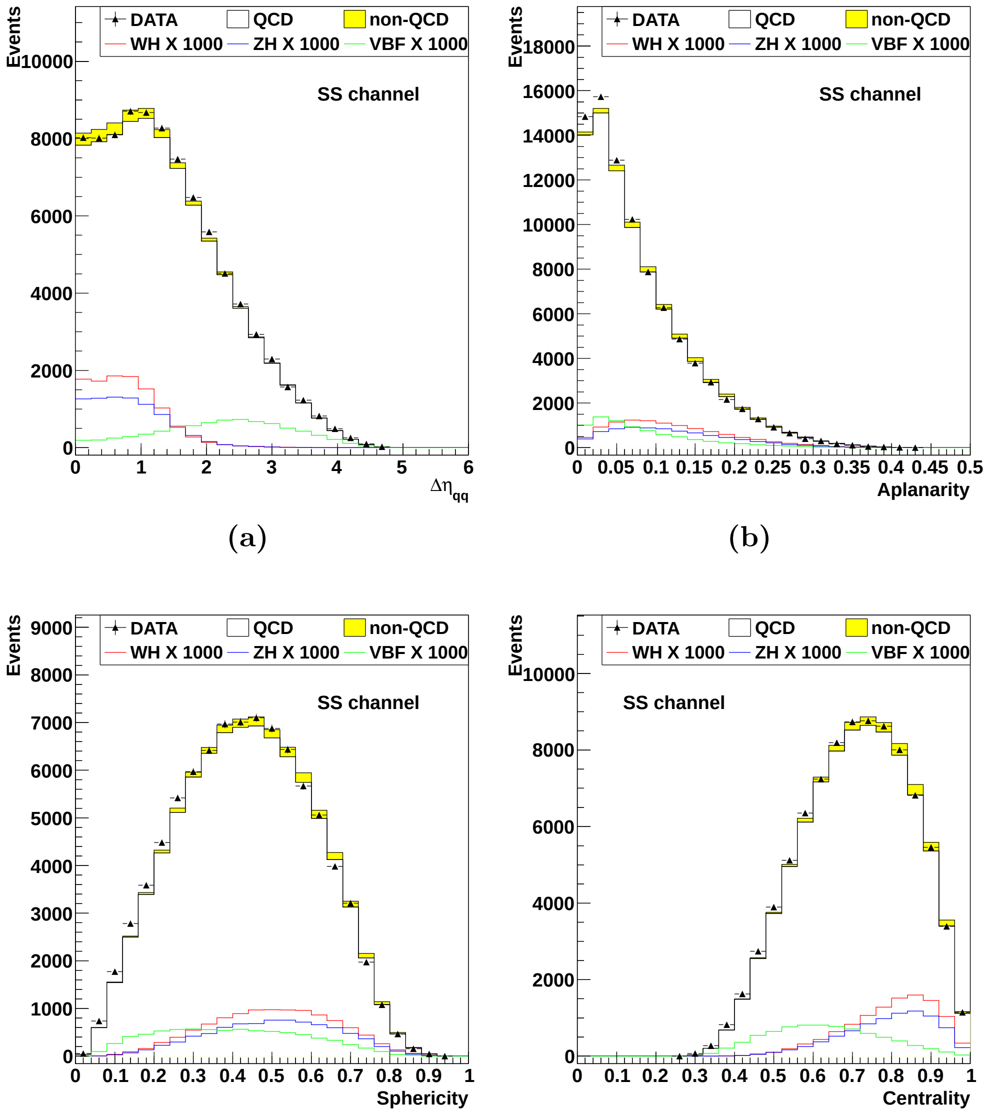

(a) (b)

(c) (d)

Figure 5.6: Data (double b-tagged) are compared with QCD multi-jet background prediction derived from the single b-tagged data multiplied by the TRF in distributions of (a) $\Delta\eta$ of the two untagged jets, (b) the transverse momentum component out of the event plane (the aplanarity) [98], (c) the summed transverse momentum squared with respect to the event axis (the sphericity) [98], and (d) the quantity of the energy which flows into the central rapidity region (the centrality) [98].

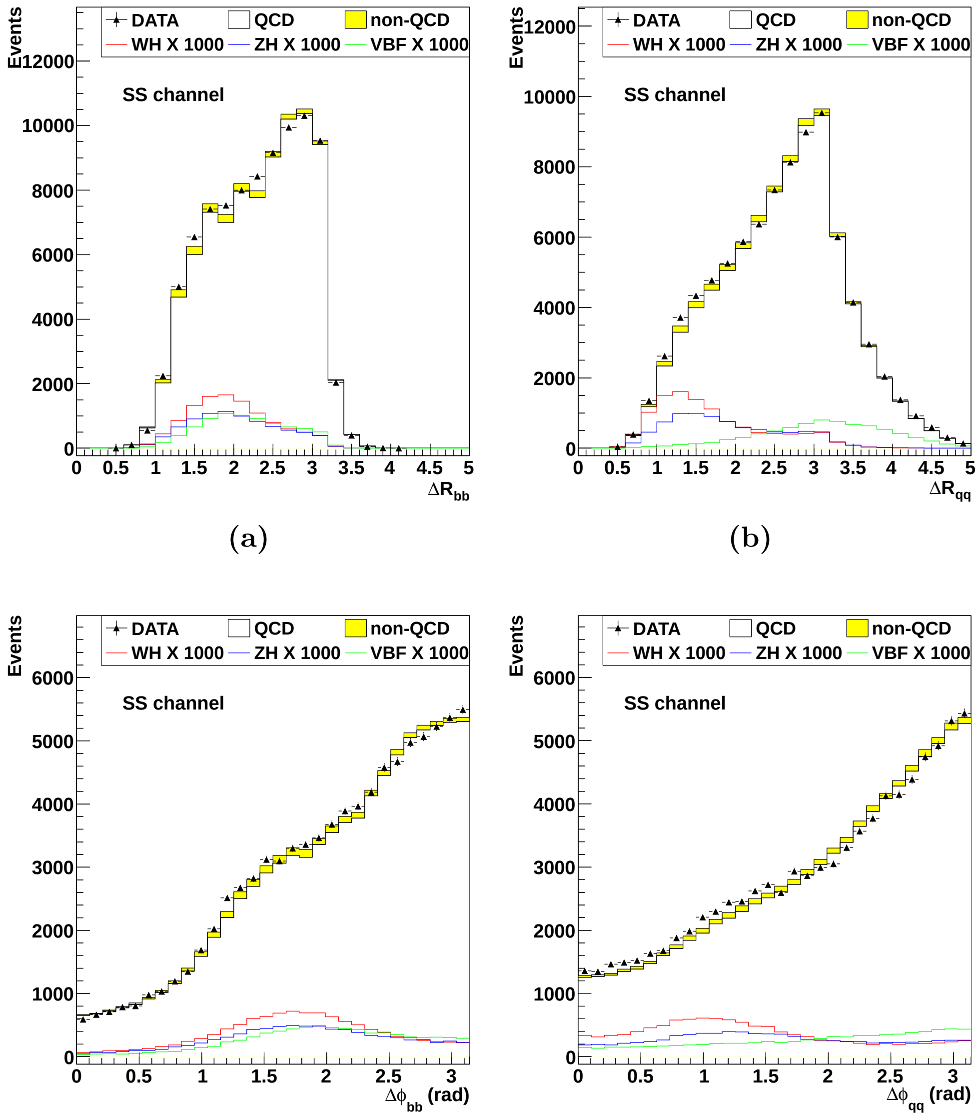

(a) **(b)**

(c) **(d)**

Figure 5.7: Data (double b-tagged) are compared with QCD multi-jet background prediction derived from the single b-tagged data multiplied by the TRF in distributions of (a) the ΔR of the two b-tagged jets and (b) of the two untagged jets, (c) the $\Delta\varphi$ of the two b-tagged jets and (d) of the two untagged jets.

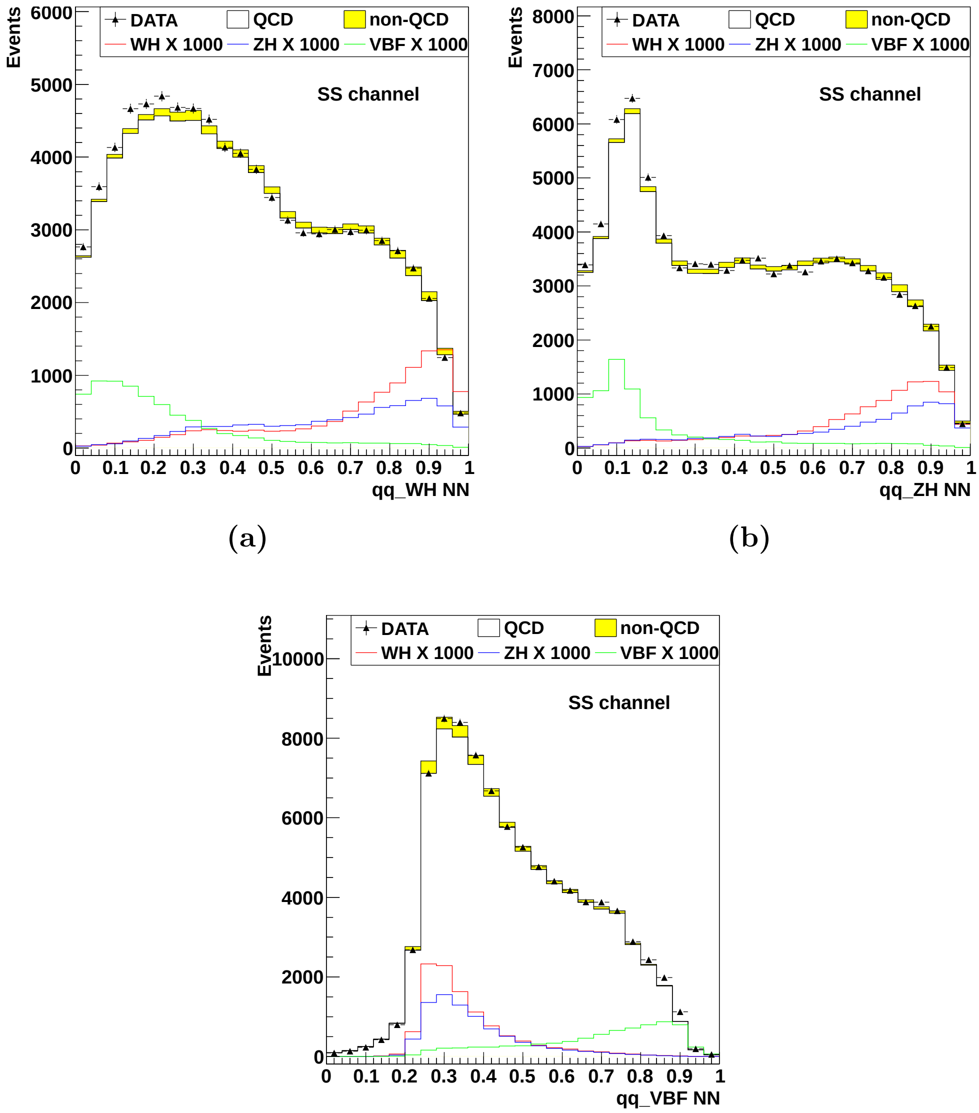

(a) (b)

(c)

Figure 5.8: Data (double b-tagged) are compared with QCD multi-jet background prediction derived from the single b-tagged data multiplied by the TRF in distributions of (a) qq_WH NN, (b) qq_ZH NN, and (c) $qq_$VBF NN (section 5.6).

Six variables are used to train the neural network for JetProb tagged jets: the jet E_T, the jet p_T, the uncorrected jet E_T, the transverse mass, the maximum p_T of the tracks inside the jet cone, and the p_T sum of all tracks within the jet cone.

The events used for the training are required to pass the selection described in section 5.2 and each b-tagged jet is required to be matched geometrically with a b parton. The matching criterion requires the ΔR between the b-jet and b parton not to exceed 0.4. SecVtx- and JetProb-tagged jets are used to train the SecVtx and JetProb neural networks, respectively.

The weights, obtained from each production process neural network, are applied to each mass point to identify which one has the best resolution. The resolution is defined as the ratio between the root mean square (RMS) and the mean value of m_{bb} distribution; the values of these two parameter are calculated with a gaussian fit in a range of 2σ around the mean value. The resolution is measured for the Higgs masses from 100 to 150 GeV/c^2 at 5 GeV/c^2 intervals. The neural network trained with VBF samples is used for the analysis as it has the best resolution (figure 5.9).

Figure 5.10 shows the m_{bb} distribution in simulated decays of 125 GeV/c^2 Higgs bosons produced through VBF, before and after b-jet energies are corrected. The mean shifts from 116 to 128 GeV/c^2 and the RMS from 15.6 to 13.7 GeV/c^2. The resolution shifts from 0.13 to 0.11, with an improvement of 18% [124].

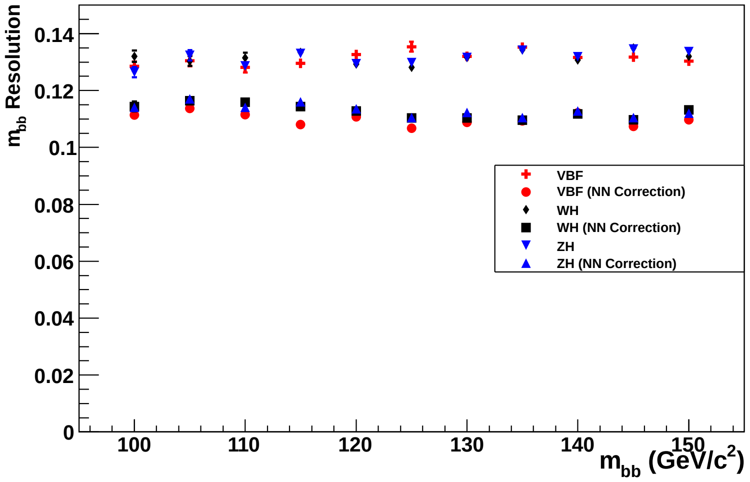

Figure 5.9: The resolution for each mass point before and after the neural network b-jet energy correction is applied.

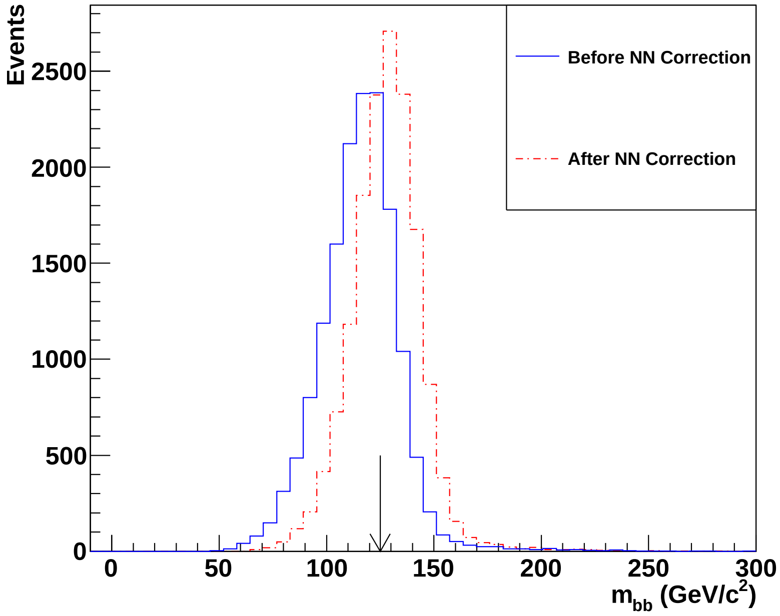

Figure 5.10: Comparison of m_{bb} distribution in simulated decays of 125 GeV/c^2 Higgs bosons produced through VBF, before and after the b-jet energy correction for a VBF Monte Carlo sample with $m_H = 125$ GeV/c^2 (indicated by the black arrow).

5.6 Untagged Jets Neural Network

The angular distributions of untagged jets (q-jets) from VH or VBF differs from the angular distributions of generic jets contained within QCD multi-jet background events. Identification of q-jets can therefore help to separate signal events from QCD multi-jet background contributions. In particular, the m_{qq} obtained from q-jets associated with the WH and ZH processes is constrained by the mass of the W and Z boson, respectively (figure 5.1b). The q-jets produced in VBF events are typically separated by large φ and η, while the q-jets in QCD multi-jet events tend to exhibit a large difference in φ and a small difference in η.
Three neural networks [125], referred to as qq_WH NN, qq_ZH NN, and $qq_$VBF NN, are trained to separate events with q-jets originating from WH, ZH, and VBF processes from background events.
The input variables are m_{qq}, $\Delta\varphi$ $\Delta\eta$, and ΔR of the two untagged jets, and the transverse momenta of each q-jet with respect to the total momentum of the

system.
The neural networks are trained using a Higgs Monte Carlo 125 GeV/c^2 sample to model signal and data-driven prediction for QCD multi-jets to model background. Special attention is paid to reject events that have three or more b quarks. Only events with exactly two b-tagged jets were used for the background. This is particularly important for the ZH process where also the Z boson could decay into b quarks. In such case it is difficult to determine whether the b-jet came from a Z or Higgs boson decay and could cause confusion in the neural network training.
The neural network output distributions are shown in figure 5.8.

5.7 Jet Width

The untagged jets (q-jets) associated with the QCD multi-jet background are a mixture of quark and gluon jets, whereas the q-jets associated with the Higgs signal are predominantly quark jets. As gluon jets tend to be broader than quark jets, the jet width is another useful variable for distinguishing potential Higgs events from the background. The jet widths measured within the calorimeter ($\langle R\rangle_{\mathrm{CAL}}$) and tracker ($\langle R\rangle_{\mathrm{TRK}}$) are defined as:

$$\begin{aligned}\langle R\rangle_{\mathrm{CAL}} &= \sqrt{\sum_{\text{towers}}\left[\frac{E_T^{\text{tower}}}{E_T^{\text{jet}}}\Big(\Delta R(\text{tower,jet})\Big)^2\right]}\\ \langle R\rangle_{\mathrm{TRK}} &= \sqrt{\sum_{\text{tracks}}\left[\frac{p_T^{\text{track}}}{p_T^{\text{jet}}}\Big(\Delta R(\text{track,jet})\Big)^2\right]},\end{aligned} \tag{5.2}$$

where ΔR(tower,jet) (ΔR(track,jet)) is the distance between the jet axis and the calorimeter tower (track). All calorimeter towers within the jet cone of $\Delta R < 0.4$ are used in the $\langle R\rangle_{\mathrm{CAL}}$ calculation. All tracks with $p_T > 1$ GeV/c and within the jet cone of $\Delta R < 0.4$ are used in the calculation of $\langle R\rangle_{\mathrm{TRK}}$.

The jet width depends not only on the parton initiating the jet but also varies with jet kinematics and detector effects. It varies as a function of jet E_T, jet η, and the number of primary vertices (N_{vtx}).
A neural network [126] is trained to parameterise the jet width as a function of these jet kinematic and detector variables; to remove these dependencies the measured jet width are rescaled to a common reference of E_T=50 GeV/c^2, η=0, and $N_{\mathrm{vtx}} = 1$. A separate neural network is trained for data and Monte Carlo.

The equations (5.3) demonstrate how the jet widths are rescaled:

$$\langle R\rangle^{Data\prime}_{CAL} = \langle R\rangle^{Data}_{CAL} \times \frac{\langle R\rangle^{Ref}_{CAL}}{f^{Data}_{CAL}(E_T, \eta, N_{\mathrm{vtx}})} \tag{5.3a}$$

$$\langle R\rangle^{MC\prime}_{CAL} = \langle R\rangle^{MC}_{CAL} \times \frac{\langle R\rangle^{Ref}_{CAL}}{f^{MC}_{CAL}(E_T, \eta, N_{\mathrm{vtx}})} \tag{5.3b}$$

$$\langle R\rangle^{Data\prime}_{TRK} = \langle R\rangle^{Data}_{TRK} \times \frac{\langle R\rangle^{Ref}_{TRK}}{f^{Data}_{TRK}(E_T)} \tag{5.3c}$$

$$\langle R\rangle^{MC\prime}_{TRK} = \langle R\rangle^{MC}_{TRK} \times \frac{\langle R\rangle^{Ref}_{TRK}}{f^{MC}_{TRK}(E_T)}. \tag{5.3d}$$

Here $\langle R\rangle^{Ref}_{CAL}$ and $\langle R\rangle^{Ref}_{TRK}$ are the data common reference jet width for the calorimeter and tracker, respectively. The functions $f^{Data/MC}_{CAL}(E_T, \eta, N_{\mathrm{vtx}})$ and $f^{Data/MC}_{TRK}(E_T)$ are the neural network data (Monte Carlo) jet width parameterisation.
After rescaling the measured jet widths, any difference in the jet width can be assumed to be due to the type of parton (quark or gluon) initiating the jet.

The neural network function is trained on a sample of untagged quark jets from the hadronic W boson decays in $t\bar{t} \to b\bar{b}l\nu qq$ $(\ell = e, \mu)$ events. The highest E_T untagged-jet pair whose invariant mass is in the range $50 - 110$ GeV/c^2 is assumed to originate from the hadronic W boson decay. The $t\bar{t}$ Monte Carlo and data q-jet width distributions are found to agree after rescaling the measured jet widths. To check that the jet width rescaling can be applied to non-$t\bar{t}$ samples, the rescaling is also applied to the q-jets in WH, ZH, and VBF Monte Carlo events. The mean rescaled jet width in all samples is consistent with the width observed in the $t\bar{t}$ sample, which verifies the independence of the corrections with respect to jet E_T, η, and N_{vtx}.

Figures 5.4c-5.5b show the corrected jet width distributions of the untagged jets measured by the calorimeter and tracker. The Higgs signal tends to lower jet width values, which implies quark-like, whereas the QCD multi-jet tends to higher jet width, which implies a mixture of quark and gluons. The jet width distributions of the Higgs signal is different to the background which shows this variable is useful for the Higgs boson search.

5.8 Classification of Higgs Boson Events

The multivariate technique allows to combine the information from several variables to optimize the separation of signal and background [125]. The efficiency of multivariate analysis significantly higher than a standard cuts analysis.

Because the VH and VBF processes have different kinematics, a dedicated neural network is trained separately for each process, resulting in three outputs. The outputs of the process-specific neural networks are combined as inputs to a grand neural network, referred to as the Higgs-NN. The output of the Higgs-NN is used to obtain the Higgs search limits.

Two criteria must be applied to select the input variables for the neural networks training: the variables must have good background-to-signal separation, and they must be well modeled by TRF.

The discriminating variables for the VH neural network training are m_{bb}, m_{qq}, the cosine of the leading-jet scattering angle in the four-jet rest-frame ($\cos(\theta_3)$) [133], the χ variable[4] [134], the calorimeter jet width of the first ($\langle R\rangle^{q_1}_{CAL}$) and second leading untagged jet ($\langle R\rangle^{q_2}_{CAL}$), the tracker jet width of the first ($\langle R\rangle^{q_1}_{TRK}$) and second leading untagged jet ($\langle R\rangle^{q_2}_{TRK}$), aplanarity[5], sphericity[6], centrality[7] [98], ΔR of the two b-tagged jets, ΔR of the two untagged jets, $\Delta\varphi$ of the two b-tagged jets, $\Delta\varphi$ of the two untagged jets, and the qq_WH and qq_ZH neural network outputs (section 5.6).

Not all variables used in the VH neural networks' training have a good discrimination power for the VBF process. For the VBF-NN training, the $\cos(\theta_3)$, the aplanarity, and the $\Delta\varphi$ of the two untagged jets are removed; the η angle of the first (η_{q_1}) and second leading untagged jet (η_{q_2}), the $\Delta\eta$ of the two untagged jets ($\Delta\eta_{qq}$), the invariant mass of four jets system, the sum of the four jets' momenta along z direction are added, and the qq_WH and qq_ZH neural network outputs are replaced by qq_VBF NN output.

Among the 17(18) variables used for the VH(VBF)-NN training those which have the most discrimination power are m_{bb} and m_{qq} (m_{qq} and $\Delta\eta_{qq}$) [124].

The distributions of the discriminating variables for the Higgs signal and background are shown in figures 5.3-5.8.

The potential Higgs boson decay produces a peak in the m_{bb} distribution that is not observed in the QCD multi-jet background (figure 5.3a). This resonance is

---

[4] χ variable is the minimum of χ_W and χ_Z where $\chi_W = \sqrt{(m_W - m_{qq})^2 + (m_H - m_{bb})^2}$ and a similar expression exists for χ_Z.

[5] Aplanarity measures the transverse momentum component out of the event plane.

[6] Sphericity is a measure of the summed transverse momentum squared with respect to the event axis.

[7] Centrality measures how much of the energy flows into the central rapidity region.

present in both channels, VH and VBF. In the m_{qq} distribution can be observed the resonance due to the W/Z decay, in the VH channel, it is not observed in the VBF channel since the two q-jets are not produced in a decay of a particle. In figures 5.4c-5.5b the jet width distributions of untagged jets of the QCD multi-jet background are broader than the Higgs signal due to the reason that is described in section 5.7. The two q-jets produced in the VBF events, produced from the two incoming quarks that each radiates a weak boson, tend to point in the forward but opposite directions. Thus the two q-jets are widely separated in the pseudo-rapidity space. These features are shown in figures 5.5c-5.6a. The qq_WH NN (figure 5.8a), qq_ZH NN (figure 5.8b), and qq_VBF NN (figure 5.8c) distributions are the outputs of three neural networks that are trained to separate the QCD multi-jet events from WH, ZH and VBF productions, respectively.

Each variable demonstrates some ability to distinguish a Higgs boson from the background. Some variables, such as the invariant mass of four jets system (figures 5.3c) and qq_WH neural network output (figure 5.8a) appear to have some mis-modeling of the background. However, the observed difference are within the shape uncertainties of the TRF QCD multi-jet prediction. These shape uncertainties are derived by testing these variables in the TAG, CONTROL, and NJET6 control regions and propagating any difference as a shape uncertainty.

The WH-NN, ZH-NN, and VBF-NN are trained using dedicated Monte Carlo samples for signal modeling. A small subset (10%) of single-tagged jet events, after random selection and application of the TRF, is used as the QCD multi-jet training sample. The remaining 90% of events are reserved for modeling the neural network output distributions. As the shapes of the kinematic distributions are found to be consistent for both b-tagging categories, the neural network is trained using SS events.

The search focuses on Higgs boson mass hypotheses in the range from 100 to 150 GeV/c^2 at 5 GeV/c^2 intervals. The sensitivity of the search is improved by using separate trainings at three specific Higgs boson masses: 100, 120, and 140 GeV/c^2. For each Higgs boson mass hypothesis, the training that gives the best search sensitivity is chosen (table 5.4) [124].

Higgs Mass Hypotesis (GeV/c^2)	Training Mass (GeV/c^2)
100	100
105 - 130	120
135 - 150	140

Table 5.4: The corresponding training mass for each Higgs mass hypotesis.

5.8.1 VBF-NN Output Correction

Only variables that are well modeled by the TRF are used to train the WH-NN, ZH-NN, and VBF-NN. As a further validation, the modeled outputs of the WH, ZH, and VBF neural networks are compared to TAG events in data. The WH-NN, ZH-NN output distributions are well modeled, but the VBF-NN presents a disagreement between observed and the TRF prediction distribution (figure 5.11a). Similar mis-modeling is observed also in the Higgs-NN output distribution. In order to improve the Higgs-NN, the VBF-NN mis-modeling is corrected reweighting the events in the signal region with a correction function derived in a region presumably devoid of signal, by assuming that the same correction works also in signal region [124]. The two control region considered are the TAG and the NJET6 region. In these regions, the same mis-modeling as in the signal region is present (figure 5.12), and it is assumed that they have the same source. The correction function is derived from a first order regression fit to the ratio of observed over the TRF prediction Higgs-NN output distribution in events from the control regions.

The correction function is derived for all three mass points used for training (100, 120, and 140 GeV/c^2) and for the two b-tagged categories (SS and SJ). To choose the optimum correction function, they are applied to events in CONTROL region and the χ^2/degree of freedom (χ^2/d.o.f.) and the Kolmogorov-Smirnov value (KS-value) (table 5.5) are calculated. The function with best values is selected as correction, and the other one is used to estimate the systematic uncertainties.

Figure 5.13 shows, for the mass point 100 GeV/c^2 in SS b-tag category, the VBF-NN output distribution in TAG, NJET6 and CONTROL region before applying of the correction function; figure 5.14 shows the distribution of VBF-NN and Higgs-NN after applying the correction function. The equivalent plots for the other mass training points in the two b-tag categories can be found in appendix A.

For the training mass at 100 and 140 GeV/c^2 in SS b-tag category, the correction function derived in the TAG region is used, and that one derived in the NJET6 region is used for the systematic uncertainties. For the 120 GeV/c^2 sample, the NJET6 correction function gives a better KS-value and χ^2/d.o.f. value. However, the difference between using the NJET6 and TAG correction function is minor, and the TAG correction function is used for this sample, too, for consistency.

For the mass points training in SJ b-tag category, the correction function derived in TAG region is used to correct the neural network, and that one derived in the NJET6 region is used to evaluate the systematic uncertainties.

Figure 5.15 show the *WH*-NN, *ZH*-NN, VBF-NN, and Higgs-NN output distribution of 120 GeV/c^2 Higgs boson events with both *b*-jets tagged by SecVtx. The VBF-NN correction function is applied to VBF-NN and Higgs-NN output distributions. The histogram shows the data, a stacked distribution of the backgrounds, and the Higgs boson signal scaled by 1000. As the QCD multi-jet background is large, it is difficult to see the non-QCD contributions and the QCD uncertainty. In the lower QCD subtracted data plot, it is easier to see how well the background is modeled. These plots show the QCD uncertainty is as large as the total non-QCD contributions and the QCD subtracted data is consistent with the non-QCD background and the QCD uncertainty. The equivalent plots for the other Higgs boson mass hypotheses can be found in appendix B.

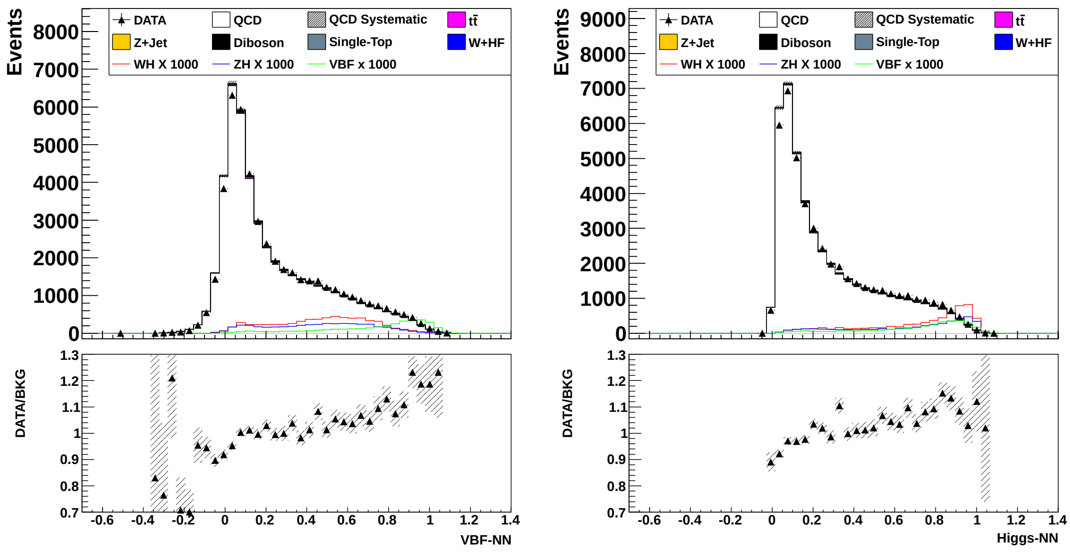

(a) **(b)**

Figure 5.11: The (a) VBF-NN and the (b) Higgs-NN output distribution for a 100 GeV/c^2 Higgs boson mass hypothesis in SS *b*-tag category. The plots below show the ratio between observed data and background prediction.

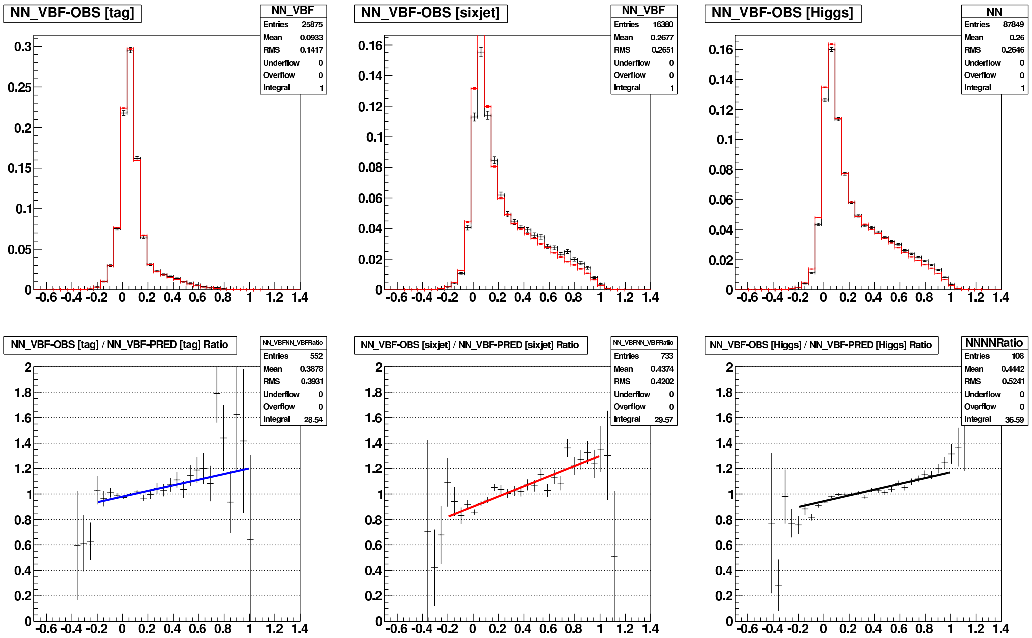

(a) **(b)** **(c)**

Figure 5.12: The VBF-NN output distribution for the 100 GeV/c^2 Higgs boson mass hypothesis in SS b-tag category in (a) TAG, (b) NJET6 and (c) signal region show the same mis-modeling. The red histograms represent the QCD multi-jet background prediction, the black histograms are the data. The plots below show the ratio between data and background prediction, the lines represent the fit of the ratio plots.

Samples	KS-value	χ^2/d.o.f.
100 STST	0.69226	0.857104
100 STJP	0.258203	1.24795
120 STST	0.302658	0.822528
120 STJP	0.102873	1.24716
140 STST	0.18663	1.38333
140 STJP	0.262354	1.87248

(a)

Samples	KS-value	χ^2/d.o.f.
100 STST	0.0472725	1.24937
100 STJP	0.0152989	1.78886
120 STST	0.994325	0.646125
120 STJP	0.00010446	2.10496
140 STST	0.0565532	1.38517
140 STJP	0.0477932	2.01858

(b)

Table 5.5: Kolmogorov-Smirnov and χ^2/d.o.f. values for the correction function derived in the (a) TAG and (b) NJET6 region and applied to events in CONTROL region.

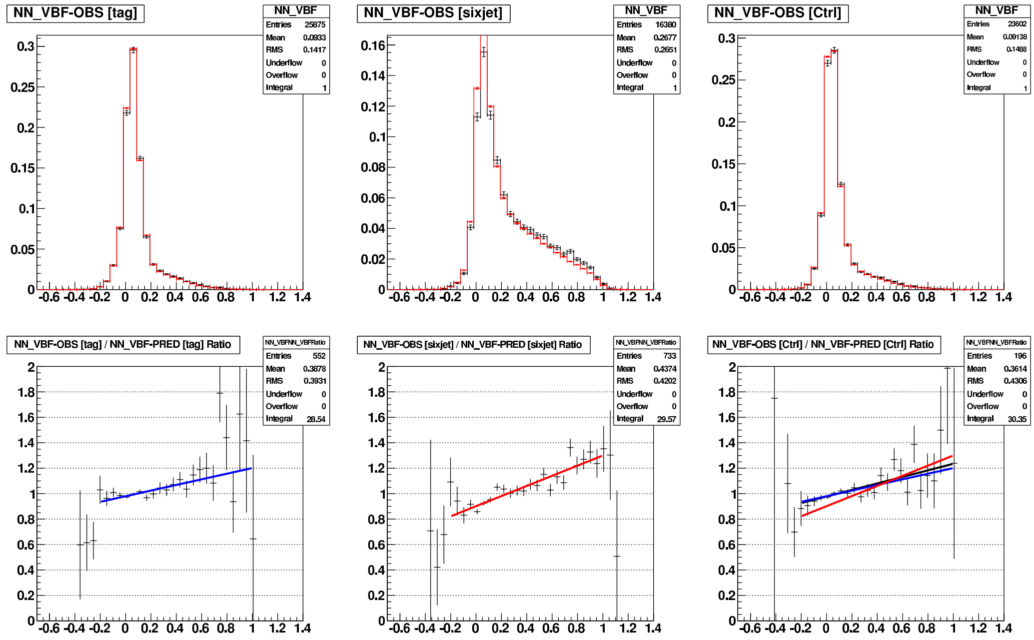

(a) **(b)** **(c)**

Figure 5.13: The VBF-NN output distribution for the 100 GeV/c^2 Higgs boson mass hypothesis in SS b-tag category in (a) TAG, (b) NJET6 and (c) CONTROL region. The red histograms represent the QCD multi-jet background prediction, the black histograms are the data. The plots below show the ratio between data and background prediction, the lines represent the fit of the ratio plots: the red line is the fit derived in NJET6 region, the blue line is the fit derived in the TAG region and the black line is the fit derived in the CONTROL region. The plot (c) shows the overlap of the fit corrections in the CONTROL region.

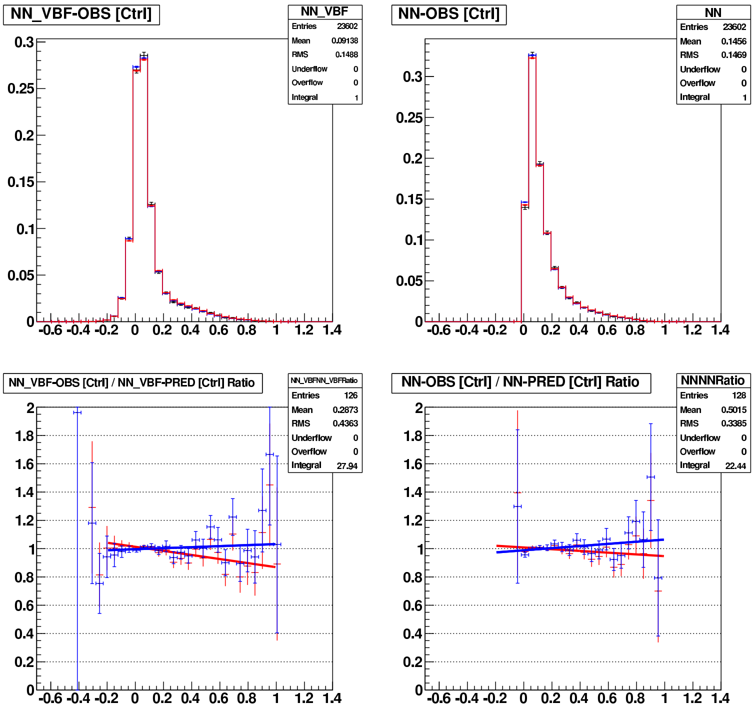

(a) **(b)**

Figure 5.14: The (a) VBF-NN and (b) Higgs-NN output distribution for the 100 GeV/c^2 Higgs boson mass hypothesis in SS b-tag category in CONTROL region after applying of the correction function. The red histograms are the QCD multi-jet background prediction after applying the correction function derived in the NJET6 region. The blue histograms are the QCD multi-jet background prediction after applying the correction function derived in TAG region. The black histograms are the data. The plots below show the ratio between data and the two corrected background prediction, the lines represent the fit of the ratio plots.

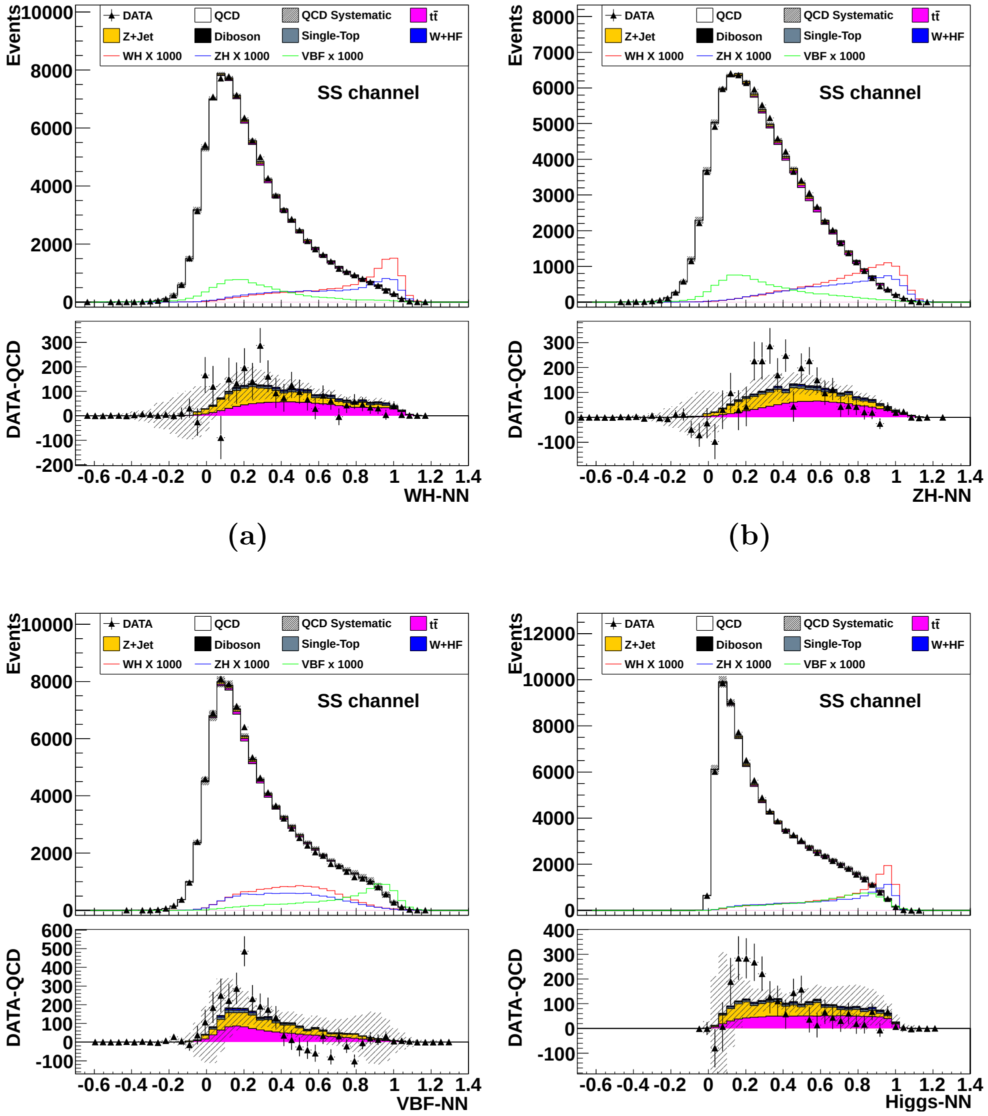

(a) (b)

(c) (d)

Figure 5.15: The (a) *WH*-NN, (b) *ZH*-NN, (c) VBF-NN and (d) Higgs-NN output distribution of 120 GeV/c^2 Higgs boson events with both b-jets tagged by SecVtx. The VBF-NN correction function is applied to VBF-NN and Higgs-NN QCD multi-jet background prediction. All backgrounds are stacked and the superimposed Higgs boson signal is scaled by 1000. As the QCD multi-jet background is large, plots of the difference of data and QCD multi-jet are plotted with a stacked plot of non-QCD background and QCD multi-jet systematic uncertainty. Both plots show that the data are consistent with the background, especially at large Higgs-NN score where the Higgs signal peaks.

Chapter 6

Systematic Uncertainties

In this chapter the sources of systematic uncertainties of the signal and background are discussed. The uncertainties can be classified in rate, that affect the normalization of the Higgs-NN output, and shape systematic uncertainties, that affect the distribution of the Higgs-NN output. The systematic uncertainties of the event rates are defined as the variations of the number of events that pass the selection requirements. The shape-related systematic uncertainties are expressed as fractional changes in binned distributions.

The systematic effects that affect the normalization of the Higgs boson and non-QCD background are the uncertainty on the jet energy scale (JES) [119], on the parton distribution function (PDF), b-tagging scale factor, initial and final state radiation (ISR and FSR), trigger efficiency, integrated luminosity, and cross section [49]. The effects that affect the shape of the Higgs boson and non-QCD backgrounds are the uncertainties on the JES, ISR, FSR, and the jet width. The shape uncertainties are evaluated by adjusting their values by $\pm 1\sigma$, and propagating this change through the event selection and Higgs-NN.

The JES affects the jet E_T related quantities, like m_{bb} and m_{qq}. However, its effect does not influence the shape of the neural network output distribution for the Higgs signal, as shown in figure 6.1. The acceptance varies by $\pm 9\%$ due to the SumEt>220.0 GeV event selection cut, and it is applied in addition to the shape uncertainty [124].

The ISR/FSR systematic uncertainties for the Higgs signal was measured modifying the parameters in the PYTHIA Monte Carlo generator [136] that control the amount of parton showering. The effect of the systematic uncertainties upon the shape of the neural network output distribution for the Higgs signal is shown in figure 6.1. This was included as a shape systematic uncertainty in the limit calculation. The VBF sample only shows shape changes from the reduction of ISR/FSR as no Monte Carlo sample was available for increased ISR/FSR. For

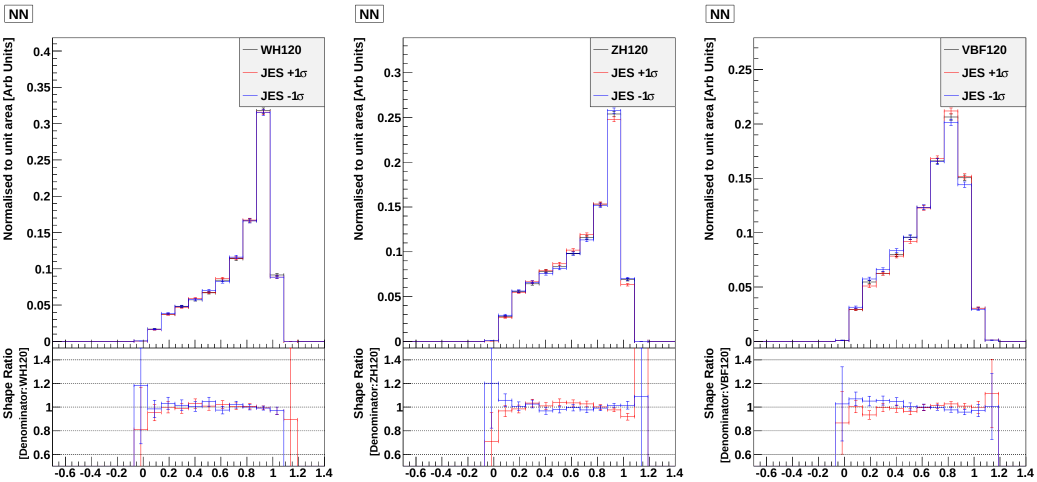

(a) JES - *WH* **(b)** JES - *ZH* **(c)** JES - VBF

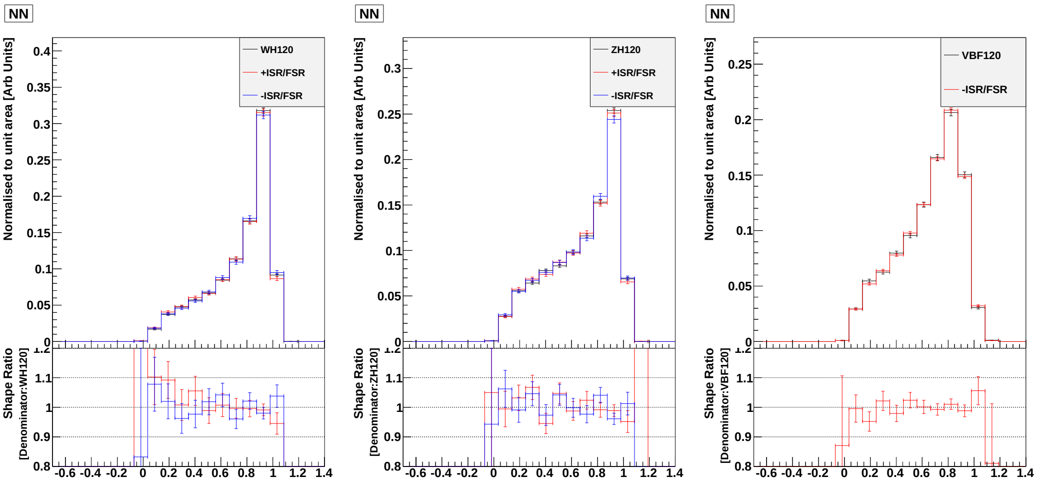

(d) ISR/FSR - *WH* **(e)** ISR/FSR - *ZH* **(f)** ISR/FSR - VBF

Figure 6.1: The Higgs-NN output distribution for the 120 GeV/c^2 Higgs boson mass hypothesis considering the $\pm 1\sigma$ variation of JES and ISR/FSR for the *WH*, *ZH* and VBF processes, respectively. The black histograms are obtained considering the nominal JES and the red(blue) histograms considering the JES shifted by +(-)1σ. The (f) VBF plot only has change in reduction of ISR/FSR as no Monte Carlo sample for increased ISR/FSR is available. The histograms are normalized to a unit area to show the variation in shape. The below plots show the ratio between shifted and nominal JES and ISR/FSR, respectively.

the limit calculation, it is assumed that the shape change for VBF is symmetric. In addition to the shape systematic uncertainties, the change in ISR/FSR affects the acceptance. There are ±3% rate systematic uncertainties for the VH and VBF Higgs signal [124].

The jet width uncertainty affects the shape of the neural network output distribution and it is evaluated in a similar fashion as the JES uncertainty. The systematic uncertainty is assigned by adding an offset to the rescaled $t\bar{t}$ Monte Carlo jet width and comparing the χ^2/d.o.f of the shifted Monte Carlo and $t\bar{t}$ data distributions with the unshifted Monte Carlo and data. The uncertainty is defined by the offset that changes the χ^2/d.o.f by ±1 unit. The calorimeter jet width uncertainty is ±2.6% and the tracker jet width uncertainty is ±5.5%. The calorimeter(tracker) jet widths are adjusted by $\pm1\sigma$ [124]. It is assumed, that the calorimeter and tracker jet width uncertainties are uncorrelated and they are evaluated separately. Figures 6.2 show the change in shape of the neural network output distribution from a $\pm1\sigma$ change of the jet width.

Only shape uncertainties are considered for the QCD multi-jet component; the normalization uncertainties were not considered as the background prediction will be floated to best fit the data. The TRF QCD shape uncertainties arise from uncertainties in the interpolation, m_{qq}, and VBF-NN correction functions. The TRF shape uncertainty is defined as the shape difference between the nominal QCD shape and a systematically shifted version.

For the nominal background prediction a TRF is measured in the TAG region (TAG-TRF) which is interpolated into the signal region. Another TRF is measured in the CONTROL region (CONTROL-TRF) and it is applied to the signal region. The systematic uncertainty for this interpolation is defined as the shape difference between the TAG- and the CONTROL-TRF (figure 6.3) [124].

In section 5.4.1 it was shown that the predicted mass, m_{qq}, is tuned using correction functions measured in the TAG region. To estimate the uncertainties due to these tuning corrections, another set of correction functions in the CONTROL region were measured. The difference in the neural network output due to the different sets of correction functions are then taken as the effect of the uncertainties from these tuning corrections (figure 6.4) [124].

In section 5.8.1 the requirement for additional tuning of the VBF-NN output was discussed. A function measured in the TAG region is used to correct the output of the VBF-NN. An alternative correction function is measured in the NJET6 region (NJET6-TRF) and is used to give an alternative background prediction. The difference between the two background shapes defines the VBF-NN correction function systematic uncertainty (figure 6.5) [124].

Table 6.1 summarizes all systematic uncertainties applied in this analysis [124].

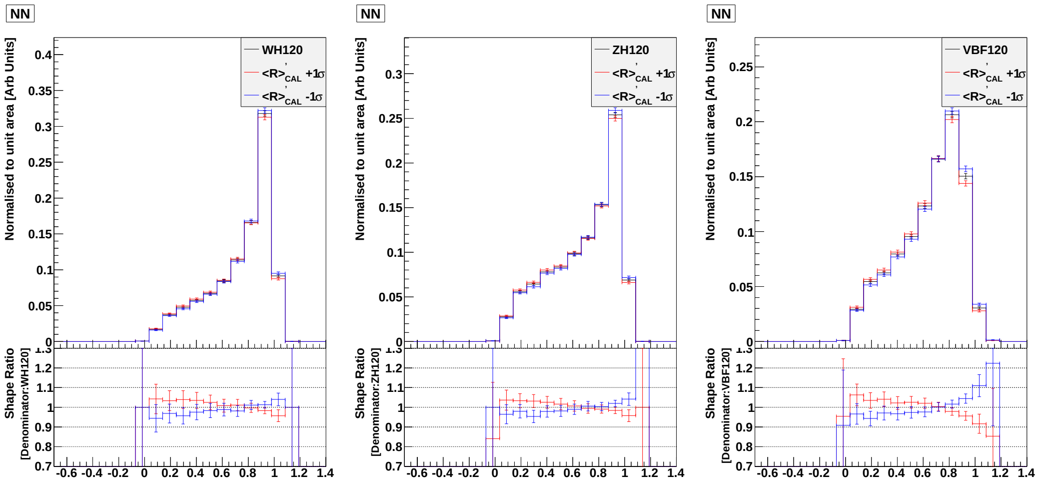

(a) $\langle R\rangle_{\mathrm{CAL}}$ - *WH* **(b)** $\langle R\rangle_{\mathrm{CAL}}$ - *ZH* **(c)** $\langle R\rangle_{\mathrm{CAL}}$ - VBF

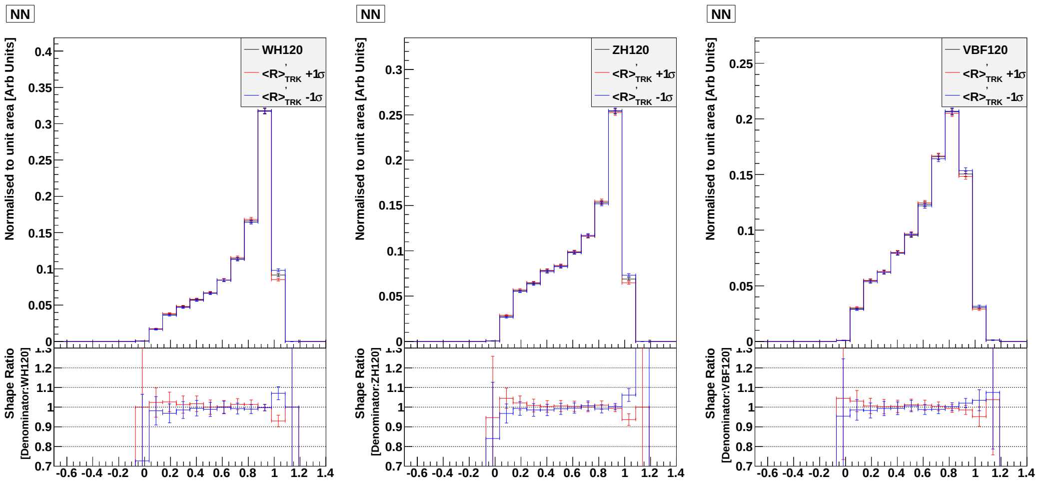

(d) $\langle R\rangle_{\mathrm{TRK}}$ - *WH* **(e)** $\langle R\rangle_{\mathrm{TRK}}$ - *ZH* **(f)** $\langle R\rangle_{\mathrm{TRK}}$ - VBF

Figure 6.2: The Higgs-NN output distribution for the 120 GeV/c^2 Higgs boson mass hypothesis considering the $\pm 1\sigma$ variation of the calorimeter and tracker jet width for the (a) *WH*, (b) *ZH* and (c) VBF processes, respectively. The black histograms are obtained considering the nominal jet width and the red(blue) histograms considering the calorimeter jet width shifted by +(-)1σ. The histograms are normalized to a unit area to show variation in shape. The below plots show the ratio between shifted and nominal jet width.

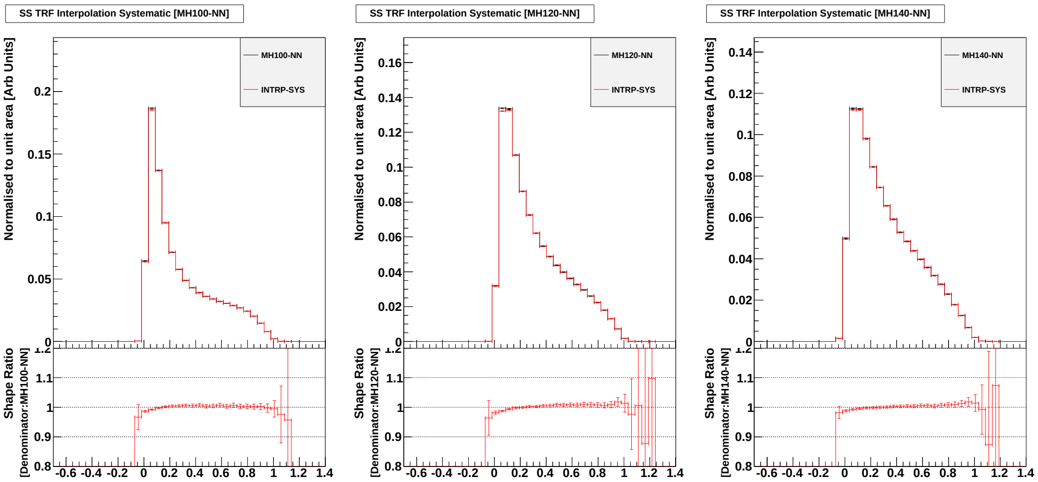

(a) SS - 100 GeV/c^2 **(b)** SS - 120 GeV/c^2 **(c)** SS - 140 GeV/c^2

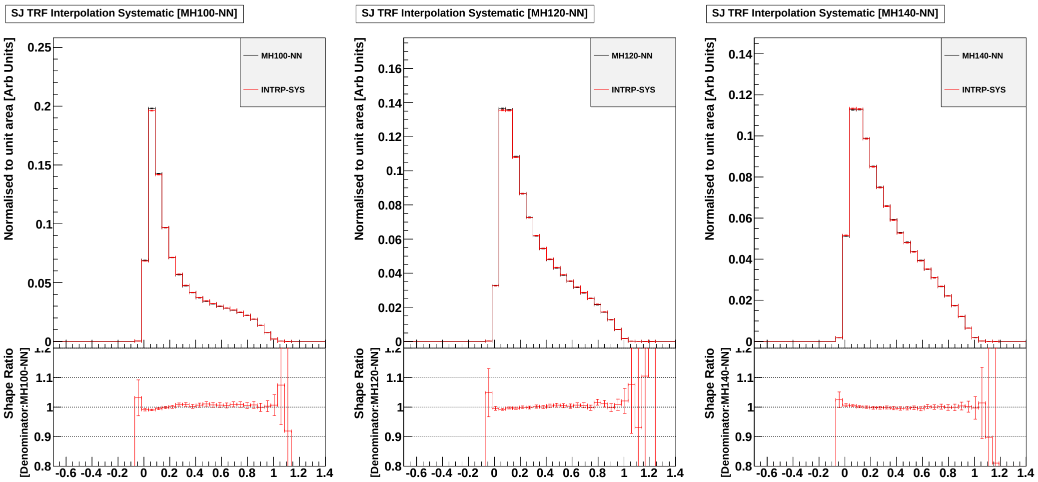

(d) SJ - 100 GeV/c^2 **(e)** SJ - 120 GeV/c^2 **(f)** SJ - 140 GeV/c^2

Figure 6.3: The variation of the Higgs-NN output distribution for the TRF interpolation uncertainty for the Higgs boson mass hypotheses: 100, 120 and 140 GeV/c^2, and for the two b-tagging categories: SS and SJ, respectively. The black histograms represent the TAG-TRFs, the red histograms represent the CONTROL-TRF. The histograms are normalized to a unit area to show variation in shape. The below plots show the ration between CONTROL-TRF and TAG-TRF.

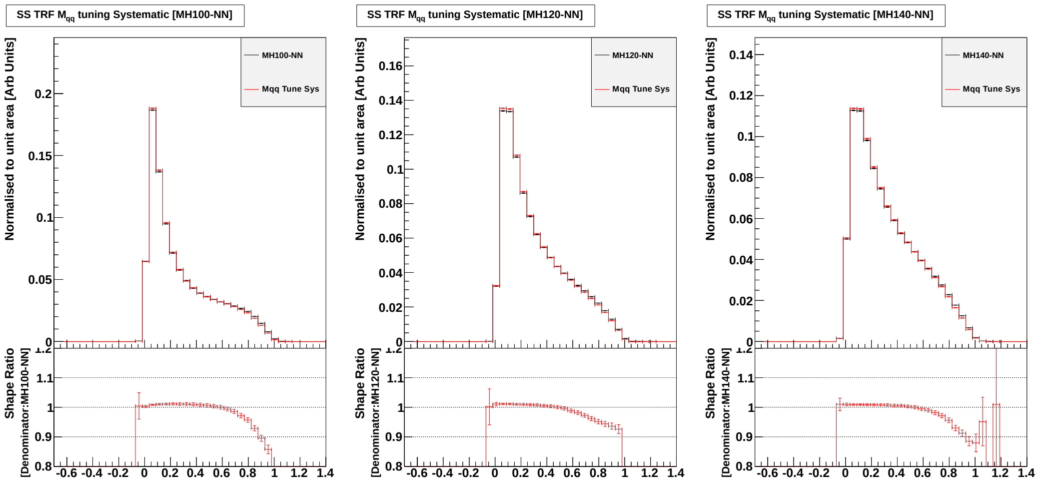

(a) SS - 100 GeV/c^2 **(b)** SS - 120 GeV/c^2 **(c)** SS - 140 GeV/c^2

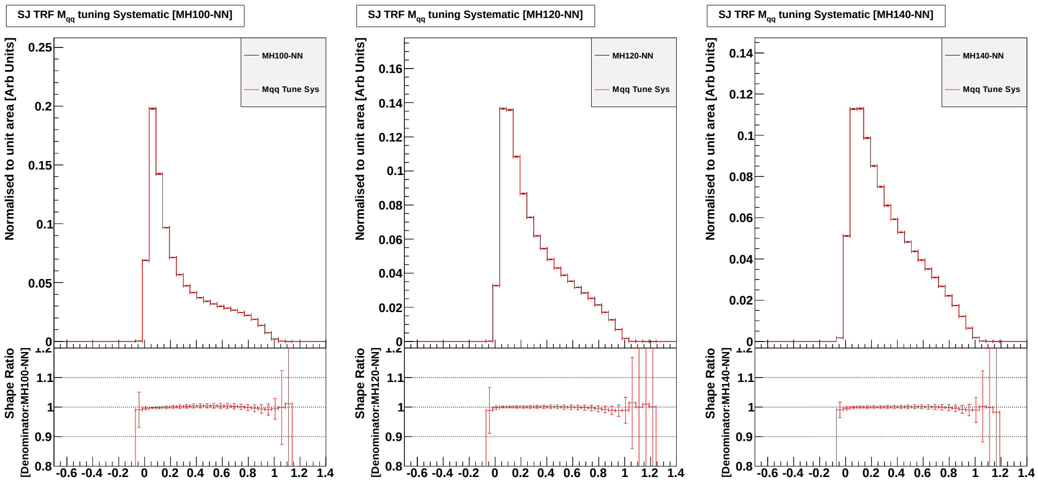

(d) SJ - 100 GeV/c^2 **(e)** SJ - 120 GeV/c^2 **(f)** SJ - 140 GeV/c^2

Figure 6.4: The variation of the Higgs-NN output distribution for the TRF m_{qq} correction uncertainty for the three Higgs boson mass hypotheses: 100, 120 and 140 GeV/c^2, and for the two b-tagging categories: SS and SJ, respectively. The black histograms represent the TAG-TRFs, the red histograms represent the CONTROL-TRF. The histograms are normalized to a unit area to show variation in shape. The below plots show the ration between CONTROL-TRF and TAG-TRF.

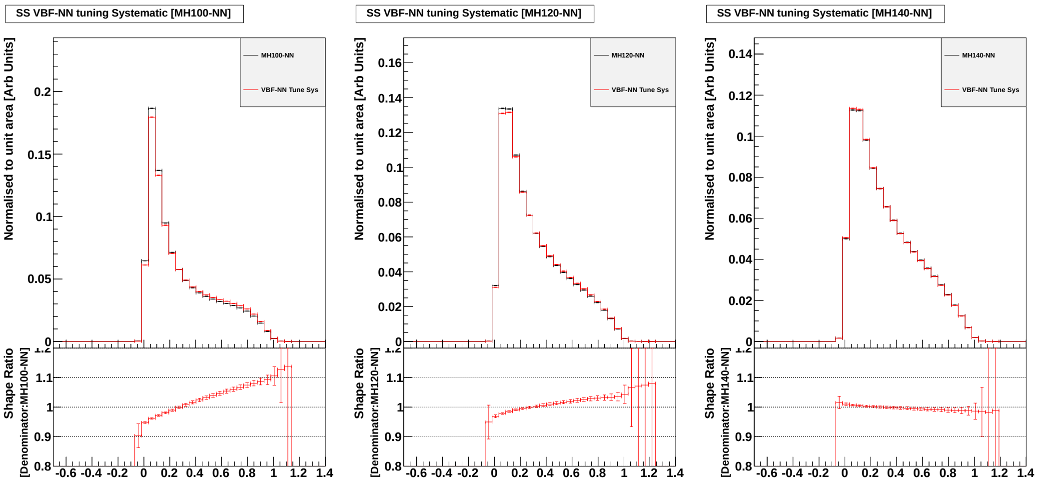

(a) SS - 100 GeV/c^2 **(b)** SS - 120 GeV/c^2 **(c)** SS - 140 GeV/c^2

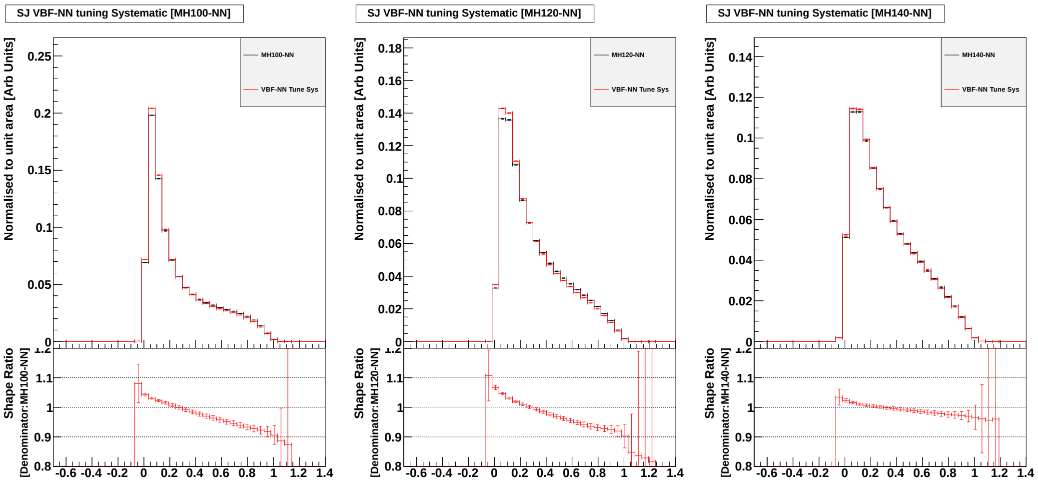

(d) SJ - 100 GeV/c^2 **(e)** SJ - 120 GeV/c^2 **(f)** SJ - 140 GeV/c^2

Figure 6.5: The variation of the Higgs-NN output distribution for the TRF VBF-NN correction uncertainty for the Higgs boson mass hypotheses: 100, 120 and 140 GeV/c^2, and for the two b-tagging categories: SS and SJ, respectively. The black histograms represent the TAG-TRFs, the red histograms represent the NJET6-TRF. The histograms are normalized to a unit area to show variation in shape. The below plots show the ratio between NJET6-TRF and TAG-TRF.

TRF (QCD multi-jet) Uncertainties	
TRF Interpolation	Shape
TRF m_{qq} Correction	Shape
TRF VBF-NN Correction	Shape
Signal and Background Uncertainties	
Luminosity	± 6% Rate
Trigger	± 3.55% Rate
SecVtx+SecVtx	± 7.1% Rate
SecVtx+JetProb	± 6.4% Rate
JES	± 9% Rate Shape
Jet Width	Shape
Cross Section Uncertainties	
$t\bar{t}$ and Single-top	± 7% Rate
Diboson (WW/WZ/ZZ)	± 6% Rate
W+HF and Z+jets	± 50% Rate
WH/ZH	± 5% Rate
VBF	± 10% Rate
Signal Uncertainties	
PDF	± 2% Rate
ISR/FSR	± 3% Rate Shape

Table 6.1: Summary of all systematic uncertainties.

Chapter 7

Results and Conclusions

Comparing the Higgs-NN output distribution with the background prediction distribution, there is no evidence of a Higgs boson signal, nor any disagreement between the predicted background and the observed data. A measure of the sensitivity of the data for Standard Model $H \to b\bar{b}$ observation is reported by setting an upper limit, using a Bayesian approach, on the number of signal events that may be present, given the experimental results.

In this chapter is described briefly the method for the limit calculation and the results obtained.

7.1 Statistical Overview

The Poisson probability of n events occurring for an expectation value μ is given by [137]:

$$p(n|\mu) = \frac{\mu^n e^{-\mu}}{n!}. \tag{7.1}$$

The Bayesian approach, used for the limit calculation, is based on the Bayes' theorem:

$$p(\mu|n) = \frac{p(n|\mu)p(\mu)}{p(n)}, \tag{7.2}$$

where $p(\mu)$ is the prior probability, i.e. the assumed probability distribution of μ before the experiment, $p(\mu|n)$ is the posterior probability distribution and $p(n)$ is the marginal probability. The limit value is based on the calculation of the posterior probability distribution.

Defining the number of signal events S and the total number of background events B, the expectation value, μ, is the sum of these two quantities, $\mu = S+B$. To forbid a negative number of expected signal events, the prior probability distribution can be written as:

$$p(\mu) = \begin{cases} 0 \quad \text{when} \quad \mu < B \\ k \quad \text{when} \quad \mu \geq B, \end{cases} \tag{7.3}$$

where k is a constant. In this hypothesis, the equation (7.2) can be rewritten as:

$$p(\mu|n) = \begin{cases} 0 \quad \text{when} \quad \mu < B \\ c_n p(n|\mu) \quad \text{when} \quad \mu \geq B, \end{cases} \tag{7.4}$$

where $p(n|\mu)$ is given by (7.1) and $c_n = k/p(n)$ is a constant for a given value of n and can be determined with normalization condition:

$$\int p(\mu|n) d\mu = 1. \tag{7.5}$$

The number of the signal events S can be written as the product of the number of calculated signal events s predicted by the Standard Model theory and a scaling factor f. The 95% credibility level is calculated using the scale factor f in order to get the limit on the multiplicative factor of the Standard Model prediction. The advantage to use f rather than S is that in case one observes a limit for f under one, the existence of the Standard Model Higgs boson can be excluded with a credibility level of 95%.

The limit integral can be written as:

$$\begin{aligned} 0.95 &= \int_0^{f_{95}} p(B + f \cdot s|D) df \\ &= \int_0^{f_{95}} c_D p(D|B + f \cdot s) df \\ &= \int_0^{f_{95}} c_D \frac{(B + f \cdot s)^D e^{-(B+f\cdot s)}}{D!} df, \end{aligned} \tag{7.6}$$

where D is the number of observed data events and it coincides with the number of observed events (n).

The measurement and the background uncertainties have to be included into the limit calculation, completing equation (7.6). It is assumed that the systematic uncertainties follow a Gaussian distribution, given a nominal value $\hat{r}$ and an uncertainty σ_r:

$$p^g(r;\hat{r},\sigma_r) = \frac{1}{\sqrt{2\pi\sigma_r^2}} e^{-\frac{(r-\hat{r})^2}{2\sigma_r^2}}. \tag{7.7}$$

In order to incorporate a Gaussian uncertainty, σ, into the limit calculation, a nuisance parameter, k, is introduced with Gaussian probability $p^g(k;1,\sigma)$. The background B can be considered to be composed by several backgrounds, $B = \sum b_i$, each one with an own uncertainty, σ_i. The expected number of events can be written in terms of k_i as:

$$\mu(f,k_i) = B(k_i) + f \cdot s = \sum_i (k_i \cdot b_i) + f \cdot s. \tag{7.8}$$

The presence of uncertainties applied to the multiple background and those ones only applied to the signal have to be taken into account by introducing nuisance parameters for all uncertainties. For this reason the equation (7.8) can be written:

$$\mu(f,k_{ij}) = \sum_{i\geq 1} \left(\left(\prod_{j\in\Delta_j} k_{ij} \right) \cdot b_i \right) + \left(\prod_{j\in\Delta_0} k_{0j} \right) \cdot f \cdot s, \tag{7.9}$$

where Δ_0 and Δ_j are the sets of indices of the nuisance parameters that apply to the signal and background, respectively.
The probability distribution is obtained by convolving the probability with a Gaussian distribution for each nuisance parameter as:

$$P(D|\mu(f,k_{ij})) = p(D|\mu(f,k_{ij})) \prod_j p_j^g(k_{ij};1,\sigma_j), \tag{7.10}$$

where $p(D|\mu(f,k_{ij}))$ is obtained by substituting equation (7.9) into equation (7.4). The credibility level integral is obtained integrating equation (7.6) over all the nuisance parameters, k_j:

$$0.95 = \int_0^{x_{95}} \left[\int P(D|\mu(f,k_{ij})) dk_1 \cdots dk_j \right] df. \tag{7.11}$$

In order to consider more the one-bin counting experiment, the equation (7.11) has to be convolved over several bins. If the probability of one bin is given by P_m, from equation (7.11), the final form of the limit integral is:

$$0.95 = \int_0^{x_{95}} \left[\int \prod_m P_m(D|\mu(f, k_{ij}))dk_1 \cdots dk_j \right] df. \tag{7.12}$$

7.2 Limit Calculation

The observed limit, the real result of the analysis, is calculated with equation (7.12) using the real data. Figure 7.1a shows the distribution of the observed limit for a Higgs boson mass hypothesis of 125 GeV/c^2. The observed limit at 95% credibility level is 9.0, indicated by the red line [124].
The results obtained from the data are compared with the results expected if the limit were obtained using background predictions only, i.e. in absence of real signal. The real data are replaced with *pseudo-data*. They are obtained by fluctuating the background within their uncertainties. The process of replacing the data with pseudo-data and calculating a corresponding limit is called a *pseudo-experiment*. The pseudo-experiments are repeated a sufficient number of times, on the order of 10^3, to have an estimate where the observed limit could be found in the absence of a real signal. The expected limit is the median of these trials. The 1σ and 2σ regions are calculated considering where the 68% and 95% of the pseudo-experiment lie around the median, respectively.
Figure 7.1b shows the distribution of expected limits from 5000 pseudo-experiments for a Higgs boson mass of 125 GeV/c^2 for the combination of the two b-tagging categories and the three production processes. The median and the $\pm 1\sigma$ and $\pm 2\sigma$ regions are shown.

The observed and expected distribution for the other Higgs boson mass hypotheses for the two b-tagging categories and for their combination are shown in appendix C.

The code used, `mclimit_cms` [138], was developed by the CDF collaboration and is part of the CDF official code.

7.3 Limits Results

Upper exclusion limits are calculated for the Higgs boson cross section using a Bayesian method to set a 95% credibility level upper limit on the $H \to b\bar{b}$ cross section. The limits are calculated for the Higgs boson mass hypotheses between 100 and 150 GeV/c^2, in 5 GeV/c^2 steps. Integration over Gaussian priors for the systematic uncertainties is performed, truncated to ensure that no prediction is negative. Correlated rate and shape uncertainties as well as uncorrelated

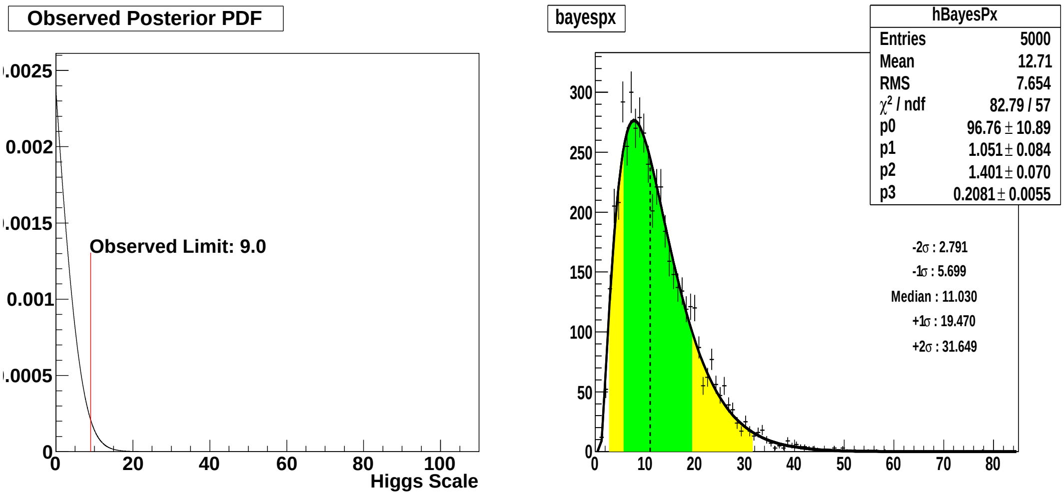

(a) **(b)**

Figure 7.1: The (a) observed posterior density and the (b) pseudo-experiment distribution for the 125 GeV/c^2 Higgs mass boson hypothesis for the combination of the two b-tagging categories.

bin-by-bin statistical uncertainties [139] are included in the analysis. The observed limits obtained from the data are compared with the limits expected if the data matched the background prediction, i.e. in absence of real signal.

Figures 7.2-7.4 and tables 7.1-7.3 show the limits from SS, SJ b-tagging categories and for their combination, respectively [124]. The observed limits agree with the expected limits inside the 1σ region.

Higgs mass (GeV/c^2)	-2σ	-1σ	Median	$+1\sigma$	$+2\sigma$	Observed
100	3.6	6.7	10.9	16.6	23.7	15.9
105	4.3	6.7	10.1	14.9	21.2	8.2
110	4.6	6.7	9.8	14.2	20.1	8.3
115	4.8	7.3	10.8	15.5	21.7	8.9
120	5.3	7.8	11.6	16.8	23.6	10.2
125	6.4	9.5	14.0	20.4	29.0	11.6
130	8.2	12.2	18.3	26.8	38.1	14.6
135	12.4	18.4	27.3	39.5	55.6	25.6
140	17.0	24.8	36.5	52.7	74.1	34.8
145	23.9	35.1	51.6	74.1	103.9	50.9
150	39.6	57.7	84.3	121.0	167.6	84.1

Table 7.1: Expected and observed 95% credibility level upper limits for the SS channel using 9.45 $\mathrm{fb}^{-1}$of $p\bar{p}$ data collected by the CDF detector. The limits are relative to the expected Higgs cross section.

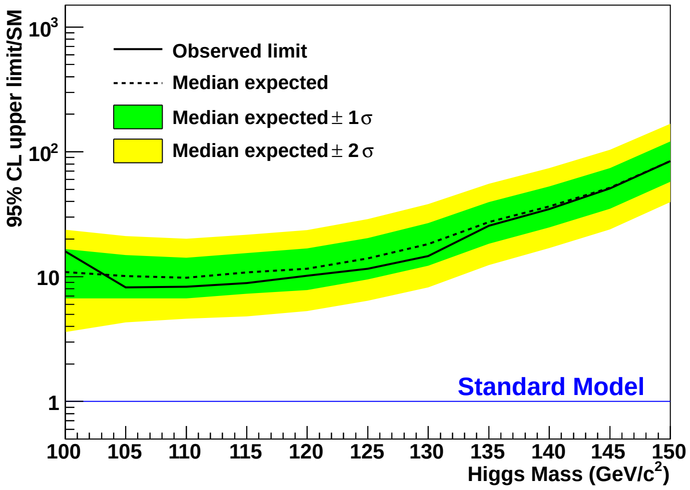

Figure 7.2: Upper limits at 95% credibility level for SS channel: the expected and observed limits are plotted as a function of the Higgs boson. The limits are relative to the expected Standard Model Higgs boson production, which includes the $H \to b\bar{b}$ branching ratio.

Higgs mass (GeV/c^2)	-2σ	-1σ	Median	$+1\sigma$	$+2\sigma$	Observed
100	7.8	10.9	15.5	22.0	30.6	12.2
105	8.7	12.2	17.3	24.5	34.2	15.0
110	8.4	11.7	16.7	23.5	32.5	13.8
115	9.3	12.7	17.9	25.2	35.1	14.7
120	10.3	14.3	20.3	28.9	40.3	15.4
125	12.7	17.6	25.1	35.5	49.3	19.4
130	16.2	22.4	32.2	46.1	65.1	24.7
135	18.6	25.6	36.2	50.8	70.2	26.1
140	24.1	32.9	46.3	65.3	90.7	33.9
145	34.8	47.6	67.0	95.2	130.6	48.0
150	56.0	76.1	104.8	142.9	185.6	78.2

Table 7.2: Expected and observed 95% credibility level upper limits for the SJ channel using 9.45 fb^{-1}of $p\bar{p}$ data collected by the CDF detector. The limits are relative to the expected Higgs cross section.

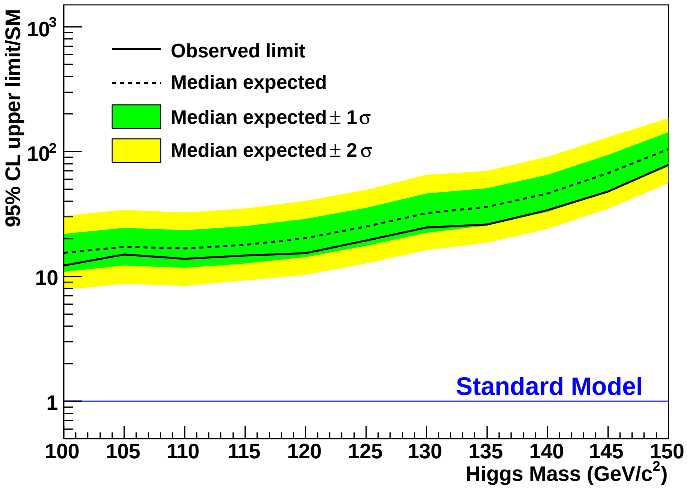

Figure 7.3: Upper limits at 95% credibility level for SJ channel: the expected and observed limits are plotted as a function of the Higgs boson. The limits are relative to the expected Standard Model Higgs boson production, which includes the $H \to b\bar{b}$ branching ratio.

Higgs mass (GeV/c^2)	-2σ	-1σ	Median	$+1\sigma$	$+2\sigma$	Observed
100	1.4	3.6	7.7	14.5	24.4	10.9
105	1.8	3.8	7.5	13.6	22.3	7.5
110	2.0	4.0	7.6	13.2	21.7	7.0
115	2.3	4.4	8.3	14.5	23.4	7.2
120	2.4	4.6	8.9	15.6	25.3	8.4
125	2.8	5.7	11.0	19.5	31.6	9.0
130	3.4	7.1	13.8	24.3	39.5	13.2
135	5.3	10.8	19.5	32.2	49.6	21.2
140	7.3	14.3	25.8	42.7	66.1	26.2
145	10.2	20.4	36.7	60.5	93.4	35.1
150	17.1	32.5	58.7	98.2	152.0	64.6

Table 7.3: Expected and observed 95% credibility level upper limits for the combined SS and SJ channels. The limits are relative to the expected Higgs cross section.

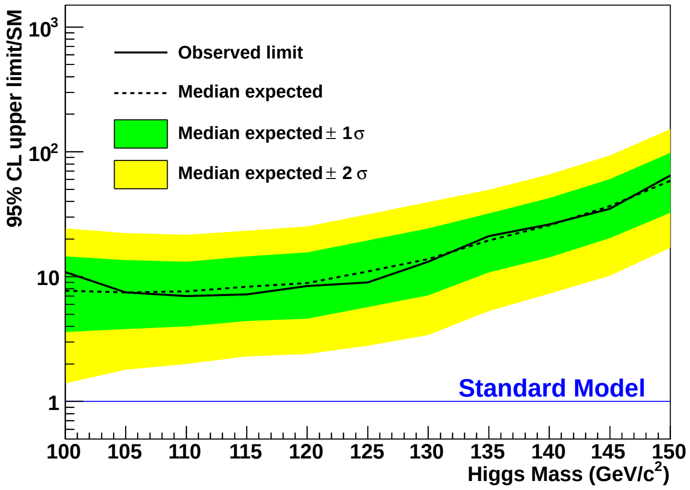

Figure 7.4: Upper limits at 95% credibility level for combined SS and SJ channels: the expected and observed limits are plotted as a function of the Higgs boson mass. The limits are relative to the expected Standard Model Higgs boson production, which includes the $H \to b\bar{b}$ branching ratio.

7.4 Conclusions

Besides the article connected to this analysis [124], other two papers were published on searches for Higgs boson in all-hadronic channel at CDF using data set of 2 fb^{-1} [140] and 4 fb^{-1} [134].
The results discussed in this thesis have halved the expected limit of the 4 fb^{-1} search [134]. Half of the improvement comes from additional data and the expanded signal region contributes an additional 17%. In the previous search [134], exclusive VH and VBF networks were used to search for Higgs bosons in non-overlapping signal regions. The two-stage neural network increases the search sensitivity by 15%.
The use of a single signal region increases the number of potential Higgs boson signal events by 20%. Both gains are above those expected from the inclusion of additional data alone.
Another 24% is achieved by the reduction of the b-jet energy resolution, adding a new jet width measurement, improving the QCD multi-jet modeling, adding more variables in the Higgs neural network and improving its training [124].
In the hypothesis to use only the m_{bb} distribution for the search, the application of multivariate techniques produced an improvement of the signal-to-background ratio from 0.0007 to 0.006, which is almost a ten-fold increase.
No significant Higgs boson signal is observed and upper exclusion limits are set on the observed Higgs cross section relative to the Standard Model rate as a function of Higgs boson mass in the range 100-150 GeV/c^2. For a 125 GeV/c^2 Higgs boson, the 95% credibility level expected (observed) limit is 11.0 (9.0) times the expected Standard Model rate [124].
This search is CDF's fourth most sensitive $H \to b\bar{b}$ search. The other searches $ZH \to l^+l^-b\bar{b}$, $WH \to l\nu b\bar{b}$, and $VH \to \not{E}_T b\bar{b}$ have an expected (observed) limit of 3.9 (7.1), 2.8 (4.9), and 3.33 (3.06) for a 125 GeV/c^2 Higgs boson, respectively. These results are connected to the leptonic decay of the weak vector bosons and the presence of smaller background compared to this search. And it is more sensitive than CDF's $t\bar{t}H$ [141] and similar to CDF's $H \to \gamma\gamma$ [142] searches, which have an expected (observed) limit of 12.6 (20.5) and 9.9 (17.0) for a 125 GeV/c^2 Higgs boson, respectively.

The CDF collaboration has developed an improved algorithm to identify b-jets [143], which improves the b-tagging rate from 39% to 54% and was used in the $ZH \to \ell\ell b\bar{b}$ [144] and $WH \to \ell\nu b\bar{b}$ [145] searches. The addition of new b-jet tagger could potentially improve this search's expected limit by an additional 40% which would lower the expected limit to 7.9 times the expected Standard Model rate for a 125 GeV/c^2 Higgs boson.

At the LHC, the Higgs decays to pairs of gauge bosons is the most sensitive channel in the mass range $120 < m_H < 200$ GeV/c^2. At the Tevatron, the searches based on Higgs boson decay to bottom-antibottom quark pairs complete the picture in smaller Higgs masses. The all-hadronic search is a unique channel at the Tevatron that has not been explored at the LHC.

After this analysis was completed, the ATLAS and CMS collaborations have reported the observation of a Higgs-like particle at a mass of $\sim 125\,\text{GeV}/c^2$ [46, 47], and the Tevatron has reported evidence for a particle decaying to $b\bar{b}$ produced in association with a W/Z boson for masses within the range 120 - 135 GeV/c^2 [48].

Figure 7.5 shows the ratios of the 95% credibility level expected and observed limit to the Standard Model cross section for the combined CDF Higgs analyses [146], included this analysis.

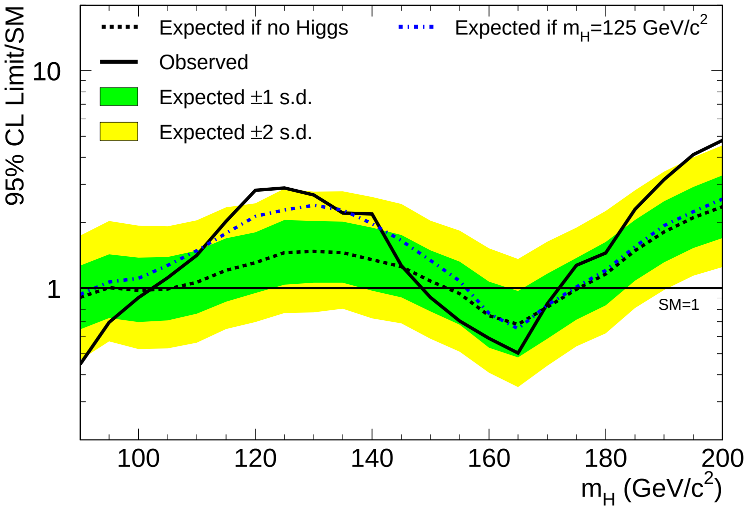

Figure 7.5: Observed and expected 95% credibility level upper limits on the ratios to the Standard Model cross section at CDF [146].

Appendix A

VBF-NN Output Correction

In this appendix, the VBF-NN output correction for each mass training and b-tagging category are provided. The plots relative to the SS b-tagging category are show in section A.1 and for the SJ b-tagging category in section A.2.

In the plots A.1, A.3, A.5, A.7, and A.9 the red histograms represent the QCD multi-jet background, the black histograms are the data. The plots below show the ratio between data and background prediction, the lines represent the fit of the ratio plots: the red line is the fit derived in the NJET6 region, the blue line is the fit derived in the TAG region and the black line is the fit derived in the CONTROL region.

In the plots A.2, A.4, A.6, A.8, and A.10 the red histograms are the TRF derived prediction for the QCD multi-jet background after applying the correction function evaluated in the NJET6 region. The blue histograms are the TRF derived prediction for the QCD multi-jet background after applying the correction function evaluated in TAG region. The black histograms are the data. The plots below show the ratio between data and TRF, the lines represent the fit of the ratio plots.

A.1 SS b-tagging category

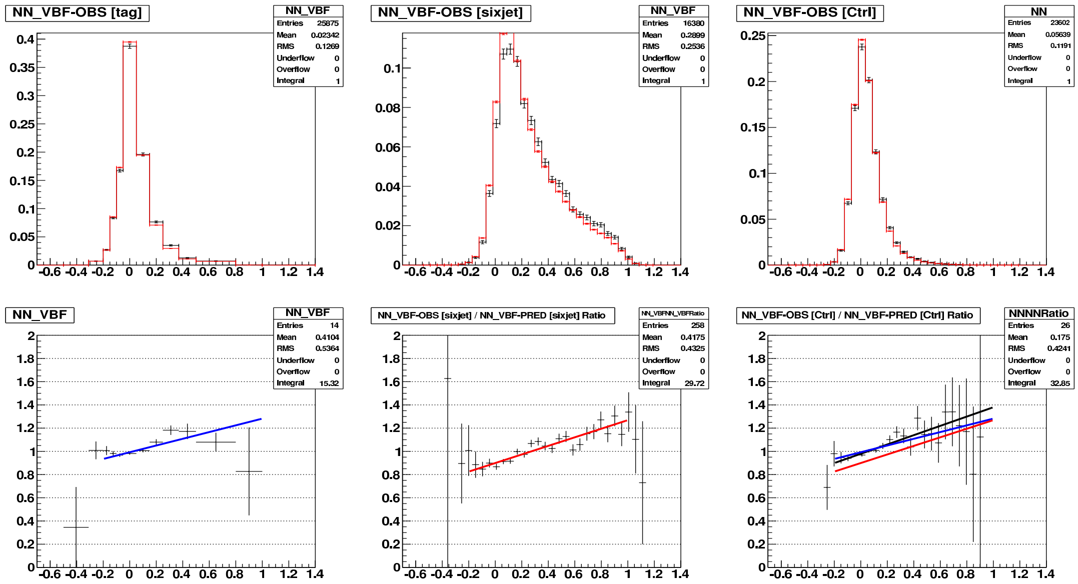

(a) **(b)** **(c)**

Figure A.1: The VBF-NN output distribution for the 120 GeV/c^2 Higgs boson mass hypothesis in SS b-tagging category in (a) TAG, (b) NJET6 and (c) CONTROL region. The plot (c) shows the overlap of the fit correction in the CONTROL region.

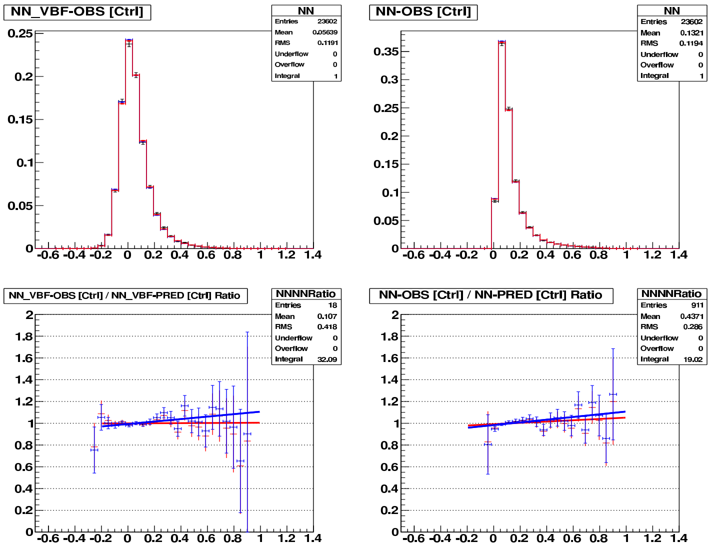

(a) **(b)**

Figure A.2: The (a) VBF-NN and (b) Higgs-NN output distribution for the 120 GeV/c^2 Higgs boson mass hypothesis in SS b-tagging category in CONTROL region after applying the correction function.

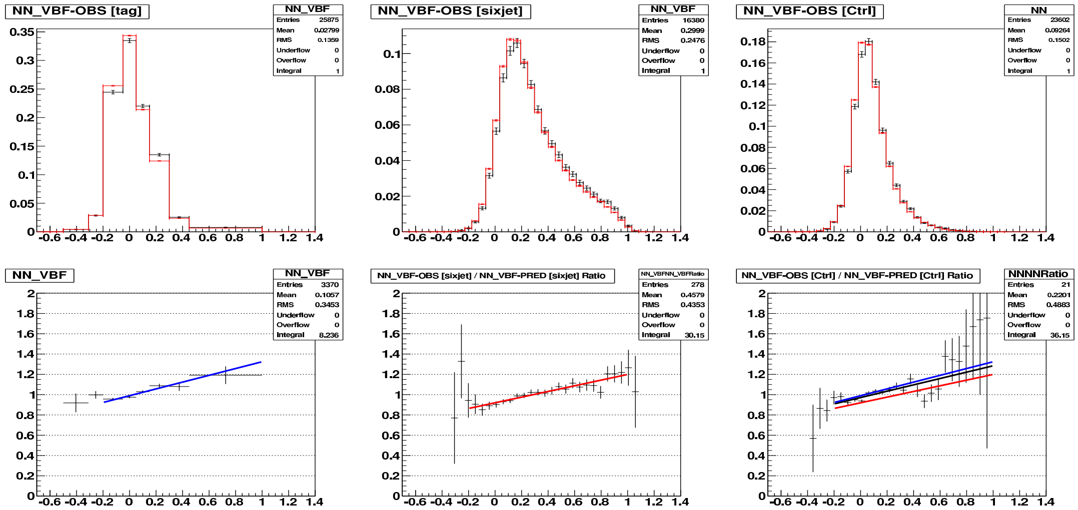

(a) **(b)** **(c)**

Figure A.3: The VBF-NN output distribution for the 140 GeV/c^2 Higgs boson mass hypothesis in SS b-tagging category in (a) TAG, (b) NJET6 and (c) CONTROL region. The plot (c) shows the overlap of the fit correction in the CONTROL region.

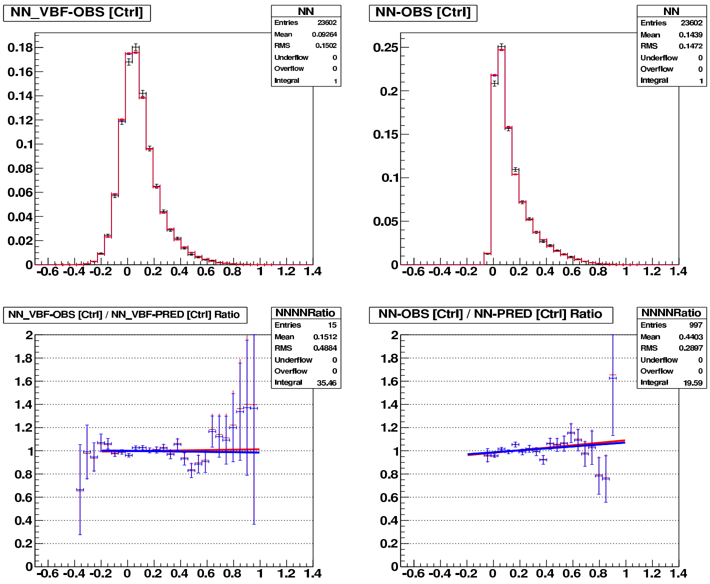

(a) **(b)**

Figure A.4: The (a) VBF-NN and (b) Higgs-NN output distribution for the 140 GeV/c^2 Higgs boson mass hypothesis in SS b-tagging category in CONTROL region after applying the correction function.

A.2 SJ *b*-tagging category

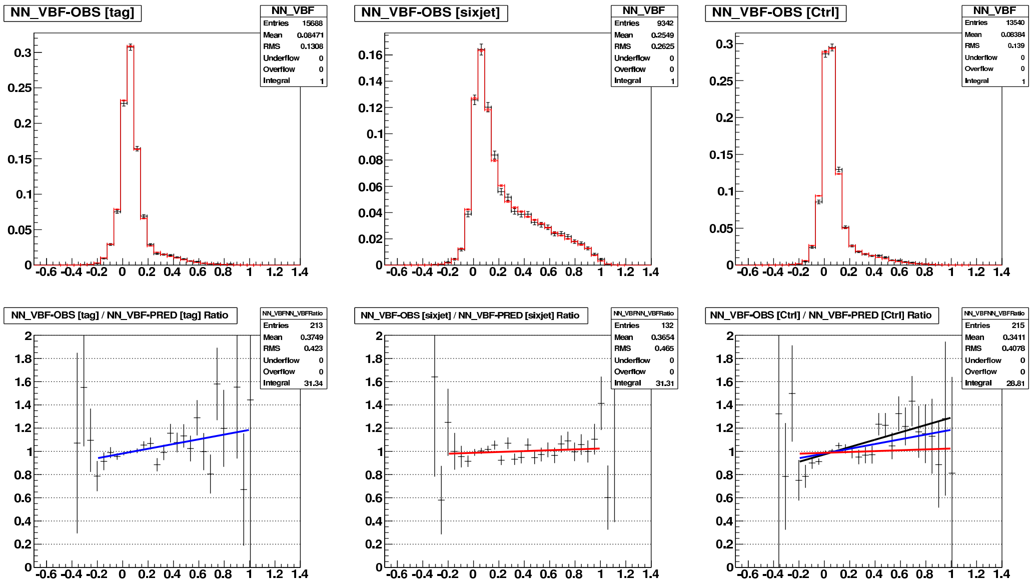

(a) **(b)** **(c)**

Figure A.5: The VBF-NN output distribution for the 100 GeV/c^2 Higgs boson mass hypothesis in SJ b-tagging category in (a) TAG, (b) NJET6 and (c) CONTROL region. The plot (c) shows the overlap of the fit correction in the CONTROL region.

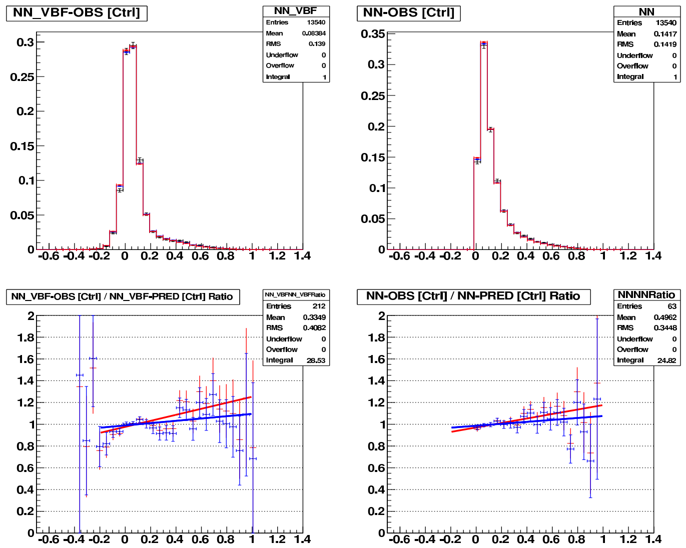

(a) **(b)**

Figure A.6: The (a) VBF-NN and (b) Higgs-NN output distribution for the 100 GeV/c^2 Higgs boson mass hypothesis in SJ b-tagging category in CONTROL region after applying the correction function.

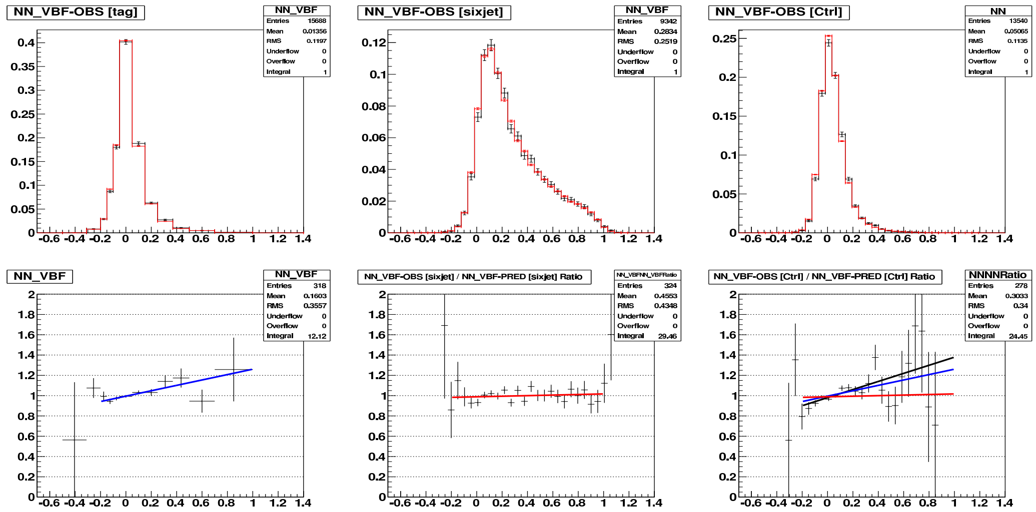

(a) **(b)** **(c)**

Figure A.7: The VBF-NN output distribution for the 120 GeV/c^2 Higgs boson mass hypothesis in SJ b-tagging category in (a) TAG, (b) NJET6 and (c) CONTROL region. The plot (c) shows the overlap of the fit correction in the CONTROL region.

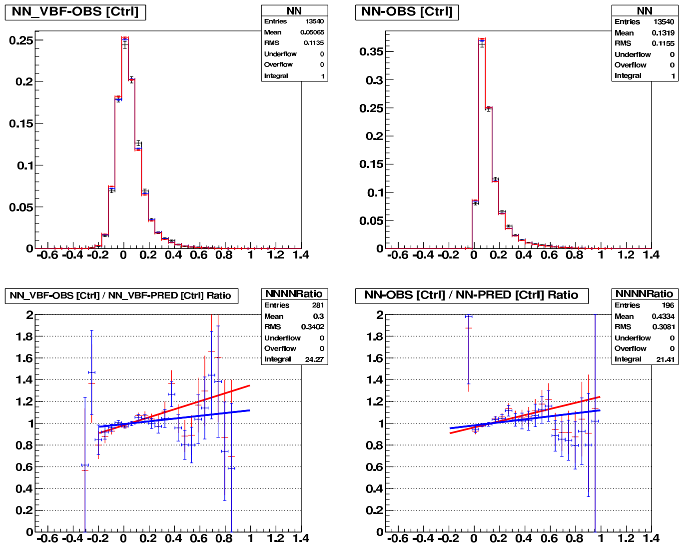

(a) **(b)**

Figure A.8: The (a) VBF-NN and (b) Higgs-NN output distribution for the 120 GeV/c^2 Higgs boson mass hypothesis in SJ b-tagging category in CONTROL region after applying the correction function.

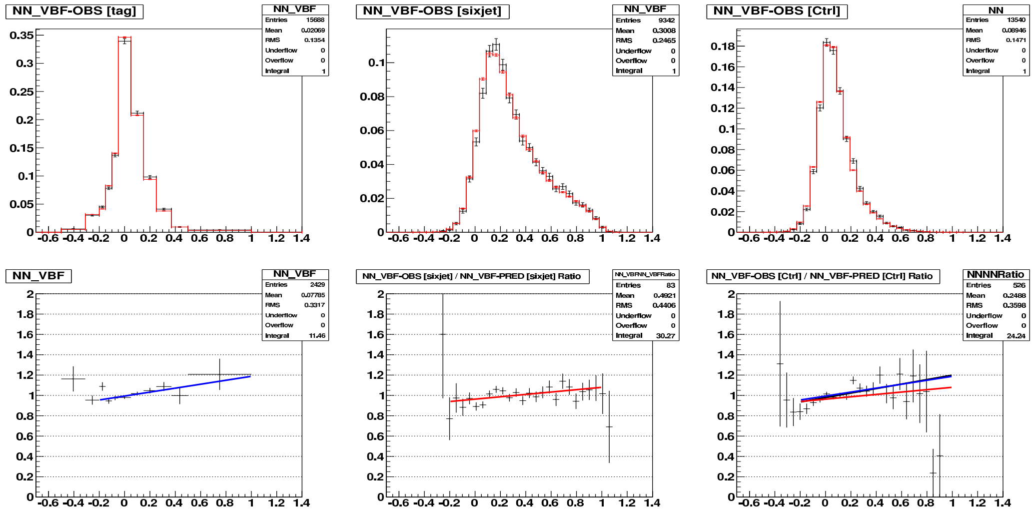

(a) **(b)** **(c)**

Figure A.9: The VBF-NN output distribution for the 140 GeV/c^2 Higgs boson mass hypothesis in SJ b-tagging category in (a) TAG, (b) NJET6 and (c) CONTROL region. The plot (c) shows the overlap of the fit correction in the CONTROL region.

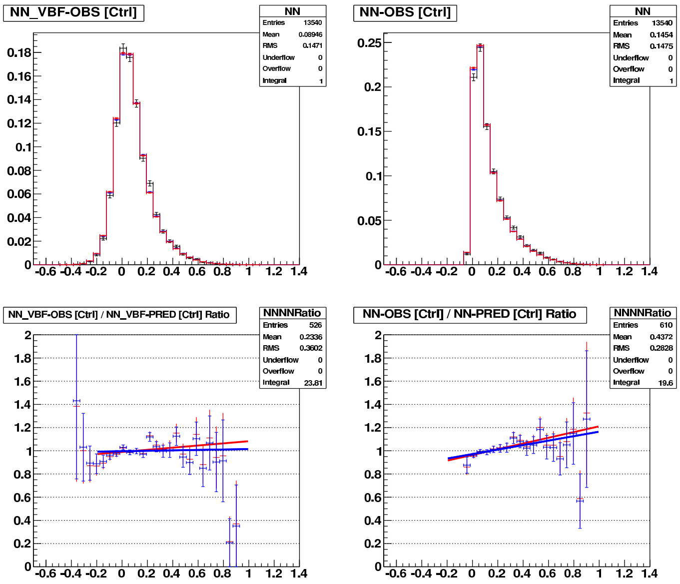

(a) **(b)**

Figure A.10: The (a) VBF-NN and (b) Higgs-NN output distribution for the 140 GeV/c^2 Higgs boson mass hypothesis in SJ b-tagging category in CONTROL region after applying the correction function.

Appendix B

Neural Network Output Distributions

In this appendix, the the WH-NN, ZH-NN, VBF-NN and Higgs-NN distribution for each Higgs boson mass hypothesis and b-tagging category are provided. The plots relative to the SS b-tagging category are show in The plots relative to the SS b-tagging category are show in section B.1 and for the SJ b-tagging category in section B.2

The VBF-NN correction function is applied to VBF-NN and Higgs-NN QCD multi-jet background prediction. All backgrounds are stacked and the superimposed Higgs boson signal is scaled by 1000. As the QCD multi-jet background is large, plots of the difference of data and QCD multi-jet are plotted with a stacked plot of non-QCD background and QCD multi-jet systematic uncertainty. Both plots show that the data are consistent with the background, especially at large Higgs-NN score where the Higgs signal peaks.

B.1 SS *b*-tagging category

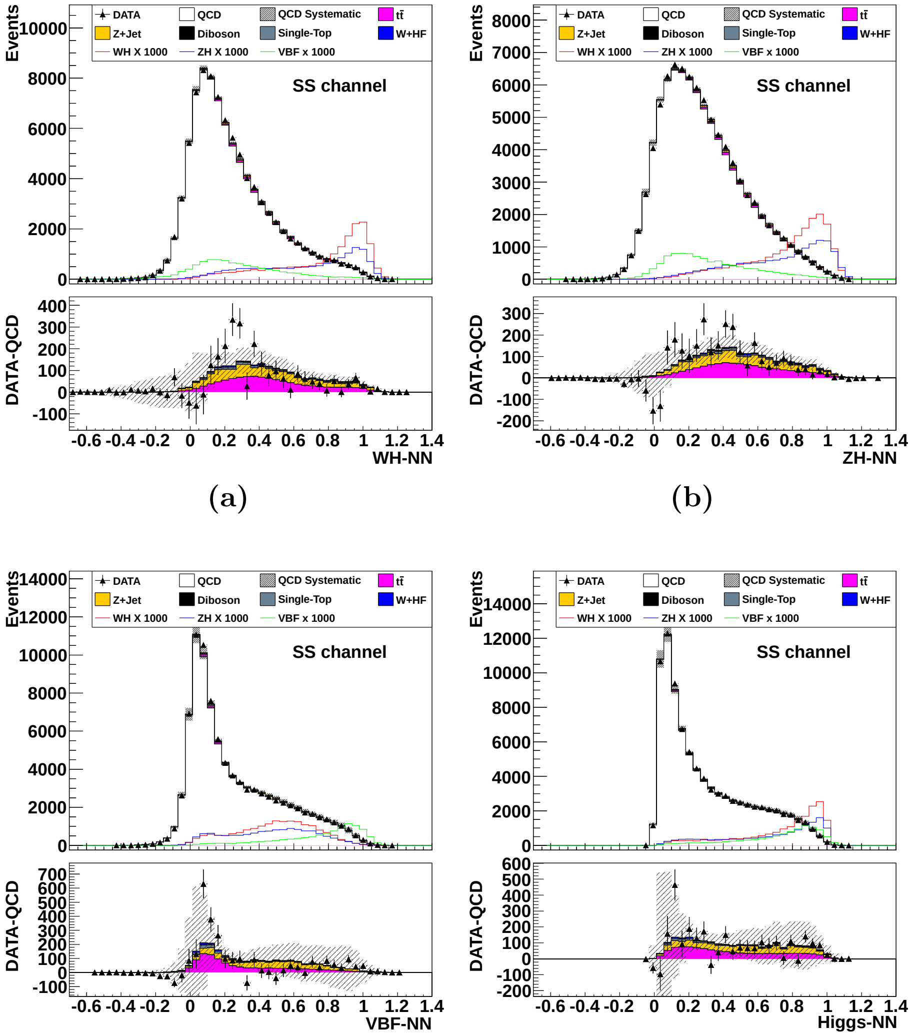

(a) (b)

(c) (d)

Figure B.1: The (a) *WH*-NN, (b) *ZH*-NN, (c) VBF-NN and (d) Higgs-NN distribution of 100 GeV/c^2 Higgs boson events in SS *b*-tagging category.

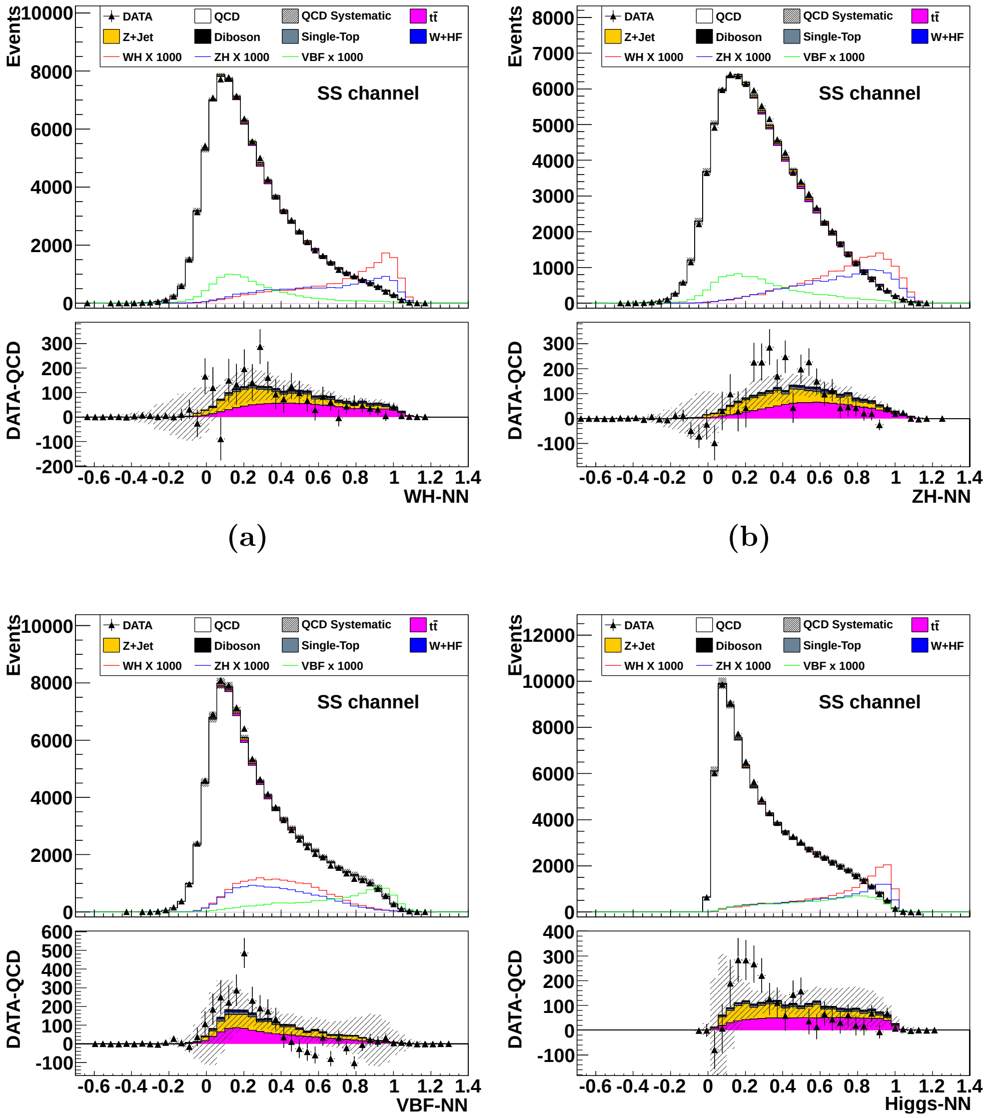

(a) (b)

(c) (d)

Figure B.2: The (a) *WH*-NN, (b) *ZH*-NN, (c) VBF-NN and (d) Higgs-NN distribution of 105 GeV/c^2 Higgs boson events in SS b-tagging category.

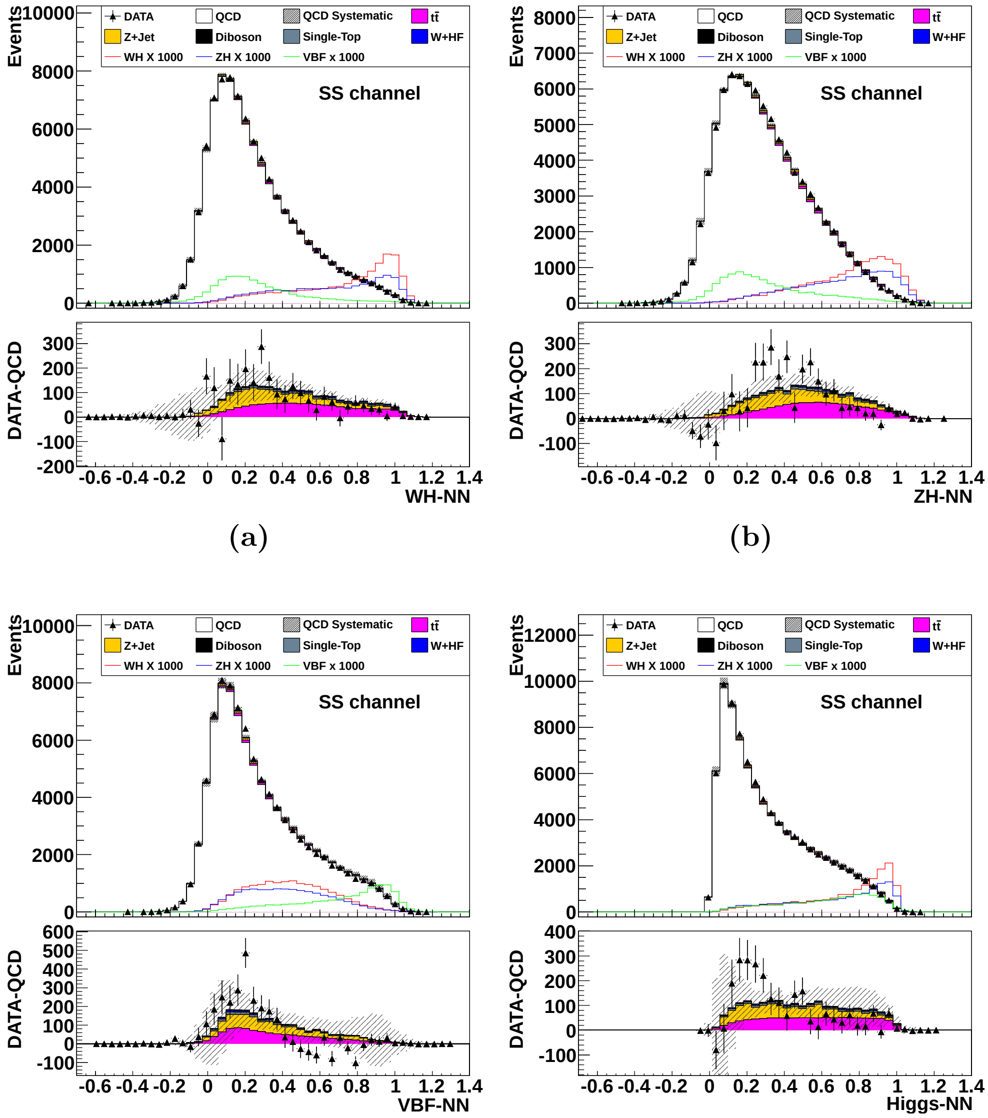

(a) **(b)** **(c)** **(d)**

Figure B.3: The (a) *WH*-NN, (b) *ZH*-NN, (c) VBF-NN and (d) Higgs-NN distribution of 110 GeV/c^2 Higgs boson events in SS b-tagging category.

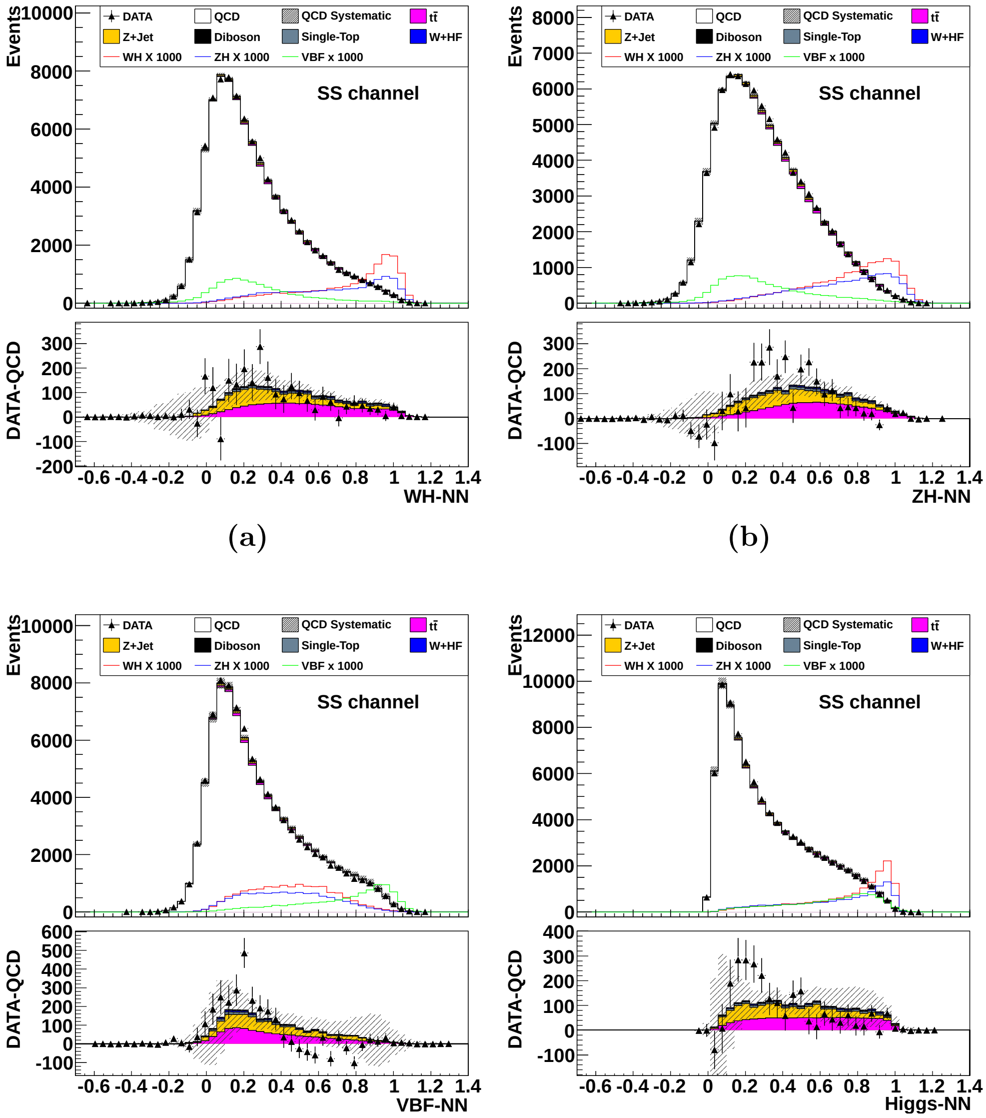

(a) (b) (c) (d)

Figure B.4: The (a) *WH*-NN, (b) *ZH*-NN, (c) VBF-NN and (d) Higgs-NN distribution of 115 GeV/c^2 Higgs boson events in SS *b*-tagging category.

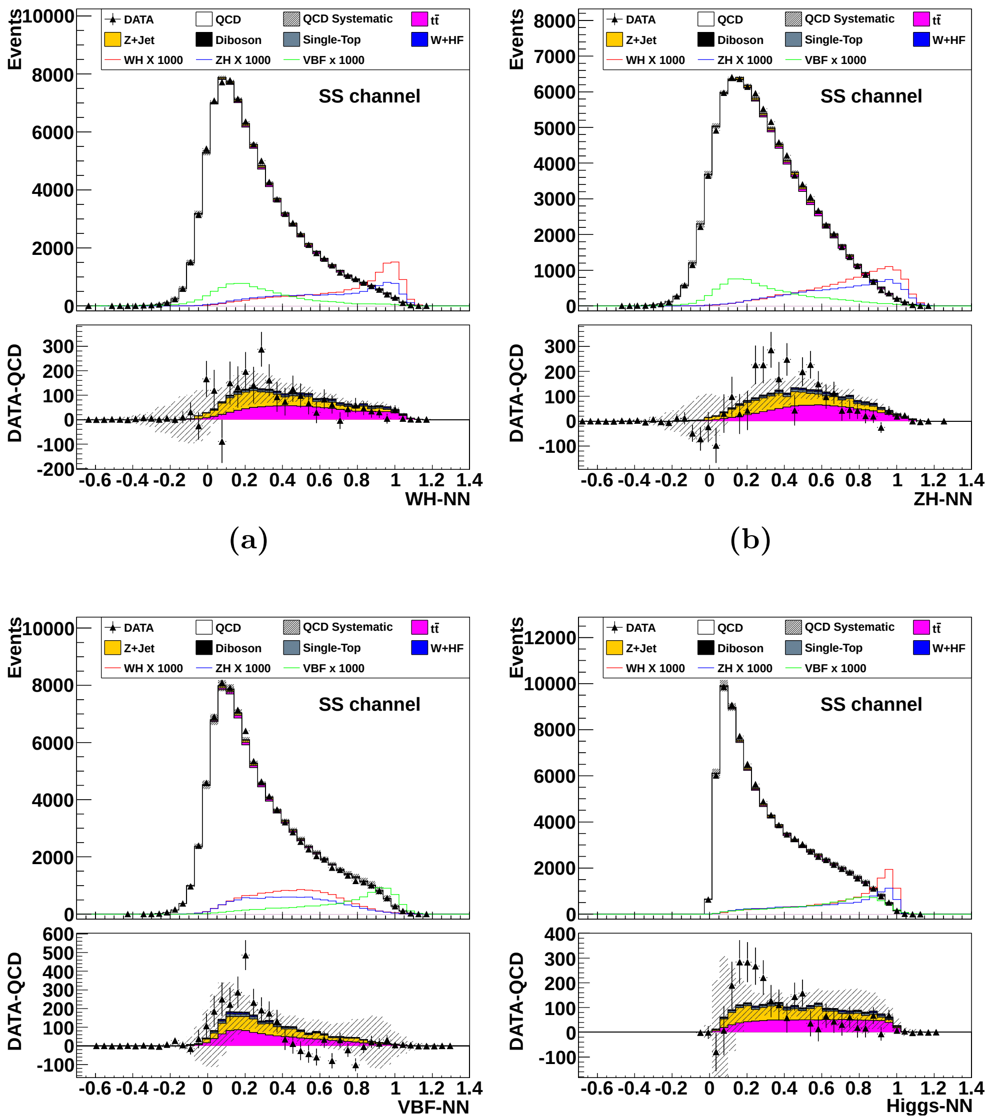

(a) **(b)**

(c) **(d)**

Figure B.5: The (a) WH-NN, (b) ZH-NN, (c) VBF-NN and (d) Higgs-NN distribution of 120 GeV/c^2 Higgs boson events in SS b-tagging category.

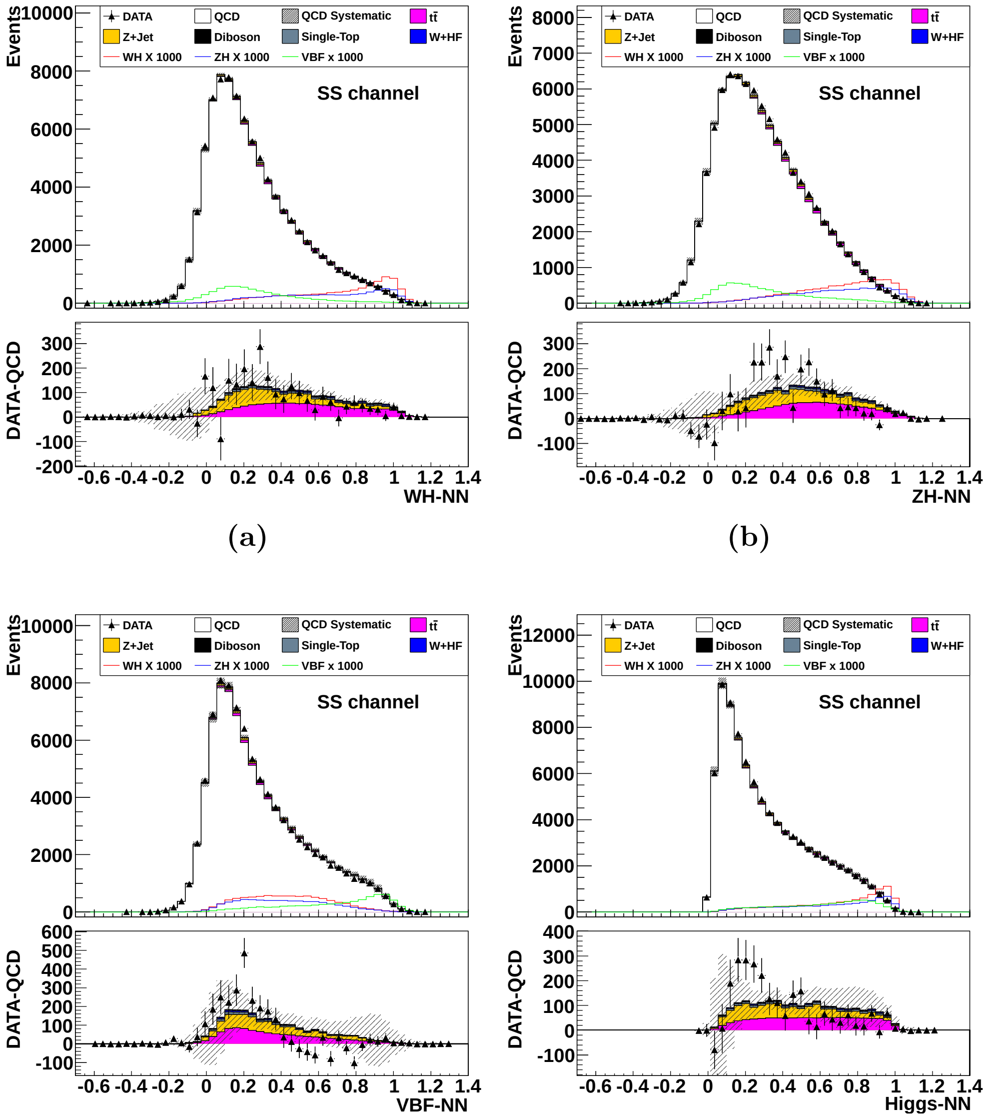

(a) (b)

(c) (d)

Figure B.6: The (a) *WH*-NN, (b) *ZH*-NN, (c) VBF-NN and (d) Higgs-NN distribution of 130 GeV/c^2 Higgs boson events in SS *b*-tagging category.

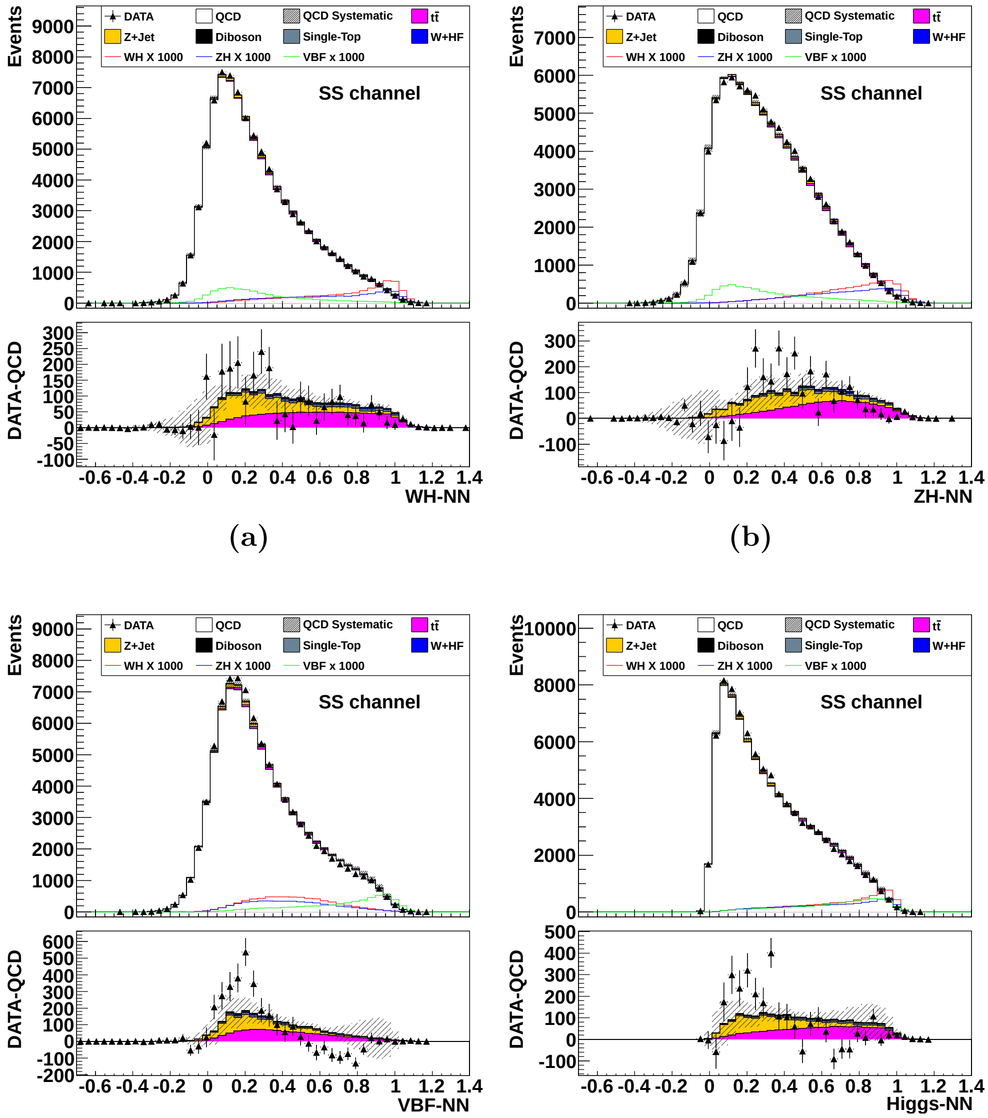

(a) (b)

(c) (d)

Figure B.7: The (a) *WH*-NN, (b) *ZH*-NN, (c) VBF-NN and (d) Higgs-NN distribution of 135 GeV/c^2 Higgs boson events in SS b-tagging category.

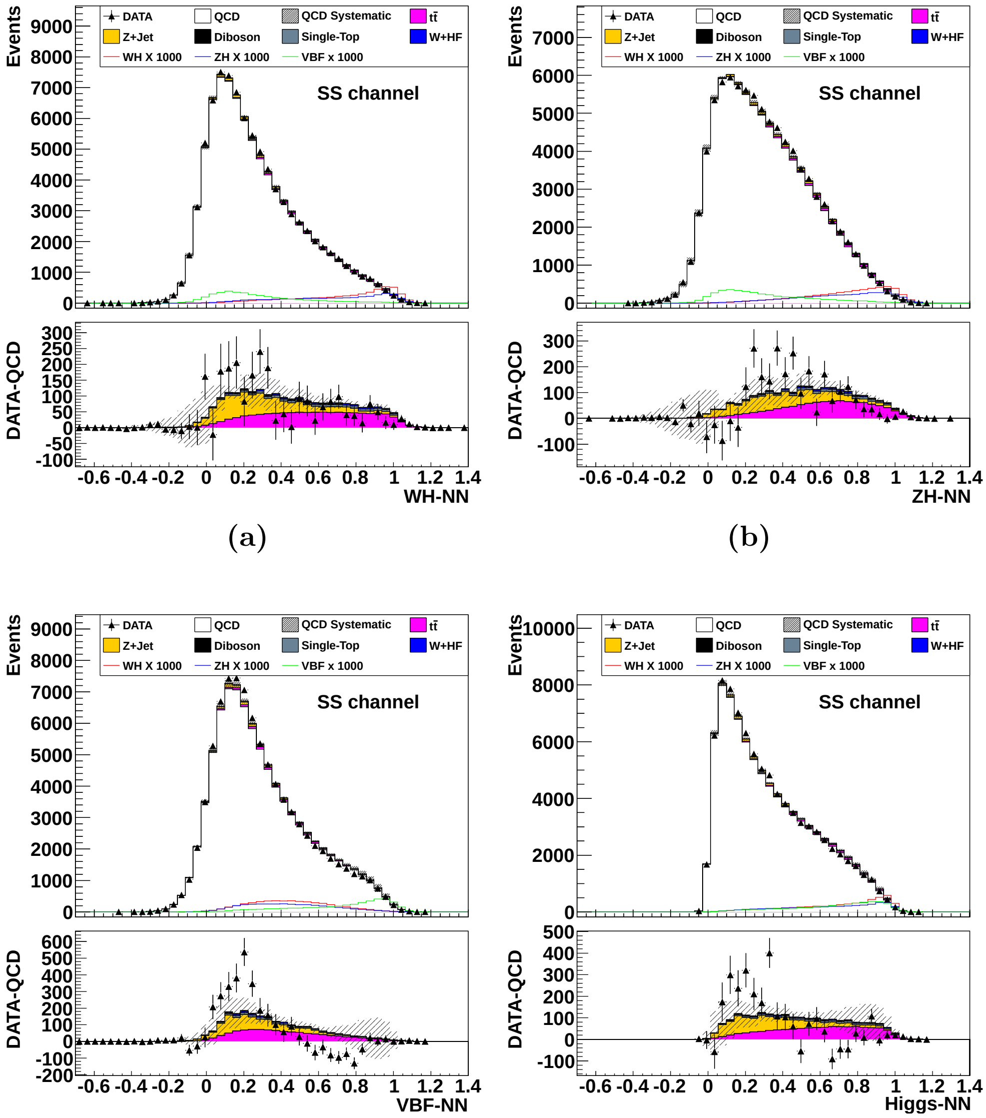

(a) **(b)**

(c) **(d)**

Figure B.8: The (a) *WH*-NN, (b) *ZH*-NN, (c) VBF-NN and (d) Higgs-NN distribution of 140 GeV/c^2 Higgs boson events in SS *b*-tagging category.

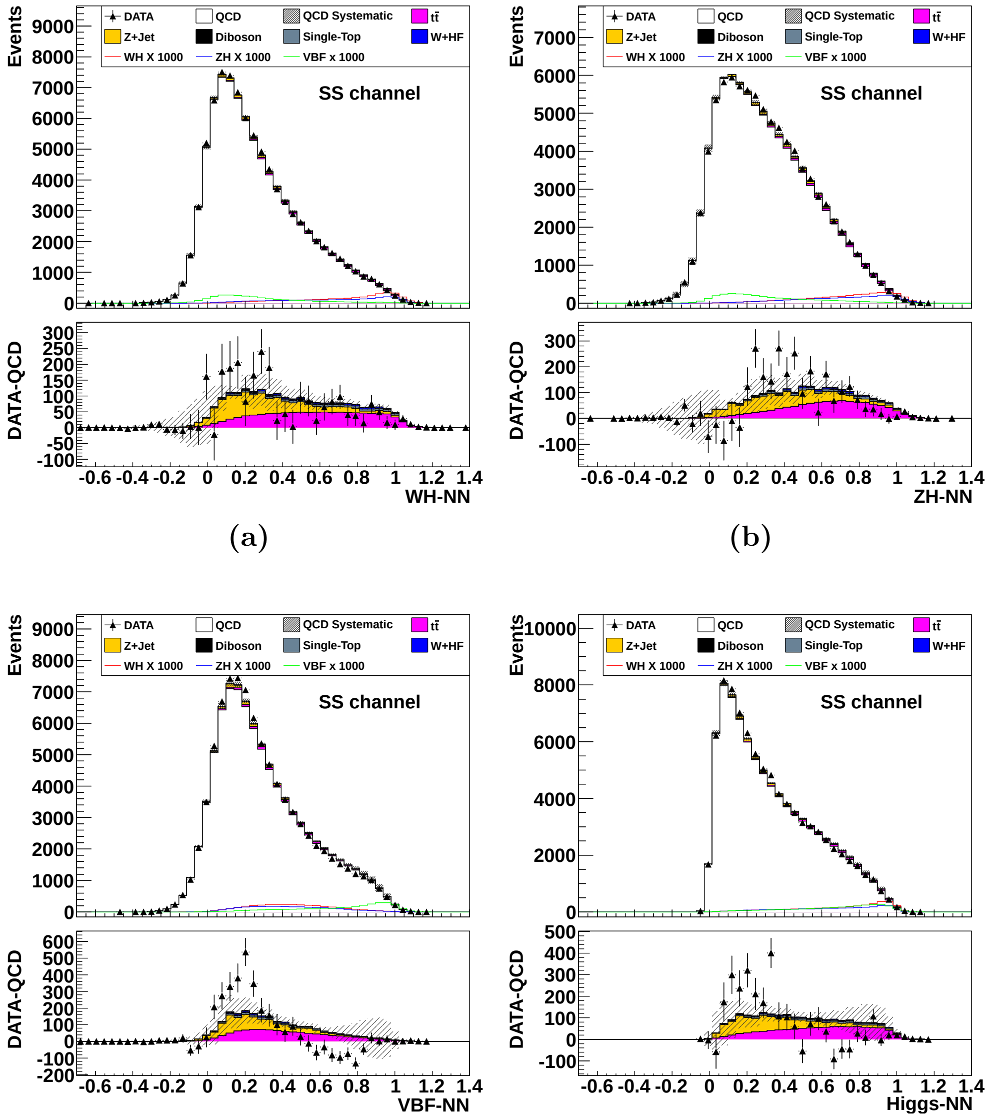

(a) **(b)**

(c) **(d)**

Figure B.9: The (a) *WH*-NN, (b) *ZH*-NN, (c) VBF-NN and (d) Higgs-NN distribution of 145 GeV/c^2 Higgs boson events in SS *b*-tagging category.

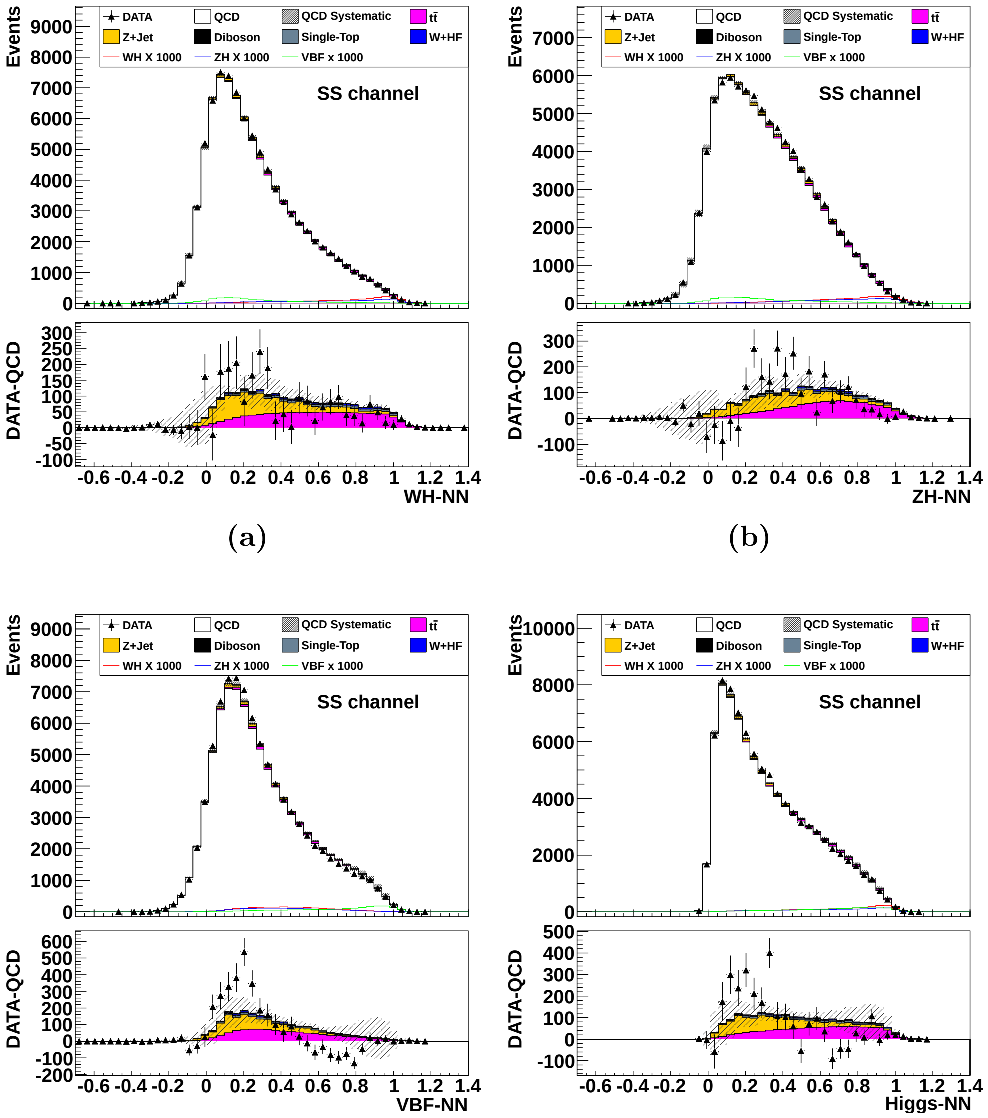

(a) (b)

(c) (d)

Figure B.10: The (a) *WH*-NN, (b) *ZH*-NN, (c) VBF-NN and (d) Higgs-NN distribution of 150 GeV/c^2 Higgs boson events in SS *b*-tagging category.

B.2 SJ b-tagging category

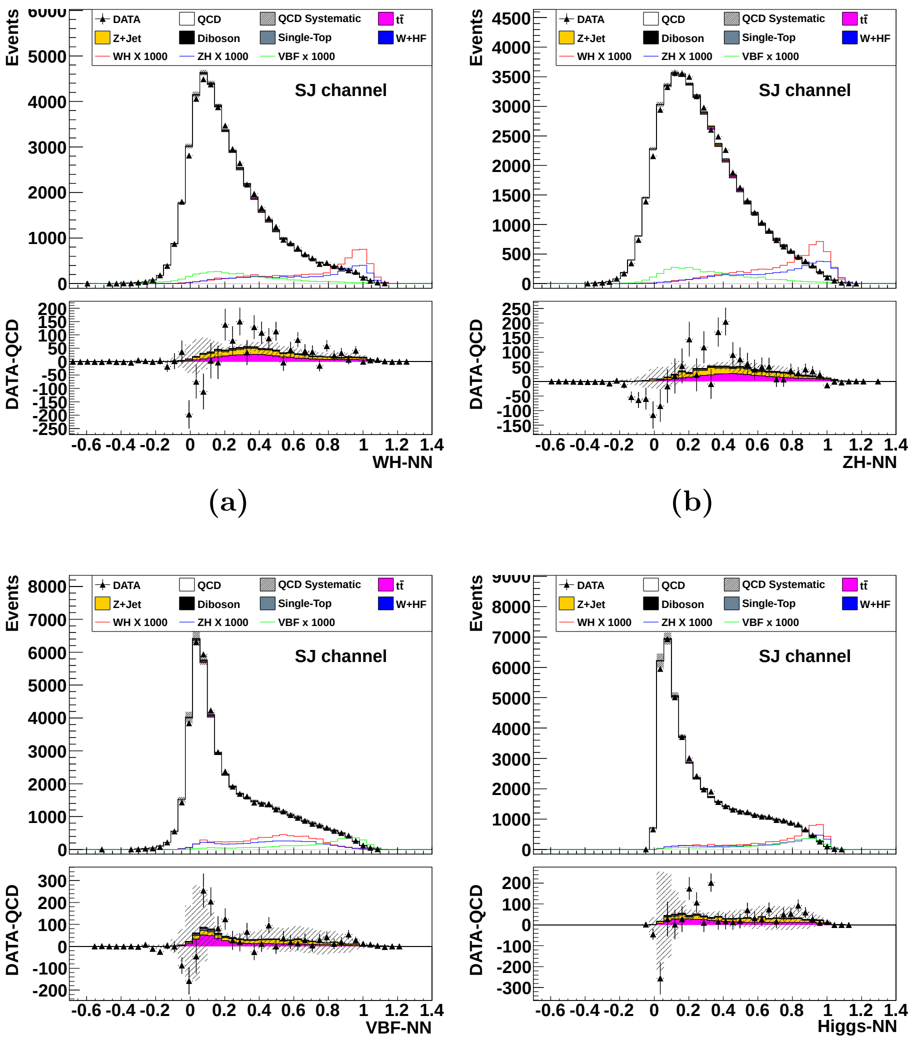

(a) (b)

(c) (d)

Figure B.11: The (a) *WH*-NN, (b) *ZH*-NN, (c) VBF-NN and (d) Higgs-NN distribution of 100 GeV/c^2 Higgs boson events in SJ b-tagging category.

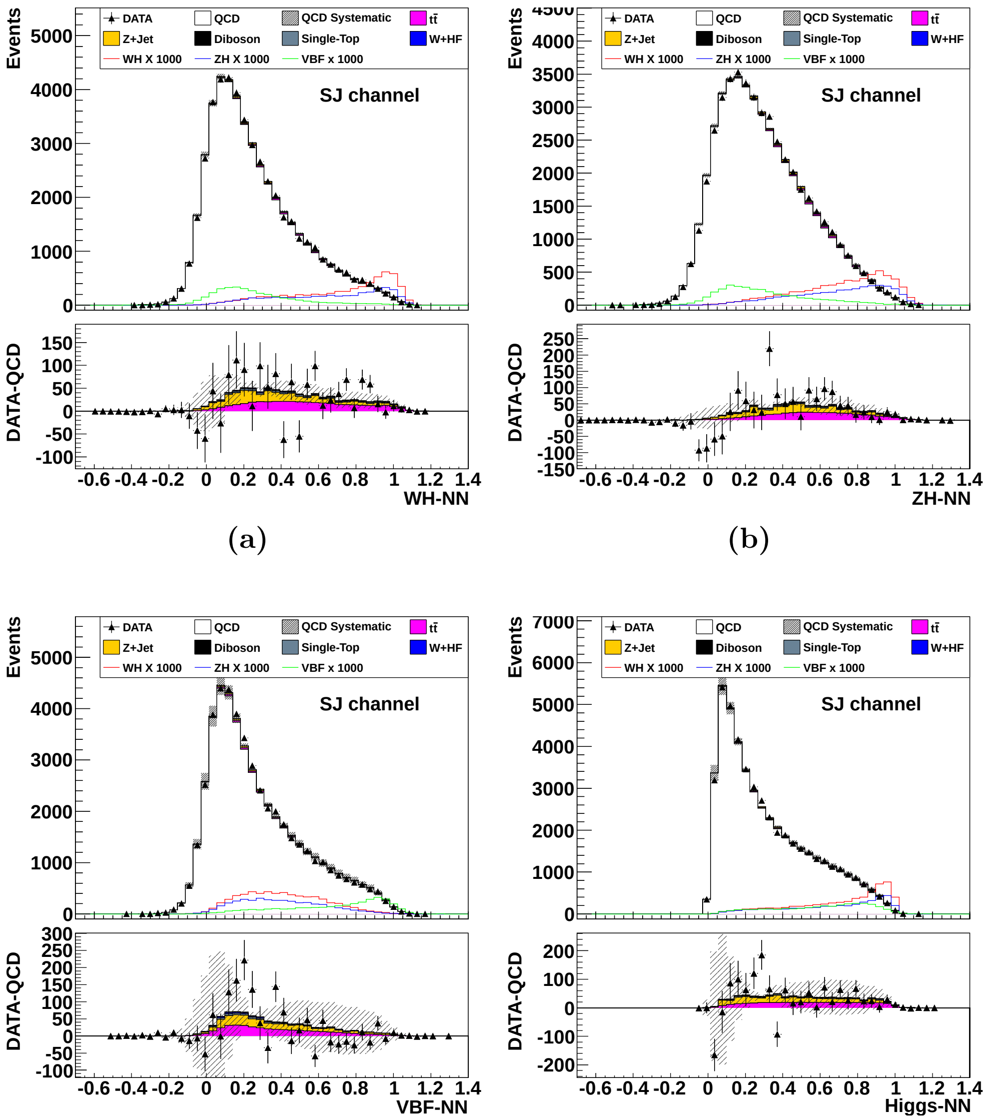

(a) (b)

(c) (d)

Figure B.12: The (a) *WH*-NN, (b) *ZH*-NN, (c) VBF-NN and (d) Higgs-NN distribution of 105 GeV/c^2 Higgs boson events in SJ *b*-tagging category.

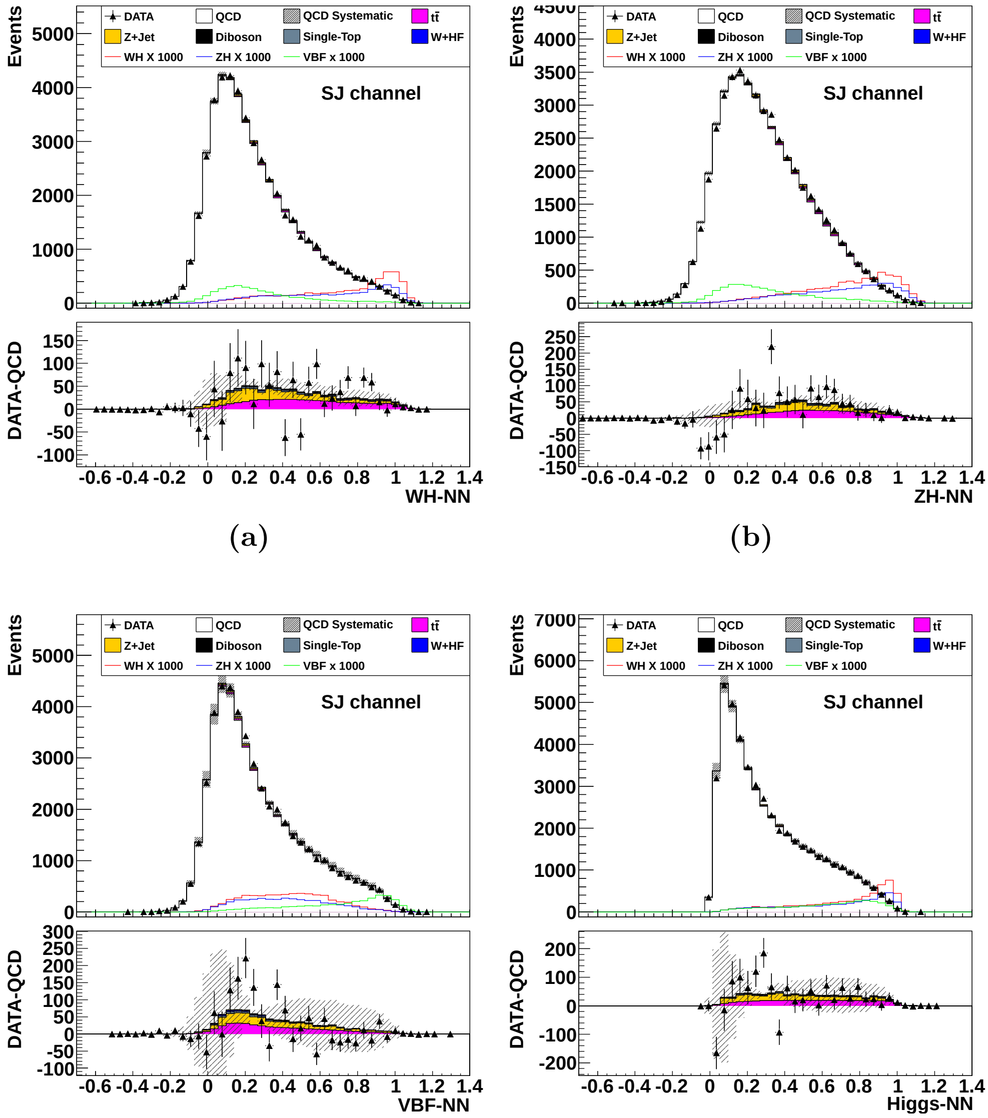

(a) (b)

(c) (d)

Figure B.13: The (a) *WH*-NN, (b) *ZH*-NN, (c) VBF-NN and (d) Higgs-NN distribution of 110 GeV/c^2 Higgs boson events in SJ *b*-tagging category.

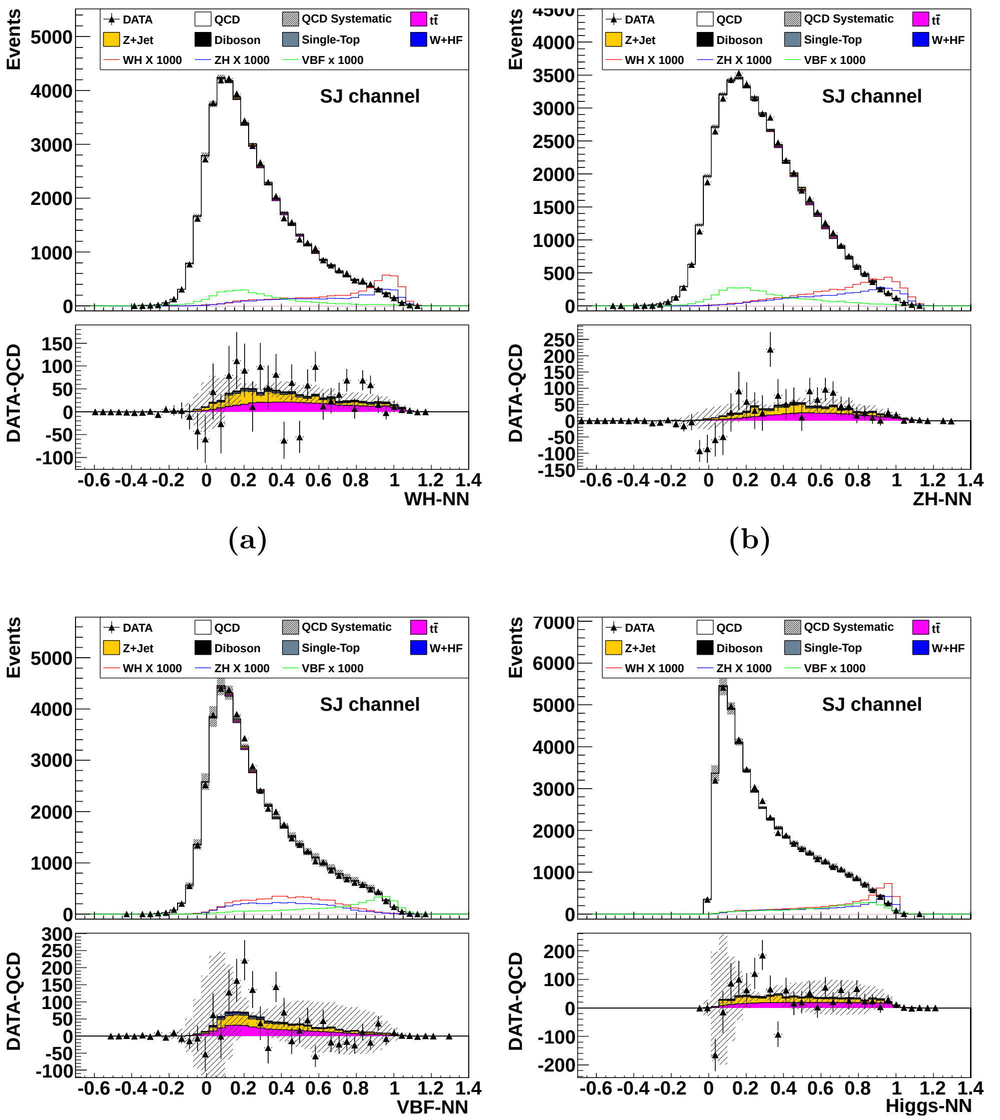

(a) (b)

(c) (d)

Figure B.14: The (a) *WH*-NN, (b) *ZH*-NN, (c) VBF-NN and (d) Higgs-NN distribution of 115 GeV/c^2 Higgs boson events in SJ b-tagging category.

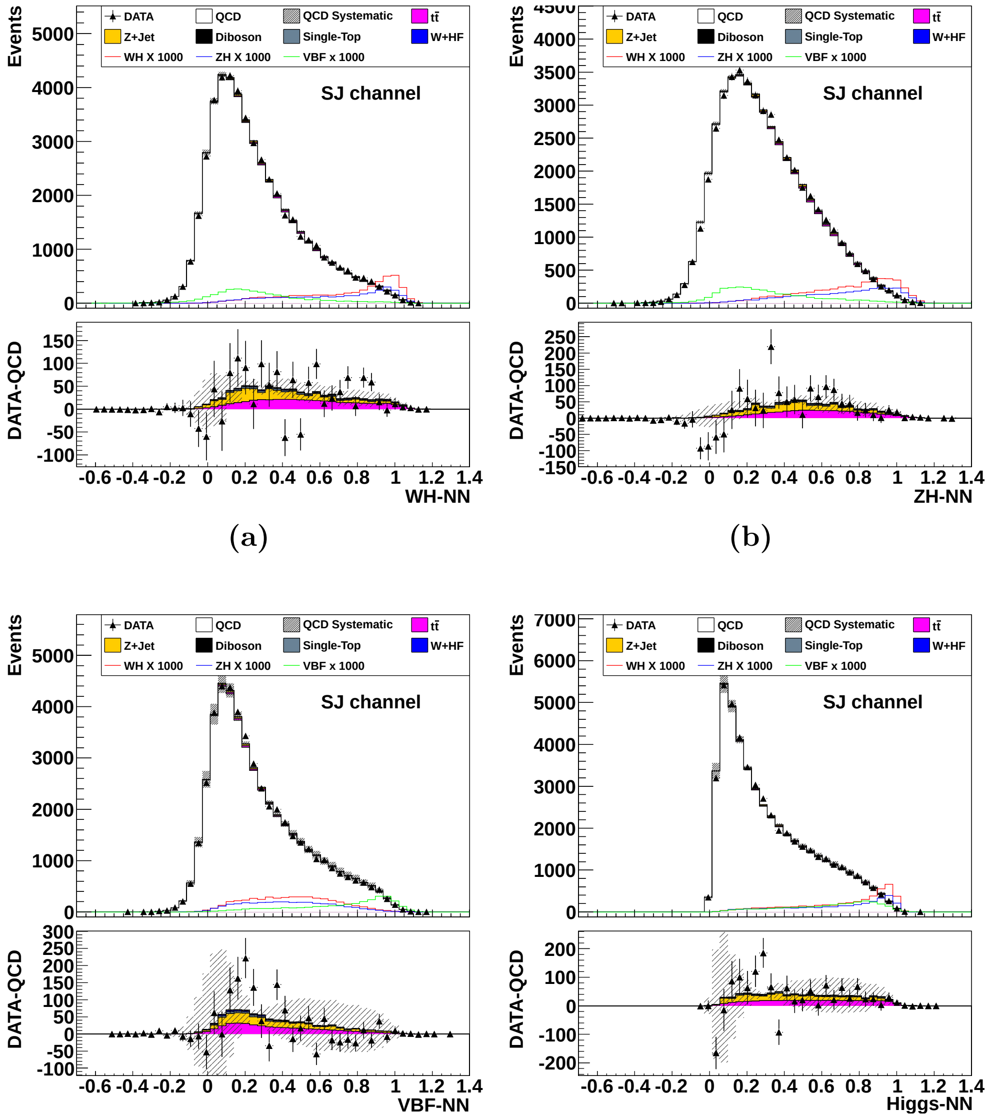

(a) (b)

(c) (d)

Figure B.15: The (a) *WH*-NN, (b) *ZH*-NN, (c) VBF-NN and (d) Higgs-NN distribution of 120 GeV/c^2 Higgs boson events in SJ b-tagging category.

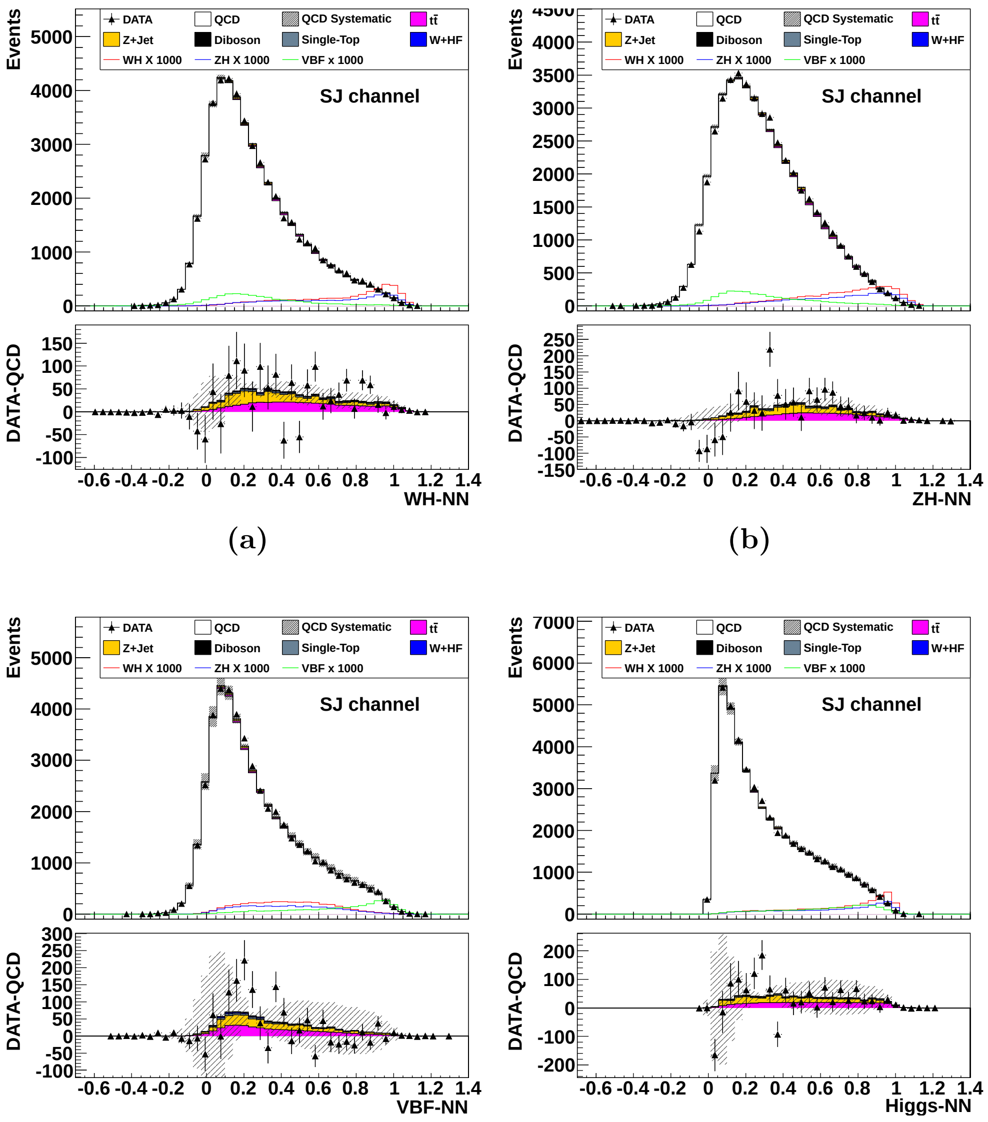

(a) (b)

(c) (d)

Figure B.16: The (a) *WH*-NN, (b) *ZH*-NN, (c) VBF-NN and (d) Higgs-NN distribution of 125 GeV/c^2 Higgs boson events in SJ *b*-tagging category.

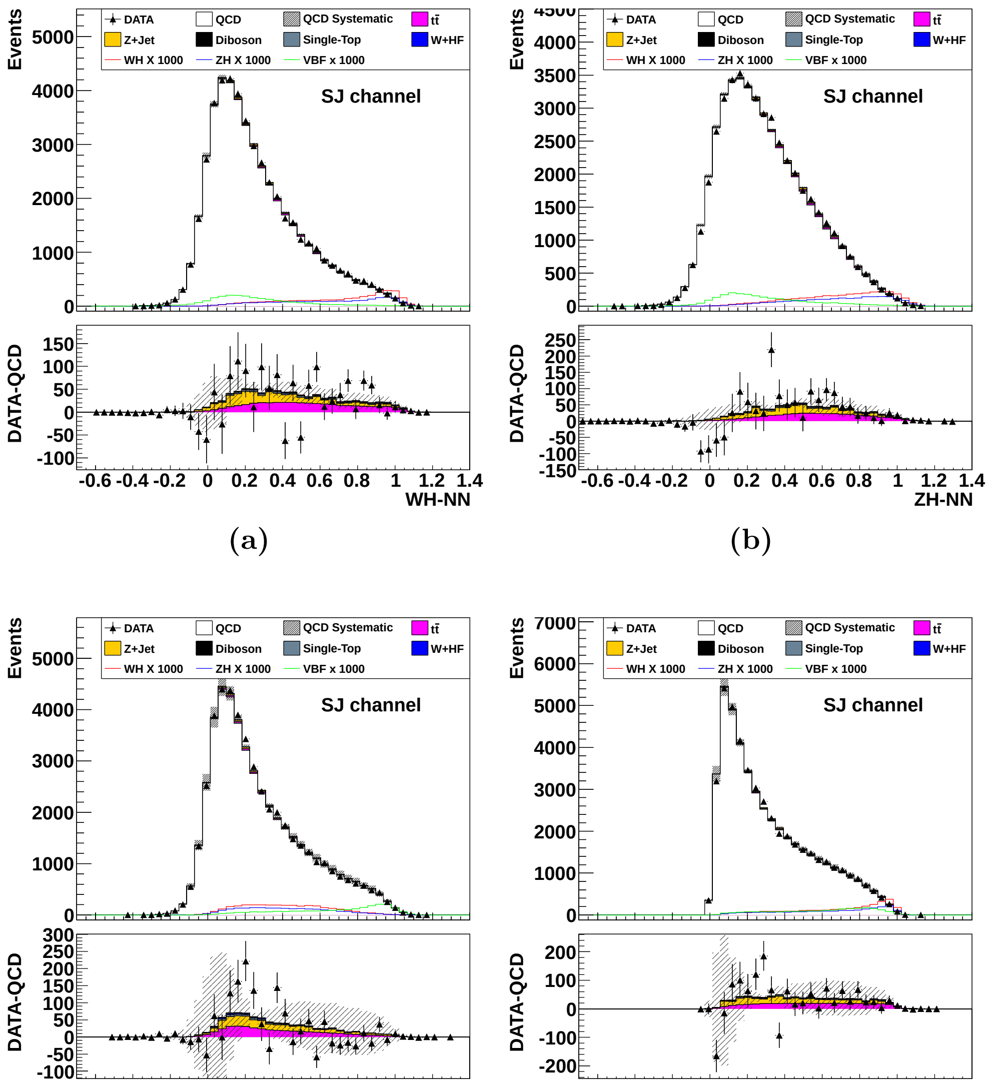

(a) (b)

(c) (d)

Figure B.17: The (a) *WH*-NN, (b) *ZH*-NN, (c) VBF-NN and (d) Higgs-NN distribution of 130 GeV/c^2 Higgs boson events in SJ b-tagging category.

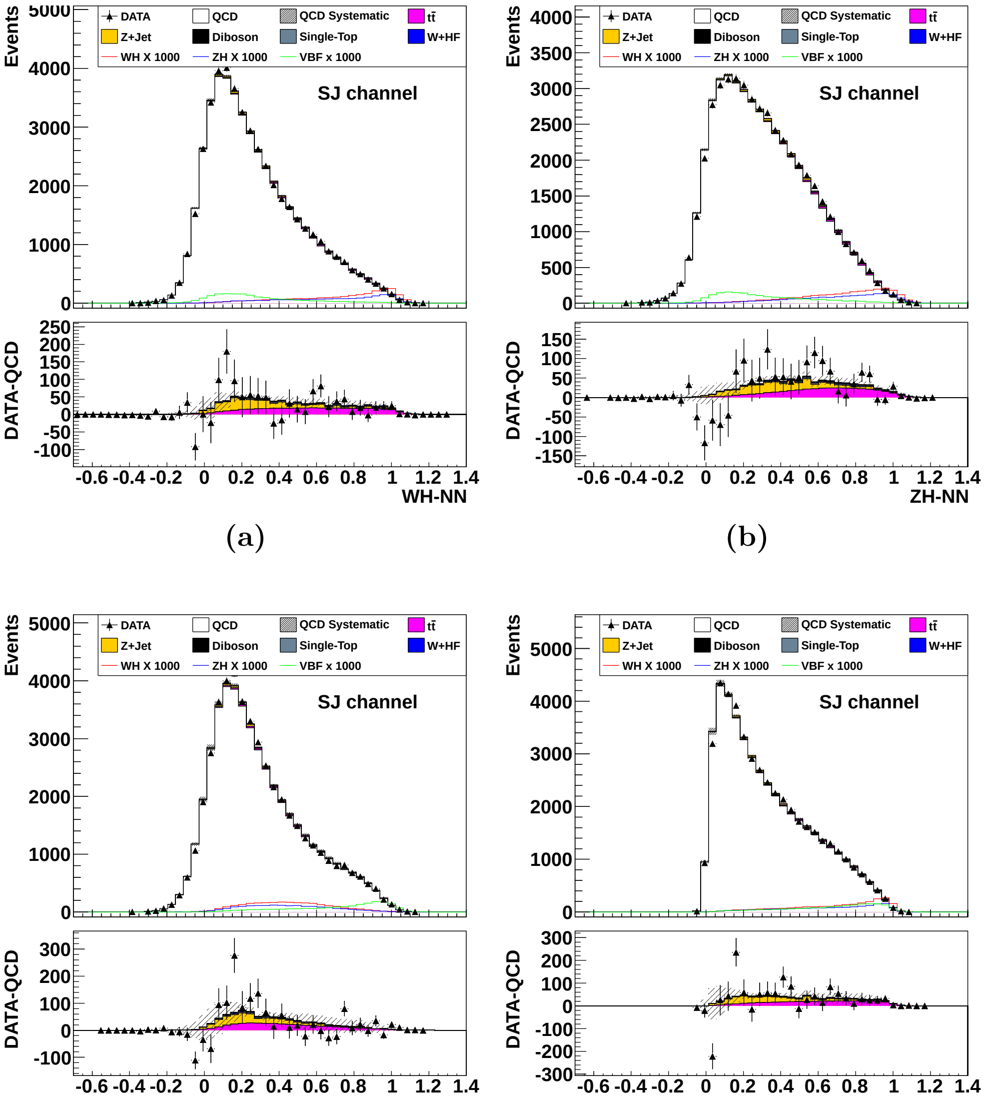

(a) (b)

(c) (d)

Figure B.18: The (a) *WH*-NN, (b) *ZH*-NN, (c) VBF-NN and (d) Higgs-NN distribution of 135 GeV/c^2 Higgs boson events in SJ b-tagging category.

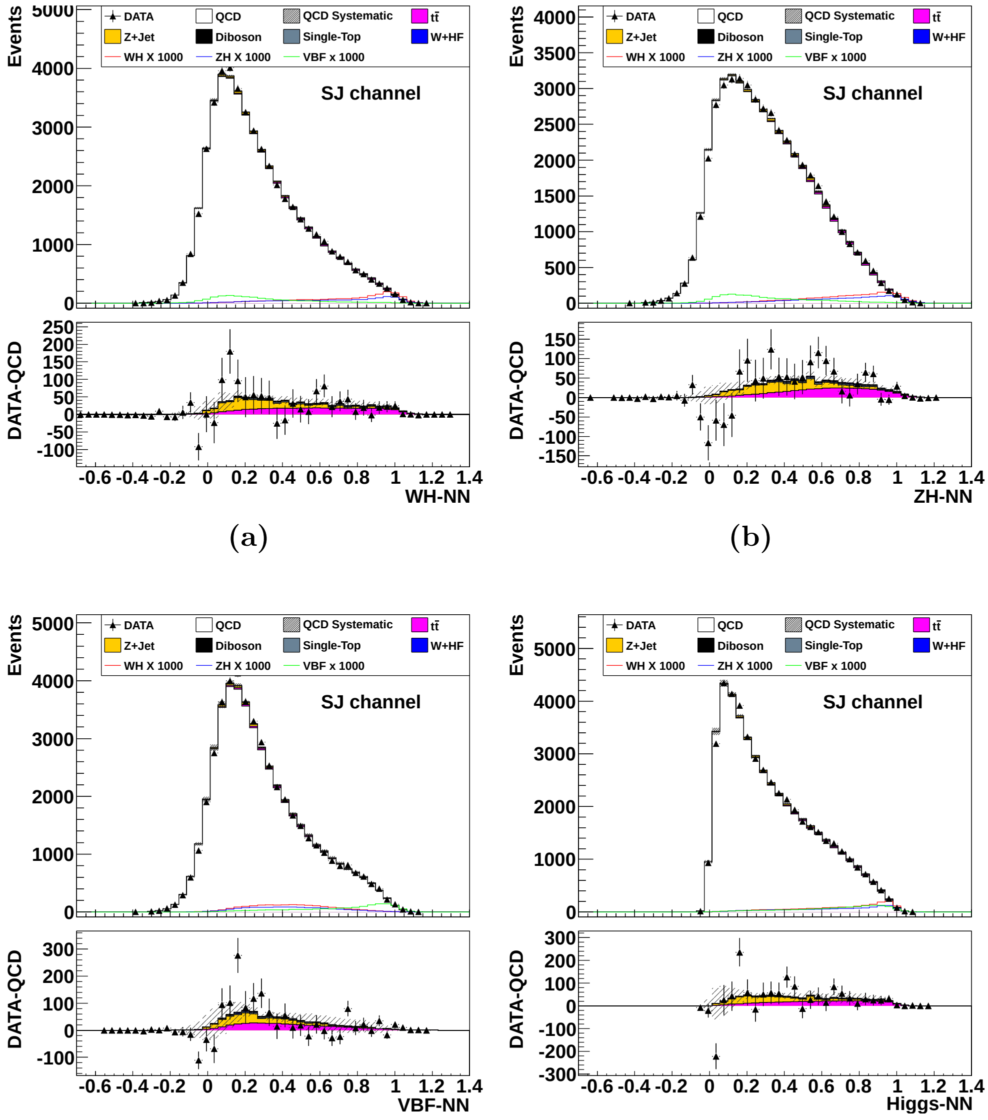

(a) (b)

(c) (d)

Figure B.19: The (a) *WH*-NN, (b) *ZH*-NN, (c) VBF-NN and (d) Higgs-NN distribution of 140 GeV/c^2 Higgs boson events in SJ b-tagging category.

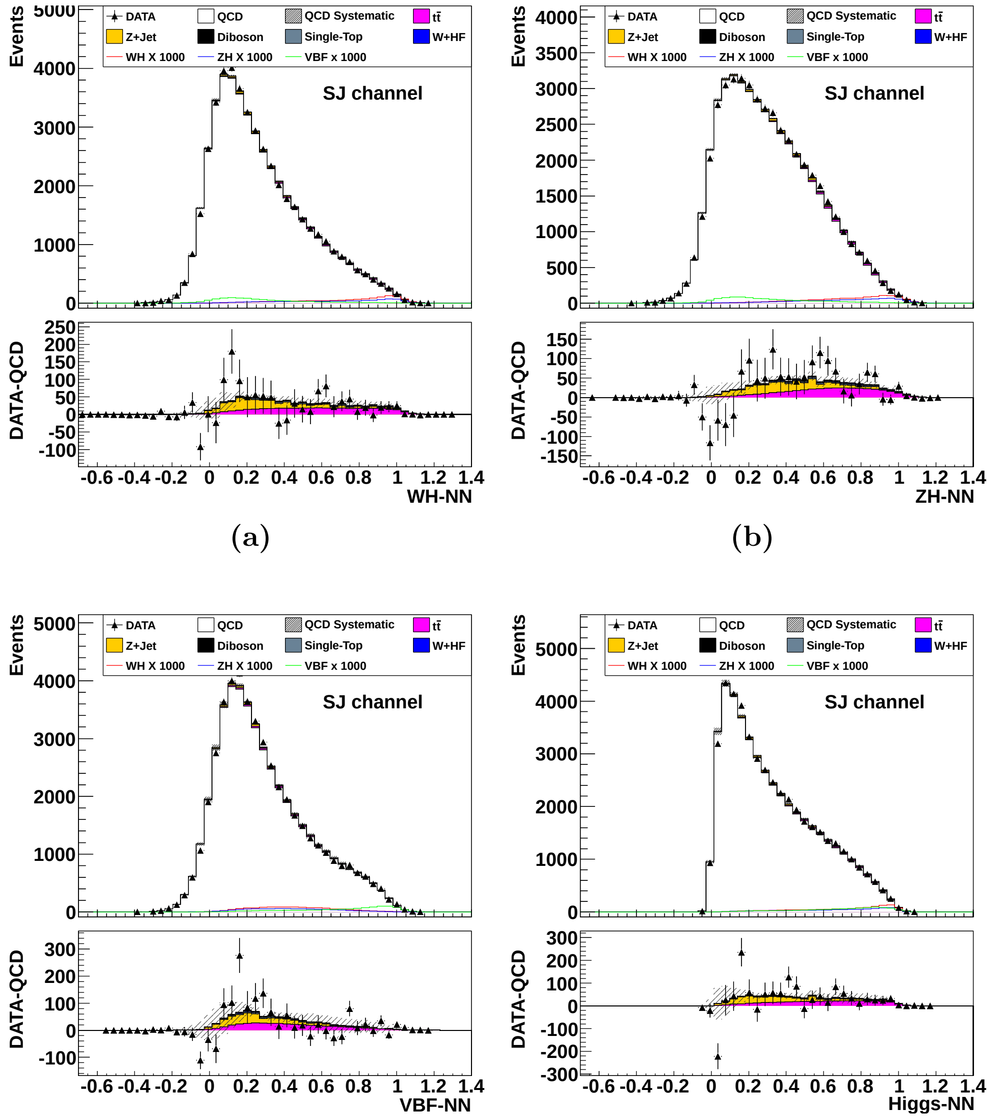

(a) **(b)**

(c) **(d)**

Figure B.20: The (a) *WH*-NN, (b) *ZH*-NN, (c) VBF-NN and (d) Higgs-NN distribution of 145 GeV/c^2 Higgs boson events in SJ *b*-tagging category.

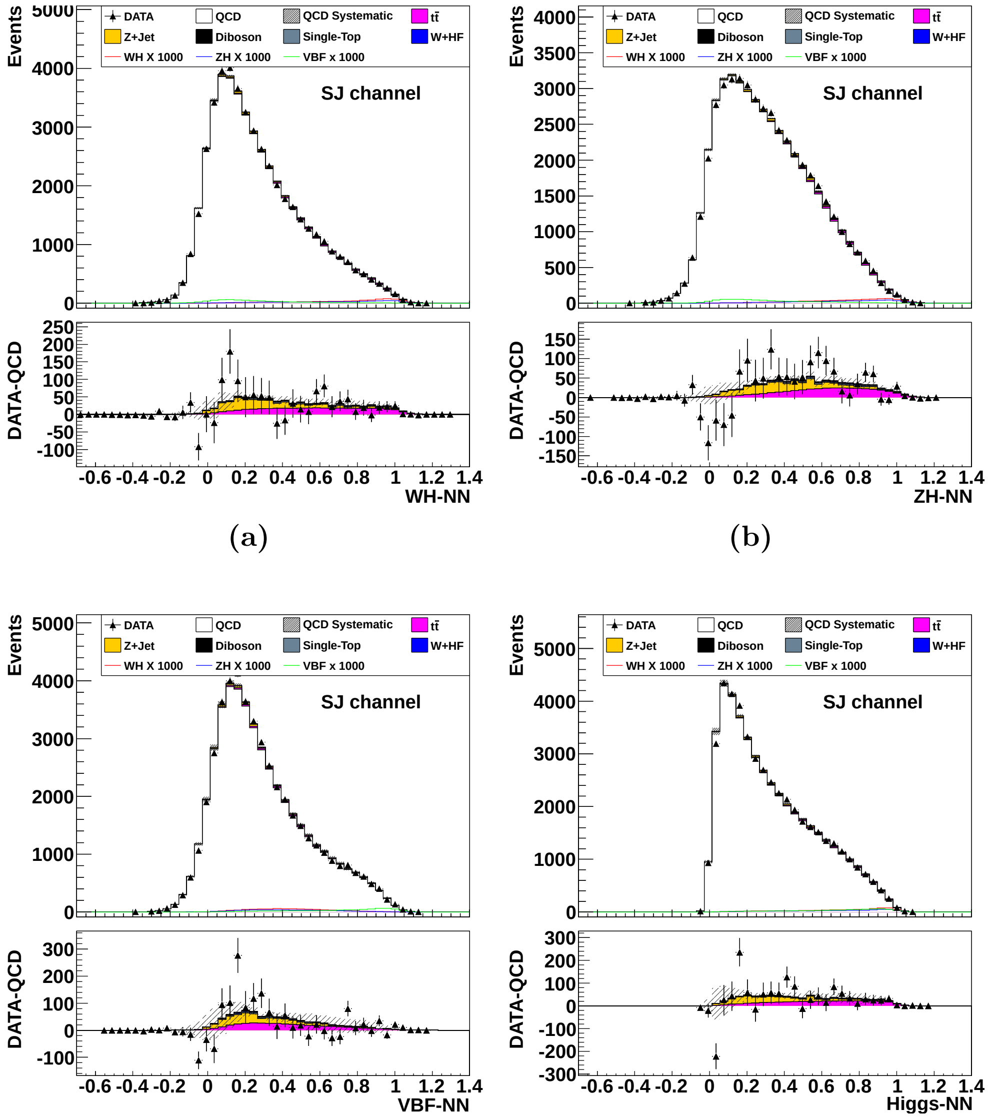

(a) (b) (c) (d)

Figure B.21: The (a) WH-NN, (b) ZH-NN, (c) VBF-NN and (d) Higgs-NN distribution of 150 GeV/c^2 Higgs boson events in SJ b-tagging category.

Appendix C

Pseudo-experiment Distributions and Observed Posterior PDF

In this appendix, the pseudo-experiment distributions used to extract the expected limits and the observed posterior PDF used to measure the observed limit for each Higgs boson mass hypothesis and b-tagging category are provided. The plots relative to the SS b-tagging category are show in section C.1, for the SJ b-tagging category in section C.2, and for their combination in section C.3.

In the plots of the observed posterior PDF, the observed limit at 95% credibility level is indicated by the red line.
The plots of pseudo-experiment distributions show the median and the $\pm 1\sigma$ and $\pm 2\sigma$ regions.

C.1 SS b-tagging category

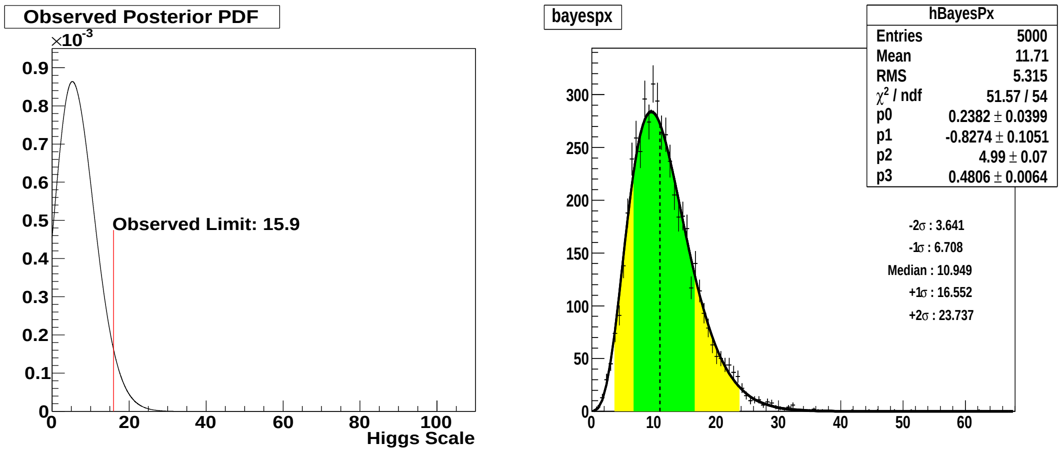

(a) 100 GeV/c^2 **(b)** 100 GeV/c^2

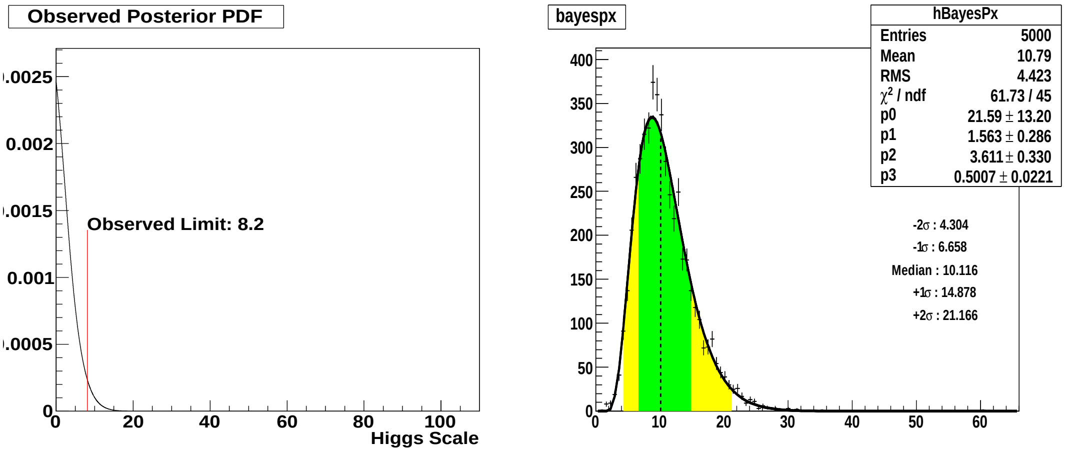

(c) 105 GeV/c^2 **(d)** 105 GeV/c^2

Figure C.1: The observed posterior densities and the pseudo-experiment distributions for the Higgs mass boson hypotheses of 100 and 105 GeV/c^2 for the SS b-tagging category.

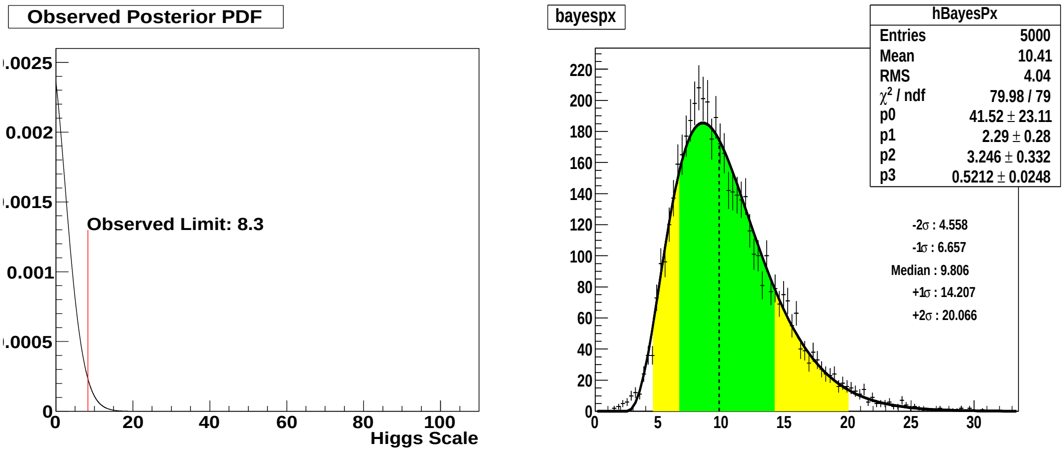

(a) 110 GeV/c^2 **(b)** 110 GeV/c^2

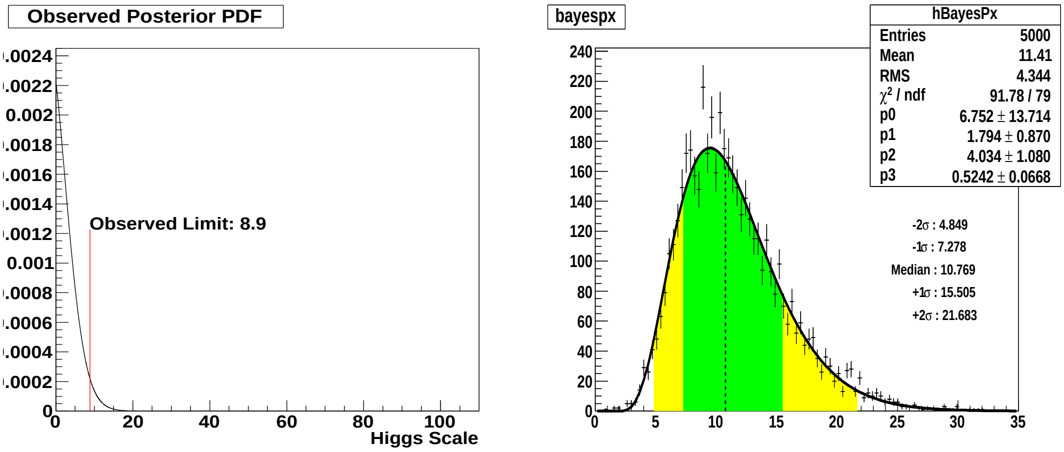

(c) 115 GeV/c^2 **(d)** 115 GeV/c^2

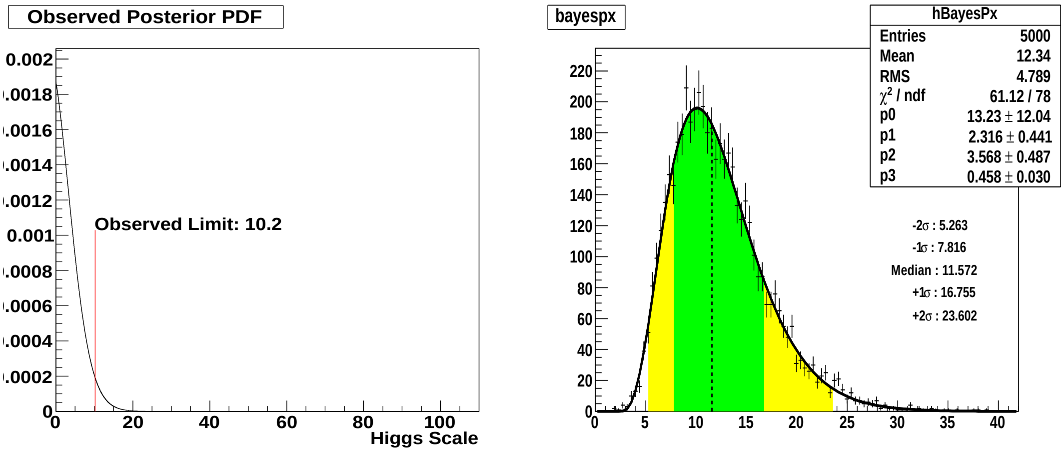

(e) 120 GeV/c^2 **(f)** 120 GeV/c^2

Figure C.2: The observed posterior densities and the pseudo-experiment distributions for a Higgs mass boson hypothesis of 110, 115, and 120 GeV/c^2 for the SS b-tagging category, respectively.

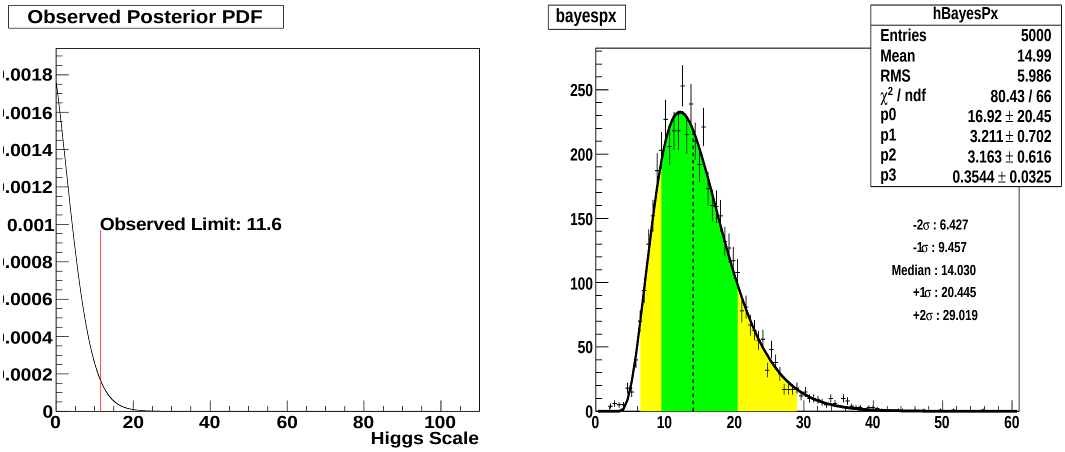

(a) 125 GeV/c^2 (b) 125 GeV/c^2

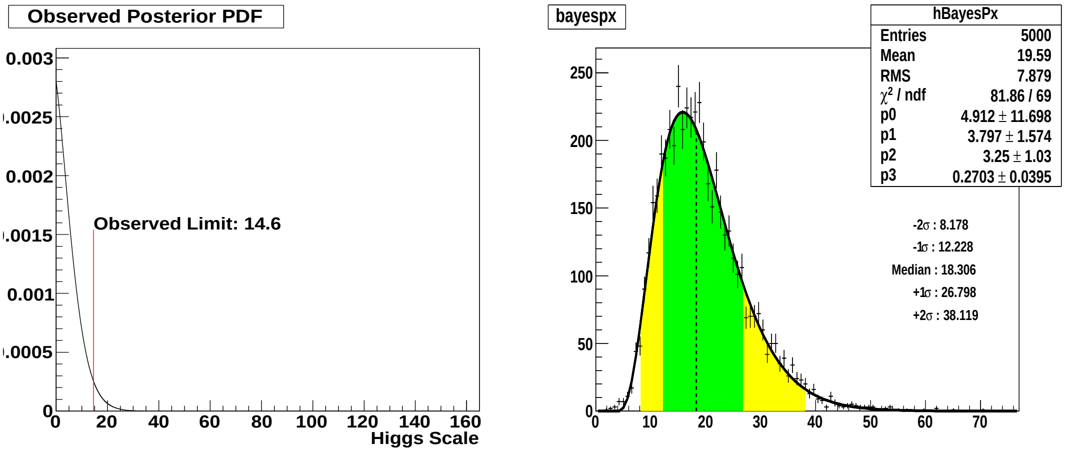

(c) 130 GeV/c^2 (d) 130 GeV/c^2

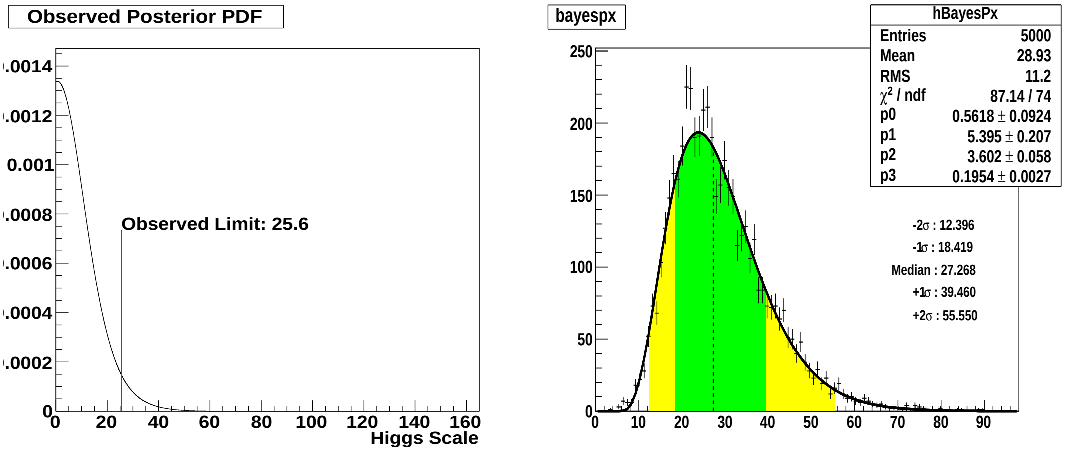

(e) 135 GeV/c^2 (f) 135 GeV/c^2

Figure C.3: The observed posterior densities and the pseudo-experiment distributions for a Higgs mass boson hypothesis of 125, 130 and 135 GeV/c^2 for the SS b-tagging category.

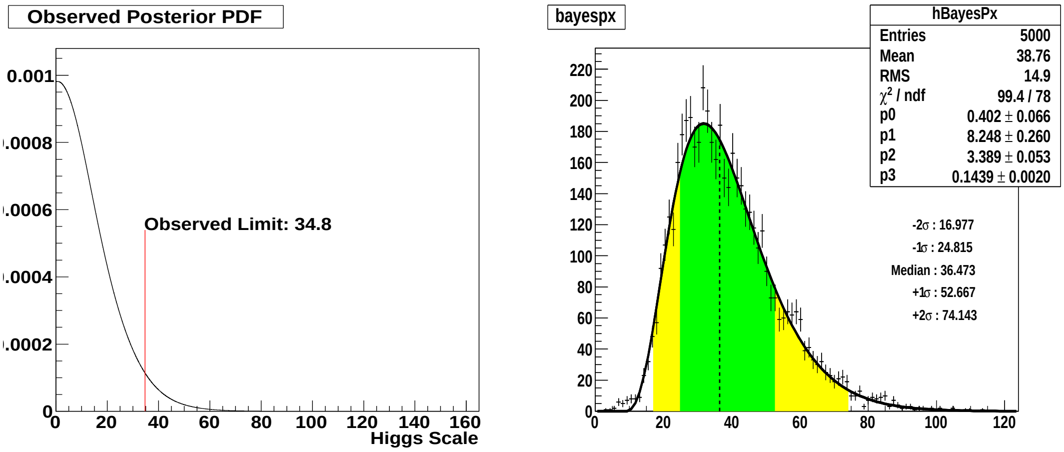

(a) 140 GeV/c^2 **(b)** 140 GeV/c^2

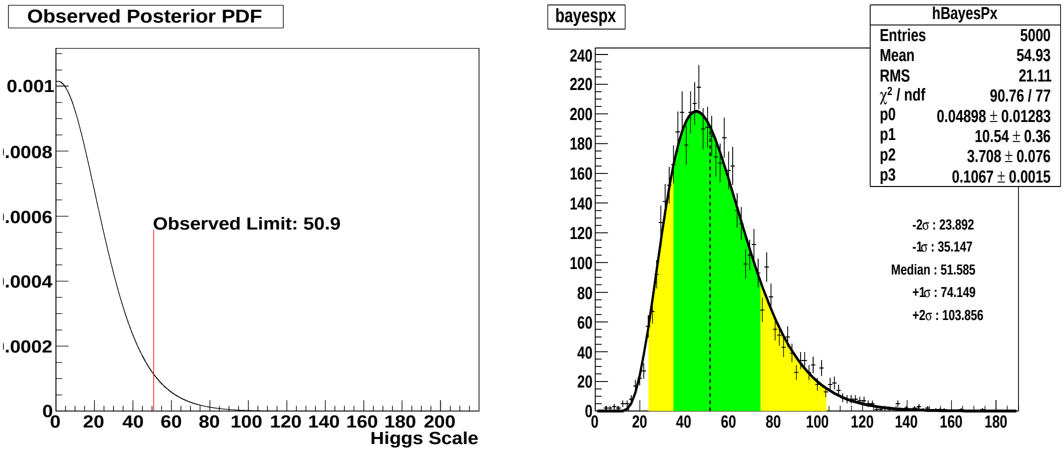

(c) 145 GeV/c^2 **(d)** 145 GeV/c^2

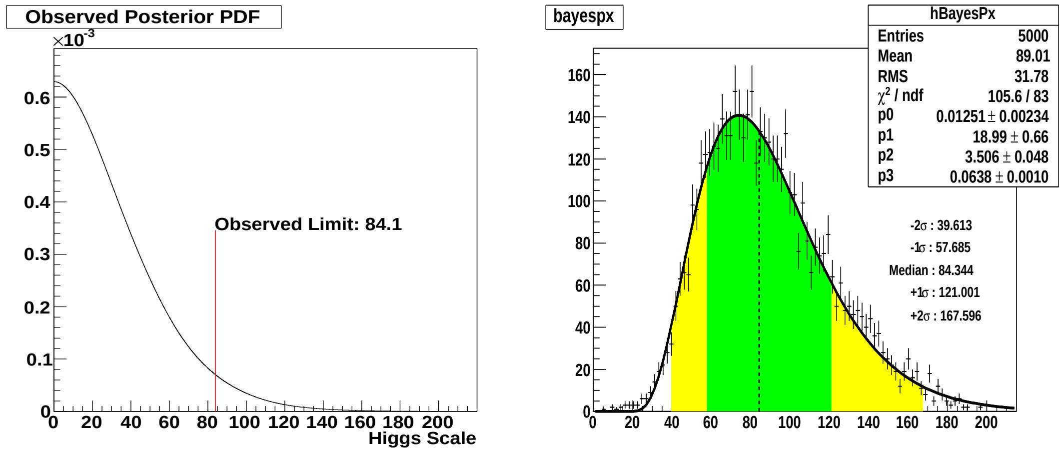

(e) 150 GeV/c^2 **(f)** 150 GeV/c^2

Figure C.4: The observed posterior densities and the pseudo-experiment distributions for a Higgs mass boson hypothesis of 140, 145, and 150 GeV/c^2 for the SS b-tagging category.

C.2 SJ b-tagging category

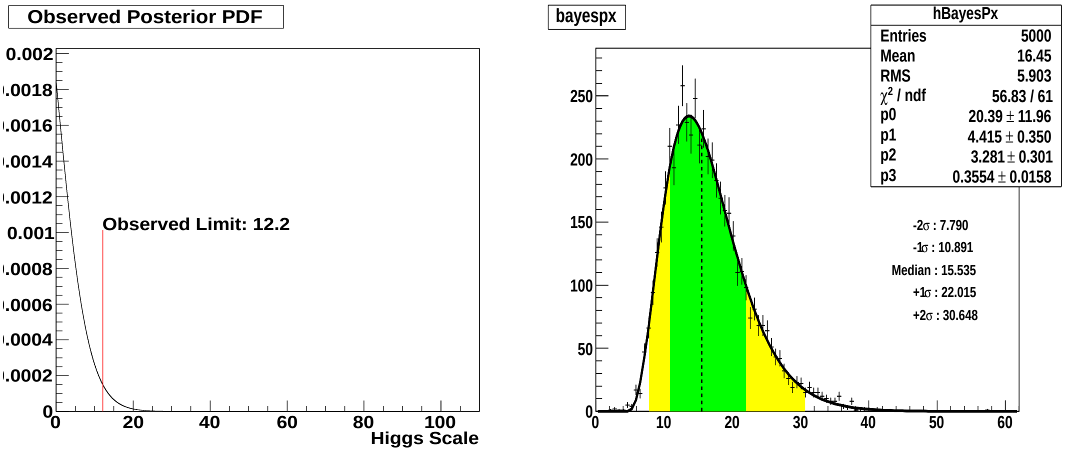

(a) 100 GeV/c^2 (b) 100 GeV/c^2

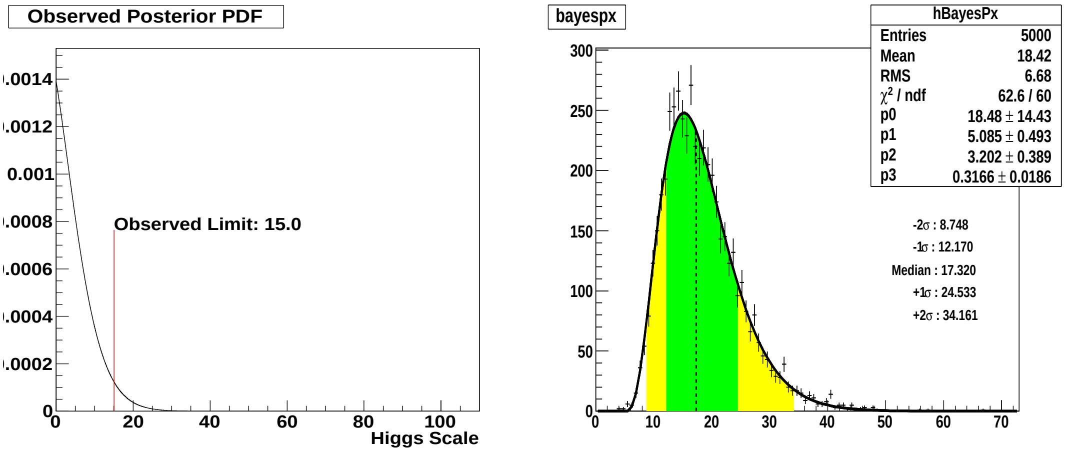

(c) 105 GeV/c^2 (d) 105 GeV/c^2

Figure C.5: The observed posterior densities and the pseudo-experiment distributions for a Higgs mass boson hypothesis of 100 and 105 GeV/c^2 for the SJ b-tagging category.

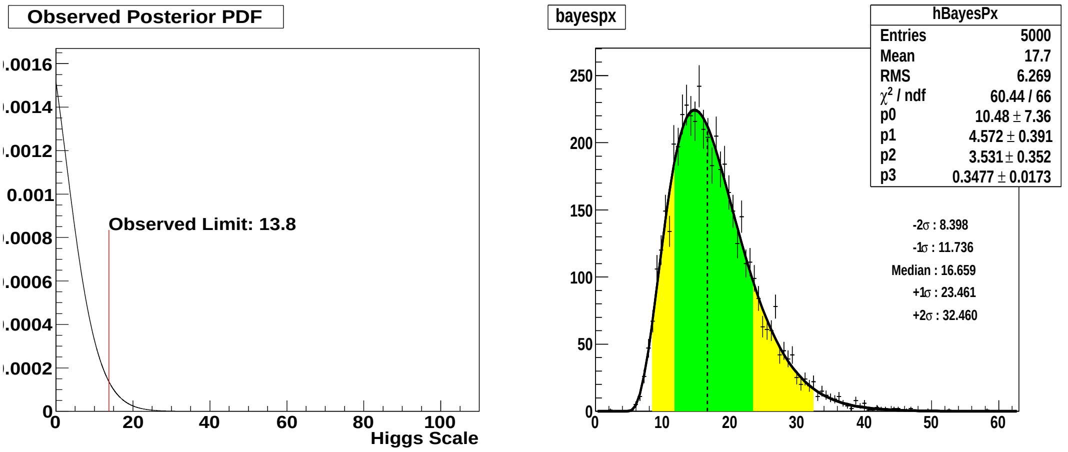

(a) 110 GeV/c^2 **(b)** 110 GeV/c^2

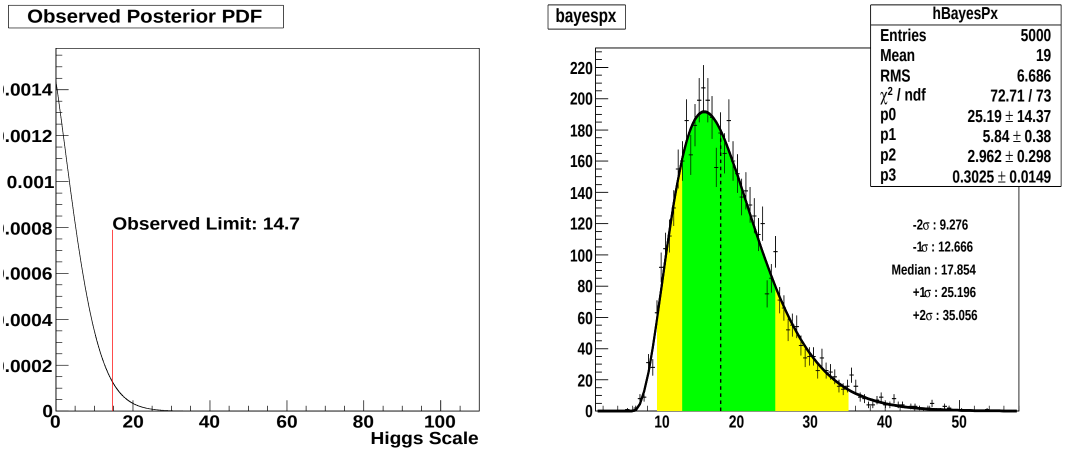

(c) 115 GeV/c^2 **(d)** 115 GeV/c^2

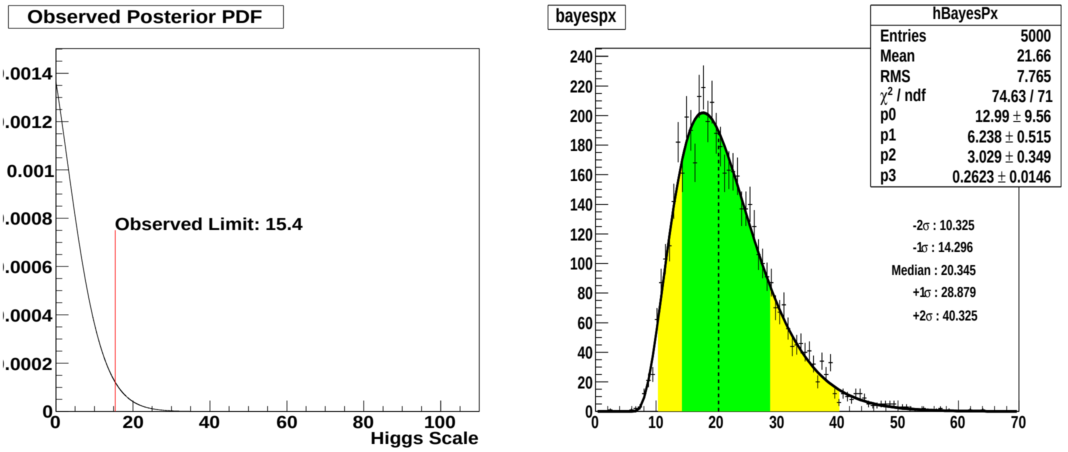

(e) 120 GeV/c^2 **(f)** 120 GeV/c^2

Figure C.6: The observed posterior densities and the pseudo-experiment distributions for a Higgs mass boson hypothesis of 110, 115, and 120 GeV/c^2 for the SJ b-tagging category.

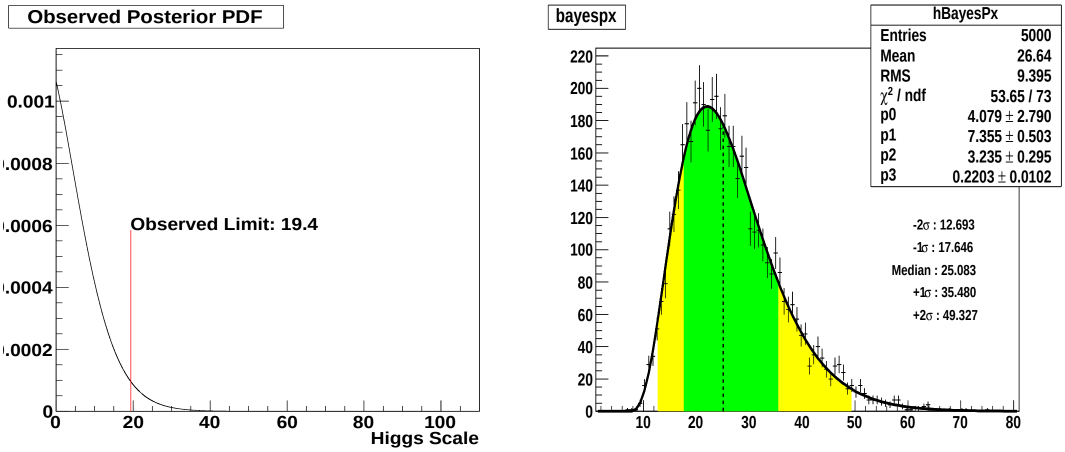

(a) 125 GeV/c^2 **(b)** 125 GeV/c^2

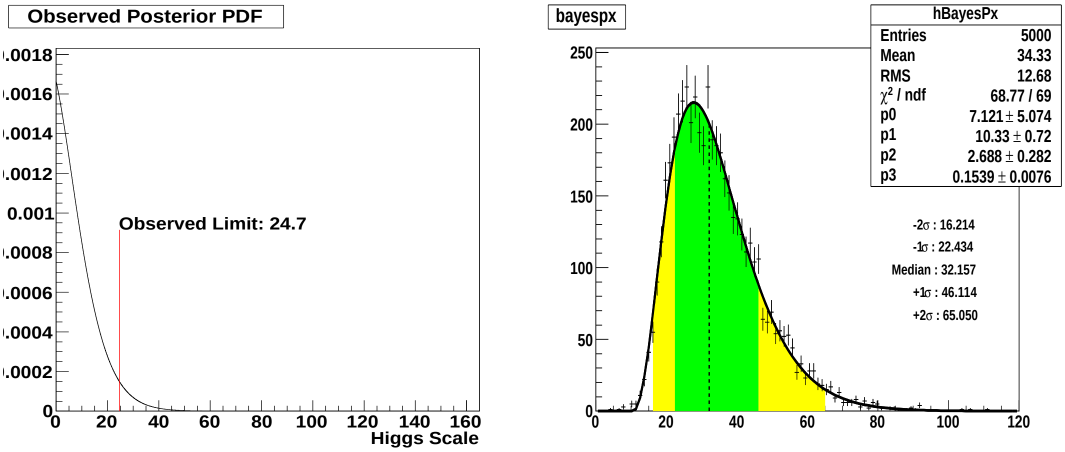

(c) 130 GeV/c^2 **(d)** 130 GeV/c^2

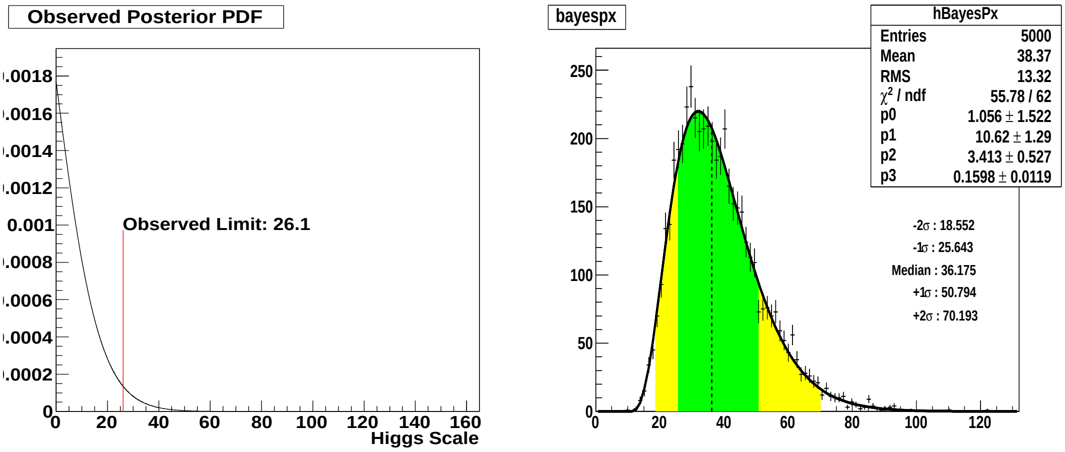

(e) 135 GeV/c^2 **(f)** 135 GeV/c^2

Figure C.7: The observed posterior densities and the pseudo-experiment distributions for a Higgs mass boson hypothesis of 125, 130, and 135 GeV/c^2 for the SJ b-tagging category.

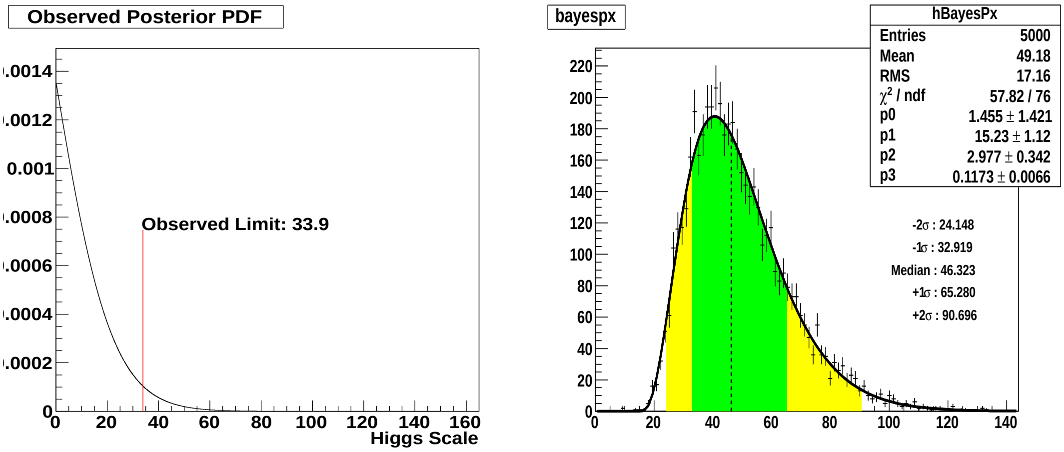

(a) 140 GeV/c^2 **(b)** 140 GeV/c^2

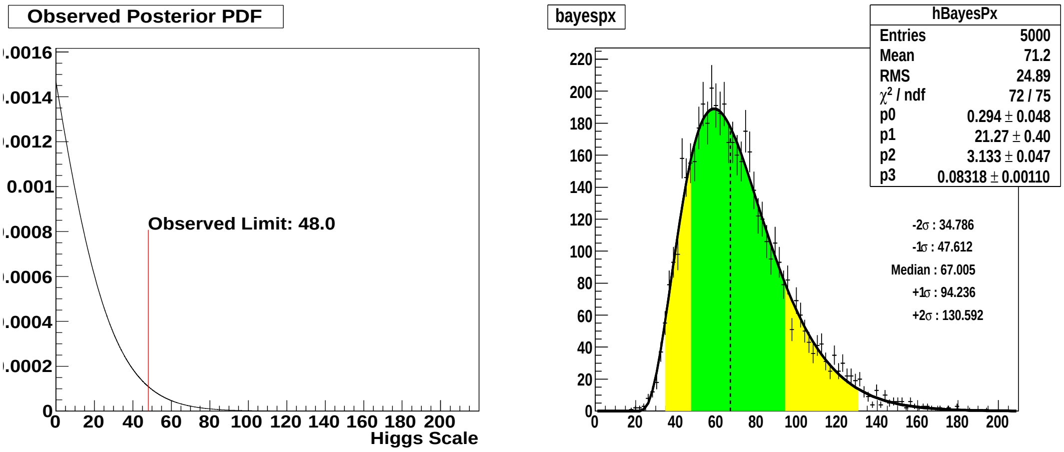

(c) 145 GeV/c^2 **(d)** 145 GeV/c^2

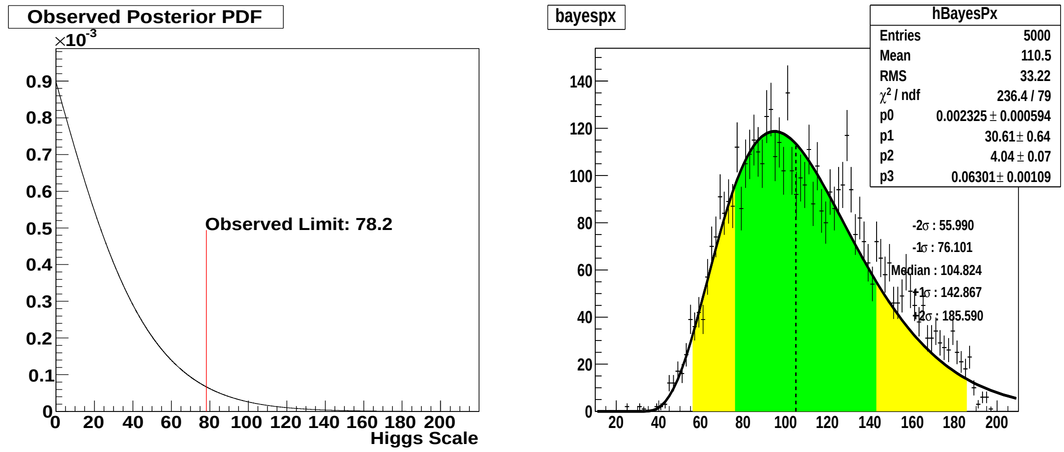

(e) 150 GeV/c^2 **(f)** 150 GeV/c^2

Figure C.8: The observed posterior densities and the pseudo-experiment distributions for a Higgs mass boson hypothesis of 140, 145, and 150 GeV/c^2 for the SJ *b*-tagging category.

C.3 SS+SJ *b*-tagging category

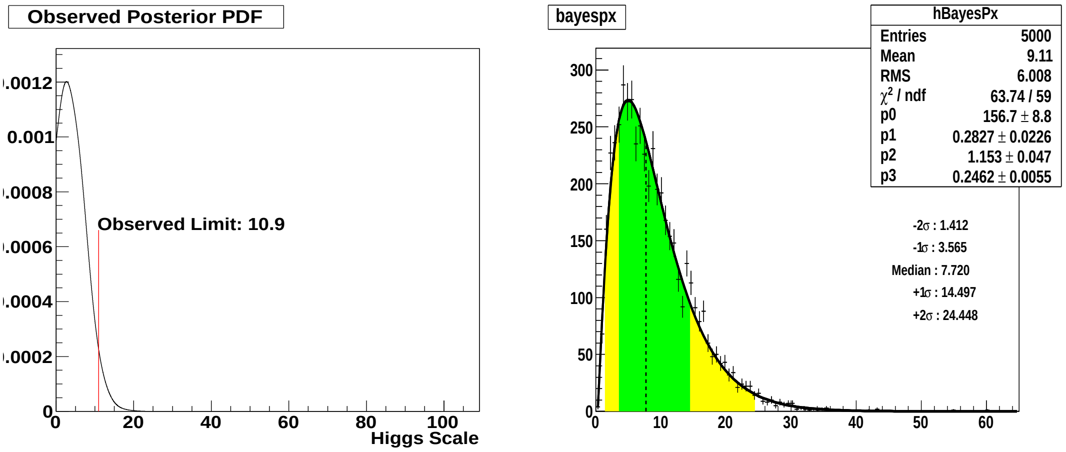

(a) 100 GeV/c^2 **(b)** 100 GeV/c^2

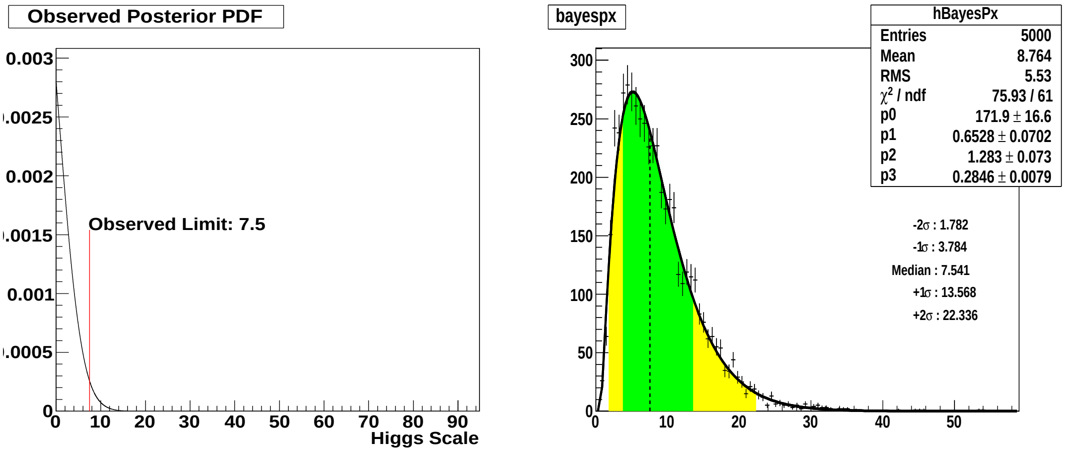

(c) 105 GeV/c^2 **(d)** 105 GeV/c^2

Figure C.9: The observed posterior densities and the pseudo-experiment distributions for a Higgs mass boson hypothesis of 100 and 105 GeV/c^2 for the SS+SJ *b*-tagging category.

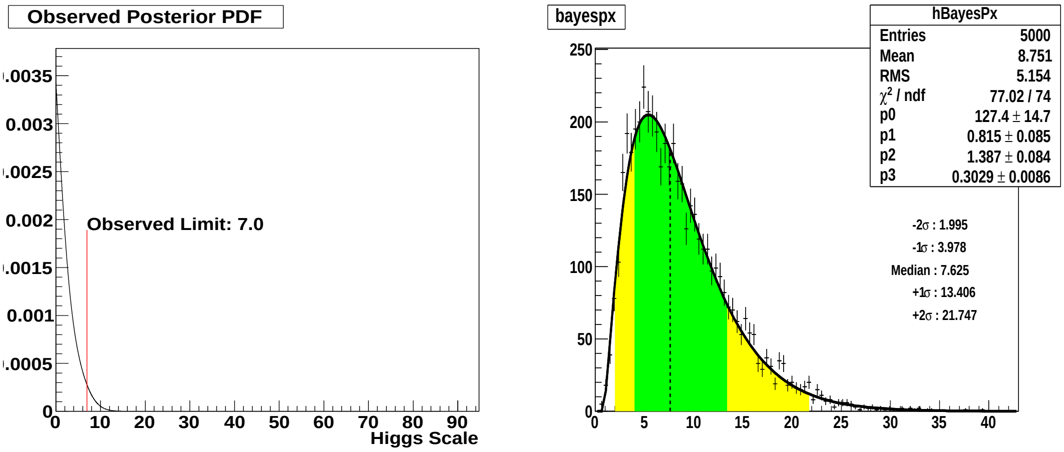

(a) 110 GeV/c^2 (b) 110 GeV/c^2

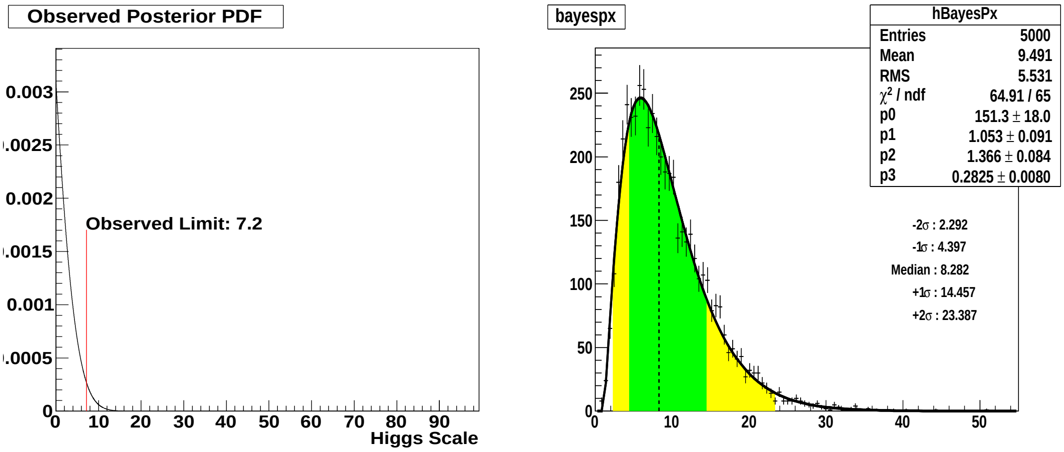

(c) 115 GeV/c^2 (d) 115 GeV/c^2

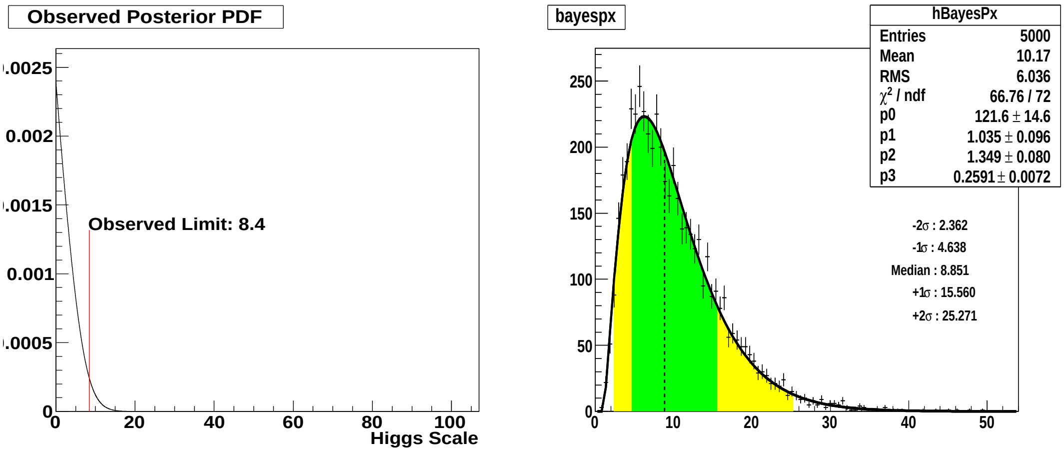

(e) 120 GeV/c^2 (f) 120 GeV/c^2

Figure C.10: The observed posterior densities and the pseudo-experiment distributions for a Higgs mass boson hypothesis of 110, 115, and 120 GeV/c^2 for the SS+SJ *b*-tagging category, respectively.

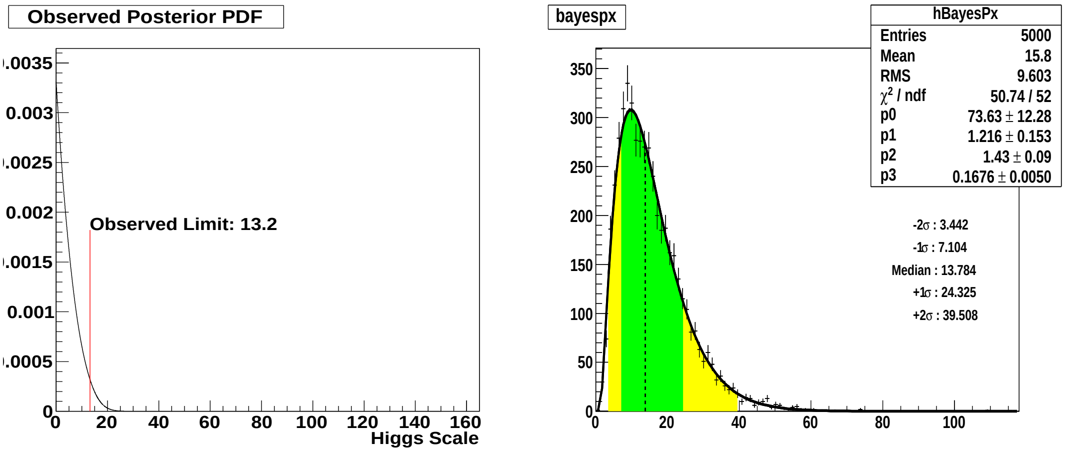

(a) 130 GeV/c^2 **(b)** 130 GeV/c^2

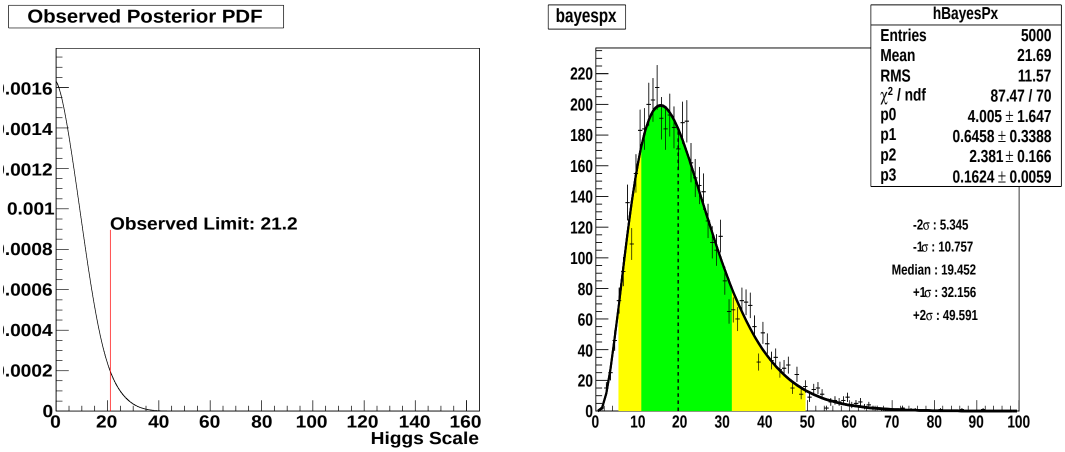

(c) 135 GeV/c^2 **(d)** 135 GeV/c^2

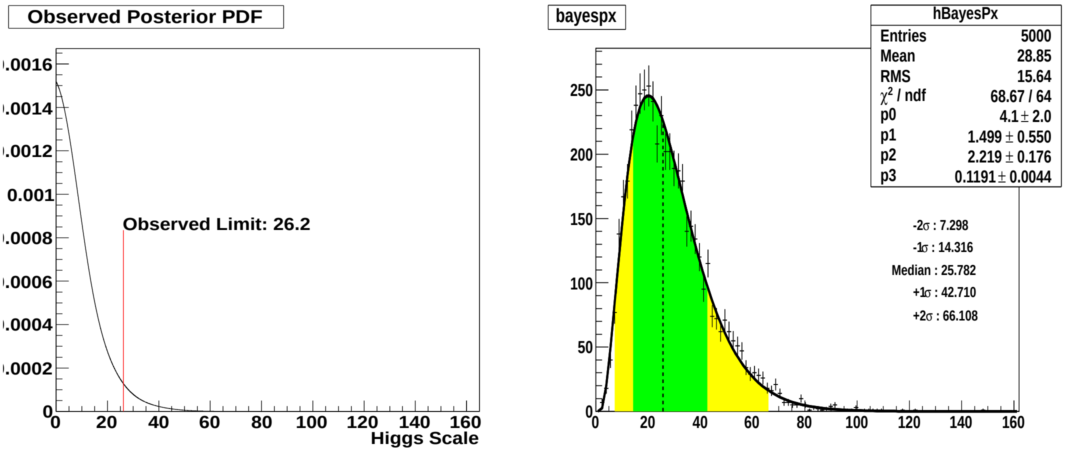

(e) 140 GeV/c^2 **(f)** 140 GeV/c^2

Figure C.11: The observed posterior densities and the pseudo-experiment distributions for a Higgs mass boson hypothesis of 130, 135 and 140 GeV/c^2 for the SS+SJ b-tagging category, respectively.

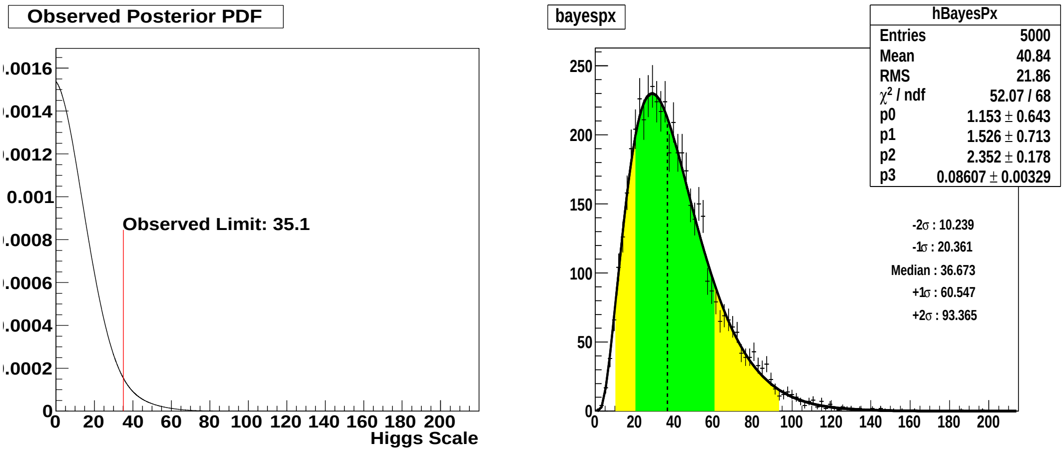

(a) 145 GeV/c^2 **(b)** 145 GeV/c^2

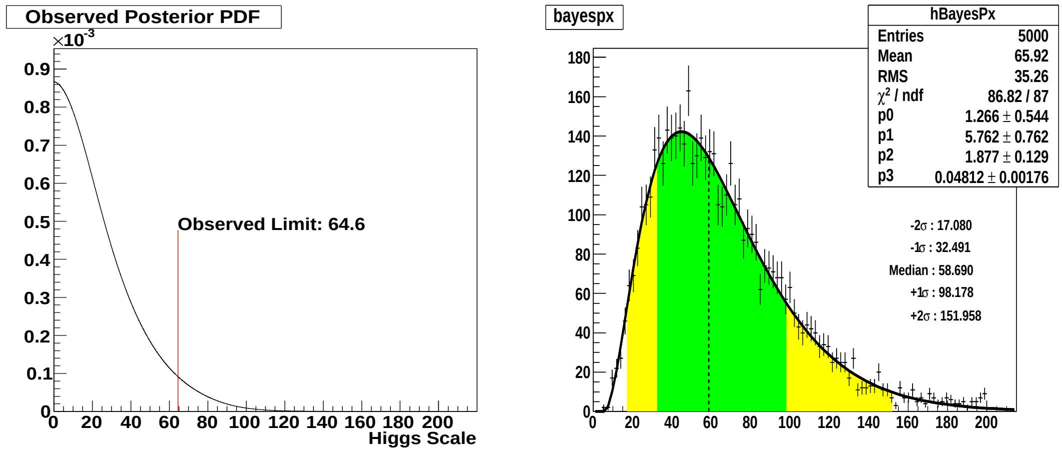

(c) 150 GeV/c^2 **(d)** 150 GeV/c^2

Figure C.12: The observed posterior densities and the pseudo-experiment distributions for a Higgs mass boson hypothesis of 145 and 150 GeV/c^2 for the SS+SJ b-tagging category, respectively.

Bibliography

[1] T. Aaltonen et al., *Top-quark mass measurement in events with jets and missing transverse energy using the full CDF data set*, *Phys. Rev. D* **88** (2013) 011101.

[2] T. Stelzer, Z. Sullivan, and S. Willenbrock, *Single top quark production via W-gluon fusion at next-to-leading order*, *Phys. Rev. D* **56** (1997) 5919.

[3] M. Jezabek and J. H. Kuhn, *QCD corrections to semileptonic decays of heavy quarks*, *Nucl. Phys. B* **314** (1989) 1.

[4] J. Beringer et al., *Review of Particle Physics*, *Phys. Rev. D* **86** (2012) 010001.

[5] S. Glashow, *Partial symmetries of weak interactions*, *Nucl. Phys.* **22** (1961) 579.

[6] A. Salam, *Weak and electromagnetic interactions*, *Conf. Proc.* **C680519** (1968) 367.

[7] S. Weinberg, *A model of leptons*, *Phys. Rev. Lett.* **19** (1967) 1264.

[8] G. 't Hooft and M. Veltman, *Regularization and renormalization of gauge fields*, *Nucl. Phys. B* **44** (1972) 189.

[9] F. Hasert et al., *Search for elastic muon-neutrino electron scattering*, *Phys. Lett. B* **46** (1973) 121.

[10] G. Arnison et al., *Experimental observation of isolated large transverse energy electrons with associated missing energy at $\sqrt{s} = 540$ GeV*, *Phys. Lett. B* **122** (1983) 103.

[11] G. Arnison et al., *Experimental observation of lepton pairs of invariant mass around 95 GeV/c^2 at the CERN SPS collider*, *Phys. Lett. B* **126** (1983) 398.

[12] P. Bagnaia et al., *Evidence for $Z^0 \to e^+e-$ at the CERN pp collider*, *Phys. Lett. B* **129** (1983) 130.

[13] H. D. Politzer, *Asymptotic freedom: An approach to strong interactions*, *Phys. Rept.* **14** (1974) 129.

[14] D. J. Gross and F. Wilczek, *Asymptotically free gauge theories. I*, *Phys. Rev. D* **8** (1973) 3633.

[15] F. Mandl and G. Shaw, *Quantum Field Theory.* Wiley, 2010.

[16] P. W. Higgs, *Broken symmetries, massless particles and gauge fields*, *Phys. Lett.* **12** (1964) 132.

[17] F. Englert and R. Brout, *Broken symmetry and the mass of gauge vector mesons*, *Phys. Rev. Lett.* **13** (1964) 321.

[18] P. W. Higgs, *Broken symmetries and the masses of gauge bosons*, *Phys. Rev. Lett.* **13** (1964) 508.

[19] A. Djouadi, J. Kalinowski, and M. Spira, *HDECAY: A program for Higgs boson decays in the standard model and its supersymmetric extension*, *Comput. Phys. Commun.* **108** (1998) 56.

[20] A. Djouadi, *The Anatomy of electro-weak symmetry breaking. I: The Higgs boson in the standard model*, *Phys. Rept.* **457** (2008) 1.

[21] S. Dawson and S. Willenbrock, *Radiative corrections to longitudinal vector boson scattering*, *Phys. Rev. D* **40** (1989) 2880.

[22] L. Durand, P. N. Maher, and K. Riesselmann, *Two-loop unitarity constraints on the Higgs boson coupling*, *Phys. Rev. D* **48** (1993) 1084.

[23] K. Riesselmann, *Large uncertainties in the cross section of elastic $W_L^+W_L^-$ scattering*, *Phys. Rev. D* **53** (1996) 6226.

[24] U. Nierste and K. Riesselmann, *Higgs sector renormalization group in the $\overline{MS}$ and on-mass-shell scheme: The breakdown of perturbation theory for a heavy Higgs boson*, *Phys. Rev. D* **53** (1996) 6638.

[25] T. P. Cheng, E. Eichten, and L.-F. Li, *Higgs phenomena in asymptotically free gauge theories*, *Phys. Rev. D* **9** (1974) 2259.

[26] B. Pendleton and G. G. Ross, *Mass and mixing angle predictions from infra-red fixed points*, *Phys. Lett. B* **98** (1981) 291.

[27] C. T. Hill, *Quark and lepton masses from renormalization group fixed points*, *Phys. Rev. D* **24** (1981) 691.

[28] J. Bagger, S. Dimopoulos, and E. Masso, *Heavy families: masses and mixinigs*, *Nucl. Phys. B* **253** (1985) 397.

[29] M. A. B. Bég, C. Panagiotakopoulos, and A. Sirlin, *Mass of the Higgs boson in the canonical realization of the Salam-Weinberg theory*, *Phys. Rev. Lett.* **52** (1984) 883.

[30] M. J. Duncan, R. Philippe, and M. Sher, *Theoretical ceiling on quark masses in the standard model*, *Phys. Lett. B* **153** (1985) 165.

[31] K. G. Wilson and J. Kogut, *The renormalization group and the ε expansion*, *Phys. Rept.* **12** (1974) 75.

[32] A. Hasenfratz, *Quantum Fields on the Computer.* World Scientific, 1992.

[33] M. Göckeler, H. A. Kastrup, T. Neuhaus, and F. Zimmermann, *Scaling analysis of the O(4)-symmetric φ^4-theory in the broken phase*, *Nucl. Phys. B* **404** (1993) 517.

[34] M. Lindner, M. Sher, and H. W. Zaglauer, *Probing vacuum stability bounds at the fermilab collider*, *Phys. Lett. B* **228** (1989) 139.

[35] M. Sher, *Precise vacuum stability bound in the standard model*, *Phys. Lett. B* **317** (1993) 159.

[36] G. Altarelli and G. Isidori, *Lower limit on the Higgs mass in the standard model: An update*, *Phys. Lett. B* **337** (1994) 141.

[37] J. A. Casas, J. R. Espinosa, and M. Quirós, *Improved Higgs mass stability bound in the standard model and implications for supersymmetry*, *Phys. Lett. B* **342** (1995) 171.

[38] M. Sher, *Electroweak Higgs potential and vacuum stability*, *Phys. Rept.* **179** (1989) 273.

[39] M. Lindner, *Implications of triviality for the standard model*, *Z. Phys. C* **31** (1986) 295.

[40] B. Grzadkowski and M. Lindner, *Stability of triviality mass bounds in the Standard Model*, *Phys. Lett. B* **178** (1986) 81.

[41] T. Hambye and K. Riesselmann, *Matching conditions and Higgs boson mass upper bounds reexamined*, *Phys. Rev. D* **55** (1997) 7255.

[42] J. Ellis, M. Gaillard, and D. Nanopoulos, *A phenomenological profile of the Higgs boson*, *Nucl. Phys. B* **106** (1976) 292.

[43] D. Jones and S. Petcov, *Heavy Higgs bosons at LEP*, *Phys. Lett. B* **84** (1979) 440.

[44] R. Barate et al., *Search for the standard model Higgs boson at LEP*, *Phys.Lett.* **B565** (2003) 61–75.

[45] S. Dittmaier and M. Schumacher, *The Higgs boson in the Standard Model - From LEP to LHC: Expectations, Searches, and Discovery of a Candidate*, *Prog. Part. Nucl. Phys.* **70** (2013) 1.

[46] G. Aad et al., *Observation of a new particle in the search for the Standard Model Higgs boson with the ATLAS detector at the LHC*, *Phys. Lett. B* **716** 1.

[47] S. Chatrchyan et al., *Observation of a new boson at a mass of 125 GeV with the CMS experiment at the LHC*, *Phys. Lett. B* **716** (2012) 30.

[48] T. Aaltonen et al., *Evidence for a particle produced in association with weak bosons and decaying to a bottom-antibottom quark pair in Higgs boson searches at the Tevatron*, *Phys. Rev. Lett.* **109** (2012) 071804.

[49] Tevatron New Physics Higgs Working Group, *Updated Combination of CDF and D0 searches for Standard Model Higgs boson production with up to 10.0 fb*$^{-1}$ *of data*, 2012. FERMILAB-CONF-12-318-E.

[50] H. M. Georgi, S. L. Glashow, M. E. Machacek, and D. V. Nanopoulos, *Higgs bosons from two-gluon annihilation in proton-proton collisions*, *Phys. Rev. Lett.* **40** (1978) 692.

[51] R. Cahn and S. Dawson, *Production of very massive Higgs bosons*, *Phys. Lett. B* **136** (1984) 196.

[52] D. Dicus and S. Willenbrock, *Higgs bosons from vector boson fusion in* e^+e^-*, ep, and pp collisions*, *Phys. Rev. D* **32** (1985) 1642.

[53] G. Altarelli, B. Mele, and F. Pitolli, *Heavy higgs production at future colliders*, *Nucl. Phys. B* **287** (1987) 205.

[54] W. Kilian, M. Krämer, and P. Zerwas, *Higgs-strahlung and WW fusion in e^+e^- collisions*, *Phys. Lett. B* **373** (1996) 135.

[55] S. L. Glashow, D. V. Nanopoulos, and A. Yildiz, *Associated production of Higgs bosons and Z particles*, *Phys. Rev. D* **18** (1978) 1724.

[56] J. Finjord, G. Girardi, and P. Sorba, *The needle in the large p_T haystack: Higgs versus quark or gluon jets together with Z_0 in hadronic reactions*, *Phys. Lett. B* **89** (1979) 99.

[57] E. Eichten, I. Hinchliffe, K. Lane, and C. Quigg, *Supercollider physics*, *Rev. Mod. Phys.* **56** (1984) 579.

[58] R. Raitio and W. W. Wada, *Higgs-boson production at large transverse momentum in quantum chromodynamics*, *Phys. Rev. D* **19** (1979) 941.

[59] Z. Kunszt, *Associated production of heavy higgs boson with top quarks*, *Nucl. Phys. B* **247** (1984) 339.

[60] A. Bagdasaryan, R. S. Egorian, S. Grigorian, and S. G. Matinyan, *Some peculiarities of conjoined hadroproduction of Standard Higgs boson and heavy quark pair*, *Sov. J. Nucl. Phys.* **46** (1987) 315.

[61] J. Ng and P. Zakarauskas, *QCD-parton calculation of conjoined production of Higgs bosons and heavy flavors in $p\overline{p}$ collisions*, *Phys. Rev. D* **29** (1984) 876.

[62] R. Barnett, H. Haber, and D. Soper, *Ultra-heavy particle production from heavy partons at hadron colliders*, *Nucl. Phys. B* **306** (1988) 697.

[63] F. Olness and W. Tung, *When is a heavy quark not a parton? Charged Higgs production and heavy quark mass effects in the QCD-based parton model* , *Nucl. Phys. B* **308** (1988) 813.

[64] D. A. Dicus and S. Willenbrock, *Higgs-boson production from heavy-quark fusion*, *Phys. Rev. D* **39** (1989) 751.

[65] E. Glover and J. van der Bij, *Higgs boson pair production via gluon fusion*, *Nucl. Phys. B* **309** (1988) 282.

[66] D. Dicus, C. Kao, and S. Willenbrock, *Higgs boson pair production from gluon fusion*, *Phys. Lett. B* **203** (1988) 457.

[67] G. Jikia, *Higgs boson pair production in high energy photon-photon collisions* , *Nucl. Phys. B* **412** (1994) 57.

[68] T. Plehn, M. Spira, and P. Zerwas, *Pair production of neutral higgs particles in gluon-gluon collisions*, *Nucl. Phys. B* **479** (1996) 46.

[69] V. Barger, T. Han, and R. J. N. Phillips, *Double higgs-boson bremsstrahlung from W and Z bosons at supercolliders*, *Phys. Rev. D* **38** (1988) 2766.

[70] A. Djouadi, W. Kilian, M. Mühlleitner, and P. Zerwas, *Production of neutral higgs-boson pairs at lhc*, *Eur. Phys. J. C* **10** (1999) 45.

[71] W. Keung, *Double Higgs from W-W fusion*, *Mod. Phys. Lett. A* **2** (1987) 765.

[72] O. Éboli, G. Marques, S. Novaes, and A. Natale, *Twin Higgs boson production*, *Phys. Lett. B* **197** (1987) 269.

[73] D. Dicus, K. Kallianpur, and S. Willenbrock, *Higgs boson pair production in the effective-W approximation*, *Phys. Lett. B* **200** (1988) 187.

[74] K. Kallianpur, *Pair production of Higgs bosons via heavy quark annihilation*, *Phys. Lett. B* **215** (1988) 392.

[75] A. Dobrovolskaya and V. Novikov, *Higgs and beyond the Standard Model. (In a search for nonstandard physics at SSC, LHC and LEP-2)*, *Z. Phys. C* **57** (1993) 685.

[76] A. Abbasabadi, W. Repko, D. Dicus, and R. Vega, *Comparison of exact and effective-gauge-boson calculations for gauge-boson fusion processes*, *Phys. Rev. D* **38** (1988) 2770.

[77] R. Ellis, I. Hinchliffe, M. Soldate, and J. V. D. Bij, *Higgs decay to $\pi^+\pi^-$: A possible signature of intermediate mass higgs bosons at high energy hadron colliders*, *Nucl. Phys. B* **297** (1988) 221.

[78] U. Baur and E. Glover, *Higgs boson production at large transverse momentum in hadronic collisions*, *Nucl. Phys. B* **339** (1990) 38.

[79] C. Kao, *Production of CP-odd Higgs bosons with large transverse momentum at hadron supercolliders* , *Phys. Lett. B* **328** (1994) 420.

[80] S. Dawson and R. Kauffman, *Production rates for Higgs boson plus multiple jets at the Superconducting Super Collider*, *Phys. Rev. Lett.* **68** (1992) 2273.

[81] R. Kauffman, S. Desai, and D. Risal, *Production of a higgs boson plus two jets in hadronic collisions*, *Phys. Rev. D* **55** (1997) 4005.

[82] V. Del Duca, W. Kilgore, C. Oleari, C. Schmidt, and D. Zeppenfeld, *Production of a Higgs boson accompanied by two jets via gluon fusion*, *Phys. Rev. Lett.* **87** (2001) 122001.

[83] V. Del Duca, A. Frizzo, and F. Maltoni, *Higgs boson production in association with three jets*, *JHEP* **0405** (2004) 064.

[84] K. Cheung, *Associated Higgs boson production with a vector boson pair at hadronic supercolliders*, *Phys. Rev. D* **49** (1994) 6224.

[85] A. Abbasabadi, W. Repko, D. Dicus, and R. Vega, *Single and double Higgs production by gauge boson fusion*, *Phys. Lett. B* **213** (1988) 386.

[86] D. Rainwater, *New method for extracting the bottom quark Yukawa coupling at the CERN Large Hadron Collider*, *Phys. Lett. B* **503** (2001) 320.

[87] A. Abbasabadi, D. Bowser-Chao, D. Dicus, and W. Repko, *Higgs-photon associated production at hadron colliders*, *Phys. Rev. D* **58** (1998) 057301.

[88] B. Mele, S. Petrarca, and A. Soddu, *A New evaluation of the $t \to cH$ decay width in the standard model*, *Phys. Lett. B* **435** (1998) 401.

[89] G. Eilam, J. L. Hewett, and A. Soni, *Rare decays of the top quark in the standard and two Higgs doublet models*, *Phys. Rev. D* **44** (1991) 1473.

[90] G. Mahlon and S. Parke, *Finite width effects in top quark decays*, *Phys. Lett. B* **347** (1995) 394.

[91] A. Bialas and P. Landshoff, *Higgs production in pp collisions by double-pomeron exchange*, *Phys. Lett. B* **256** (1991) 540.

[92] M. Boonekamp, R. Peschanski, and C. Royon, *Inclusive Higgs boson and dijet production via double pomeron exchange*, *Phys. Rev. Lett.* **87** (2001) 251806.

[93] B. Cox, J. Forshaw, and B. Heinemann, *Double diffractive higgs and di-photon production at the Tevatron and LHC*, *Phys. Lett. B* **540** (2002) 263.

[94] V. Khoze, A. Martin, and M. Ryskin, *Prospects for new physics observations in diffractive processes at the LHC and Tevatron*, *Eur.Phys.J.* **C23** (2002) 311.

[95] A. Kaidalov, V. Khoze, A. Martin, and M. Ryskin, *Central exclusive diffractive production as a spin-parity analyser: From Hadrons to Higgs*, *Eur. Phys. J. C* **31** (2003) 387.

[96] V. Khoze, A. Martin, and M. Ryskin, *Diffractive Higgs production: Myths and reality*, *Eur. Phys. J. C* **26** (2002) 229.

[97] J. Baglio, *Phenomenology of the Higgs at the hadron colliders: from the Standard Model to Supersymmetry.* PhD thesis, Université Paris-Sud 11, 2011.

[98] T. Sjöstrand et al., *PYTHIA 6.2: Physics and manual*, 2001.

[99] H. Lai et al., *Global QCD analysis of parton structure of the nucleon: CTEQ5 Parton Distributions*, *Eur. Phys. J. C.* **12** (2000) 375.

[100] J. Baglio and A. Djouadi, *Predictions for Higgs production at the Tevatron and the associated uncertainties*, *JHEP* **1010** (2010) 064.

[101] P. Bolzoni, F. Maltoni, S.-O. Moch, and M. Zaro, *Higgs Boson Production via vector boson fusion at next-to-next-to-leading order in QCD*, *Phys. Rev. Lett.* **105** (2010) 011801.

[102] A. Denner, S. Heinemeyer, I. Puljak, D. Rebuzzi, and M. Spira, *Standard Model Higgs boson branching ratios with uncertainties*, *Eur. Phys. J. C* **71** (2011) 1753.

[103] Fermilab Accelerator Operations Rookie Books, *Tevatron Rookie Book.* http://www-bdnew.fnal.gov/operations/rookie_books/Tevatron_v2.3.pdf.

[104] Fermilab Accelerator Operations Rookie Books, *Accelerator Concepts.* http://www-bdnew.fnal.gov/operations/rookie_books/Concepts_v3.6.pdf.

[105] Fermilab Accelerator Operations Rookie Books, *Linac Rookie Book.* http://www-bdnew.fnal.gov/operations/rookie_books/LINAC_RB_v2_3.pdf.

[106] Fermilab Accelerator Operations Rookie Books, *Booster Rookie Book*. http://www-bdnew.fnal.gov/operations/rookie_books/Booster_V4.1.pdf.

[107] Fermilab Accelerator Operations Rookie Books, *Main Injector Rookie Book*. http://www-bdnew.fnal.gov/operations/rookie_books/Main_Injector_v1.1.pdf.

[108] Fermilab Accelerator Operations Rookie Books, *Antiproton Source Rookie Book*. http://www-bdnew.fnal.gov/operations/rookie_books/Pbar_v2.2.pdf.

[109] Tevatron Luminosity. http://www.fnal.gov/pub/now/tevlum.html.

[110] P. Lukens, *The CDF IIb detector Technical design report*, 2003. FERMILAB-DESIGN-2003-01.

[111] E. Brücken, *Observation of central exclusive diphoton production at the tevatron*. PhD thesis, University of Helsinki, 2013.

[112] T. K. Nelson, *The CDF Layer 00 detector*, *Int. J. Mod. Phys.* **A16S1C** (2001) 1091.

[113] K. Bland, *Search for the Standard Model Higgs boson in the diphoton final state in $p\bar{p}$ collisions at $\sqrt{s} = 1.96$ TeV using the CDF II detector*. PhD thesis, Baylor University, 2012.

[114] W. Budgett et al., *The Good Run List*, 2001. CDF Internal Note 5613.

[115] M. Martinez, V. Sorin, and S. Camarda, *GOOD RUN LIST v45 Page*. http://www-cdf.fnal.gov/internal/dqm/goodrun/v45/goodv45.html.

[116] A. Bhatti et al., *Proposal for Level-2 calorimeter trigger upgrade*, 2006. CDF Internal Note 8415.

[117] Y.-C. Chen, A. Mitra, S.-Y. Tsai, and S.-M. Wang, *New MultiJet Trigger*, 2008. CDF Internal Note 9326.

[118] A. Mitra, S.-Y. Tsai, and S.-M. Wang, *Study of multijet triggers for the all-hadronic Higgs search*, 2009. CDF Internal Note 9954.

[119] A. Bhatti et al., *Determination of the jet energy scale at the Collider Detector at Fermilab*, *Nucl. Instr. and Meth. in Phys. A* **566** (2006) 375.

[120] D. E. Acosta et al., *Measurement of the $t\bar{t}$ production cross section in $p\bar{p}$ collisions at $\sqrt{s} = 1.96$ TeV using lepton + jets events with secondary vertex b−tagging*, *Phys. Rev. D* **71** (2005) 052003.

[121] A. Abulencia et al., *Measurement of the $t\bar{t}$ Production Cross Section in $p\bar{p}$ collisions at $\sqrt{s}$ = 1.96-TeV using Lepton + Jets Events with Jet Probability b-tagging*, *Phys. Rev. D* **74** (2006) 072006.

[122] A. Acosta, V. Necula, P. Pfeiffer, M. Schmitt, A. Sukhanov, D. Tsybychev, and S. Wang, *Introduction to Run II Jet Probability Heavy Flavor Tagger.* CDF Internal Note 6315.

[123] A. Jain, J. Mao, and K. M. Mohiuddin, *Artificial neural networks: a tutorial*, *Computer* **29** (1996) 31.

[124] T. Aaltonen et al., *Search for the Higgs boson in the all-hadronic final state using the full CDF data set*, *JHEP* **1302** (2013) 004.

[125] A. Hoecker et al., *TMVA: Toolkit for multivariate data analysis*, 2007.

[126] R. Brun and F. Rademakers, *ROOT - An Object Oriented Data Analysis Framework*, *Nucl. Inst. and Math. in Phys. Res. A* **389** (1997) 81.

[127] F. Abe et al., *Topology of three-jet events in $p\bar{p}$ collisions at $s = 1.8$ TeV*, *Phys. Rev. D* **45** (1992) 1448.

[128] M. Mangano, M. Moretti, F. Piccinini, R. Pittau, and A. Polosa, *ALPGEN, A generator for hard multiparton processes in hadronic collisions*, *JHEP* **07** (2003) 1.

[129] E. Gerchtein and M. Paulini, *CDF detector simulation framework and performance*, 2003. CHEP-2003-TUMT005.

[130] R. Brun et al., *GEANT 3: user's guide for Geant 3.10, Geant 3.11, CERN-DD-EE-84-01* (1987).

[131] S. Grinstein and D. Sherman, *SecVtx scale factors and mistag matrices for the 2007 Summer Conferences*, 2007. CDF Internal Note 8910.

[132] Tevatron New Phenomena and Higgs Working Group, *Combined CDF and D0 upper limit on Standard Model Higgs boson production with up to 8.6* fb^{-1} *of data*, 2011. FERMILAB-CONF-11-354-E.

[133] S. Geer and T. Asakawa, *Analysis of multijet events produced at high energy hadron colliders*, *Phys. Rev. D* **53** (1996) 4793.

[134] T. Aaltonen et al., *Search for the Higgs boson in the all-hadronic final state using the CDF II detector*, *Phys. Rev. D* **84** (2011) 52010.

[135] T. Aaltonen, A. Buzatu, B. Kilminster, Y. Nagai, and W. Yao, *Improved b-jet Energy Correction for $H \to b\bar{b}$ Searches at CDF*, 2011.

[136] Joint Physics Group, *ISR/FSR Prescription.* http://www-cdf.fnal.gov/internal/physics/joint_physics/agenda/20050527-minutes.html.

[137] M. J. Frank, *A search for the Standard Model Higgs boson produced in association with a W boson.* PhD thesis, Baylor University, 2011.

[138] T. Junk, *MClimit Software Page.* http://www-cdf.fnal.gov/ trj/mclimit/production/mclimit.html.

[139] T. Aaltonen et al., *Combination of Tevatron searches for the Standard Model Higgs boson in the W^+W^- decay mode*, *Phys. Rev. Lett.* **104** (2010) 061802.

[140] T. Aaltonen et al., *A search for the associated production of the Standard Model Higgs boson in the all-hadronic channel*, *Phys. Rev. Lett.* **103** (2009) 221801.

[141] T. Aaltonen et al., *Search for the standard model Higgs boson produced in association with top quarks using the full CDF data set*, *Phys. Rev. Lett.* **109** (2012) 181802.

[142] T. Aaltonen et al., *Search for a Higgs boson in the diphoton final state using the full CDF data set from $p\bar{p}$ collisions at $\sqrt{s}$ =1.96 TeV*, *Phys. Lett. B* **717** (2012) 173.

[143] J. Freeman, T. Junk, M. Kirby, Y. Oksuzian, T. Phillips, F. Snider, M. Trovato, J. Vizan, and W. Yao, *Introduction to HOBIT, a b-jet identification tagger at the CDF experiment optimized for light Higgs boson searches*, *Nucl. Instr. and Meth. in Phys. A* **697** (2013) 64.

[144] T. Aaltonen et al., *Search for the Standard Model Higgs boson decaying to a $b\bar{b}$ pair in events with two oppositely charged leptons using the full CDF data set*, *Phys. Rev. Lett.* **109** (2012) 111803.

[145] T. Aaltonen et al., *Search for the Standard Model Higgs boson decaying to a $b\bar{b}$ pair in events with one charged lepton and large missing transverse energy using the full CDF data set*, *Phys. Rev. Lett.* **109** (2012) 111804.

[146] T. Aaltonen et al., *Combination of searches for the Higgs boson using the full CDF data set*, *Phys. Rev. D* **88** (2013) 052013.